UNIVERSITAT DE BARCELONA

A Multifaceted Computational Study of the Structural, Energetic, and Electronic Properties of Titania Nanostructures

Miguel Recio Poo

A Multifaceted Computational Study of the Structural, Energetic, and Electronic Properties of Titania Nanostructures

Miguel Recio Poo

UNIVERSITAT DE BARCELONA

Memòria presentada por

Miguel Recio Poo

Per a optar al grau de Doctor per la

Universitat de Barcelona

Programa de doctorat en Química Teòrica i Modelització Computacional

A Multifaceted Computational Study of the Structural, Energetic, and Electronic Properties of Titania Nanostructures

Dirigida per:

Prof. Stefan T. Bromley
Universitat de Barcelona

Dr. Ángel Morales García
Universitat de Barcelona

Tutor:

Prof. Francesc Illas Riera
Universitat de Barcelona

UNIVERSITAT DE BARCELONA

Barcelona. 2025

Memòria presentada por

Miguel Recio Poo

Per a optar al grau de Doctor per la

Universitat de Barcelona

Programa de doctorat en Química Teòrica i Modelització Computacional

Un estudi computacional multifacètic de les propietats estructurals, energètiques i electròniques de les nanostructures de titània

Dirigida per:

Prof. Stefan T. Bromley
Universitat de Barcelona

Dr. Ángel Morales García
Universitat de Barcelona

Tutor:

Prof. Francesc Illas Riera
Universitat de Barcelona

UNIVERSITAT DE BARCELONA

Barcelona. 2025

A mi familia

Abstract

The devastating climatic and environmental effects of burning fossil fuels are now firmly established, emphasizing the urgent need for reliable and renewable energy sources. One promising alternative is hydrogen, which can be produced through photocatalytic water splitting using sunlight. Among various semiconductor materials explored for this purpose, titanium dioxide (TiO_2), also known as titania, stands out due to its chemical stability, non-toxicity, and low cost compared to other candidates like metal sulfides or perovskites. However, despite these advantages, TiO_2 alone is not an efficient photocatalyst for water splitting due to its large bandgap, which limits visible-light absorption, and its high charge recombination rates. Nevertheless, it serves as a suited model system for understanding fundamental photocatalytic processes and can be functionalized—via doping, heterostructuring, or surface modifications—to create more efficient photocatalytic agents. Given its widespread use in photocatalysis, photovoltaics, and environmental remediation, gaining a detailed understanding of the structural and electronic properties of TiO_2 at the nanoscale is essential for developing more effective and optimized photoactive materials.

In this thesis, we systematically investigate the structural, electronic, thermodynamic, and excited states properties of TiO_2 nanosystems, focusing on the role of hydroxylation and the influence of nanostructuring. Through a combination of classical and *ab initio* molecular dynamics, density functional theory (DFT), time-dependent DFT (TD-DFT), and nonadiabatic molecular dynamics (NA-MD), we explore how size, crystallinity, and surface functionalization influence the stability and electronic properties of such TiO_2 systems. We show that increasing hydroxylation leads to a convergence in structural and electronic properties between amorphous and crystalline nanoparticles (NPs), giving rise to “crystalike” structures—amorphous nanomaterials that mimic the electronic behaviour of the photoactive anatase crystalline phase. Additionally, our refined model for the ligand-induced dipole effect (LIDE) reveals a nonlinear dependence of electronic energy level shifts on hydroxyl coverage, allowing for precise tuning of conduction and valence band positions. In the context of thermodynamics, we develop an analytical function to approximate the

vibrational contributions to the Gibbs free energy of formation ($\Delta G_f(T,p)$) as a function of NP size and hydroxylation degree. This function enables corrections to $\Delta G_f(T,p)$ calculations based on 0 K total energies, avoiding the need for computationally expensive vibrational frequency calculations. The effect of these corrections diminishes for larger systems but remains significant for NPs up to tens of nanometers in diameter. This approach bridges the gap between computational methods suited for small clusters and those applicable to extended surfaces, allowing for efficient phase diagram calculations of nanosystems interacting with their environment. Finally, by explicitly exploring the excited-state dynamics using NA-MD methodologies, we rigorously analyse the radiative and nonradiative relaxation processes in small TiO_2 nanoclusters. Here we provide an accurate description of charge carrier recombination which is an important factor that determines photocatalytic performance.

Beyond analysing how hydroxylation and size influence TiO_2-based nanomaterials, this thesis introduces new computational models to more accurately describe the thermodynamics and electronic properties of nanostructures. These developments improve the theoretical frameworks available for studying nanoscale materials, particularly in the context of photocatalysis and electronic structure tuning. In this way, by advancing our fundamental understanding of TiO_2 at the nanoscale, this work contributes to the ongoing development of more efficient photocatalytic and optoelectronic materials.

Keywords: Photocatalysis, titania, hydration, semiconductors, excited states.

Resum

Els devastadors efectes climàtics i ambientals de la combustió de combustibles fòssils estan àmpliament establerts, subratllant la necessitat urgent de fonts d'energia fiables i renovables. Una alternativa prometedora és l'hidrogen, que es pot produir mitjançant la fotocatàlisi de l'aigua amb llum solar. Entre els diversos materials semiconductors explorats per a aquest propòsit, el diòxid de titani (TiO_2), també conegut com a titània, destaca per la seva estabilitat química, no toxicitat i baix cost en comparació amb altres candidats com els sulfurs metàl·lics o les perovskites. No obstant això, malgrat aquests avantatges, el TiO_2 per si sol no és un fotocatalitzador eficient per a la fotòlisi de l'aigua a causa del seu ample band gap, que limita l'absorció de llum visible, i de les seves altes taxes de recombinació de càrrega. Tot i així, serveix com a sistema model excel·lent per comprendre els processos fotocatalítics fonamentals i pot ser funcionalitzat —mitjançant dopatge, heteroestructuració o modificacions de superfície— per crear agents fotocatalítics més eficients. Donat el seu ampli ús en fotocatàlisi, fotovoltaica i remediació ambiental, obtenir una comprensió detallada de les propietats estructurals i electròniques del TiO_2 a escala nanomètrica és essencial per desenvolupar materials més efectius i optimitzats.

En aquesta tesi, investiguem sistemàticament les propietats estructurals, electròniques i termodinàmiques de les nanoestructures de TiO_2, centrant-nos en el paper de la hidroxilació i la influència de la nanoestructuració. A través d'una combinació de dinàmica molecular clàssica i *ab initio*, teoria del funcional de la densitat (DFT), DFT dependent del temps (TD-DFT) i dinàmica molecular no adiabàtica (NA-MD), explorem com la mida, la cristal·linitat i la funcionalització de la superfície influeixen en l'estabilitat i les propietats electròniques de les nanopartícules (NPs) de TiO_2. Demostrem que l'augment de la hidroxilació condueix a una convergència en les propietats estructurals i electròniques entre les NPs amorfes i cristal·lines, donant lloc a estructures "cristaloides" —nanomaterials amorfs que imiten el comportament electrònic de la fase cristal·lina fotoactiva de l'anatasa. A més, el nostre model refinat per a l'efecte de dipol induït per lligands (LIDE) revela una dependència no lineal dels desplaçaments dels nivells d'energia electrònica respecte a la cobertura d'hidroxil,

permetent un ajust precís de les posicions de les bandes de conducció i valència.

En el context de la termodinàmica, desenvolupem una funció analítica per aproximar les contribucions vibracionals a l'energia lliure de Gibbs de formació ($\Delta G_f(T,p)$) en funció de la mida de la NP i del grau d'hidroxilació. Aquesta funció permet corregir els càlculs de $\Delta G_f(T,p)$ basats en energies totals a 0 K, evitant la necessitat de càlculs costosos de freqüències vibracionals. L'efecte d'aquestes correccions disminueix en sistemes més grans, però continua sent significatiu per a NPs de fins a desenes de nanòmetres de diàmetre. Aquest enfocament permet connectar els mètodes computacionals adequats per a petits clústers amb aquells aplicables a superfícies esteses, facilitant el càlcul eficient de diagrames de fase de nanosistemes en interacció amb el seu entorn. Finalment, mitjançant l'exploració explícita de la dinàmica en estat excitat utilitzant NA-MD, analitzem rigorosament els processos de relaxació radiativa i no radiativa en petits nanoclústers de TiO_2. Això ens permet descriure amb precisió la recombinació de portadors de càrrega, un factor clau que determina el rendiment fotocatalític.

Més enllà d'analitzar com la hidroxilació i la mida influeixen en els nanomaterials basats en TiO_2, aquesta tesi introdueix nous models computacionals per descriure amb més precisió la termodinàmica i les propietats electròniques de les nanoestructures. Aquests avenços milloren els marcs teòrics disponibles per estudiar materials a nanoescala, especialment en el context de la fotocatàlisi i l'ajust de l'estructura electrònica. En aprofundir en la comprensió fonamental del TiO_2 a escala nanomètrica, aquest treball contribueix al desenvolupament continu de materials fotocatalítics i optoelectrònics més eficients.

Paraules clau: Fotocatàlisi, titània, hidratació, semiconductors, estats excitats.

Agradecimientos

Esta tesis no podría haberse completado sin la inestimable ayuda de muchas personas que han formado parte de mi camino durante estos últimos cuatro años y medio.

En primer lugar, como es natural, he de agradecer a mis directores de tesis, Stefan T. Bromley y Ángel Morales García, cuyas enseñanzas y paciencia han sido una constante durante mi tesis. Más allá del acierto en sus múltiples enfoques, es de destacar la combinación entre la perseverancia de Ángel y la creatividad de Stefan—un equilibrio que ha resultado muy fructífero, como prueban los distintos trabajos publicados en estos años. Asimismo, agradezco profundamente a mi tutor, Francesc Illas Riera, por sus valiosos consejos, que han trascendido el marco de esta tesis, ofreciéndome una visión más amplia sobre la carrera científica y sus *tempos*—una perspectiva que solo otorgan la experiencia y el buen hacer.

También quiero expresar mi gratitud a Alexey Akimov, supervisor durante mis estancias en la University at Buffalo, por su cálida acogida en su grupo de investigación. Sus enseñanzas han sido fundamentales para el desarrollo de esta tesis, permitiéndome incorporar metodologías novedosas y nuevas herramientas de trabajo. Extiendo este agradecimiento a los estudiantes de su grupo, especialmente a Mohammad Shakiba y Qingxin Zhang, quienes, con paciencia y generosidad, respondieron a todas mis dudas y facilitaron mi integración en dicho equipo, con el que sigo colaborando activamente.

De regreso a Barcelona y a su Universitat, quiero dar las gracias a los distintos compañeros de despacho y departamento que me han acompañado en estos años. Aunque el inicio de mi tesis estuvo marcado por la compleja situación de aislamiento impuesta por la COVID-19, en los últimos años el ambiente ha sido mucho más acogedor, favoreciendo conversaciones enriquecedoras que han hecho el día a día más llevadero. Es importante para mí agradecer también a los distintos profesores a quienes he podido asistir en tareas de docencia durante estos años. Aunque fueron periodos breves, la oportunidad de impartir clases a

alumnos universitarios por primera vez ha sido un hito en mi trayectoria que siempre recordaré.

Fuera del ámbito académico, mi familia ha sido un pilar indispensable para cursar mis estudios y realizar esta tesis. Su apoyo ha sido fundamental, no solo en el plano emocional, sino también en el económico, permitiéndome dedicarme plenamente a la investigación. Tener padres docentes universitarios ha sido un privilegio cuyo valor he aprendido a apreciar con el tiempo.

Del mismo modo, Caro, mis amigos de Asturias y Barcelona y mis compañeros de piso Santi y Toni—también amigos—, han sido un gran apoyo en mi rutina diaria, escuchando y aconsejando de manera desinteresada. A día de hoy, sois la gente que más presencia tiene en mi vida y no hace falta que me explaye detallando la importancia que tenéis.

A todos ellos, gracias, esta tesis es en parte vuestra.

Abbreviations

NP - Nanoparticle

QC - Quantum **C**onfinement

UV - Ultrav**i**olet

PEC – Photoelectrochemical **C**ell

VB - Valence **B**and

CB - Conduction **B**and

OER - Oxygen **E**volution **R**eaction

HER - Hydrogen **E**volution **R**eaction

MD - Molecular **D**ynamics

AIMD – ***Ab Initio*** **M**olecular **D**ynamics

DFT - Density **F**unctional **T**heory

AIAT - ***Ab Initio*** **A**tomistic **T**hermodynamics

TD-DFT - Time-**D**ependent **D**ensity **F**unctional **T**heory

NA-MD - Non**a**diabatic **M**olecular **D**ynamics

PES - Potential **E**nergy **S**urface

GULP - General **U**tility **L**attice **P**rogram

FHI-AIMS - **F**ritz **H**aber **I**nstitute ***Ab Initio*** **M**aterials **S**imulations

GPW - Gaussian and **P**lane **W**aves

PBE - Perdew-**B**urke-**E**rnzerhof

CI - **C**onfiguration **I**nteraction

CC - **C**oupled **C**luster

KS - Kohn-**S**ham

LDA - Local **D**ensity **A**pproximation

GGA - Generalized **G**radient **A**pproximation

B3LYP - Becke, **3**-Parameter, **L**ee–**Y**ang–**P**arr

CAM-B3LYP - Coulomb-**A**ttenuating **M**ethod **B3LYP**

NAO - Numeric **A**tom-Centered **O**rbital

TZVP - Triple-**Z**eta **Va**lence Plus **P**olarization

SCF - Self-**C**onsistent **F**ield

DOS - Density **O**f **S**tates

CT – **C**harge **T**ransfer

ST - **S**pin **T**ransfer

EET - **E**xcitation **E**nergy **T**ransfer

TD-SE - Time-**D**ependent **S**chrödinger **E**quation

CPA - Classical **P**ath **A**pproximation

NAC - Non**a**diabatic **C**oupling

NBRA - Neglect **O**f **B**ack-**R**eaction **A**pproximation

MQCD - Mixed **Q**uantum-**C**lassical **D**ynamics

TD-KS - Time-**D**ependent **K**ohn-**S**ham

TDA - Tamm-**D**ancoff **A**pproximation

TSH - Trajectory **S**urface **H**opping

FSSH - Fewest **S**witches **S**urface **H**opping

DISH - Decoherence-**I**nduced **S**urface **H**opping

IDA - Instantaneous **D**ecoherence at **A**ttempted Hops

mSDM - Modified **S**implified **D**ecay Of **M**ixing

LD - Local **D**iabatization

HOMO – **H**ighest **O**ccupied **M**olecular **O**rbital

LUMO – **L**owest **U**noccupied **M**olecular **O**rbital

LIDE – Ligand **I**nduced **D**ipole **E**ffect

CBM – **C**onduction **B**and **M**inimum

VBM – **V**alence **B**and **M**aximum

SP – **S**ingle **P**article

MB – **M**any-**B**ody

RSF – **R**ange-**S**eparated **F**unctionals

List of figures

TABLE OF CONTENTS

1 INTRODUCTION

The ability to control and manipulate materials at the nanoscale has led to huge advancements in diverse fields, from electronics to energy conversion and catalysis. Nanostructuring materials not only modifies their electronic and optical properties but also enhances their surface reactivity, enabling novel functionalities that differ significantly from their bulk counterparts. Furthermore, the interaction between nanostructured materials and their environment—such as the adsorption of gas molecules—plays a crucial role in determining their physicochemical behaviour. Adsorbates, including water, oxygen, and other reactive species, can alter surface states, charge distribution, and reactivity, making them key factors in applications like sensing, catalysis, and photovoltaics.

Among nanostructured materials, titanium dioxide (TiO_2), or titania, stands out as a widely studied system due to its versatile photocatalytic properties and technological relevance. This thesis investigates how key structural factors—including size, crystallinity, and surface interactions—shape the ground and excited state properties of TiO_2 nanostructures - mainly nanoparticles (NPs). Using computational modelling, we analyse how these variables influence the electronic structure of these systems, which provides insights into their photocatalytic performance. The theoretical work in this thesis provides a general platform for a deeper understanding of semiconductor NPs and how they can be tuned for photocatalysis and related processes.

Before moving to a detailed discussion of the properties of TiO_2 nanosystems, we first review key contributions that have shaped our understanding of size-dependent effects in inorganic materials, particularly semiconductors.

1.1 Nanostructuring materials

Reducing material dimensions from the macroscopic to the nanoscale profoundly alters physical, chemical, and electronic properties. As the system size reduces, materials transition through distinct size regimes, each with characteristic structural and electronic behaviours. At the smallest scales, nanoclusters (approximately < 100 atoms) exist in the "Every Atom Counts" regime, where quantum effects dominate. The discrete nature of electronic states leads to significant variations in optical, electronic, and catalytic properties.[1,2] Nanoclusters, for instance, exhibit molecular-like behaviour, where the addition or

removal of a single atom can critically affect stability and reactivity.[3] At this extreme small size, the structure lacks long-range order and depends heavily on synthesis conditions and environmental interactions. As nanoclusters grow, they transition into amorphous or partially ordered phases, where short-range order persists but long-range crystallinity is still absent.[4,5] In this regime, surface effects remain dominant, but bulk-like properties begin to emerge. Amorphous materials, for example, often exhibit lower density, different optical absorption edges, and higher defect concentrations, which can enhance catalytic activity but may reduce charge carrier mobility.[6]

With increasing size, NPs (which number of atoms ranges from approximately 10^2 to 10^6) adopt shapes that minimize surface energy (see Figure 1.1). The shapes of crystalline NPs can be described by the Wulff construction, which predicts equilibrium crystal morphologies based on facet-specific surface energies.[7] These facets influence catalytic and electronic properties, making them crucial in applications like photocatalysis and photovoltaics.[8] At even larger scales, bulk-like properties dominate, though surfaces remain critical in defining overall material behaviour. Surface terminations influence charge separation efficiency in semiconductors, with high-energy facets providing active sites for reactions.[9] Surface reconstructions, passivation, and defect states further impact carrier recombination rates and surface charge density, affecting photocatalytic and electronic performance.[10]

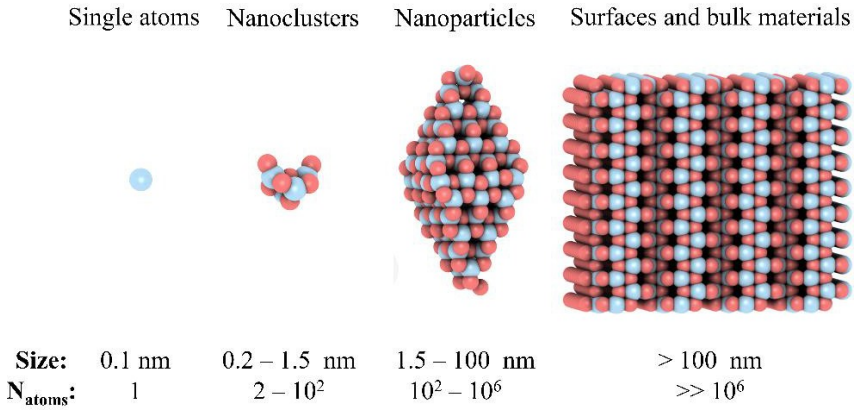

Figure 1.1 Geometric structure of single atoms, nanoclusters, nanoparticles, surfaces and bulk materials.

Generally, reducing material dimensions to the nanoscale leads to significant changes in a wide range of properties, including electronic, optical, mechanical, thermal, and catalytic behaviours.[11-14] Such size-dependent phenomena not only distinguish nanomaterials from their bulk counterparts but also enable the design of nanosystems with tailored properties for applications in energy conversion, catalysis, and beyond.[15] A general framework for understanding nanoscale material properties can be described in terms of a scalable versus non-scalable regime (see Figure 1.2).[16] In the scalable regime, properties such as electronic structure, thermodynamic stability, and catalytic activity follow a predictable size-dependent trend, often describable by power laws. This corresponds to a smooth transition from bulk materials to nanoscale systems. However, at the smallest size scale, in the non-scalable "Every Atom Counts" regime, every atomic addition or removal can introduce abrupt changes in properties.

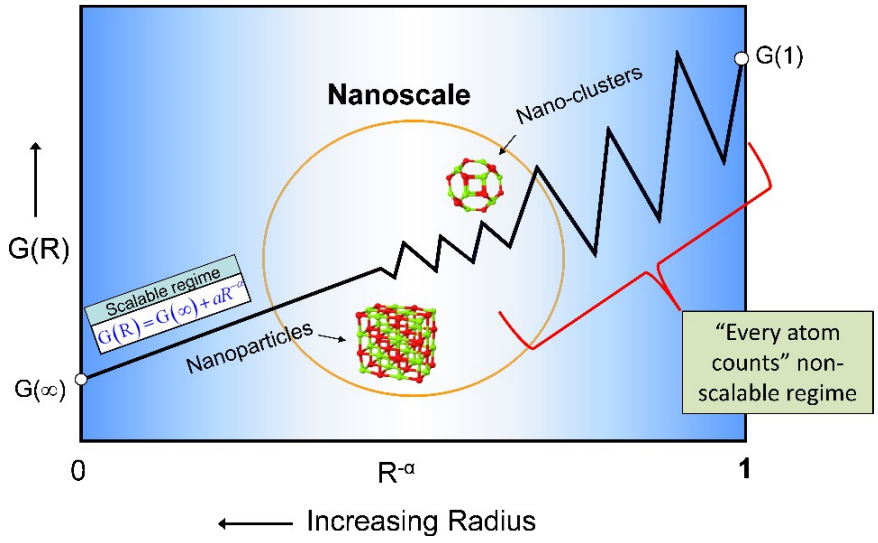

Figure 1.2: Schematic representation of the nanoparticle size regime that we focus on (circled area) with respect to an arbitrary property G(R), where R is the system radius (adapted from reference 16).

This is particularly relevant in nanoclusters, where quantum confinement effects and surface interactions play a dominant role in dictating structural and functional characteristics. In NPs, two fundamental effects drive the evolution

of electronic and optical properties: quantum confinement (QC) and surface-to-volume ratio effects. QC arises when the size of a NP becomes comparable to or smaller than the de Broglie wavelength of electrons. In this regime, the continuous electronic bands seen in bulk materials break down into discrete energy levels, leading to an increase in bandgap energy (as depicted in Figure 1.3). This phenomenon has been extensively studied in semiconductor nanocrystals, such as CdSe, or TiO_2, where controlling NP size allows for precise tuning of optoelectronic properties.[17,18] For example, in small semiconductor NPs of 1-2 nm, QC shifts the conduction and valence bands apart, affecting their ability to absorb light and participate in charge transfer reactions.[19,20]

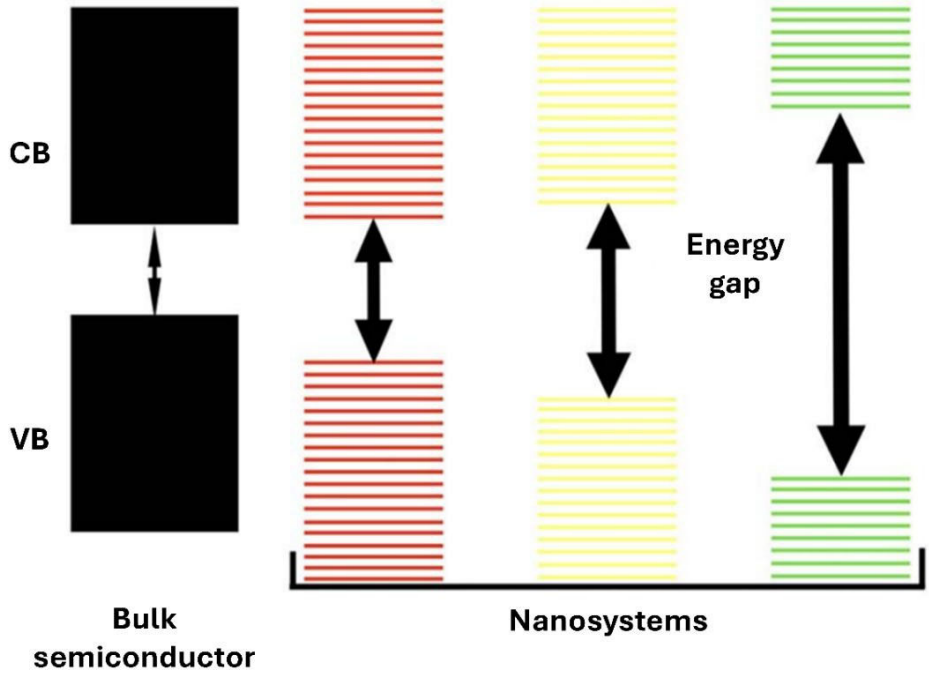

Figure 1.3: Schematic representation of the quantum confinement effect on the energy levels of a material with decreasing size. CB and VB stand, respectively, for Conduction Band and Valence Band.

Surface-to-volume ratio effects become increasingly significant as particle size decreases. A greater proportion of atoms reside at or near the surface, making interfacial phenomena dominant. This enhanced surface reactivity influences

adsorption, catalytic activity, and overall electronic properties, particularly in semiconductors.[21] The combined impact of QC and increased surface contributions results in pronounced size-dependent shifts in optical properties. Semiconductor NPs exhibit a blue shift in absorption and emission spectra as size decreases, a trend well-documented in materials like CdS and ZnO.[22] Similarly, metal NPs, such as gold, show strong variations in surface plasmon resonance with changing size.[23] These tunable optical properties are crucial for applications in solar energy conversion, photocatalysis, and optoelectronic devices.

Beyond electronic and optical characteristics, nanoscale reduction also impacts mechanical strength, thermal transport, and catalytic activity. Mechanical properties improve at the nanoscale due to reduced defect densities and enhanced grain boundary effects.[24] Nanocrystalline materials often exhibit increased hardness and strength compared to their bulk counterparts, as observed in studies on ultrafine-grained metals and ceramics.[25] These enhancements arise because dislocation movement—the primary mechanism of plastic deformation in bulk materials—is significantly hindered in nanostructured systems.[26]

Thermal conductivity also changes drastically at reduced dimensions due to enhanced phonon scattering at grain boundaries and surfaces.[27] In materials such as silicon nanowires, nanoscale effects lead to a significant reduction in thermal conductivity compared to bulk silicon, a crucial property for thermoelectric applications.[28] By carefully controlling size and morphology, researchers can engineer nanostructured materials with tailored thermal properties for heat management in electronics and energy harvesting technologies.[29]

Perhaps the most profound nanoscale effect is observed in catalysis. The high surface area of nanomaterials provides more active sites for chemical reactions, while their altered electronic structure enhances catalytic efficiency.[30] A striking example is gold: while bulk gold is chemically inert, nanoscale gold becomes a highly active catalyst for oxidation reactions.[31] Similar principles apply to semiconductor nanostructures, where surface properties and charge carrier dynamics dictate photocatalytic performance.[32] The interplay between QC, surface chemistry, and defect states plays a crucial role in optimizing materials for water splitting, environmental remediation, and solar fuel generation.[33]

1.2 Role of hydration

The importance of nanostructuring materials is further highlighted by the fact that hydration—and, more broadly, interactions with adsorbates—becomes particularly influential at the nanoscale. In nanosystems, a significant fraction of atoms resides at or near the surface, so interactions with water molecules and hydroxyl groups can profoundly reshape the local atomic structure, modifying the material's electrostatic environment.[34] These effects play a pivotal role in defining the structural, electronic, and catalytic properties of nanomaterials, making hydration a key determinant of their functionality and performance.

Structurally, hydration can induce surface reconstruction, amorphization, or stabilization of metastable phases, particularly in oxide-based nanomaterials.[6] The adsorption of water molecules alters the arrangement of surface atoms, sometimes causing lattice distortions or promoting the stabilization of specific crystal facets to minimize surface energy.[35] In TiO_2, for instance, hydration influences phase stability and morphology in NPs, playing a crucial role in defining the material's functional properties.[34] The interaction of water with surface sites can also modify the expression of different crystallographic facets, further impacting reactivity and catalytic efficiency.[8]

Beyond structural changes, hydration has profound electronic effects**,** primarily through the ligand-induced dipole effect (LIDE).[36] When water, hydroxyl groups, or organic ligands adsorb onto a semiconductor surface, they create interfacial dipoles that shift the conduction and valence band edges, effectively tuning the material's electronic energy levels. This phenomenon has been widely observed in metal oxides and colloidal quantum dots, where hydration-induced dipole layers can significantly influence charge transport, electron-hole recombination rates, and overall photocatalytic performance.[37-39] Such experimental and theoretical studies suggest that hydration-induced dipoles can shift semiconductor band edges by several hundred meV, demonstrating their critical role in fine-tuning electronic properties.

Hydration effects are particularly relevant in photocatalysis and electrochemical applications, where surface interactions with water molecules directly

impact charge transfer dynamics. In black TiO_2, the introduction of thiocyanate ligands created a strong interfacial dipole, leading to a 0.6 eV shift in band structure and significantly improving charge separation efficiency for photocatalytic CO_2 reduction.[40] Similar hydration-induced band structure modifications have been reported in ZnO or Fe_2O_3, where water adsorption alters surface electronic states and enhances catalytic activity.[41,42] The magnitude of these effects depends strongly on NP size, crystal facets, and environmental conditions**,** with smaller NPs being more susceptible to hydration due to their higher surface energy and increased density of active sites. In several metal oxides, hydration often leads to the formation of surface hydroxyl groups, which play a crucial role in charge trapping, catalytic activity, and interfacial charge transfer.[6,43] Depending on their adsorption geometry and local electronic structure, these hydroxyl groups can either facilitate or hinder charge separation.[44]

1.3 The Honda-Fujishima Experiment (1972)

Among the various semiconductors that exhibit size-dependent properties, TiO_2 has gained significant attention due to its stability, abundance, and unique electronic characteristics. While TiO_2 was originally studied for its optical and electronic properties, its catalytic potential at the nanoscale later became a key focus. The ability of titania to absorb ultraviolet (UV) light and participate in photochemical reactions set the stage for one of the most influential discoveries in photocatalysis. This discovery demonstrated, for the first time, that TiO_2 could facilitate water splitting under UV irradiation. This groundbreaking experiment conducted by Akira Fujishima and Kenichi Honda in 1972 marked the first demonstration of photocatalytic water splitting, setting the foundation for the field of artificial photosynthesis.[45]

In this experiment, Fujishima and Honda employed a photoelectrochemical (PEC) cell, with an n-type TiO_2 (rutile) electrode acting as the photoanode and a platinum (Pt) counter-electrode (see Figure 1.4). The PEC cell was irradiated with UV light, which had energy exceeding the bandgap of bulk titania (around 3.0 to 3.2 eV). The absorbed photons excited electrons from the valence band of TiO_2 to its conduction band, leaving behind positively charged holes. The electrons travelled through an external circuit to the Pt electrode, where they

reduced protons in the solution to hydrogen gas. Meanwhile, the holes in the TiO_2 oxidized water at the anode, generating oxygen gas.

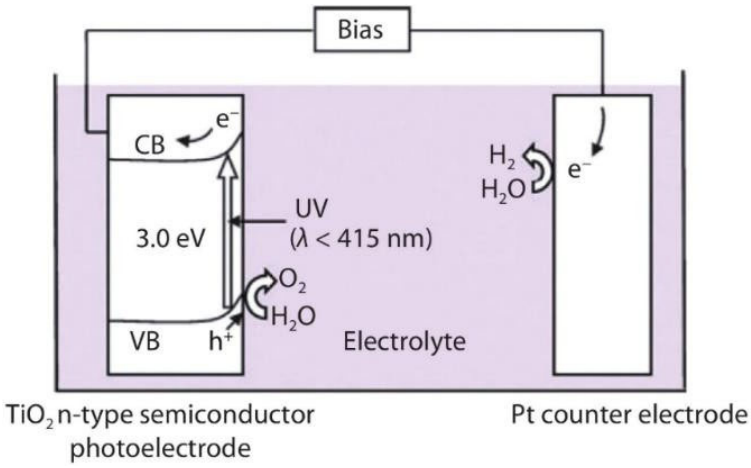

Figure 1.4: Schematic illustration of water splitting using a TiO_2 n-type semiconductor photoelectrode (adapted from reference 33). Upon UV illumination ($\lambda < 415$ nm), TiO_2 absorbs photons with energy ≥ 3.0 eV, exciting electrons (e^-) from the VB to the CB, leaving behind holes (h^+). The holes drive water oxidation at the TiO_2 surface, generating O_2 and protons in the electrolyte. Electrons travel through an external circuit under applied bias to the Pt counter electrode, where they facilitate H_2 evolution.

This discovery became known as the Honda-Fujishima effect, illustrating the potential of semiconductor photocatalysts to employ solar energy for driving redox reactions. However, TiO_2 could only utilize the UV portion of sunlight, which represents less than 5% of the total solar spectrum. Despite this limitation, the experiment was a significant step toward solar-driven hydrogen production, a clean and renewable energy source.

The original setup achieved a modest quantum efficiency and energy conversion efficiency of approximately 0.4% under sunlight, with later experiments confirming these values.[46] While the efficiency was low, the experiment proved the concept of using solar energy for water splitting, opening new research ways aimed at improving semiconductor performance and expanding their light absorption to the visible range.

The Honda-Fujishima experiment also ignited extensive interest in titania-based photocatalysis, leading to decades of research focused on enhancing the photocatalytic properties of titania. These efforts include material modifications, such as doping with metal and non-metal elements, to extend TiO_2's light absorption into the visible spectrum and improve charge separation efficiency. Before moving into all these advances, it is important to understand how the photocatalytic process takes place in such titania systems.

1.4 Photocatalytic water splitting

Titania-based photocatalytic water splitting became a promising technology for solar energy conversion to chemical energy by generating hydrogen (H_2) and oxygen (O_2) through light-driven reactions. In short, the process involves three key steps (see Figure 1.5): photon absorption to excite electrons from the valence to the conduction band, charge carrier separation and migration to the surface, and surface redox reactions where water molecules are split into H_2 and O_2.

When TiO_2 is irradiated with light of energy equal to or greater than its band gap, electrons in the valence band are excited to the conduction band, leaving behind holes in the VB:

$$TiO_2 + h\nu \rightarrow \underset{CB}{e^-} + \underset{VB}{h^+} \tag{1.1}$$

This process generates electron-hole pairs, which are the primary charge carriers driving subsequent redox reactions. Such photogenerated electrons and holes must migrate to the surface of the photocatalyst to participate in surface reactions. Efficient charge separation is critical to avoid recombination, which dissipates the energy as heat.

At the surface of TiO_2, the holes in the VB oxidize water molecules to produce oxygen:

$$2H_2O + 4h^+_{VB} \rightarrow O_2 + 4H^+ \tag{1.2}$$

Simultaneously, electrons in the CB reduce protons to generate hydrogen:

$$4H^+ + 4e^-_{CB} \rightarrow 2H_2 \quad (1.3)$$

The overall reaction is:

$$H_2O \rightarrow H_2 + \frac{1}{2}O_2 \quad (1.4)$$

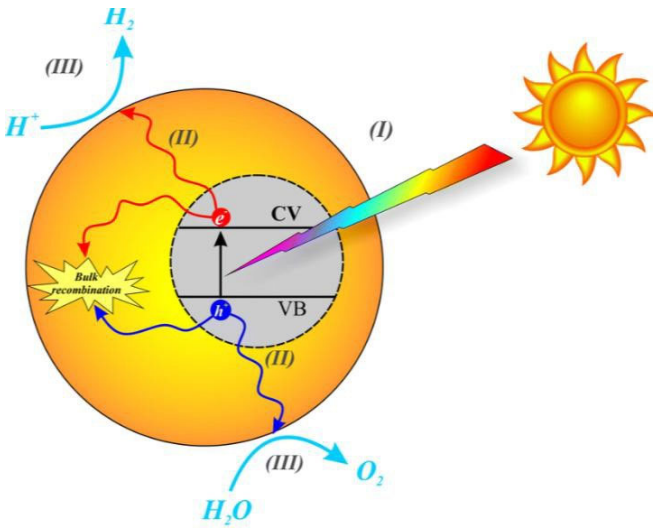

Figure 1.5: Key steps in photocatalytic water splitting using titania: (I) photon adsorption to excite electrons; (II) charge carrier separation; (III) surface redox reactions.[47]

This reaction is thermodynamically uphill, requiring an input of 237.13 kJ/mol of Gibbs free energy.

1.5 Evolution of Titania in Photocatalysis

Following the pioneering work of Fujishima and Honda in 1972, significant advancements have been made in the field of titania photocatalysis. In the mid-to-late 1970s, researchers began exploring methods to improve the photocatalytic performance of TiO_2 by addressing the critical issue of charge carrier recombination. Studies revealed that much of the inefficiency in TiO_2-based photocatalysis are caused by the rapid recombination of photogenerated electron-

hole pairs before they could participate in the redox reactions necessary for water splitting.[21,48,49] A significant breakthrough occurred in 1977 when Schrauzer and Guth showed that powdered TiO_2 loaded with platinum could effectively promote the decomposition of water when exposed to sunlight.[50] The platinum acted as a co-catalyst, aiding in electron transfer and minimizing recombination by functioning as an electron trap, which ultimately improved hydrogen production.

Further improvements in charge separation were achieved by optimizing the surface properties of TiO_2. Researchers discovered that nanostructuring the material, such as by creating TiO_2 NPs and nanotubes, significantly increased its surface area and, consequently, the number of active sites for the water splitting reaction.[51,52] These nanostructures also reduced the diffusion distance for charge carriers, which helped decrease recombination rates, as hinted in section 1.1.[51] In this way, the use of TiO_2 NPs offers distinct advantages over bulk and surface-specific models, particularly in photocatalytic applications. Besides the vastly increased surface-to-volume ratio, NPs allow for precise control over their morphology, with specific crystal facets, such as (101) in anatase TiO_2, demonstrating superior activity due to efficient charge separation and intermediate stabilization.[53]

Advances in synthesis methods have further impact the development of TiO_2 nanomaterials with tailored properties for photocatalysis. Techniques such as solvothermal and hydrothermal synthesis, chemical vapor deposition (CVD), and sol-gel processing have enabled researchers to precisely control the size, shape, and crystalline phase of TiO_2 nanostructures.[54,55] High-resolution transmission electron microscopy (HR-TEM) and scanning electron microscopy (SEM) have been critical in characterizing these materials, revealing the influence of specific morphologies, such as nanotubes and nanowires, on photocatalytic performance.[56-58] TEM imaging has confirmed that single-crystalline anatase NPs with well-defined (101) and (001) facets (Figure 1.6) exhibit superior charge separation efficiency and catalytic activity compared to bulk materials. These innovations also extend to novel materials like black TiO_2, produced through hydrogenation or other reduction techniques.[59]

Titanium dioxide mainly exists in two crystalline forms: rutile and anatase. Both have been thoroughly researched for their photocatalytic abilities. Anatase, which has a larger bandgap of about 3.2 eV compared to rutile's 3.0 eV, tends to be more effective in photocatalysis, especially in water splitting, as explained below. Although rutile is the thermodynamically stable phase at the bulk scale, anatase becomes more stable at the nanoscale, particularly for particles with diameters below approximately 14 nm.[60] This size-dependent stability makes anatase especially attractive for applications involving TiO_2 nanoparticles, such as photocatalysis or environmental remediation, particularly in hydrated environments. However, care must be taken during thermal processing, as anatase can irreversibly transform into the less active rutile phase at elevated temperatures—typically beginning around 500 °C for nanoparticles larger than ~14–16 nm, depending on particle size, synthesis method, and atmosphere. In contrast, ultra-small anatase nanoparticles (e.g., 1–2 nm in diameter) are significantly more resistant to this transformation due to their high surface-to-volume ratio and kinetic stabilization, and may retain the anatase phase even at temperatures exceeding 500 °C.[6]

The higher energy of the electrons generated by light in anatase enables stronger oxidation reactions on its surface, making it more efficient in facilitating the essential redox processes involved in water splitting. Besides, anatase has slower electron-hole recombination rates than rutile, which increases the chances that the photogenerated charge carriers will engage in surface reactions before they recombine.[61,62] The relative ease in which photo-generated excitons in anatase can reach the surface is another key factor explaining this polymorphic difference in photocatalytic performance. [63]

The size-dependent properties of NPs also contribute significantly to their photocatalytic superiority. Below approximately 5 nm, TiO_2 NPs transition into core-shell or amorphous phases, facilitating unique reaction pathways that improve photocatalytic performance.[64] These quantum effects, including size-induced modifications to the band structure, enable NPs to exploit a broader portion of the solar spectrum (a capability that bulk materials lack). Moreover, NPs' ability to optimize morphology enables the fine-tuning of reactivity. For instance, anatase NPs dominated by (101) facets exhibit enhanced photo-

oxidation activity compared to flatter crystals.[65] These unique features of NPs are not replicable in bulk or purely surface-oriented models. While bulk TiO_2 provides valuable insights into fundamental properties, it fails to account for the nanoscale-specific phenomena critical to photocatalysis. Thus, the transition to NP-based systems represents a significant leap in advancing TiO_2's application in renewable energy and environmental remediation.

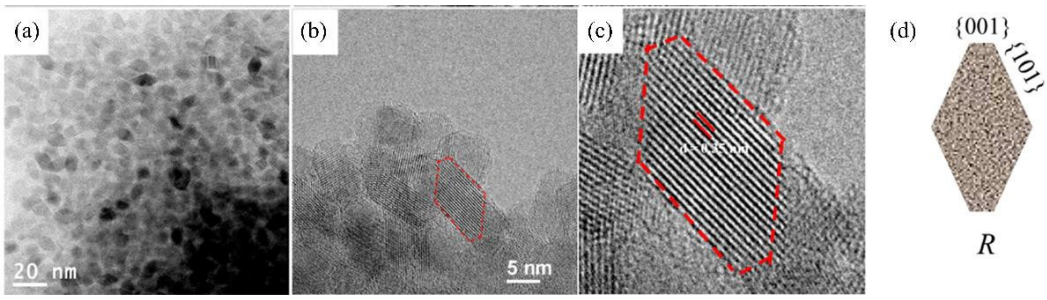

Figure 1.6: TEM (a) and HR-TEM (b, c) images of rhombic anatase TiO_2 nanocrystals produced by solvothermal synthesis. The insets in the HR-TEM images evidence the exposition of the (001) and (101) crystal surfaces. The 2D geometrical model of the nanocrystal and its exposed surfaces is reported in (d).

The fundamental limitation of TiO_2, its UV-only activation, remained a major obstacle in NPs. To extend titania's photoactivity into the visible light spectrum, extensive research has been conducted on metal (e.g., iron[66], copper[67]) and non-metal (e.g., nitrogen,[68] carbon[69,70]) doping with foreign atoms. Anatase has been the favoured polymorph for doping experiments due to its higher intrinsic photocatalytic activity, which provides a more robust platform for enhancing visible light absorption. It has been demonstrated that N-doping introduces mid-gap states above the valence band of titania that can serve as traps for charge carriers, thereby enhancing the visible light response.[71,72] Mid-gap states can sometimes delay recombination by temporarily trapping charge carriers, allowing them to migrate to reactive surface sites and participate in photocatalytic reactions. However, if the trapped charge carriers cannot efficiently move to reaction sites, these mid-gap states may instead act as recombination centres, reducing overall efficiency. For this reason, optimizing the type and concentration of dopants is critical to achieving a balance between enhanced light absorption and efficient charge separation.

One of the most significant advancements in photocatalytic water splitting came with the development of Z-scheme systems, which mimic the two-step excitation process in natural photosynthesis.[73-75] In a Z-scheme, two different semiconductors are used: one for driving the oxygen evolution reaction (OER) and the other for the hydrogen evolution reaction (HER). This method expands the range of light absorption and improves the separation of charge carriers, making it a very effective approach for increasing the efficiency of solar-to-hydrogen conversion. In Z-scheme systems, anatase TiO_2 often acts as one of the two semiconductors, paired with a complementary material that absorbs visible light. Common pairings include bismuth vanadate ($BiVO_4$)[76,77] and graphitic carbon nitride (g-C_3N_4),[78] which leverage anatase's robust oxidation capabilities and the visible light absorption properties of the partner material.

Both $BiVO_4$ and g-C_3N_4 have also been extensively studied as independent materials for visible light-driven water splitting, due to their favourable bandgaps and photocatalytic properties.[79-81] In fact, while anatase TiO_2 has remained a key system for photocatalytic research, several alternative materials with narrower bandgaps have emerged as promising candidates for visible light-driven water splitting. The aforementioned $BiVO_4$, for example, has attracted attention for its efficient visible light absorption (~2.4 eV) and high photocatalytic activity for oxygen evolution. Other examples are cadmium sulfide (CdS)[82] or tantalum oxynitride (TaON).[83]

Nevertheless, although these materials often show superior visible light responsiveness, TiO_2, especially in its anatase form, remains advantageous due to its chemical stability, non-toxicity, abundance, and ease of synthesis. These attributes make TiO_2 not only a cost-effective solution but also an invaluable model system for investigating the fundamentals of photocatalysis. Its well-characterized properties facilitate studies on the influence of surface hydration, defect states, and charge carrier dynamics, which can then be extrapolated to more efficient yet expensive materials.

Photocatalytic water splitting using titania calls for a detailed analysis of how water interacts with titania nanosystems, as this interaction is fundamental to the entire process. Water not only serves as the reactant—providing protons

and electrons for hydrogen evolution and oxygen production—, but also strongly influences the structural and electronic properties of the photocatalyst. The synergy between anatase TiO_2 and water is fundamental: hydration facilitates surface reactions, enhances charge separation, and promotes the formation of reactive intermediates critical for water splitting and hydrogen generation. The specific mechanisms of hydration/hydroxylation of the titania nanosystems, together with the influence on titania structural and electronic properties will be detailed later in the Results chapter, as it represents one of the main research points within this thesis.

1.6 Goal and Outline of the Thesis

Over five decades after the groundbreaking discovery that the anatase polymorph of titanium dioxide can drive water splitting under ultraviolet light, this system remains essential for understanding photocatalytic principles and advancing related applications. It is also worth noting other interesting applications of anatase titania, such as in photovoltaics,[84] CO_2 reduction,[85] sunscreens,[86] or anti-pollution building.[87,88] Furthermore, the adoption of TiO_2 NPs has revolutionized photocatalysis by offering a vastly increased surface-to-volume ratio, reduced charge carrier diffusion distances, and tunable properties at the nanoscale.

Building on these foundations, this thesis investigates the ground and excited state properties of titania NPs, with a particular emphasis on its behaviour under hydration and light exposure. To achieve this, a comprehensive set of computational methodologies is employed. The selected approaches—Classical and *Ab Initio* Molecular Dynamics (MD), Density Functional Theory (DFT), *Ab Initio* Atomistic Thermodynamics (AIAT), Time-Dependent Density Functional Theory (TD-DFT), and Nonadiabatic Molecular Dynamics (NA-MD)—together provide a detailed understanding of nano-TiO_2, encompassing its structural stability, electronic characteristics, and dynamic behaviours in photocatalytic applications.

As a first step, MD simulations are used to model the thermal and structural stability of TiO_2 NPs, particularly in relation to hydroxylation. These simulations reveal how nano- TiO_2 interacts with water at the atomic scale, offering

insights into the structural adaptations and stability of NPs under varying thermal conditions. Building upon these insights, DFT is employed to optimize the structure of titania systems and determine electronic band structure and bandgap, which are crucial for understanding their electronic properties and photocatalytic functionality.

After examining the electronic structure and structural properties of nano- TiO_2 at the ground-state level, this thesis transitions into the thermodynamic realm to explore the energetics of hydration. In this context, the validity of the AIAT approach and its applicability to nanoscale systems are critically assessed. A refined, size-dependent framework is proposed, producing more realistic Phase Diagrams that define stability regions associated with various hydration degrees. These diagrams serve as valuable guidelines for selecting optimal hydration degrees under specific conditions.

To address the excited-state properties of nanoscale titania, TD-DFT is employed to model its behaviour under light exposure. TD-DFT provides insights into the material's response to photoexcitation, including its capacity to drive redox reactions. Building on these results, NA-MD investigates the real-time dynamics of excited states, offering a comprehensive view of charge separation, recombination, and energy dissipation processes in both bare and hydrated TiO_2 nanoclusters. For the first time, this thesis uses NA-MD to examine how water influences excited-state processes in nano- TiO_2, directly addressing a critical aspect of photocatalytic efficiency and identifying strategies to optimize its performance.

This thesis is organized into seven chapters. Following the introduction, Chapter 2 presents the theoretical background and methodologies, providing detailed descriptions of the approaches outlined above. Chapters 3 through 5 discuss the results in a logical progression. Chapter 3 focuses on the effects of surface hydroxylation and morphology on the stability and electronic structure of TiO_2 NPs. Chapter 4 explores the size-dependent thermodynamic properties of titania, and their implications for photocatalytic activity. Chapter 5 dives into the excited-state dynamics of hydrated TiO_2, examining how size and hydration affect energy transfer and relaxation processes. Chapter 6 synthesizes the

insights gained, presenting general conclusions and their broader implications for renewable energy and photocatalysis. Chapter 7 outlines the contributions of the PhD candidate to various publications produced during the thesis years (2020-2025). Lastly, the appendix gathers the Supplementary Information documents of all five papers presented throughout this thesis.

1.7 References

[1] Brus, L. E. Electron–electron and electron-hole interactions in small semiconductor crystallites: The size dependence of the lowest excited electronic state. *J. Chem. Phys.* **1984**, *80*(9), 4403-4409.

[2] Halperin, F. W. Quantum size effects in metal particles. *Rev. Mod. Phys.* **1986**, *58*(3), 533.

[3] Jena, P.; Castleman Jr, A. W. Clusters: A bridge across the disciplines of physics and chemistry. *Proc. Natl. Acad. Sci. U.S.A.* **2006**, *103*(28), 10560-10569.

[4] Ferrando, R., Jellinek, J., & Johnston, R. L. Nanoalloys: from theory to applications of alloy clusters and nanoparticles. *Chem. Rev.* **2008**, *108*(3), 845-910.

[5] Murray, C. B., Kagan, C. R., & Bawendi, M. G. Synthesis and characterization of monodisperse nanocrystals and close-packed nanocrystal assemblies. *Annu. Rev. Mater. Sci.* **2000**, *30*(1), 545-610.

[6] Zhang, H.; Banfield, J. F. Understanding polymorphic phase transformation behavior during growth of nanocrystalline aggregates: insights from TiO_2. *J. Phys. Chem. B* **2000**, *104*(15), 3481-3487.

[7] Wulff, G. Xxv. zur frage der geschwindigkeit des wachsthums und der auflösung der krystallflächen. *Z. Kristallogr. Cryst. Mater.* **1901**, *34*(1-6), 449-530.

[8] Yang, H. G.; Sun, C. H.; Qiao, S. Z.; Zou, J.; Liu, G.; Smith, S. C.; Cheng, H. M.; Lu, G. Q. Anatase TiO_2 single crystals with a large percentage of reactive facets. *Nature* **2008**, *453*(7195), 638-641.

[9] Liu, G.; Jimmy, C. Y.; Lu, G. Q.; Cheng, H. M. Crystal facet engineering of semiconductor photocatalysts: motivations, advances and unique properties. *Chem. Comm.* **2011**, *47*(24), 6763-6783.

[10] Kavan, L.; Grätzel, M.; Gilbert, S. E.; Klemenz, C.; Scheel, H. J. Electrochemical and photoelectrochemical investigation of single-crystal anatase. *J. Am. Chem. Soc.* **1996**, *118*(28), 6716-6723.

[11] Xia, Y.; Yang, P.; Sun, Y.; Wu, Y.; Mayers, B.; Gates, B.; Yin, Y.; Kim, F; Yan, H. One-dimensional nanostructures: synthesis, characterization, and applications. *Adv. Mater.* **2003**, *15*(5), 353-389.

[12] Roduner, E. Size matters: why nanomaterials are different. *Chem. Soc. Rev.* **2006**, *35*(7), 583-592.

[13] Kelly, K. L.; Coronado, E.; Zhao, L. L.; Schatz, G. C. The optical properties of metal nanoparticles: the influence of size, shape, and dielectric environment. *J. Phys. Chem. B* **2003**, *107*(3), 668-677.

[14] Li, X.; Wang, X.; Zhang, L.; Lee, S.; Dai, H. Chemically derived, ultrasmooth graphene nanoribbon semiconductors. *Science* **2008**, 319(5867), 1229-1232.

[15] Alivisatos, A. P. Semiconductor clusters, nanocrystals, and quantum dots. *Science* **1996**, *271*(5251), 933-937.

[16] Bromley, S. T.; de PR Moreira, I.; Neyman, K. M.; Illas, F. Approaching nanoscale oxides: models and theoretical methods. *Chem. Soc, Rev.* **2009**, *38*(9), 2657-2670.

[17] Murray, C.; Norris, D. J.; Bawendi, M. G. Synthesis and characterization of nearly monodisperse CdE (E= sulfur, selenium, tellurium) semiconductor nanocrystallites. *J. Am. Chem. Soc.* **1993**, *115*(19), 8706-8715.

[18] Efros, A. L.; Efros, A. L. Interband absorption of light in a semiconductor sphere. *Sov. Phys. Semicond* **1982**, *16*(7), 772-775.

[19] Klimov, V. I.; Mikhailovsky, A. A.; Xu, S.; Malko, A.; Hollingsworth, J. A.; Leatherdale, C. A.; Eisle, H.-J.; Bawendi, M. G. Optical gain and stimulated emission in nanocrystal quantum dots. *Science* **2000**, *290*(5490), 314-317.

[20] Recio-Poo, M.; Morales-Garcia, Á.; Illas, F.; Bromley, S. T. Tuning electronic levels in photoactive hydroxylated titania nanosystems: combining the ligand dipole effect and quantum confinement. *Nanoscale* **2024**, *16* (18), 8975−8985.

[21] Hoffmann, M. R.; Martin, S. T.; Choi, W.; Bahnemann, D. W. Environmental Applications of Semiconductor Photocatalysis. *Chem. Rev.* **1995**, *95*, 69.

[22] Kamat, P. V. Meeting the clean energy demand: nanostructure architectures for solar energy conversion. *J. Phys. Chem. C* **2007**, *111*(7), 2834-2860.

[23] Link, S.; El-Sayed, M. A. Size and temperature dependence of the plasmon absorption of colloidal gold nanoparticles. *J. Phys. Chem. B* **1999**, *103*(21), 4212-4217.

[24] Meyers, M. A.; Mishra, A.; Benson, D. J. Mechanical properties of nanocrystalline materials. *Prog. Mater. Sci.* **2006**, *51*(4), 427-556.

[25] Arzt, E. Size effects in materials due to microstructural and dimensional constraints: a comparative review. *Acta Mater.* **1998**, *46*(16), 5611-5626.

[26] Gleiter, H. Nanocrystalline materials. In *Advanced Structural and Functional Materials: Proceedings of an International Seminar Organized by Deutsche Forschungsanstalt für Luft-und Raumfahrt (DLR), Köln,* June **1991** (pp. 1-37). Springer Berlin Heidelberg.

[27] Cahill, D. G.; Ford, W. K.; Goodson, K. E.; Mahan, G. D.; Majumdar, A.; Maris, H. J.; Merlin, R.; Phillpot, S. R. Nanoscale thermal transport. *J. Appl. Phys.* **2003**, *93*(2), 793-818.

[28] Chen, G.; Dames, C. Thermal conductivity of nanostructured thermoelectric materials. In *D. M. Rowe (Ed.), Thermoelectrics handbook,* **2005**.

[29] Majumdar, A. Thermoelectricity in semiconductor nanostructures. *Science* **2004**, *303*(5659), 777-778.

[30] Bell, A. T. The impact of nanoscience on heterogeneous catalysis. *Science* **2003**, *299*(5613), 1688-1691.

[31] Haruta, M. Size-and support-dependency in the catalysis of gold. *Catal. Today* **1997**, *36*(1), 153-166.

[32] Linsebigler, A. L.; Lu, G.; Yates Jr, J. T. Photocatalysis on TiO_2 surfaces: principles, mechanisms, and selected results. *Chem. Rev.* **1995**, *95*(3), 735-758.

[33] Kudo, A.; Miseki, Y. Heterogeneous photocatalyst materials for water splitting. *Chem. Soc. Rev.* **2009**, *38*(1), 253-278.

[34] Diebold, U. The surface science of titanium dioxide. *Surf. Sci. Rep.* **2003**, *48*(5-8), 53-229.

[35] Barnard, A.; Zapol, P. A model for the phase stability of arbitrary nanoparticles as a function of size and shape. *J. Chem. Phys.* **2004**, *121*(9), 4276–4283.

[36] Yang, S.; Prendergast, D.; Neaton, J. B. Tuning semiconductor band edge energies for solar photocatalysis via surface ligand passivation. *Nano Lett.* **2012**, *12*(1), 383-388.

[37] Yaacobi-Gross, N.; Soreni-Harari, M.; Zimin, M.; Kababya, S.; Schmidt, A.; Tessler, N. Molecular control of quantum-dot internal electric field and its application to CdSe-based solar cells. *Nat. Mater.* **2011**, *10*(12), 974-979.

[38] Brown, P. R.; Kim, D.; Lunt, R. R.; Zhao, N.; Bawendi, M. G.; Grossman, J. C.; Bulovic, V. Energy level modification in lead sulfide quantum dot thin films through ligand exchange. *ACS Nano* **2014**, *8*(6), 5863-5872.

[39] Kroupa, D. M.; Vörös, M.; Brawand, N. P.; McNichols, B. W.; Miller, E. M.; Gu, J.; Nozik, A. J.; Sellinger, A.; Galli, G.; Beard, M. C. Tuning colloidal quantum dot band edge positions through solution-phase surface chemistry modification. *Nat. Commun.* **2017**, *8*(1), 15257.

[40] Fu, F. Y.; Shown, I.; Li, C. S.; Raghunath, P.; Lin, T. Y.; Billo, T.; Chen, K. H. KSCN-induced interfacial dipole in black TiO_2 for enhanced photocatalytic CO_2 reduction. *ACS Appl.* **2019**, *11*(28), 25186-25194.

[41] Çetin, Y. A.; Escorihuela, L.; Martorell, B.; Serratosa, F. Revisiting Water Adsorption on TiO_2 and ZnO Surfaces: An SCC-DFTB Molecular Dynamics Study. *ACS Omega* **2025**, *10*(5), 4449–4457.

[42] Yamamoto, S.; Kendelewicz, T.; Newberg, J. T.; Ketteler, G.; Starr, D. E.; Mysak, E. R.; Andersson, K. J.; Ogasawara, H.; Bluhm, H.; Salmeron, M.; Brown, G. E.; Nilsson, A. Water adsorption on α-Fe2O3 (0001) at near ambient conditions. *J. Phys. Chem. C* **2010**, *114*(5), 2256-2266.

[43] Henderson, M. A. A surface science perspective on TiO_2 photocatalysis. *Surf. Sci. Rep.* **2011**, *66*(6-7), 185-297.

[44] Pan, X.; Yang, M. Q.; Fu, X.; Zhang, N.; Xu, Y. J. Defective TiO_2 with oxygen vacancies: synthesis, properties and photocatalytic applications. *Nanoscale* **2013**, *5*(9), 3601-3614.

[45] Fujishima, A.; Honda, K. Electrochemical Photolysis of Water at a Semiconductor Electrode. *Nature* **1972**, *238*(5358), 37–38.

[46] Fujishima, A.; Kohayakawa, K.; Honda, K. Hydrogen production under sunlight with an electrochemical photocell. *J. Electrochem. Soc.* **1975**, *122*(11), 1487.

[47] Kumaravel, V.; Mathew, S.; Bartlett, J.; Pillai, S. C. Photocatalytic hydrogen production using metal doped TiO_2: A review of recent advances. *Appl. Catal. B: Environ*. **2019**, *244*, 1021-1064.

[48] Ali, S.; Ismail, P. M.; Khan, M.; Dang, A.; Ali, S.; Zada, A.; Fazal Raziq; Khan, I.; Khan, M. S.; Muhammad Ateeq; Khan, W.; Bakhtiar, S. H.; Ali, H.; Wu, X.; Shah, A.; Ajayan Vinu; Yi, J.; Xia, P.; Qiao, L. Charge transfer in TiO_2-based photocatalysis: fundamental mechanisms to material strategies. *Nanoscale* **2024**, *16*(9), 4352–4377.

[49] Guo, Q.; Zhou, C.; Ma, Z.; Yang, X. Fundamentals of TiO_2 Photocatalysis: Concepts, Mechanisms, and Challenges. *Adv. Mater.* **2019**, *31*(50), 1901997.

[50] Schrauzer, G. N.; Guth, T. D. Photolysis of water and photoreduction of nitrogen on titanium dioxide. *J. Am. Chem. Soc.* **1977**, *99*(22), 7189–7193.

[51] He, H.; Liu, C.; Dubois, K.; Jin, T.; Louis, M. E.; Li, G. Enhanced Charge Separation in Nanostructured TiO_2 Materials for Photocatalytic and Photovoltaic Applications. *Chem. Mater.* **2012**, *24*(37), 11841–11849.

[52] Hernández, S.; Hidalgo, D.; Sacco, A.; Chiodoni, A.; Lamberti, A.; Cauda, V.; Tresso, E.; Saracco, G. Comparison of photocatalytic and transport properties of TiO_2 and ZnO nanostructures for solar-driven water splitting. *Phys. Chem. Chem. Phys.* 2015, *17*(12), 7775–7786.

[53] Pigeot-Rémy, S.; Dufour, F.; Herissan, A.; Ruaux, V.; Maugé, F.; Hazime, R.; Foronato, C.; Guillard, C.; Chaneac, C.; Durupthy, O.; Colbeau-Justin, C.; Cassaignon, S. Bipyramidal anatase TiO_2 nanoparticles, a highly efficient photocatalyst? Towards a better understanding of the reactivity. *Appl. Catal. B: Environ.* **2017**, *203*, 324–334.

[54] Chen, X.; Mao, S. S. Titanium dioxide nanomaterials: synthesis, properties, modifications, and applications. *Chem. Rev.* **2007**, *107*(7), 2891–2959.

[55] Ding, Y.; Ding, B.; Kanda, H.; Usiobo, O. J.; Gallet, T.; Yang, Z.; Liu, Y.; Huang, H.; Sheng, J.; Liu, C.; Yang, Y.; Queloz, V. I. E.; Zhang, X.; Audinot, J.-N.; Redinger, A.; Dang, W.; Mosconic, E.; Luo, W.; De Angelis, F.; Wang, M. *Nat. Nanotechnol.* **2022**, *17*(6), 598–605.

[56] D'Arienzo, M.; Dozzi, M. V.; Redaelli, M.; Credico, B. D.; Morazzoni, F.; Scotti, R.; Polizzi, S. Single-crystalline TiO_2 nanoparticles for stable and efficient perovskite modules. *J. Phys. Chem. C* **2015**, *119*(22), 12385–12393.

[57] A. Aashish; Ramakrishnan, R.; J.D. Sudha; Sankaran, M.; G. Krishna Priya. Nanocubes of rutile titania for enhanced visible light photocatalytic applications. *Mater. Chem. Phys*. **2015**, *157*, 31.38.

[58] Aguilera Mandujano, A.; Serrato-Rodriguez, Synthesis and characterization of titania/graphene nanocomposite for application in photocatalysis. *J. Rev. Mex. Fís.* **2020**, *66*(5), 610–616.

[59] Chen, X.; Liu, L.; Huang, F. Black titanium dioxide (TiO_2) nanomaterials. *Chem. Soc. Rev.* **2015**, *44*(7), 1861–1885.

[60] Zhang, H.; Banfield, J. F. Structural Characteristics and Mechanical and Thermodynamic Properties of Nanocrystalline TiO_2. *Chem. Rev.* **2014**, *114*(19), 9613–9644.

[61] Wang, X.; Kafizas, A.; Li, X.; Savio, J. P.; Tang, J.; Parkin, I. P.; Durrant, J. R. Transient absorption spectroscopy of anatase and rutile: the impact of morphology and phase on photocatalytic activity. *J. Phys. Chem. C* **2015**, *119*(19), 10439–10447.

[62] Sclafani, A.; Herrmann, J. M. Comparison of the photoelectronic and photocatalytic activities of various anatase and rutile forms of titania in pure liquid organic phases and in aqueous solutions. *J. Phys. Chem.* **1996**, *100*(32), 13655–13661.

[63] Samanta, B.; Morales-García, Á.; Illas, F.; Goga, N.; Anta, J. A.; Calero, S.; Bieberle-Hütter, A.; Libisch, F.; Muñoz-García, A. B.; Pavone, M.; Caspary Toroker, M. Challenges of modeling nanostructured materials for photocatalytic water splitting. *Chem. Soc. Rev.* **2022**, *51*(9), 3794–3818.

[64] Morales-García, Á.; Macià Escatllar, A.; Illas, F.; Bromley, S. T. Understanding the interplay between size, morphology and energy gap in photoactive TiO_2 nanoparticles. *Nanoscale* **2019**, *11*(18), 9032–9041.

[65] Lazzeri, M.; Vittadini, A.; Selloni, A. Structure and energetics of stoichiometric anatase surfaces. *Phys. Rev. B* **2001**, *63*(15).

[66] Wang, C.; Bahnemann, D. W.; Dohrmann, J. K. A novel preparation of iron-doped TiO_2 nanoparticles with enhanced photocatalytic activity. *Chem. Commun.* **2000**, *16*, 1539–1540.

[67] Yadav, H. M.; Otari, S. V.; Koli, V. B.; Mali, S. S.; Hong, C. K.; Pawar, S. H.; Delekar, S. D. Preparation and characterization of copper-doped anatase TiO_2 nanoparticles with visible light photocatalytic antibacterial activity. *J. Photochem. Photobiol., A* **2014**, *280*, 32–38.

[68] Asahi, R.; Morikawa, T.; Ohwaki, T.; Aoki, K.; Taga, Y. Visible-light photocatalysis in nitrogen-doped titanium oxides. *Science* **2001**, *293*, 269.

[69] Nagaveni, K.; Hegde, M. S.; Ravishankar, N.; Subbanna, G. N.; Madras, G. Synthesis and Structure of Nanocrystalline TiO_2 with Lower Band Gap Showing High Photocatalytic Activity. *Langmuir* **2004**, *20*, 2900.

[70] Kamisaka, H.; Adachi, T.; Yamashita, K. Theoretical study of the structure and optical properties of carbon-doped rutile and anatase titanium oxides. *J. Chem. Phys.* **2005**, *123*, 084704.

[71] Zhang, J.; Wu, Y.; Xing, M.; Leghari, S. A. K.; Sajjad, S. Development of modified N doped TiO_2 photocatalyst with metals, nonmetals and metal oxides. *Energy Environ. Sci.* **2010**, *3*, 715.

[72] Di Valentin, C.; Pacchioni, G.; Selloni, A.; Livraghi, S.; Giamello, E. Characterization of Paramagnetic Species in N-Doped TiO_2 Powders by EPR Spectroscopy and DFT Calculations. *J. Phys. Chem. B* **2005**, *109*, 11414.

[73] Abe, R. Recent progress on photocatalytic and photoelectrochemical water splitting under visible light irradiation. *J. Photochem. Photobiol., C* **2010**, *11*, 179.

[74] Maeda, K. Z-scheme water splitting using two different semiconductor photocatalysts. *ACS Catal.* **2013**, *3*, 1486.

[75] Wang, Y.; Suzuki, H.; Xie, J.; Tomita, O.; Martin, D. J.; Higashi, M.; Kong, D.; Abe, R.; Tang, J. Mimicking Natural Photosynthesis: Solar to Renewable H_2 Fuel Synthesis by Z-Scheme Water Splitting System. *Chem. Rev.* **2018**, *118*, 5201.

[76] Wang, Q.; Domen, K. Mimicking Natural Photosynthesis: Solar to Renewable H_2 Fuel Synthesis by Z-Scheme Water Splitting Systems. *Chem. Rev.* **2019**, *120*(2), 919–985.

[77] Kato, H.; Hori, M.; Konta, R.; Shimodaira, Y.; Kudo, A. Construction of Z-scheme Type Heterogeneous Photocatalysis Systems for Water Splitting into H_2 and O_2 under Visible Light Irradiation. *Chem. Lett.* **2004**, *33*(10), 1348–1349.

[78] Li, H.; Tu, W.; Zhou, Y.; Zou, Z. Z-Scheme photocatalytic systems for promoting photocatalytic performance: recent progress and future challenges. *Adv. Sci.* **2016**, *3*(11), 1500389.

[79] Teoh, W. Y.; Scott, J.; Amal, R. Progress in heterogeneous photocatalysis: from classical radical chemistry to engineering nanomaterials and solar reactors. *J. Phys. Chem. Lett.* **2012**, *3*(5), 629–639.

[80] Fan, H.-T.; Jiang, T.; Li, H.; Wang, D.; Wang, L.; Zhai, J.; He, D.; Wang, P.; Xie, T. Effect of $BiVO_4$ Crystalline Phases on the Photoinduced Carriers Behavior and Photocatalytic Activity. *J. Phys. Chem. C* **2012**, *116*(3), 2425–2430.

[81] Ma, D.; Zhang, Z.; Zou, Y.; Chen, J.; Shi, J.-W. The progress of g-C3N4 in photocatalytic H_2 evolution: From fabrication to modification. *Coord. Chem. Rev.* **2024**, *500*, 215489.

[82] Nasir, J. A.; Rehman, Z. U.; Shah, S. N. A.; Khan, A.; Butler, I. S.; Catlow, C. R. A. Recent developments and perspectives in CdS-based photocatalysts for water splitting. *J. Mater. Chem. A* **2020**, *8*(40), 20752–20780.

[83] Higashi, M.; Abe, R.; Ishikawa, A.; Takata, T.; Ohtani, B.; Domen, K. Z-scheme overall water splitting on modified-TaON photocatalysts under visible light ($\lambda < 500$ nm). *Chem. Lett.* **2007**, *37*(2), 138–139.

[84] Bai, Y.; Mora-Sero, I.; De Angelis, F.; Bisquert, J.; Wang, P. Titanium dioxide nanomaterials for photovoltaic applications. *Chem. Rev.* **2014**, *114*, 10095−10130.

[85] Xu, Q.; Yu, J.; Zhang, J.; Zhang, J.; Liu, G. Cubic anatase TiO_2 nanocrystals with enhanced photocatalytic CO_2 reduction activity. *Chem. Comm.* **2015**, *51*(37), 7950–7953.

[86] Kapilashrami, M; Zhang, Y.;Liu, Y.-S.; Hagfeldt, A.; Guo, J. Probing the Optical Property and Electronic Structure of TiO_2 Nanomaterials for Renewable Energy Applications. *J. Chem. Rev.* **2014**, *114*, 9662–9707.

[87] Schneider, J.; Matsuoka, M.; Takeuchi, M.; Zhang, J.; Horiuchi, Y.; Anpo, M.; Bahnemann, D. W. Understanding TiO_2 Photocatalysis: Mechanisms and Materials. *Chem. Rev.* **2014**, *114*, 9919–9986.

[88] Ryu, J.; Choi, W. Substrate-Specific Photocatalytic Activities of TiO_2 and Multiactivity Test for Water Treatment Application. *Environ. Sci. Technol.* **2008**, *42*, 294-300.

2 METHODOLOGY

This chapter outlines the theoretical and computational methodologies employed to investigate the structural, electronic, and dynamic properties of anatase TiO_2 nanosystems and their interactions with aqueous environments. While the choice of methodologies is inherently motivated by the scientific interest in titania and its relevance to photocatalysis, the primary focus of this chapter resides in the underlying theoretical frameworks and computational techniques. References to the specific systems studied and the parameters employed will be limited to cases where the diversity of possible methodological approaches requires highlighting the specific choices made in this research.

As part of the Theoretical Chemistry and Computational Modelling doctoral program, this research extensively utilizes advanced computational codes and simulations. These tools are described alongside the key concepts and theoretical principles underpinning their application. Throughout this chapter, references to specific computational codes are provided—typically at the end of the corresponding sections—while ensuring that the main emphasis remains on the theoretical background that forms the foundation of these methodologies. The methodologies are organized into the following sections:

Wavefunction-Based Quantum Mechanics (Section 2.1): This section introduces the wavefunction concept, the Schrödinger equation, and the Born-Oppenheimer approximation, which provide the foundation for constructing the potential energy surface (PES) and exploring quantum mechanical properties of molecular systems.

Molecular Dynamics Simulations (Section 2.2): This section focuses on the application of Molecular Dynamics (MD) to explore the PES and obtain minimum-energy structures. Subsections 2.2.1 and 2.2.2 respectively detail the characteristics of classical MD and *Ab Initio* MD (AIMD). Lastly, Subsection 2.2.3 covers the fundamentals of MD, including thermodynamic ensembles, time integration, and temperature and pressure control.

Density Functional Theory – DFT (Section 2.3): This section describes the principles and practical implementation of DFT, highlighting its application in structural optimization and electronic property calculations. It begins with the Hohenberg-Kohn Theorems (2.3.1) and Kohn-Sham Equations (2.3.2),

followed by a discussion of exchange-correlation functionals (2.3.3) and dispersion forces (2.3.4), and concludes with the computational implementation of DFT (2.3.5).

Thermodynamics and Gibbs Free Energy (Section 2.4): Thermodynamic principles are introduced to connect molecular simulations with macroscopic properties. Subsection 2.4.1 outlines general thermodynamic concepts, while Subsection 2.4.2 focuses on *Ab Initio* Atomistic Thermodynamics (AIAT) and the computation of the Gibbs free energy of hydration. Finally, in 2.4.3, the *p*-*T* phase diagrams are introduced.

Excited states (Section 2.5): This section discusses methodologies for simulating excited-state dynamics. Subsections 2.5.1 and 2.5.2 introduces wavefunction representation and Non-Adiabatic Molecular Dynamics (NA-MD) foundations. The rest of the section details the different steps required to compute the evolution of the excited states in the context of mixed quantum-classical dynamics.

2.1 Quantum Mechanics: The wavefunction and the Schrödinger Equation

2.1.1 The Concept of the Wavefunction

In quantum mechanics, the wavefunction, denoted as $\Psi(\mathbf{r}, t)$ serves as a mathematical representation of the quantum state of a physical system. It encapsulates all the information about the particles within the system, including their spatial, temporal, and quantum properties. The square of the wavefunction's modulus, $|\Psi(\mathbf{r}, t)|^2$, provides the probability density for finding a particle at a given position $\mathbf{r}$ at time t, linking the abstract quantum description to observable physical phenomena. Throughout this text, boldface symbols denote vectors, specifically the position coordinates of particles in three-dimensional space.

The wavefunction is inherently a complex-valued function, often expressed in the form $\Psi(\mathbf{r}, t) = A(\mathbf{r}, t)e^{i\varphi(\mathbf{r},t)}$, where $A(\mathbf{r}, t)$ is the amplitude and $\varphi(\mathbf{r}, t)$ is the phase. This complex nature allows the wavefunction to encode both the magnitude and the phase of a system's quantum state, enabling interference

effects that are essential to quantum mechanics. The phase information, although not directly observable, plays a critical role in quantum coherence and superposition.

For systems involving multiple particles, such as electrons and nuclei, the wavefunction becomes a function of all particle coordinates, $\Psi(\mathbf{r_1}, \mathbf{r_2}, \ldots, \mathbf{r_N}; \mathbf{R_1}, \mathbf{R_2}, \ldots, \mathbf{R_M})$. Here, $\mathbf{r_1}, \mathbf{r_2}, \ldots, \mathbf{r_N}$ represent the positions of electrons, and $\mathbf{R_1}, \mathbf{R_2}, \ldots, \mathbf{R_M}$ represent the positions of nuclei. This high-dimensional function contains information about the correlated positions and momenta of all particles, reflecting the entangled nature of quantum systems. As the number of particles increases, solving for Ψ becomes computationally challenging due to the exponential growth in complexity. This motivates the need for theoretical tools and approximations, which will be discussed further in the context of quantum dynamics.

2.1.2 The Schrödinger Equation

The wavefunction's evolution and the governing principles of quantum systems are formalized through the Schrödinger equation.[1] This equation encapsulates the dynamics and properties of quantum systems, providing a cornerstone of quantum mechanics. The time-dependent Schrödinger equation is expressed as:

$$\hat{H}\Psi(\mathbf{r}, t) = i\hbar \frac{\partial}{\partial t}\Psi(\mathbf{r}, t) \tag{2.1}$$

where $\hat{H}$ is the Hamiltonian operator, which represents the total energy of the system (kinetic + potential energy), and $\hbar$ is the reduced Planck's constant. For stationary states, where the system's properties do not explicitly change with time, the time-independent Schrödinger equation is used:

$$\hat{H}\Psi(\mathbf{r}) = E\Psi(\mathbf{r}), \tag{2.2}$$

where E is the energy eigenvalue corresponding to the eigenstate $\Psi(\mathbf{r})$. This form is crucial for determining the energy levels of quantum systems, such as atoms and molecules, and is foundational to quantum chemistry and spectroscopy.

The Hamiltonian operator, $\hat{H}$, governs the behavior of this wavefunction and is expressed as the sum of kinetic and potential energy terms for both the electrons and the nuclei. In atomic units, the full Hamiltonian is:

$$\begin{aligned} \hat{H} &= \hat{T}_e + \hat{T}_N + \hat{V}_{eN} + \hat{V}_{ee} + \hat{V}_{NN} \\ \hat{T}_e + \hat{T}_N &= -\sum_{i=1}^{N} \frac{\nabla_i^2}{2} - \sum_{j=1}^{M} \frac{\nabla_j^2}{2M_j} \\ \hat{V}_{eN} + \hat{V}_{ee} + \hat{V}_{NN} &= -\sum_{i,j} \frac{Z_j}{|\mathbf{r}_i - \mathbf{R}_j|} + \sum_{i<i'} \frac{1}{|\mathbf{r}_i - \mathbf{r}_{i'}|} + \sum_{j<j'} \frac{Z_j Z_{j'}}{|\mathbf{R}_j - \mathbf{R}_{j'}|} \end{aligned} \tag{2.3}$$

Here, $\mathbf{r}_i$ and $\mathbf{r}_{i'}$ represent the positions of electrons, while $\mathbf{R}_j$ and $\mathbf{R}_{j'}$ represent the positions of nuclei. The first two terms of Equation (2.3) ($\hat{T}_e$, $\hat{T}_N$) represent the kinetic energy of electrons and nuclei, respectively; the third term ($\hat{V}_{eN}$) accounts for electron-nuclear attraction; the fourth ($\hat{V}_{ee}$) corresponds to electron-electron repulsion; and the last one ($\hat{V}_{NN}$) describes nuclear-nuclear repulsion.

The solutions to the time-independent Schrödinger equation reveal the quantized energy levels of bound systems, a key result consistent with experimental observations like atomic spectra. However, solving the Schrödinger equation for systems with many interacting particles becomes computationally intractable due to the exponential growth in complexity with the number of particles. Approximations and numerical methods, such as Hartree-Fock (HF)[2,3] and DFT,[4] are used to tackle this challenge. For relativistic effects, which are significant for heavy nuclei or high velocities, the Schrödinger equation is replaced by relativistic extensions like the Dirac equation.[5]

The Born-Oppenheimer approximation simplifies the Schrödinger equation for multi-particle systems by decoupling the motion of electrons and nuclei. This approximation relies on the large mass difference between electrons and nuclei, which results in vastly different timescales for their motion. Under this approximation, the total wavefunction can be expressed as:

$$\Psi(\mathbf{r_1}, \ldots, \mathbf{R_1}, \ldots) = \psi_{\text{nuc}}(\mathbf{R_1}, \mathbf{R_2}, \ldots)\psi_{\text{el}}(\mathbf{r_1}, \mathbf{r_2}, \ldots; \mathbf{R_1}, \mathbf{R_2}, \ldots), \tag{2.4}$$

where ψ_{el} is the electronic wavefunction, which depends parametrically on the nuclear positions $\{\boldsymbol{R_j}\}$ and ψ_{nuc} is the nuclear wavefunction that evolves on the potential energy surface.

2.1.3 The Potential Energy Surface

The Potential Energy Surface (PES) arises naturally from this separation. For fixed nuclear coordinates $\{\boldsymbol{R_j}\}$, the electronic Schrödinger equation is solved to obtain the electronic energy $E_{el}(\{\boldsymbol{R_j}\})$, which includes contributions from the electron kinetic energy, electron-electron interactions, and electron-nucleus attraction. This electronic energy acts as an effective potential for the nuclear wavefunction:

$$\hat{H}_{nuc}\,\psi_{nuc}(\mathbf{R_1},\dots) = \left[-\sum_{j=1}^{M}\frac{\nabla_j^2}{2M_j} + E_{el}(\{\mathbf{R_j}\}) + V_{NN}(\{\mathbf{R_j}\})\right]\psi_{nuc}(\mathbf{R_1},\dots) \qquad (2.5)$$

The PES, $E_{el}(\{\mathbf{R_j}\}) + V_{NN}(\{\mathbf{R_j}\})$, is a high-dimensional hypersurface that describes how the energy of the system varies with the nuclear positions. Minima on the PES correspond to stable equilibrium geometries, while saddle points represent transition states critical for understanding reaction mechanisms. The shape of the PES determines molecular vibrations, reaction pathways, and energy barriers.

In computational studies, the PES is explored using a variety of methods, each suited to different aspects of molecular systems. For example, classical molecular dynamics (MD) simulations are often employed to explore the PES by simulating nuclear motion over time, enabling the identification of stable structures and sampling energy landscapes. Such approaches are computationally efficient and particularly valuable for large systems or when initializing geometries for further refinement.

2.2 Molecular Dynamics Simulations: Classical and *Ab Initio* Approaches

Molecular dynamics simulations are a widely employed computational technique used to study the time evolution of molecular systems by solving Newton's equations of motion. In this approach, atoms and molecules are modelled as classical or quantum particles, depending on the methodology employed. Classical MD[6] treats particles as classical entities, whereas *Ab Initio* Molecular Dynamics (AIMD)[7] incorporates quantum mechanical principles for a more accurate depiction of atomic interactions.

2.2.1 Classical MD simulations

Classical MD simulations are widely used to study the time evolution of molecular systems by solving Newton's equations of motion. In this approach, atoms and molecules are treated as classical particles whose dynamics are governed by the PES of the system. The potential energy, $U(\mathbf{r_1}, \mathbf{r_2}, \dots, \mathbf{r_N})$, is a function of the atomic positions and is derived from empirical or semi-empirical force fields. Newton's equations of motion for each particle *i* are expressed as:

$$m_i \frac{d^2\mathbf{r}_i}{dt^2} = -\nabla U(\mathbf{r_1}, \mathbf{r_2}, \dots, \mathbf{r_N}), \tag{2.6}$$

where m_i is the mass of the i-th particle, $\mathbf{r}_i$ its position vector, and ∇U the gradient of the potential energy with respect to its coordinates. The trajectory of each particle is determined by integrating these equations over discrete time steps, yielding the positions and velocities of all atoms as functions of time.

MD simulations operate on the assumption that atomic interactions can be captured by potential energy functions, which define the "force fields" acting on atoms and molecules. These simulations proceed by discretizing time into small steps, applying classical mechanics iteratively to update atomic positions and velocities.

In classical MD simulations, the potential energy U is a critical quantity that governs atomic interactions and determines the forces acting on particles. This

potential energy is typically divided into two main contributions: bonded interactions and non-bonded interactions. These contributions are modelled using predefined mathematical expressions that constitute a force field. A force field is a set of parameters and functional forms tailored to represent the physical and chemical properties of a system. While the general decomposition of U into bonded and non-bonded terms is consistent across force fields, the specific functional forms and parameterizations vary depending on the chosen force field.

Bonded interactions represent forces that maintain the structural integrity of molecules and include:

- **Bond stretching:** Modelled as a harmonic potential around an equilibrium bond length r_0 with force constant k_b.
- **Angle bending:** Similar to bond stretching, this uses a harmonic potential to penalize deviations from the equilibrium bond angle θ_0, with force constant k_θ.
- **Torsional (dihedral) rotations:** These describe the energy associated with rotations around bonds, expressed using periodic functions defined by parameters V_n, n, and γ.

Non-bonded interactions describe forces between atoms not directly connected by bonds. These include:

- **Van der Waals (Lennard-Jones) interactions:** These forces are modelled by the Lennard-Jones potential,[8] parameterized by ϵ_{ij} (the depth of the potential well) and σ_{ij} (the finite distance at which the potential is zero).
- **Electrostatic (Coulombic) interactions:** Governed by the charges q_i and q_j on particles, these forces depend on their separation r_{ij} and the permittivity of free space ϵ_0.

2.2.1.1 Force Fields for Inorganic Systems

The choice of force field determines how interatomic interactions are parameterized, and different force fields are designed to accurately model specific types of materials. Unlike biomolecular or organic force fields, which commonly use a Lennard-Jones $1/r^{12} - 1/r^6$ potential for van der Waals interactions, inorganic force fields often employ an exponential repulsive term to capture short-range repulsion more accurately. This is particularly important in modeling ionic and metal-oxide systems, where atomic interactions are dominated by Coulombic forces and polarization effects.

One widely used formulation is the Buckingham potential,[9] which expresses the non-bonded energy as:

$$U_{\text{non-bonded}}(r) = Ae^{-Br} - \frac{C}{r^6} \tag{2.7}$$

where *A* and *B* define the short-range repulsive interaction, typically fitted to quantum mechanical calculations or experimental data, while *C* represents the attractive dispersion interaction.

This form of the potential was first introduced by Buckingham and has been widely used in metal oxides, minerals, and ceramic materials (e.g., Matsui & Akaogi, 1991, for TiO_2[10]). The Buckingham potential provides a more realistic description of ionic repulsion compared to the empirical Lennard-Jones 12-6 form.

Additionally, inorganic force fields often lack dihedral terms, as the structural flexibility in these systems arises mainly from bond stretching, angle bending, and non-bonded interactions rather than rotatable covalent bonds.

A general potential energy function for inorganic systems can be expressed as:

$$U = \sum_{\text{bonds}} k_b(r - r_0)^2 + \sum_{\text{angles}} k_\theta(\theta - \theta_0)^2 + \sum_{i<j} \left[A_{ij}e^{-B_{ij}r_{ij}} - \frac{C_{ij}}{r_{ij}^6} + \frac{q_i q_j}{4\pi\epsilon_0 r_{ij}}\right] \tag{2.8}$$

where bond stretching (k_b) and angle bending (k_θ) terms describe covalent interactions. Non-bonded interactions include the Buckingham-type repulsion and dispersion terms. Lastly, electrostatics ($\frac{q_i q_j}{4\pi\epsilon_0 r_{ij}}$) are critical in inorganic systems, particularly those involving metal oxides.

In this work, the PES of TiO_2 systems is explored using the GULP (General Utility Lattice Program) software,[11] which supports a wide range of interatomic potentials and advanced optimization techniques. To accurately describe the structural and dynamical properties of TiO_2, two specialized interatomic potentials are employed: NanoTiO[12] and FFTiOH[13].

The NanoTiO force field was developed to address the limitations of existing metal-oxide interatomic potentials (IPs), particularly the Matsui-Akaogi one, which tends to overstabilize highly coordinated, compact Ti-O clusters that are not representative of realistic structures. To overcome this issue, NanoTiO employs a modified parameterization strategy that combines elements from different potential models to better capture the structural diversity of titanium dioxide systems. One key improvement in NanoTiO is the incorporation of a hybrid parameterization approach, where a portion of Ti and O ions are treated using Flikkema and Bromley (FB) parameters, originally developed for $(SiO_2)_n$ nanoclusters.[14] Unlike the MA potential, which favours six-coordinated Ti centres, the FB potential Favors four-coordinated Ti centres, leading to more open and flexible structures. By replacing 30–50% of the MA-parameterized centres with FB-parameterized centres, the force field effectively promotes lower-energy $(TiO_2)_n$ clusters that better reflect realistic structural configurations.

In addition to this mixed MA-FB parameterization, NanoTiO also incorporates a re-parameterization of the MA potential, specifically increasing the oxygen-oxygen (O-O) repulsion for short-range interactions (1.5–2.5 Å). This adjustment counteracts the MA potential's inherent tendency to form excessively compact structures, while still preserving the Ti-O interaction parameters. The result is a force field that allows for less compact configurations with fewer highly coordinated Ti centres, leading to more physically meaningful predictions of TiO_2 properties.

Building upon this foundation, the FFTiOH force field was developed to explicitly account for hydroxylation effects on TiO_2 surfaces. Similar to FFSiOH for hydroxylated silica, FFTiOH incorporates additional parameterization to capture Ti–OH interactions, making it particularly suitable for modelling wet TiO_2 interfaces, catalysis, and adsorption.

While NanoTiO is optimized for bulk TiO_2 and its nanostructures, ensuring oxygen coordination and cluster stability, FFTiOH extends this capability by explicitly treating hydroxylation, enabling a more accurate representation of hydrated TiO_2 surfaces and interface interactions. This enhanced description of Ti–OH bonding is crucial for photocatalysis, adsorption, and aqueous environments, making FFTiOH ideal for studying water and organic molecule interactions with TiO_2 in catalytic and environmental processes.

2.2.2 *Ab Initio* Molecular Dynamics Simulations

Ab Initio Molecular Dynamics simulations provide a robust framework for exploring the potential energy surface with quantum mechanical precision. Unlike classical MD, which relies on parameterized interatomic potentials, AIMD calculates forces directly from first-principles electronic structure methods. At each time step, the electronic Schrödinger equation is solved for the current nuclear configuration, yielding the electronic energy $E_{\mathrm{el}}(\{\mathbf{R_j}\})$ and its gradients. These gradients define the forces acting on the nuclei, which govern their motion according to Newton's second law:

$$m_i \frac{d^2\mathbf{R}_i}{dt^2} = -\nabla_i E_{\mathrm{el}}(\{\mathbf{R_j}\}) \tag{2.9}$$

where m_i and $\mathbf{R}_i$ represent the mass and position vector of the i-th nucleus, respectively, and $\nabla_i E_{\mathrm{el}}(\{\mathbf{R_j}\})$ is the gradient of the electronic energy with respect to $\mathbf{R}_i$. This integration of quantum mechanical force calculations with classical equations of motion enables AIMD to model systems where electronic effects, such as charge transfer or polarization, are critical. In AIMD, the PES is inherently quantum mechanical, arising from the solution of the electronic Schrödinger equation. The electronic energy, $E_{\mathrm{el}}(\{\mathbf{R_j}\})$, captures contributions from the kinetic energy of electrons, electron-electron repulsions, and electron-

nucleus attractions, which collectively govern nuclear interactions. By avoiding the explicit decomposition into bonded and non-bonded terms as in classical MD, AIMD provides an accurate and holistic representation of molecular systems. However, this comes with significant computational costs, restricting the method to smaller systems or shorter simulation times.

For this work, AIMD simulations were performed using the CP2K software package,[15] a widely used program for atomistic simulations that integrates quantum and classical approaches. CP2K employs a mixed Gaussian and plane wave (GPW) basis set for electronic structure calculations, which combines the efficiency of Gaussian functions with the accuracy of plane waves for describing electronic interactions.[16] Core electrons are treated using pseudopotentials, specifically optimized for computational efficiency and accuracy in representing the ionic cores, while valence electrons are explicitly considered.[17] This combination allows CP2K to achieve an excellent balance between computational performance and precision, making it suitable for complex systems like titania (TiO_2).

DFT calculations within CP2K were performed using the Perdew-Burke-Ernzerhof (PBE) exchange-correlation functional,[18] known for its reliability in describing structural and electronic properties of materials. The PBE functional effectively captures the coordination environments of titanium atoms, hydration dynamics, and other electronic effects crucial to understanding the photocatalytic activity of TiO_2. CP2K's efficiency also makes it feasible to simulate systems over extended timescales compared to other AIMD frameworks, allowing for the exploration of dynamic phenomena in greater detail.

2.2.3 Fundamentals of MD

2.2.3.1 Thermodynamic Ensembles

MD simulations are conducted under different thermodynamic ensembles, which impose specific macroscopic constraints on the system. These ensembles determine how the system exchanges energy, particles, or volume with its surroundings:

1. **Microcanonical Ensemble (NVE):** The NVE ensemble conserves the number of particles N, volume V, and total energy E. It represents an isolated system with no interaction with the surroundings. The equations of motion are integrated directly, making it suitable for studying natural dynamics without external influence.

2. **Canonical Ensemble (NVT):** The NVT ensemble maintains a fixed N, V, and temperature T. Temperature control is achieved using a thermostat, allowing energy exchange between the system and an external heat bath. This ensemble is appropriate for studying processes under constant thermal conditions.

3. **Isothermal-Isobaric Ensemble (NPT):** In the NPT ensemble, the number of particles N, pressure P, and temperature T are held constant. Both temperature and pressure are controlled through thermostats and barostats, making it ideal for simulating structural and thermodynamic properties under real-world conditions.

4. **Grand Canonical Ensemble (μVT):** The μVT ensemble fixes the chemical potential μ, volume V, and temperature T. The number of particles in the system fluctuates as particles exchange with an external reservoir. This ensemble is used for studying adsorption or desorption phenomena.

In this thesis, the NVT ensemble was employed for both classical MD (GULP) and AIMD (CP2K) simulations. This choice allowed for the precise control of temperature while maintaining a fixed system volume, which is ideal for exploring the structural stability of hydrated TiO_2 clusters.

Once the appropriate thermodynamic ensemble is chosen, the equations of motion must be solved numerically to compute the system's time evolution. Additionally, maintaining ensemble-specific conditions, such as constant temperature and pressure, requires efficient thermostats and barostats.

2.2.3.2 Time Integration

Once the thermodynamic constraints are defined, the system's time evolution is calculated by numerically integrating Newton’s equations of motion. The

most commonly used integration algorithms in MD are the Verlet[19] and Velocity Verlet[20] schemes.

In the Verlet algorithm, the new position $\mathbf{r}(t + \Delta t)$ is calculated using the current position $\mathbf{r}(t)$ and the previous position $\mathbf{r}(t - \Delta t)$:

$$\mathbf{r}(t + \Delta t) = 2\mathbf{r}(t) - \mathbf{r}(t - \Delta t) + \frac{F(t)}{m}\Delta t^2 \tag{2.10}$$

where $\mathbf{F}(t) = -\nabla U(\mathbf{r}(t))$ is the force acting on the particle, m is its mass, and Δt is the time step. This method is computationally efficient and avoids explicit computation of velocities.

The Velocity Verlet algorithm extends the Verlet scheme by incorporating velocities explicitly, providing a more complete description of the system's dynamics:

$$\begin{aligned} \mathbf{r}(t + \Delta t) &= \mathbf{r}(t) + \mathbf{v}(t)\Delta t + \frac{\mathbf{F}(t)}{2m}\Delta t^2 \\ \mathbf{v}(t + \Delta t) &= \mathbf{v}(t) + \frac{\mathbf{F}(t) + \mathbf{F}(t + \Delta t)}{2m}\Delta t \end{aligned} \tag{2.11}$$

This algorithm ensures better energy conservation, making it the method of choice for both classical MD and AIMD simulations. For this study, the Velocity Verlet algorithm was used with a time step of 1 fs in both GULP and CP2K simulations, ensuring a balance between accuracy and computational efficiency.

2.2.3.3 Thermodynamic Control: Temperature and Pressure

To simulate systems under controlled thermodynamic conditions, thermostats and barostats are employed. These algorithms regulate the system's temperature and pressure to maintain specific ensemble conditions.

For temperature control, the Nose-Hoover thermostat is particularly effective.[21] It extends the system's equations of motion by coupling the dynamics to a fictitious heat bath. The equations of motion are modified as:

$$\frac{d\mathbf{r}_i}{dt} = \mathbf{v}_i, \quad \frac{d\mathbf{v}_i}{dt} = \frac{\mathbf{F}_i}{m_i} - \zeta \mathbf{v}_i$$
$$\frac{d\zeta}{dt} = \frac{1}{Q}\left(\sum_i \frac{m_i \mathbf{v}_i^2}{3Nk_BT} - 1\right) \tag{2.12}$$

where ζ is a coupling parameter controlling the heat exchange, Q is a parameter related to the thermal inertia, and T is the target temperature. This thermostat ensures proper sampling of the canonical ensemble.

Another commonly used thermostat is the Berendsen thermostat, which scales particle velocities to adjust the system temperature.[22] While computationally efficient, it does not rigorously sample the canonical ensemble and is generally used during equilibration phases.

In this study, the Nose-Hoover thermostat was employed in both classical MD (GULP) and AIMD (CP2K) simulations, with a target temperature of 300 K. This setup ensured accurate thermal control and proper canonical ensemble sampling.

For pressure control, the Berendsen barostat operates similarly by scaling the simulation box dimensions to maintain the target pressure. The box dimensions are adjusted according to:

$$\frac{dV}{dt} = -\frac{1}{\tau_P}(P - P_0)V, \tag{2.13}$$

where V is the system volume, P is the instantaneous pressure, P_0 is the target pressure, and τ_P is the pressure coupling constant. This method is particularly effective for stabilizing systems in the isothermal-isobaric (NPT) ensemble.

2.3 Density Functional Theory (DFT)

Quantum mechanics provides a rigorous framework for understanding the electronic structure of matter. However, solving the many-body Schrödinger

equation for systems with multiple electrons is computationally prohibitive due to the exponential scaling of the wavefunction. DFT offers an alternative approach by focusing on the electron density $\rho(\mathbf{r})$ instead of the many-electron wavefunction. This reduction in complexity makes DFT computationally efficient while retaining sufficient accuracy, enabling the study of large systems

Unlike wavefunction-based methods such as Configuration Interaction (CI) or Coupled Cluster (CC),[23] which are accurate but computationally expensive, DFT scales polynomially with the number of electrons. This efficiency makes it an indispensable tool for studying the structural and electronic properties of large clusters and surfaces, including their interaction with water molecules, as explored in this thesis.

The theoretical foundation of DFT is rooted in the Hohenberg-Kohn theorems,[4] which establish the electron density as the central quantity in determining the ground-state (GS) properties of a quantum system.

2.3.1 Overview of DFT Principles

The Hohenberg-Kohn Theorems

-First Theorem: The ground-state electron density $\rho(\mathbf{r})$ uniquely determines the external potential $V_{ext}(\mathbf{r})$, and thus all properties of a many-electron system, including its wavefunction and total energy, are functionals of $\rho(\mathbf{r})$. This relationship reduces the complexity of the quantum problem:

$$\rho(\mathbf{r}) \xrightarrow{uniqueness} V_{ext}(\mathbf{r}) \xrightarrow{Schrödinger\ eq.} \Psi \xrightarrow{properties} \text{All GS observables}$$

-Second Theorem: For any trial density $\rho(\mathbf{r})$ that is non-negative and integrates to the correct number of electrons, the total energy functional $E[\rho]$ satisfies the variational principle:

$$E[\rho] \geq E_0, \tag{2.14}$$

where E_0 is the true ground-state energy corresponding to the exact GS density $\rho_0(\mathbf{r})$. The true GS density minimizes $E[\rho]$.

These theorems provide the conceptual foundation for DFT, demonstrating that all GS properties of a system are encoded in the electron density.

The total energy functional $E[\rho(\mathbf{r})]$, calculated within the Kohn-Sham framework, provides the basis for constructing the PES of a system. As detailed earlier in the chapter, the PES represents the total energy as a function of the nuclear coordinates and is central to understanding molecular structure, reactivity, and dynamics.

In structural optimization, the aim is to locate the global or local minima on the PES, which correspond to stable or metastable configurations of the system. The Hohenberg-Kohn theorems ensure that the PES is uniquely determined by the electron density $\rho(\mathbf{r})$, linking nuclear positions, electronic configurations, and energy.

This framework is critical for studying TiO_2 NPs, where interactions with water molecules, surface properties, and structural stability are governed by the topography of the PES. Understanding features such as minima (stable structures) and barriers (reaction pathways) provides insights into photocatalytic activity and surface dynamics.

2.3.2 The Kohn-Sham Equations

Building on the Hohenberg-Kohn theorems, Kohn and Sham introduced in 1965 a practical framework to make DFT computationally feasible.[24] The key idea was to replace the interacting many-electron system with a fictitious system of non-interacting electrons that reproduces the same GS electron density $\rho(\mathbf{r})$. This simplification transforms the complex many-body quantum problem into a more tractable one, while retaining the essential physics encoded in the electron density.

To achieve this, the total energy functional $E[\rho]$ of the system is expressed as:

$$E[\rho] = T[\rho] + \int V_{\text{ext}}(\mathbf{r})\rho(\mathbf{r})\ d\mathbf{r} + J[\rho] + E_{\text{xc}}[\rho] \qquad (2.15)$$

where each term has a specific physical meaning:

- $T[\rho]$ represents the kinetic energy of the fictitious system of non-interacting electrons that yields the same electron density $\rho(\mathbf{r})$. It is given by:

$$T[\rho] = \sum_i \int \psi_i^*(\mathbf{r}) \left(-\frac{\hbar^2}{2m}\nabla^2\right) \psi_i(\mathbf{r}) \; d\mathbf{r} \tag{2.16}$$

where $\psi_i(\mathbf{r})$ are the Kohn-Sham (KS) single-particle orbitals. While T[ρ] is not the true kinetic energy of the interacting electrons, it accounts for the dominant contribution, with the remaining part included in the exchange-correlation energy $E_{\text{xc}}[\rho]$:

- $\int V_{\text{ext}}(\mathbf{r})\rho(\mathbf{r}) \; d\mathbf{r}$ accounts for the interaction of the electrons with the external potential $V_{\text{ext}}(\mathbf{r})$, which includes the Coulomb attraction between electrons and nuclei and any other external fields.
- $J[\rho]$ is the classical Coulomb (Hartree) term, describing the classical electrostatic interaction between electrons. It is expressed as:

$$J[\rho] = \frac{1}{2}\int\int \frac{\rho(\mathbf{r})\rho(\mathbf{r}')}{|\mathbf{r}-\mathbf{r}'|} \; d\mathbf{r} \; d\mathbf{r}' \tag{2.17}$$

where $|\mathbf{r}-\mathbf{r}'|$ is the distance between two points $\mathbf{r}$ and $\mathbf{r}'$. This term, being purely classical, does not include quantum mechanical effects such as exchange or correlation.

- $E_{\text{xc}}[\rho]$, the exchange-correlation energy functional, is the most crucial and challenging term. It encompasses all the quantum mechanical effects beyond the non-interacting kinetic energy and classical Coulomb terms. Specifically, it includes:
    - Exchange Energy, originating from the antisymmetry of the many-electron wavefunction due to the Pauli exclusion principle.[25]
    - Correlation Energy, accounting for the correlated motion of electrons due to their mutual Coulomb repulsion.

Among these terms, $E_{\mathrm{xc}}[\rho]$ is the only one not explicitly known and must be approximated. Despite this, practical approximations, such as the Local Density Approximation (LDA)[24] and Generalized Gradient Approximation (GGA),[18] have been highly successful in predicting a wide range of material properties.

2.3.3 Exchange-correlation functionals

The accuracy of the Kohn-Sham formalism hinges on the quality of the approximation for $E_{\mathrm{xc}}[\rho]$. This term encapsulates the intricacies of quantum mechanical exchange and correlation effects, which are essential for predicting GS properties with high fidelity. The development of efficient and reliable approximations has led DFT to become one of the most widely used theoretical tools for studying molecular and condensed matter systems.

One of the simplest and most historically significant approximations is the Local Density Approximation. LDA assumes that the exchange-correlation energy at each point in space depends only on the local electron density, $\rho(\mathbf{r})$, as it would in a uniform electron gas. The functional form of $E_{\mathrm{xc}}^{\mathrm{LDA}}$ is parameterized using data from homogeneous electron gas systems, typically derived from quantum Monte Carlo simulations.[26] This approximation works well for systems with nearly uniform densities, such as metals and simple bulk materials.[24,27] However, it struggles in systems with significant density variations, such as molecules, surfaces, and nanostructures.[18,28] These limitations often result in overbinding, where atoms are predicted to have shorter bond lengths and higher cohesive energies than observed experimentally.[29] Despite these shortcomings, LDA remains computationally efficient and is often used as a starting point for more complex calculations.

Building upon LDA, the Generalized Gradient Approximation introduces the gradient of the electron density, $\nabla\rho(\mathbf{r})$ into the functional. This additional term enables GGA to account for density inhomogeneities, making it more suitable for molecular systems, surfaces, and materials with complex electronic structures:

$$E_{\mathrm{xc}}^{\mathrm{PBE}}[\rho] = \int \rho(\mathbf{r})\epsilon_{\mathrm{xc}}(\rho, \nabla\rho)\, d\mathbf{r} \tag{2.18}$$

where $\epsilon_{\mathrm{xc}}(\rho, \nabla\rho)$ represents the exchange-correlation energy density as a function of both the local density and its gradient. GGA functionals like PBE are particularly effective for systems where the electron density varies significantly, such as surfaces. For instance, PBE has been successfully applied to study the surface properties of anatase TiO_2, where such variations play a critical role.[30-32] However, GGA functionals often underestimate band gaps, a limitation that can affect the accuracy of electronic property predictions for semiconductors like TiO_2.[31]

To overcome the limitations of LDA and GGA, hybrid functionals incorporate a fraction of exact exchange energy from Hartree-Fock (HF) theory. A widely used example is the B3LYP (Becke, 3-parameter, Lee–Yang–Parr) functional,[28,33,34] defined as:

$$E_{\mathrm{xc}}^{\mathrm{B3LYP}} = (1-a)E_{x}^{\mathrm{LDA}} + aE_{x}^{\mathrm{HF}} + b\Delta E_{x}^{\mathrm{GGA}} + E_{c}^{\mathrm{LDA}} + c\Delta E_{c}^{\mathrm{GGA}} \tag{2.19}$$

where the coefficients *a*, *b*, and *c* balance the contributions from different exchange and correlation components. Hybrid functionals like B3LYP and PBE0[35] are particularly valuable for systems requiring precise predictions of electronic properties, such as band gaps, or for analysing charge transfer processes.

An important variant of hybrid functionals is CAM-B3LYP (Coulomb-Attenuating Method B3LYP),[36] which introduces range separation into the exchange energy. By combining short-range exact exchange with long-range corrections, CAM-B3LYP is particularly suited for studying charge-transfer excitations and long-range electronic interactions. This makes it an excellent choice for investigating the excited-state dynamics of TiO_2 NPs and their interactions with water molecules under photoactivation.

In this thesis, DFT is applied to study TiO_2 nanosystems, focusing on their structural optimization, electronic structure, and hydration properties. GGA functionals such as PBE were employed for initial optimizations due to their

computational efficiency and ability to capture surface properties. To achieve greater accuracy, hybrid functionals like PBE0, B3LYP and CAM-B3LYP were used to refine predictions of band gaps, charge distributions, and excited-state properties. These functionals played a crucial role in understanding the photocatalytic behaviour of anatase TiO_2, where the interplay of surface dynamics and electronic structure governs interactions with water molecules and reactivity under light activation.

2.3.4 Dispersion forces

While standard exchange-correlation functionals, such as GGA (e.g., PBE), describe many electronic properties well, they often fail to accurately account for the long-range components of dispersion interactions (including van der Waals forces)[37,38]. These interactions are critical for describing weak interatomic forces that influence adsorption, binding energies, and structural stability, particularly for systems involving molecular interactions on surfaces.

To address this limitation, several dispersion correction schemes have been developed to supplement DFT calculations. One widely used approach is the Tkatchenko-Scheffler (TS) dispersion correction, which refines van der Waals interactions by making the C_6 dispersion coefficients environment-dependent.[39] Unlike early empirical approaches, TS derives its parameters using Hirshfeld partitioning, where the electron density of each atom is estimated based on its free-atom reference state. This allows the method to dynamically scale atomic polarizabilities and dispersion coefficients, ensuring a more accurate, system-dependent correction to dispersion interactions. The total dispersion energy in the TS scheme is expressed as:

$$E_{\text{disp}} = -\frac{1}{2}\sum_{A,B} s_6 \frac{C_6^{AB}}{R_{AB}^6} f_{\text{damp}}(R_{AB}) \tag{2.20}$$

where C_6^{AB} are the dispersion coefficients derived from the electron density, R_{AB} is the distance between atoms A and B, s_6 is a scaling factor specific to

the chosen functional, and $f_{\text{damp}}(R_{AB})$ is a damping function that avoids overestimation at short interatomic distances.

Another widely adopted method is the DFT-D3 dispersion correction developed by Grimme, which takes a semi-empirical approach by introducing a pairwise correction term to account for dispersion interactions. [40] Unlike TS, DFT-D3 applies pre-tabulated atomic dispersion coefficients, but introduces an extended formulation that includes three-body interactions (D3(BJ) variant) and coordination number dependence, further improving its accuracy. The total DFT-D3 energy is given by:

$$E_{\text{DFT-D3}} = E_{\text{KS-DFT}} - E_{\text{disp}} \tag{2.21}$$

where $E_{\text{KS-DFT}}$ is the usual self-consistent Kohn-Sham energy as obtained from the chosen density functional. The dispersion correction itself (E_{disp}) consists of the sum of two-body and three-body interaction terms, with the most significant two-body term expressed as:

$$E^{(2)} = \sum_{A,B} \sum_{n=6,8,10,\ldots} s_n \frac{C_n^{AB}}{R_{AB}^n} f_{\text{damp},n}(R_{AB}) \tag{2.22}$$

where C_n^{AB} are the dispersion coefficients for each atomic pair, R_{AB}^n is the interatomic distance, s_n is a scaling factor, $f_{\text{damp},n}(R_{AB})$ is the damping function ensuring short-range behavior is properly treated.

2.3.5 Implementation of DFT: Parameters and Computational Details

In practice, the accuracy of DFT calculations relies on the careful selection of computational parameters, including basis sets, cutoff energies, k-point sampling, and methods for including dispersion corrections. This thesis employs the Fritz Haber Institute *ab initio* materials simulation (FHI-aims) code,[41] an all-electron electronic structure code based on numeric atom-centred orbitals (NAOs), which offers a robust and efficient framework for accurate calculations of both molecular and periodic systems. The following subsections

outline the key computational details and parameters used in this work. Although plane-wave methods combined with pseudopotentials are widely used for periodic systems due to their scalability and efficiency, they require approximations to handle core electrons. This can introduce inaccuracies in systems where core states play an important role. By contrast, FHI-aims' all-electron approach ensures a complete and precise description of the electronic wavefunctions near atomic nuclei. This makes it particularly advantageous for studying systems like TiO_2, where core-level states influence bonding and electronic properties.[42]

2.3.5.1 Basis sets

In FHI-aims, basis sets are constructed hierarchically to ensure systematic convergence of energies and electronic properties. The NAOs are localized and designed to describe both the near-nuclear and bonding regions with high precision:

$$\varphi_{nlm}(\mathbf{r}) = R_{nl}(r)Y_{lm}(\theta, \phi) \tag{2.23}$$

where $\mathbf{r} = (r, \theta, \phi)$ is the position vector in spherical coordinates; $R_{nl}(r)$ is the radial part of the orbital, which is represented numerically on a grid; and $Y_{lm}(\theta, \phi)$ is the angular part, represented by the spherical harmonics.

This localization enables computational efficiency while maintaining accuracy, particularly in the description of core and valence states.

Unlike plane-wave basis sets, which require the use of pseudopotentials to approximate the effects of core electrons, the all-electron nature of FHI-aims eliminates this approximation. By explicitly treating core electrons, FHI-aims provides a more accurate representation of electronic wavefunctions near atomic nuclei, which is particularly important for systems where core states significantly influence chemical bonding and electronic properties. This feature is advantageous in structural optimization and the calculation of detailed electronic structure properties, such as band gaps and charge distributions.

In this thesis, the calculations were run commonly employing a light tier-1 numerical atom-centred orbital basis set, which has an accuracy comparable to a Triple-Zeta Valence plus Polarization (TZVP) Gaussian-type orbital basis set for TiO_2.[32]

2.3.5.2 Energy cutoff and k-point sampling

The numerical grids used for integration and self-consistent field (SCF) calculations are critical to ensuring convergence of total energies and derived properties. In FHI-aims, these grids are controlled by numerical cutoff parameters. For this work, the "tight" settings were employed for all TiO_2 systems, ensuring reliable convergence of total energies, forces, and other key properties. The "tight" settings represent a compromise between accuracy and computational efficiency, providing dense grids for accurate evaluation of both near-nuclear and interatomic regions. This is particularly important for systems with strong electron localization or polarizability, such as TiO_2 NPs and surfaces.

For periodic calculations, such as those involving TiO_2 surfaces, accurate integration over the Brillouin zone[43,44] is achieved through k-point sampling. In this work, a Monkhorst-Pack grid was employed to sample the reciprocal space.[45-47] The density of the k-point grid was carefully chosen based on the size and symmetry of the system to balance computational cost and accuracy.

2.3.5.3 Dispersion corrections

In the context of TiO_2, DFT-D3 is particularly useful for modelling interactions between water molecules and TiO_2 surfaces, where hydrogen bonding and van der Waals forces significantly affect adsorption geometry and energetics. The inclusion of dispersion corrections ensures that such interactions are accurately represented, providing a more realistic description of the hydration and catalytic properties of TiO_2 NPs.[48]

When performing AIMD and TD-DFT (Time-Dependent DFT) simulations in CP2K, the DFT-D3 dispersion correction was explicitly accounted for to improve the accuracy of intermolecular interactions. However, when conducting DFT calculations in FHI-aims, the Tkatchenko-Scheffler dispersion correction was applied instead. While different dispersion correction schemes were

employed, both are established approaches that significantly enhance the treatment of dispersive interactions compared to standard GGA functionals. Minor quantitative differences may arise in adsorption energies or structural parameters; however, these are very unlikely to affect our observed trends or the consistency of results within each computational framework.

2.4 Thermodynamics and Gibbs Free Energy

Thermodynamics provides the framework for understanding the stability, reactivity, and phase behaviour of materials, particularly in realistic environmental conditions involving temperature and pressure. Moreover, it provides insight into how hydration modifies the electronic and structural properties of systems such as TiO_2. For instance, the dissociative adsorption of water influences the surface hydroxylation, which in turn affects the material's catalytic and photoelectronic characteristics. These effects are captured through a combination of enthalpic contributions (from DFT-derived energetics) and entropic considerations (arising from configurational and vibrational states), making thermodynamic analysis indispensable for the design and optimization of TiO_2-based applications.

2.4.1 General Concepts of Thermodynamics

Thermodynamic behaviour is governed by the four fundamental laws:

1. **Zeroth Law:** Establishes thermal equilibrium and forms the basis for defining temperature.
2. **First Law:** Conservation of energy, expressed as:

$$\Delta U = q + W \tag{2.24}$$

where ΔU is the change in internal energy, q is heat exchanged, and w is work done on the system.

3. **Second Law:** Introduces entropy (S) and dictates that the total entropy of the universe increases in spontaneous processes:

$$\Delta S_{\text{universe}} = \Delta S_{\text{system}} + \Delta S_{\text{surroundings}} > 0 \tag{2.25}$$

4. **Third Law:** States that the entropy of a perfect crystal approaches zero as temperature approaches absolute zero.

These laws underpin the concepts of energy, entropy, and free energy, providing tools for analysing equilibrium and reaction dynamics.

State functions-properties dependent only on the current state of the system-, are central to thermodynamic analysis. Key functions include:

- **Internal Energy ($\boldsymbol{U}$)**: Total energy of a system.
- **Enthalpy ($\boldsymbol{H}$)**: Heat content at constant pressure:

$$H = U + PV \tag{2.26}$$

  where P is pressure and V is volume.

- **Gibbs Free Energy ($\boldsymbol{G}$)**: A thermodynamic potential that combines enthalpy and entropy to predict the spontaneity of processes:

$$G = H - TS \tag{2.27}$$

A negative Gibbs free energy change ($\Delta G < 0$) indicates a spontaneous process under constant pressure and temperature.

For example, in hydration processes studied in this thesis, the Gibbs free energy quantifies the stability of TiO_2 clusters in aqueous environments. It accounts for both enthalpic contributions, such as solute-solvent interactions, and entropic effects, such as the rearrangement of water molecules.

2.4.2 *Ab Initio* Atomistic Thermodynamics and Surface Adsorption

Ab Initio Atomistic thermodynamics (AIAT) combines DFT-derived energies with classical thermodynamic principles to study systems at realistic conditions.[49,50] For a surface or molecular system in contact with a reservoir, the Gibbs free energy can be expressed as:

$$G = G_{\text{solid}} + G_{\text{reservoir}} + \Delta G_{\text{surface}} \tag{2.28}$$

where G_{solid} is the free energy of the material, $G_{\text{reservoir}}$ accounts for interactions with the reservoir, and $\Delta G_{\text{surface}}$ reflects surface-specific contributions, such as adsorption and hydration.

By integrating DFT calculations of internal energy terms with vibrational and configurational contributions, the full thermodynamic landscape of the system can be explored. This approach is critical for understanding hydration dynamics and stability, as applied to TiO_2 in this thesis.

A fundamental aspect of surface thermodynamics is the study of adsorption processes, which play a key role in catalysis, corrosion, and sensing applications. *Ab initio* thermodynamics, by bridging quantum mechanical calculations with classical thermodynamic principles, provides a predictive framework for assessing the stability of adsorbed species under varying temperature and pressure conditions.

The partitioning of the Gibbs free energy in this formalism allows for a systematic analysis of surface-specific phenomena while maintaining consistency with bulk and reservoir thermodynamics. This makes AIAT a powerful tool for investigating material behaviour at the atomic level, with direct implications for real-world applications.

For homogeneous surfaces, such as single-crystal planes, the surface free energy per unit area (γ) is defined as:

$$\gamma = \frac{1}{A}[G_{\text{solid}} + G_{\text{gas}} + \Delta G_{\text{surf}}] \tag{2.29}$$

where A is the surface area. The interplay between these terms determines the stability of the surface under given environmental conditions.

Adsorption introduces changes to the surface free energy due to the interaction of adsorbates with the surface. To quantify this, the Gibbs free energy of adsorption (ΔG_{ads}) is defined relative to the clean surface and the chemical potential of the adsorbate:

$$\Delta G_{\text{ads}} = \frac{1}{A}[G_{\text{surface}}(\text{ads}) - G_{\text{surface}}(\text{clean}) - \mu_{\text{adsorbate}} \Delta N_{\text{adsorbate}}] \tag{2.30}$$

Here, $\Delta N_{\text{adsorbate}}$ is the change in the number of adsorbates on the surface, and $\mu_{\text{adsorbate}}$ is the chemical potential of the adsorbate, which depends on the temperature (T) and pressure (p) of the reservoir:

$$\mu_{\text{adsorbate}}(T,p) = \mu^{\circ}_{\text{adsorbate}}(T) + k_B T \ln\left(\frac{p}{p^{\circ}}\right) \tag{2.31}$$

where $\mu^{\circ}_{\text{adsorbate}}(T)$ is the chemical potential at standard pressure (p°) and is derived from the partition function of the adsorbate as an ideal gas. This partition function accounts for translational, rotational, vibrational, and electronic degrees of freedom:

$$Q_{\text{tot}} = \frac{1}{N!}(q_{\text{trans}}\, q_{\text{rot}}\, q_{\text{vib}}\, q_{\text{electr}})^N \tag{2.32}$$

where q_{trans}, q_{rot}, q_{vib}, q_{electr} represent the contributions from translational, rotational, vibrational, and electronic motions, respectively. The evaluation of these terms relies on the ideal gas law and assumes separability of nuclear, electronic, and vibrational motions under the Born-Oppenheimer approximation.

The principles of AIAT extend the treatment of the chemical potential to solid-phase systems, combining DFT-derived total energies with vibrational and configurational contributions. For solids, the Gibbs free energy can be decomposed into:[50,51]

$$G = E_{\text{total}} + F_{\text{vib}} + F_{\text{conf}} + pV \tag{2.33}$$

where E_{total} is the total (internal) energy calculated from DFT, F_{vib} is the vibrational free energy, F_{conf} is the configurational free energy, pV.

E_{total} dominates the free energy and is calculated with high accuracy using DFT. This ensures that AIAT leverages the predictive power of first-principles methods, enabling reliable thermodynamic reasoning under finite T and p conditions. While lower-level methods like semi-empirical potentials can also be

used, their reduced accuracy limits the reliability of thermodynamic predictions.

The vibrational free energy, F_{vib}, arises from atomic vibrations and is computed using the phonon density of states (DOS), $\sigma(\omega)$. For solids, it is expressed as:

$$F_{\text{vib}}(T) = \int \sigma(\omega) F_{\text{vib}}(T, \omega)\ d\omega \tag{2.34}$$

where:

$$F_{\text{vib}}(T, \omega) = k_B T \ln(1 - e^{-\hbar\omega/k_B T}) + \frac{\hbar\omega}{2} \tag{2.35}$$

Here, the first term represents the thermal vibrational contribution, and the second term is the zero-point energy. For surfaces, the vibrational DOS $\sigma(\omega)$ can differ significantly from the bulk, and surface-specific vibrational contributions must be computed.

However, direct evaluation of surface vibrational contributions using DFT is computationally prohibitive. AIAT relies on a crucial assumption: the differences in Gibbs free energy terms, rather than their absolute values, determine quantities such as the Gibbs free energy of adsorption (ΔG_{ads}) or the surface free energy (γ). These differences allow for error cancellation, particularly between similar configurations such as the bulk and the surface.

The vibrational contribution to ΔG_{ads} is given as:

$$F_{\text{vib,ads}}(T) = -\frac{1}{A}[\int (\sigma_{surf}(\omega) - \sigma_{\text{bulk}}(\omega))F_{\text{vib}}(T, \omega)] - \mu_{\text{adsorbate}}(T) \tag{2.36}$$

where $\sigma_{\text{surf}}(\omega)$ and $\sigma_{\text{bulk}}(\omega)$ are the phonon DOS for the surface and bulk, respectively. These terms capture only the changes in vibrational properties between the bulk and the surface, focusing on surface-specific phenomena.

The assumptions made in AIAT, such as the cancellation of errors in Gibbs free energy differences, significantly simplify the treatment of vibrational contributions. Although vibrational free energy terms are not negligible, their influence

on adsorption and surface stability can be reliably approximated by focusing on relative changes. This approach ensures computational efficiency while maintaining the predictive power of first-principles methods, making AIAT a robust framework for studying adsorption processes and surface thermodynamics in complex systems like TiO_2.

Lastly, the configurational free energy, F_{conf}, accounts for the entropy associated with the arrangement of atoms or species on the surface or in the bulk. Fully evaluating this term is computationally demanding, as it requires sampling the extensive configuration space of possible structures. While modern statistical mechanics techniques, such as Monte Carlo simulations, are designed for this purpose, their direct application to electronic structure theories remains computationally prohibitive due to the need for a vast number of free energy evaluations.

To circumvent this challenge, the real system is often mapped onto a simpler, discretized model system, the Hamiltonian of which is computationally efficient to evaluate. One prominent approach for such mappings is the lattice-gas Hamiltonian or cluster expansion methods.[52-54] These techniques discretize the configuration space into a lattice of adsorption sites or local clusters, parameterized using DFT calculations. While uncertainties arise in how accurately the model represents the real system, these methods often yield deeper insights into the governing mechanisms and thermodynamic trends.

An alternative, simpler approach, which is the focus here, involves screening a selection of known or potentially relevant ordered surface structures. The most stable structure is identified by determining which configuration minimizes the surface free energy or Gibbs free energy of adsorption under specific (T, p) conditions. At sufficiently low temperatures, the remaining configurational entropy per unit area arises primarily from a limited number of defects in these ordered structures. This residual entropy can be estimated for specific cases, but its contribution is generally minor compared to the energy differences between ordered configurations.

For TiO_2, an essential material in photocatalysis, photovoltaics, and environmental remediation, hydration processes are integral to its structural and

functional properties. These hydration processes influence surface reactivity, electronic structure, and photocatalytic efficiency. This process plays a pivotal role in stabilizing surface structures, mediating chemical reactions, and determining the energetics of adsorption and desorption processes. The Gibbs free energy of hydration ($\Delta G_{\text{hydration}}$) quantifies the thermodynamic favourability of this interaction, linking molecular-scale processes to macroscopic stability under varying environmental conditions.

2.4.3 Phase Diagrams

By minimizing ΔG_{ads} for each possible adsorption configuration (i.e., degree of adsorption), the most stable phase can be determined at any given (T, p). These stability regions are then mapped onto p-T phase diagrams (see Figure 2.1), which serve as powerful tools for visualizing the stability of adsorbed species across a range of temperature and pressure conditions.

The transitions between different adsorption degrees are marked by phase boundaries, where the Gibbs free energy of competing phases is equal. At low temperatures and high pressures, adsorbed phases with high coverage are typically favoured, while at high temperatures or low pressures, desorption is more likely, leading to clean or sparsely covered surfaces.

For example, in a simple adsorption system with multiple surface configurations, the phase diagram might reveal distinct regions where low-coverage, high-coverage, or clean surface phases dominate. The curvature of the phase boundaries reflects the nonlinear dependence of the chemical potential on T and p, as described by the logarithmic term in the chemical potential expression (Equation 2.31).

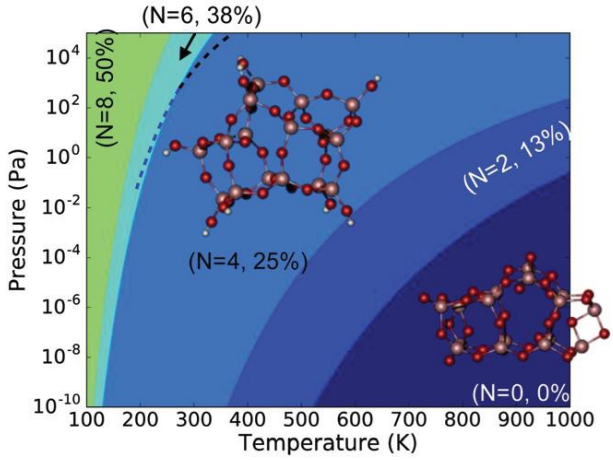

Figure 2.1: Example for *p–T* phase diagram for titania nanoclusters adapted from reference 13. Blue and black dashed lines indicate the equilibrium vapour pressure with ice and liquid water respectively. The colours in the *p–T* phase diagram regions relate to the degree of hydration (the darker the colour, the lower the hydration degree).

2.5 Fundamentals of Trajectory-Based Methods for Nonadiabatic Dynamics

The analysis of excited states is crucial for understanding the efficiency and functionality of photocatalytic materials such as inorganic semiconductors.[55-57] The interaction between light and matter leads to the generation of excited electronic states, initiating charge transfer, spin transfer, and excitation energy transfer processes. The competition between charge carrier separation, recombination, and energy dissipation directly impacts the photocatalytic performance, making the study of non-equilibrium quantum dynamics essential.[58-60]

Modelling these excited-state processes requires a nonadiabatic (NA) description, as it involves the inclusion of multiple electronic states and their couplings, which cannot be captured by a single-state (adiabatic) approach. While full quantum mechanical methods can describe such dynamics with high accuracy, they are computationally expensive and impractical for large, multidimensional systems like TiO_2. As a result, trajectory-based quantum-classical and semiclassical approaches have been developed to approximate NA effects

efficiently.[61-64] These approaches rely on methodological "building blocks" that enable the simulation of electronic transitions and energy relaxation pathways in complex materials. Understanding and applying these methods is essential for accurately modelling the excited-state dynamics of TiO_2 NPs and optimizing their photocatalytic properties.

2.5.1 Diabatic and adiabatic representation

In quantum mechanics, the state of a system can be described by a wavefunction $|\boldsymbol{\Psi}\rangle$ or, for pure states, equivalently by a density matrix operator $\hat{\boldsymbol{\rho}} = |\boldsymbol{\Psi}\rangle\langle\boldsymbol{\Psi}|$. More generally, the density matrix formalism allows for the description of both pure and mixed states, whereas the wavefunction representation applies only to pure states.

The wavefunction is an abstract entity that encapsulates the state of the system but does not inherently specify how this state is represented. To work with this wavefunction practically, we choose a specific representation, defining it in terms of key variables that describe the system's dynamics. For example, one might focus on the electronic degrees of freedom and represent the wavefunction in terms of electronic coordinates as $\Psi(\mathbf{r})=\langle\mathbf{r}|\Psi\rangle$, where $\mathbf{r}$ denotes the positions of electrons, and $\Psi(\mathbf{r})$ is the projection of the abstract state $|\Psi\rangle$ onto the coordinate representation.

The choice of basis for representing the wavefunction or density matrix greatly influences the mathematical and physical interpretation of the problem. Commonly used bases include the adiabatic and diabatic representations, which differ in how they define the elementary states of the system. Adiabatic states, $|\psi_{\text{adi}}\rangle$, are eigenstates of the electronic Hamiltonian $\hat{H}_{el}(\mathbf{r}, \mathbf{R})$ at each fixed nuclear configuration $\mathbf{R}$. These states form a natural basis when energy levels are well-separated and smoothly vary with nuclear motion. However, when energy levels are close or electronic state couplings (such as vibronic or electronic couplings) become significant, nonadiabatic couplings arise (due to the time-dependent ansatz used to describe the wavefunction in this basis), making calculations more complex. Counterintuitively, stronger diabatic coupling can actually enhance adiabatic behaviour by suppressing nonadiabatic transitions.

In contrast, diabatic states, $|\psi_{\mathrm{dia}}\rangle$, are defined as the ones that eliminate the diabatic couplings. This is achieved by defining the states such that the derivative couplings between them are zero, or nearly so (those are called quasi-diabatic states). While strictly diabatic states are rarely available in complex systems,[65] they can be approximated as quasi-diabatic states that simplify the description of transitions and interactions between electronic states. For example, diabatic states are particularly useful for modelling chemical reactions, where electrons may transfer between atoms as nuclei move.[66,67]

The wavefunction is invariant under a change of representation, but its components transform according to a unitary matrix U, such that $|\psi_{\mathrm{adi}}\rangle = |\psi_{\mathrm{dia}}\rangle U$. Correspondingly, the Hamiltonian in these representations is related by $\hat{H}_{adi} = U^{\dagger}\hat{H}_{dia}U$. This flexibility allows one to choose the representation that best suits the problem at hand, whether focusing on the smooth energy surfaces of the adiabatic basis or the interaction-driven dynamics emphasized in the diabatic basis.

These ideas are foundational for understanding nonadiabatic dynamics, where the interplay of electronic and nuclear motions demands a representation that accurately captures the coupled behaviour of these subsystems. Adiabatic and diabatic representations provide complementary tools for tackling these challenges, whether the goal is to study energy levels or transitions in quantum systems.

2.5.2 Nonadiabatic Molecular dynamics

These concepts provide the framework for understanding nonadiabatic molecular dynamics (NA-MD), where the breakdown of the Born-Oppenheimer approximation requires accounting for coupled electronic and nuclear motions. In such cases, the evolution of electronic states cannot be considered independently of nuclear motion, requiring a more refined approach to capture the interplay between these subsystems. The total wavefunction, $X(\mathbf{r}, \mathbf{R}, t)$, which depends on the positions of all electrons, nuclei, and time, evolves according to the time-dependent Schrödinger equation (TD-SE):

$$i\hbar \frac{\partial X(\mathbf{r}, \mathbf{R}, t)}{\partial t} = \hat{H}(\mathbf{r}, \mathbf{R})\mathrm{X}(\mathbf{r}, \mathbf{R}, t) \tag{2.37}$$

Here, the variable **r** refers collectively to the spatial components and spin-coordinates for all electrons, and the variable **R** refers collectively to the spatial components of all nuclei. $\hat{H}(\mathbf{r}, \mathbf{R})$ is the total Hamiltonian, comprising the nuclear kinetic energy operator $\hat{T}_R(\mathbf{R})$ and the electronic Hamiltonian operator $\hat{H}_{el}(\mathbf{r}, \mathbf{R})$:

$$\hat{H}(\mathbf{r}, R) = \hat{T}_R(\mathbf{R}) + \hat{H}_{el}(\mathbf{r}, \mathbf{R}) \tag{2.38}$$

where $\hat{H}_{el}$ contains all terms of Equation 2.3 except for the nuclear-nuclear repulsion potential.

The total wavefunction can be factorized into components representing the slow-moving nuclear and fast-moving electronic subsystems:

$$X(\mathbf{r}, \mathbf{R}, t) = \sum_I \chi_I(\mathbf{R}, t)\Psi_I(\mathbf{r}; \mathbf{R}) \tag{2.39}$$

where $\chi_I(\mathbf{R}, t)$ represents the nuclear wavefunction, which depends functionally on nuclear coordinates **R**, while $\Psi_I(\mathbf{r}; \mathbf{R})$ denotes the electronic wavefunction, which depends parametrically on **R**. This ansatz leads to coupled equations describing the dynamics of both subsystems. However, due to the computational complexity of solving these coupled equations for systems with many degrees of freedom, approximations are necessary.

One commonly employed approach is the classical path approximation (CPA), which treats the nuclear subsystem as moving along classical trajectories $R(t)$. This reduces the computational cost by simplifying the nuclear dynamics to scale linearly with the number of degrees of freedom. Under CPA, the total wavefunction is expressed as:

$$X(\mathbf{r}, \mathbf{R}(t), t) = \sum_I c_I(t)\Psi_I(\mathbf{r}; \mathbf{R}(t)) \tag{2.40}$$

where $c_I(t)$ are time-dependent amplitudes representing the contribution of the I-th electronic state, and $\Psi_I(\mathbf{r}; \mathbf{R}(t))$ are stationary electronic wavefunctions. Substituting this ansatz into the TD-SE and projecting onto the electronic wavefunctions yields a differential equation for the amplitudes:

$$i\hbar \frac{\partial c_I}{\partial t} = \sum_J (E_I \delta_{IJ} - i\hbar d_{IJ}) c_J \tag{2.41}$$

Here, E_I is the energy of the I-th electronic state, and d_{IJ} is the scalar nonadiabatic coupling (NAC) term given by:

$$d_{IJ} = \langle \Psi_I(\mathbf{r}; \mathbf{R}(t)) | \frac{\partial}{\partial t} | \Psi_J(\mathbf{r}; \mathbf{R}(t)) \rangle = \dot{\mathbf{R}} \cdot d_{IJ} \tag{2.42}$$

where d_{IJ} is the nonadiabatic coupling vector, and $\dot{\mathbf{R}}$ denotes the time derivative of the nuclear coordinates. The NAC term d_{IJ} quantifies the coupling between electronic states due to nuclear motion and is critical for describing transitions between states.

To further simplify nonadiabatic simulations, the Neglect of Back-Reaction Approximation (NBRA) is often employed.[68-70] NBRA assumes that electronic transitions do not significantly influence nuclear dynamics, meaning that nuclear motion is treated as independent of electronic state changes, while electronic transitions still depend on nuclear motion. This approximation reduces computational cost because nuclear trajectories can be precomputed using classical or semiclassical dynamics, allowing electronic evolution to be solved as a separate post-processing step rather than solving fully coupled nonadiabatic equations. While NBRA omits some important physical interactions, it provides a practical approach for simulating large systems and long timescales, particularly when detailed quantum-classical coupling is computationally prohibitive. In many cases,[71-73] this approximation still yields meaningful insights into excited-state dynamics, including charge carrier relaxation, energy transfer, and photochemical reactions.

The coherent evolution of electronic amplitudes, as governed by the above Equation 2.39, forms the basis of mixed quantum-classical dynamics (MQCD) methods. The electronic structure methods used to compute the energies and wavefunctions in this equation—such as Hartree-Fock, DFT, and TD-DFT—are crucial for practical NA-MD simulations. TD-DFT, in particular, provides an efficient means of describing excited-state phenomena and is explored in detail in the following subsection.

2.5.3 TD-DFT

Time-dependent density functional theory (TD-DFT) serves as a computationally efficient extension of traditional DFT for handling time-dependent phenomena. First proposed by Runge and Gross,[74] TD-DFT establishes a one-to-one mapping between time-dependent potentials and electron density, analogous to the Hohenberg-Kohn theorem for ground-state DFT. A widely used implementation of TD-DFT is the real-time propagation approach, where the system's evolution is governed by the time-dependent Kohn-Sham (TD-KS) equation:

$$i\frac{\partial}{\partial t}\psi_i(\mathbf{r},t) = \hat{h}_{KS}(\mathbf{r},t)\psi_i(\mathbf{r},t) \tag{2.43}$$

where $\psi_i(\mathbf{r}, t)$ represents the time-dependent Kohn-Sham orbitals, and $\hat{h}_{KS}(\mathbf{r},t)$ is the time-dependent Fock-like operator. This Hamiltonian includes the time-dependent exchange-correlation potential, $v_{XC}[\rho(\mathbf{r}', t')](\mathbf{r}, t)$, which is inherently nonlocal in both space and time. Due to the nonlocality of the time coordinate, approximations such as the adiabatic approximation are employed, wherein v_{XC} is treated as time-local.

For weakly perturbing external fields, TD-DFT is often applied using the linear-response formalism (LR-TDDFT). This involves solving a matrix eigenvalue problem, as formulated by Casida:[75]

$$\begin{pmatrix} A & B \\ B & A \end{pmatrix}\begin{pmatrix} X \\ Y \end{pmatrix} = \omega \begin{pmatrix} I & 0 \\ 0 & -I \end{pmatrix}\begin{pmatrix} X \\ Y \end{pmatrix} \tag{2.44}$$

Here, X and Y are coefficients representing single-electron transition amplitudes, where X describes excitation amplitudes, and Y accounts for de-excitation amplitudes. The matrices A and B describe the system's excitation energies and coupling terms, governing the response of the system under time-dependent perturbations.

$$A_{ia,jb} = \delta_{ij}\delta_{ab}\Delta E_{ai} + 2K_{ia,jb},\ B_{ia,jb} = 2K_{ia,jb} \tag{2.45}$$

where $K_{ia,jb}$, the coupling matrix, incorporates the Coulomb and exchange-correlation interactions:

$$K_{ia,jb} = \int d^3\,\mathbf{r} \int d^3\,\mathbf{r}'\psi_i(\mathbf{r})\psi_a(\mathbf{r})\left[\frac{1}{|\mathbf{r}-\mathbf{r}'|} + f_{XC}(\mathbf{r},\mathbf{r}',\omega)\right]\psi_j(\mathbf{r}')\psi_b(\mathbf{r}') \tag{2.46}$$

Within the adiabatic approximation, the exchange-correlation kernel, $f_{XC}(\mathbf{r},\mathbf{r}',\omega)$ becomes frequency-independent, simplifying the calculations by relying on GS exchange-correlation functionals.

Further simplifications are often applied using the Tamm-Dancoff approximation (TDA),[76] wherein the B matrix in Casida's equation is set to zero. This reduces the eigenvalue problem to:

$$AX_k = \omega_k X_k \tag{2.47}$$

where X_k provides the coefficients of the k-th excitation, and ω_k corresponds to its excitation energy.

TD-DFT, particularly in its linear-response TDA approximation forms, has become an indispensable tool for studying excited states in large systems due to its computational efficiency and scalability.[77,78,79] Its application to systems like TiO_2 NPs has enabled detailed analyses of optical properties, exciton dynamics, and charge transfer processes.[61,62] However, while TD-DFT is widely used, its accuracy is highly sensitive to the choice of exchange-correlation functionals, especially for systems involving charge transfer excitations or

strongly correlated electronic states.[80] For instance, widely used GGA methods, such as PBE, often fail to capture excitonic effects and can yield unphysical results, such as negative energies for charge-transfer excitations.[81] In this thesis, CP2K code was employed to compute TD-DFT excitations using PBE, PBE0, and B3LYP functionals, which allowed to explore the trade-offs between computational efficiency and accuracy. While PBE0 and B3LYP improved the description of charge-transfer excitations compared to PBE, their higher computational cost limited their application to smaller systems.

2.5.4 Trajectory Surface Hopping

Among the various methods developed within this NA-MD framework, trajectory surface hopping (TSH) has emerged as one of the most effective mixed quantum-classical approaches for simulating nonadiabatic transitions.[66,82,83] In TSH methods, the nuclear subsystem evolves classically, while the electronic subsystem evolves quantum mechanically. This approach circumvents the computational expense of fully quantum mechanical treatments for large systems by allowing the nuclei to move on single, state-specific potential energy surfaces rather than an averaged PES. The electronic state amplitudes evolve according to the time-dependent Schrödinger equation, as shown in Equation 2.35.

The nuclei are propagated on the active PES determined by the current electronic state, with probabilities for transitioning between states (i.e., "surface hopping") computed based on NACs. Tully's Fewest Switches Surface Hopping (FSSH)[66] algorithm is one of the most widely used TSH methods, wherein the transition probability between two states, *I* and *J*, is given by:

$$P_{I\to J}(t) = \Delta t \frac{2\mathrm{Re}\left(R \cdot d_{IJ} c_I^*(t) c_J(t)\right)}{|c_I(t)|^2} \tag{2.48}$$

If a random number $\zeta \in [0,1]$ satisfies $\zeta < P_{I\to J}(t)$, the system hops to the new electronic state J. Following a hop, nuclear momenta are adjusted to ensure conservation of total energy, typically by rescaling the momenta along the direction of the NAC vector. However, if the nuclei lack sufficient kinetic energy

to satisfy energy conservation, the hop is deemed "frustrated," and the system remains on the original PES.

2.5.4.1 Role of decoherence in TSH

To improve the physical realism of TSH simulations, various decoherence algorithms have been developed. Decoherence accounts for the gradual loss of quantum coherence in the electronic subsystem, influenced by nuclear motion and environmental factors. Among these, the revised version of the Decoherence-Induced Surface Hopping (DISH),[84,85] the Instantaneous Decoherence at Attempted Hops (IDA),[86] and the Modified Simplified Decay of Mixing (mSDM)[85] schemes were employed in this thesis, each addressing specific challenges inherent in TSH.

The original DISH method, developed by Jaeger and Prezhdo,[84] combines the principles of surface hopping with a stochastic treatment of decoherence. Unlike traditional TSH, where surface hopping is triggered by probabilistic transitions based on NACs, DISH inherently links surface hopping to decoherence events. The stochastic component of DISH introduces decoherence by intermittently modifying the wavefunction: it either projects the wavefunction onto one of the adiabatic states, effectively collapsing the coherent superposition, or projects a given state out of the superposition, reducing its contribution. The decoherence rate for a given state is computed as:

$$\tau_i^{-1} = \sum_{j \neq i} |c_j|^2 \tau_{ij}^{-1} \tag{2.49}$$

where τ_{ij}^{-1} is the pure dephasing rate derived from state energy fluctuations and NAC dynamics. DISH ensures that surface hops coincide with decoherence, providing a physical justification for hopping events without requiring ad hoc adjustments to hopping probabilities. DISH has demonstrated improved accuracy in modelling nonadiabatic processes, particularly in systems with strong electronic-nuclear coupling. However, its reliance on predefined decoherence rates may still limit its applicability in systems with highly dynamic environments. The 2023 revision of the DISH algorithm refines its treatment of decoherence, incorporating a more gradual approach similar to that of mSDM, as

detailed below. As in the original DISH method, decoherence occurs through stochastic projections, where the superposition is either projected onto the decohered (pointer) state or that state is projected out of the coherent superposition. Additionally, the 2023 revision addresses certain limitations or ambiguities present in the original DISH formulation, improving the consistency of its application.

The IDA method, proposed by Nelson and Tretiak, simplifies the treatment of decoherence by applying it at every attempted surface hop, regardless of whether the hop succeeds or fails. During each hop attempt, the IDA algorithm collapses the electronic state amplitudes to align with the current active state, ensuring that decoherence is consistently enforced throughout the hopping process.:

$$c_f = 1, \quad c_i = 0 \text{ for all } i \neq f \tag{2.50}$$

This approach ensures that the wavefunction remains consistent with the active state, effectively suppressing spurious coherence that may arise from failed hops. While computationally efficient, IDA is most suitable for systems where decoherence predominantly occurs at transitions between states, as it does not account for gradual coherence loss over time.

The mSDM (modified simplified decay of mixing) algorithm builds on the original decay of mixing method by Granucci and Persico,[87] incorporating improvements to better capture electronic dephasing. mSDM introduces time-dependent modifications to the electronic state amplitudes at every integration step:

$$C'_i = C_i \exp\left(-\frac{\Delta t}{\tau_{if}}\right), \quad C'_f = C_f \sqrt{1 - \sum_{i \neq f} |C'_i|^2} \tag{2.51}$$

Here, τ_{if} represents the dephasing timescale, which is dynamically computed using energy gap fluctuations:

$$\tau_{if}^{-1} = \sqrt{\frac{5\langle \delta E_{if}^2 \rangle}{12\hbar^2}} \tag{2.52}$$

This formulation accounts for state-dependent dephasing rates, allowing mSDM to adapt to varying degrees of coherence loss across different states. Unlike the original DISH and IDA methods, mSDM enables a gradual decay of coherence, which helps prevent abrupt state collapses and provides a more physically realistic description of decoherence, particularly in systems with weakly coupled states.

2.5.4.2 NA-MD workflow computational implementation

To simulate the coupled evolution of nuclei and electrons effectively, the adiabatic electronic states $\{\Psi_I(\mathbf{R}(t))\}$ are tracked over time as they evolve due to changes in nuclear geometry. The local diabatization (LD) method is often employed for robust integration of the TD-SE, enabling accurate computation of NACs and ensuring the electronic amplitudes remain consistent over time.[88,89] The LD method also facilitates efficient handling of large systems by allowing electronic and nuclear timesteps to be synchronized.

Surface hopping simulations are typically performed using multiple trajectories to capture the stochastic nature of electronic transitions. Nuclear trajectories are initialized from equilibrated molecular dynamics simulations, and electronic transitions are stochastically sampled. Averaging over several initial conditions and stochastic realizations of the TSH process improves the statistical reliability of the results. Such workflows often involve hundreds of realizations for each trajectory, with results averaged to determine relaxation time scales and associated uncertainties.

To finalize this chapter, it is important to note that the Libra software suite[90,91,92] was utilized for performing the NA-MD calculations discussed in this work. Libra provides a robust Python-based framework that supports various surface hopping and decoherence algorithms (under NBRA for atomistic cases). It allows systematic exploration of model systems and adapts efficiently to diverse material properties. The NA-MD workflow (depicted in Figure 2.2) involves

the initialization of nuclear trajectories from molecular dynamics simulations, followed by electronic state propagation and surface hopping. The coupled dynamics are averaged over multiple trajectories and initial conditions to obtain statistically significant results. More details of the workflow are provided in Section 5.2. In the case of TiO_2 NPs, this approach provides valuable insights into charge carrier relaxation, recombination, and energy transfer mechanisms critical to photocatalysis.

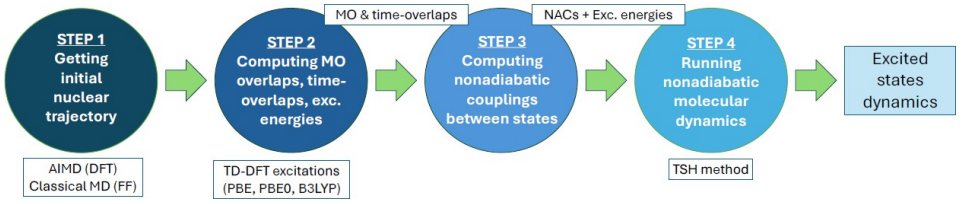

Figure 2.2: NA-MD workflow for computing the dynamics of excited states. Step 1 and Step 2 are performed within CP2K code; while Step 2, Step 3 and Step 4 rely on Libra software.

2.6 References

[1] Schrödinger, E. Quantisierung als eigenwertproblem. *Ann. Phys.* **1928**, *385*(13), 437-490.

[2] Hartree, D. R. The wave mechanics of an atom with a non-coulomb central field. Part II. Some results and discussion. *Math. Proc. Camb. Philos. Soc.* **1928**, *24*(1), 111-132

[3] Fock, V. A. Näherungsmethode zur Lösung des quantenmechanischen Mehrkörperproblems. *Z. Phys.* **1930**, *61*(1), 126-148.

[4] Hohenberg, P.; Kohn, W. Inhomogeneous Electron Gas. *Phys. Rev.* **1964**, *136*(3B), B864-B871.

[5] Dirac, P. A. M. The quantum theory of the electron. *Proc. R. Soc. Lond. Series A* **1928**, *117*(778), 610-624.

[6] Rahman, A. Correlations in the Motion of Atoms in Liquid Argon. *Phys. Rev.* **1964**, *136*(2A), A405-A411.

[7] Car, R.; Parrinello, M. Unified Approach for Molecular Dynamics and Density-Functional Theory. *Phys. Rev. Lett.* **1985**, 55(22), 2471-2474.

[8] Lennard-Jones, J. E. On the Determination of Molecular Fields. *Proc. R. Soc. Lond. Series A* **1924**, *106*(738), 463-477.

[9] Buckingham, R. A. The classical equation of state of gaseous helium, neon and argon. *Proc. R. Soc. Lond. Series A.* **1938**, *168*(933), 264-283.

[10] Matsui, M., & Akaogi, M. Molecular dynamics simulation of the structural and physical properties of the four polymorphs of TiO_2. *Mol. Simul.* **1991**, *6*(4-6), 239-244.

[11] Gale, J. D.; Rohl, A. L. The general utility lattice program (GULP). *Mol. Simul.* **2003**, *29*(5), 291-341.

[12] Lamiel-Garcia, O.; Cuko, A.; Calatayud, M.; Illas, F.; Bromley, S. T. Predicting size-dependent emergence of crystallinity in nanomaterials: titania nanoclusters versus nanocrystals. *Nanoscale* **2017**, *9*, 1049-1058.

[13] Cuko, A.; Escatllar, A. M.; Calatayud, M.; Bromley, S. T. Properties of hydrated TiO_2 and SiO_2 nanoclusters: dependence on size, temperature and water vapour pressure. *Nanoscale* **2018**, *10*, 21518-21532.

[14] Flikkema, E.; Bromley, S. T. A new interatomic potential for nanoscale silica. *Chem. Phys. Lett.* **2003**, *378*(5-6), 622-629.

[15] Kühne, T. D.; Iannuzzi, M.; Del Ben, M.; Rybkin, V. V.; Seewald, P.; et al. CP2K: An electronic structure and molecular dynamics software package-Quickstep: Efficient and accurate electronic structure calculations. *J. Chem. Phys.* **2020**, *152*, No. 194103.

[16] VandeVondele, J.; Hutter, J. Gaussian basis sets for accurate calculations on molecular systems in gas and condensed phases. *J. Chem. Phys.* **2007**, *127*, No. 114105.

[17] Hartwigsen, C.; Goedecker, S.; Hutter, J. Relativistic separable dual-space Gaussian pseudopotentials from H to Rn. *Phys. Rev. B* **1998**, *58*, 3641.

[18] Perdew, J. P.; Burke, K.; Ernzerhof, M. Generalized gradient approximation made simple. *Phys. Rev. Lett.* **1996**, *77*, 3865.

[19] Verlet, L. Computer “experiments" on classical fluids. I. Thermodynamical properties of Lennard-Jones molecules. *Phys. Rev.* **1967**, *159*(1), 98.

[20] Swope, W. C.; Andersen, H. C.; Berens, P. H.; Wilson, K. R. A computer simulation method for the calculation of equilibrium constants for the formation of physical clusters of molecules: Application to small water clusters. *J. Chem. Phys.* **1982**, *76*(1), 637-649.

[21] Evans, D. J.; Holian, B. L. The nose−hoover thermostat. *J. Chem. Phys.* **1985**, *83*, 4069−4074.

[22] Berendsen, H. J.; Postma, J. V.; Van Gunsteren, W. F.; DiNola, A. R. H. J.; Haak, J. R. Molecular dynamics with coupling to an external bath. *J. Chem. Phys.* **1984**, *81*(8), 3684-3690.

[23] Čížek, Jiří. On the Correlation Problem in Atomic and Molecular Systems. Calculation of Wavefunction Components in Ursell-Type Expansion Using Quantum-Field Theoretical Methods. *J. Chem. Phys*. **1966**, *45*(11),4256–4266.

[24] Kohn, W.; Sham, L. J. Self-consistent equations including exchange and correlation effects. *Phys. Rev.* **1965**, *140*(4A), A1133.

[25] Pauli, W. Pauli exclusion principle. *Naturwiss* **1924**, *12*, 741.

[26] Ceperley, D. M.; Alder, B. J. Ground state of the electron gas by a stochastic method. *Phys. Rev. Lett.* **1980**, *45*(7), 566.

[27] Jones, R. O.; Gunnarsson, O. The density functional formalism, its applications and prospects. *Rev. Mod. Phys.* **1989**, *61*(3), 689.

[28] Becke, A. D. Density-functional exchange-energy approximation with correct asymptotic behavior. *Phys. Rev. A* **1988**, *38*(6), 3098-3100.

[29] Perdew, J. P.; Chevary, J. A.; Vosko, S. H.; Jackson, K. A.; Pederson, M. R.; Singh, D. J.; Fiolhais, C. Atoms, molecules, solids, and surfaces: Applications of the generalized gradient approximation for exchange and correlation. *Phys. Rev. B* **1992**, *46*(11), 6671

[30] Labat, F.; Baranek, P.; Adamo, C. Structural and electronic properties of selected rutile and anatase TiO_2 surfaces: an ab initio investigation. *J. Chem. Theory Comput.* **2008**, *4*(2), 341-352.

[31] Mahmood, T.; Cao, C.; Ahmed, R.; Saeed, M. A.; Ahmed, M. Comparative study of structural and electronic properties of TiO_2 at GGA and GGA+ U level. *J. Optoelectron. Adv. M.* **2014**, *16*, 117-122.

[32] Lamiel-Garcia, O.; Ko, K. C.; Lee, J. Y.; Bromley, S. T.; Illas, F. When anatase nanoparticles become bulklike: properties of realistic TiO_2 nanoparticles in the 1–6 nm size range from all electron relativistic density functional theory based calculations. *J. Chem. Theory Comput.* **2017**, *13*(4), 1785-1793.

[33] Lee, C.; Yang, W.; Parr, R. G. Development of the Colle-Salvetti correlation-energy formula into a functional of the electron density. *Phys. Rev. B: Condens. Matter* **1988**, *37*, 785.

[34] Becke, A. D. Density-functional thermochemistry. I. The effect of the exchange-only gradient correctio. *J. Chem. Phys.* **1993**, *98*, 5648.

[35] Adamo, C.; Barone, V. Toward reliable density functional methods without adjustable parameters: The PBE0 model. *J. Chem. Phys.* **1999**, *110*(13), 6158-6170.

[36] Yanai, T.; Tew, D. P.; Handy, N. C. A new hybrid exchange–correlation functional using the Coulomb-attenuating method (CAM-B3LYP). *Chem. Phys. Lett.* **2004**, *393*(1-3), 51-57.

[37] Margenau, H. Van der Waals forces. *Rev. Mod. Phys.* **1939**, *11*(1), 1.

[38] Grimme, S.; Hansen, A.; Brandenburg, J. G.; Bannwarth, C. Dispersion-corrected mean-field electronic structure methods. *Chem. Rev.* **2016**, *116*(9), 5105-5154.

[39] Tkatchenko, A.; Scheffler, M. Accurate Molecular Van Der Waals Interactions from Ground-State Electron Density and Free-Atom Reference Data. *Phys. Rev. Lett.* **2009**, *102*(7), 073005.

[40] Grimme, S.; Antony, J.; Ehrlich, S.; Krieg, H. A consistent and accurate ab initio parametrization of density functional dispersion correction (DFT-D) for the 94 elements H-Pu. *J. Chem. Phys.* **2010**, *132*(15), 154104.

[41] Blum, V.; Gehre, R.; Hanke, F.; Havu, P.; Havu, V.; Ren, X.; Reuter, K.; Scheffler, M. Ab initio molecular simulations with numeric atom-centered orbitals. *Comput. Phys. Commun.* **2009**, *180*, 2175–2196.

[42] Sanjines, R.; Tang, H.; Berger, H.; Gozzo, F.; Margaritondo, G.; Lévy, F. Electronic structure of anatase TiO_2 oxide. *J. Appl. Phys.* **1994** , *75*(6), 2945-2951.

[43] Strutt, M. J. Eigenschwingungen einer Saite mit sinusförmiger Massenverteilung. *Ann. Phys.* **1928**, *390*(2), 129-136.

[44] Bloch, F. Quantum mechanics of electrons in crystal lattices. *Z. Phys.* **1928**, *52*, 555-600.

[45] Baldereschi, A. Mean-value point in the Brillouin zone. *Phys. Rev. B* **1973**, *7*(12), 5212.

[46] Chadi, D. J.; Cohen, M. L. Special points in the Brillouin zone. *Phys. Rev. B* **1973**, *8*(12), 5747.

[47] Monkhorst, H. J.; Pack, J. D. Special points for Brillouin-zone integrations. *Phys. Rev. B* **1976**, *13*(12), 5188.

[48] Moellmann, J.; Ehrlich, S.; Tonner, R.; Grimme, S. A DFT-D study of structural and energetic properties of TiO_2 modifications. *J. Phys. Condens. Matter* **2012**, *24*(42), 424206.

[49] Reuter, K.; Scheffler, M. First-Principles Atomistic Thermodynamics for Oxidation Catalysis: Surface Phase Diagrams and Catalytically Interesting Regions. *Phys. Rev. Lett.* **2003**, *90*, 046103.

[50] Reuter, K.; Scheffler, M. Composition, structure, and stability of as a function of RuO_2 (110) oxygen pressure. *Phys. Rev. B* **2001**, *65*, 035406.

[51] Reuter, K.; Scheffler, M. Composition and structure of the RuO_2 (110) surface in an O_2 and CO environment: Implications for the catalytic formation of CO_2. *Phys. Rev. B* **2003**, *68*(4), 045407.

[52] Reuter, K.; Stampf, C.; Scheffler, M. Ab initio atomistic thermodynamics and statistical mechanics of surface properties and functions. *Handbook of materials modeling: methods* **2005**, 149-194.

[53] Stocks, G. M.; Nicholson, D. M. C.; Shelton, W. A.; Györffy, B. L.; Pinski, F. J.; Johnson, D. D.; Staunton, J. B.; Ginatempo, B.; Turchi, P. E. A.; Sluiter, M. First principles theory of disordered alloys and alloy phase stability. *Statics and dynamics of alloy phase transformations* **1994**, 305-359.

[54] Sanchez, J. M.; Ducastelle, F.; Gratias, D. Generalized cluster description of multicomponent systems. *Physica A: Statistical Mechanics and its Applications* **1984**, *128*(1-2), 334-350.

[55] Osterloh, F. E. Inorganic nanostructures for photoelectrochemical and photocatalytic water splitting. *Chem. Soc. Rev.* **2013**, *42*(6), 2294-2320.

[56] Tan, H. L.; Abdi, F. F.; Ng, Y. H. Heterogeneous photocatalysts: an overview of classic and modern approaches for optical, electronic. *Chem. Soc. Rev.* **2019***, 48*(5)*,* 1255-1271.

[57] Djurišić, A. B.; He, Y.; Ng, A. Visible-light photocatalysts: Prospects and challenges. *APL Mater.* **2020**, *8* (3), No. 030903.

[58] Nijamudheen, A.; Akimov, A. V. Quantum Dynamics Effects in Photocatalysis. In *Visible-Light-Active Photocatalysis: Nanostructured Catalyst Design, Mechanisms, and Applications*; Ghosh, S., Ed.; Wiley-VCH Verlag Gmbh & Co. KGaA: Weinheim, **2018**; 527−566.

[59] Akimov, A. V.; Neukirch, A. J.; Prezhdo, O. V. Theoretical insights into photoinduced charge transfer and catalysis at oxide interfaces. *Chem. Rev.* **2013**, *113*(6), 4496-4565.

[60] Prezhdo, O. V. Photoinduced dynamics in semiconductor quantum dots: Insights from time-domain ab initio studies. *Acc. Chem. Res.* **2009**, *42*(12), 2005-2016.

[61] Nam, Y.; Li, L.; Lee, J. Y.; Prezhdo, O. V. Size and shape effects on charge recombination dynamics of TiO_2 nanoclusters. *J. Phys. Chem. C* **2018**, *122*, 5201−5208.

[62] Nam, Y.; Li, L.; Lee, J. Y.; Prezhdo, O. V. Strong influence of oxygen vacancy location on charge carrier losses in reduced TiO_2 nanoparticles. *J. Phys. Chem. Lett.* **2019**, *10*, 2676−2683.

[63] Smith, B.; Akimov, A. V. Hot Electron Cooling in Silicon Nanoclusters via Landau-Zener Nonadiabatic Molecular Dynamics: Size Dependence and Role of Surface Termination. *J. Phys. Chem. Lett.* **2020**, *11*, 1456−1465.

[64] Smith, B.; Shakiba, M.; Akimov, A. V. Nonadiabatic dynamics in Si and CdSe nanoclusters: many-body vs single-particle treatment of excited states. *J. Chem. Theory Comput.* **2021**, *17*, 678−693.

[65] Mead, C. A.;Truhlar, D. G. Conditions for the definition of a strictly diabatic electronic basis for molecular systems. *J. Chem. Phys.* **1982**, *77*(12), 6090-6098.

[66] Tully, J. C. Molecular dynamics with electronic transitions. *J. Chem. Phys.* **1990**, *93*(2), 1061-1071.

[67] Baer, M. *Beyond Born-Oppenheimer: electronic nonadiabatic coupling terms and conical intersections*. John Wiley & Sons. **2006**

[68] Craig, C. F.; Duncan, W. R.; Prezhdo, O. V. Trajectory Surface Hopping in the Time-Dependent Kohn-Sham Approach for Electron-Nuclear Dynamics. *Phys. Rev. Lett.* **2005**, 95, 163001.

[69] Duncan,W. R.; Craig, C. F.; Prezhdo, O. V. Time-Domain Ab Initio Study of Charge Relaxation and Recombination in Dye-Sensitized TiO_2. *J. Am. Chem. Soc.* **2007**, *129*, 8528−8543.

[70] Prezhdo, O. V.; Duncan, W. R.; Prezhdo, V. V. Photoinduced Electron Dynamics at the Chromophore−Semiconductor Interface: A Time-Domain Ab Initio Perspective. *Prog. Surf. Sci.* **2009**, *84*, 30−68.

[71] Smith, B.; Shakiba, M.; Akimov, A. V. Nonadiabatic dynamics in Si and CdSe nanoclusters: many-body vs single-particle treatment of excited states. *J. Chem. Theory Comput.* **2021**, *17*, 678−693.

[72] Smith, B.; Shakiba, M.; Akimov, A. V. Crystal symmetry and static electron correlation greatly accelerate nonradiative dynamics in lead halide perovskites. *J. Phys. Chem. Lett.* **2021**, *12*, 2444−2453.

[73] Recio-Poo, M.; Shakiba, M.; Illas, F.; Bromley, S. T.: Akimov, A. V.; Morales-García, A. Hydration Accelerates Radiative and Nonradiative Recombination in Small TiO_2 Nanoclusters. *J. Phys. Chem. C* **2025**, 129, 3, 1806–1823.

[74] Runge, E.; Gross, E. K. U. Density-Functional Theory for Time-Dependent Systems. *Phys. Rev. Lett.* **1984**, *52*, 997–1000.

[75] Casida, M. E. Time-dependent density functional response theory for molecules. In *Recent Advances In Density Functional Methods: (Part I)* **1995**, 155-192.

[76] Hirata, S.; Head-Gordon, M. Time-Dependent Density Functional Theory within the Tamm–Dancoff Approximation. *Chem. Phys. Lett.* **1999**, *314*, 291–299.

[77] Jiang, X.; Zheng, Q.; Lan, Z.; Saidi, W. A.; Ren, X.; Zhao, J. Real-time GW-BSE investigations on spin-valley exciton dynamics in monolayer transition metal dichalcogenide. *Sci. Adv.* **2021**, *7*, 33759.

[78] Dreuw, A.; Head-Gordon, M. Single-reference ab initio methods for the calculation of excited states of large molecules. *Chem. Rev,* **2005**, *105*(11), 4009-4037.

[79] Grimme, S.; Neese, F. Double-hybrid density functional theory for excited electronic states of molecules. *J. Chem. Phys.* **2007**, *127*(15), 154116.

[80] Zhu, Y.; Long, R. Density Functional Theory Half-Electron Self-Energy Correction for Fast and Accurate Nonadiabatic Molecular Dynamics. *J. Phys. Chem. Lett.* **2021**, *12*, 10886−10892.

[81] Liu, W.; Settels, V.; Harbach, P. H.; Dreuw, A.; Fink, R. F.; Engels, B. Assessment of TD-DFT-and TD-HF-based approaches for the prediction of exciton coupling parameters, potential energy curves, and electronic characters of electronically excited aggregates. *J. Comput. Chem.* **2011**, *32*, 1971−1981.

[82] Barbatti, M. Nonadiabatic dynamics with trajectory surface hopping method. *Wiley Interdiscip. Rev. Comput. Mol. Sci.* **2011**, *1*(4), 620-633.

[83] Wang, L.; Akimov, A.; Prezhdo, O. V. Recent progress in surface hopping: 2011–2015. *J. Phys. Chem. Lett.* **2016**, *7*(11), 2100-2112.

[84] Jaeger, H. M.; Fischer, S.; Prezhdo, O. V. Decoherence-Induced Surface Hopping. *J. Chem. Phys.* **2012**, *137*, 22A545.

[85] Smith, B.; Akimov, A. V. A comparative analysis of surface hopping acceptance and decoherence algorithms within the neglect of back-reaction approximation. *J. Chem. Phys.* **2019**, *151*,124107.

[86] Nelson, T.; Fernandez-Alberti, S.; Roitberg, A. E.; Tretiak, S. Nonadiabatic excited-state molecular dynamics: Treatment of electronic decoherence. *J. Chem. Phys.* **2016**, *138*, 224111.

[87] Granucci, G.; Persico, M. Critical appraisal of the fewest switches algorithm for surface hopping. *J. Chem. Phys.* **2007**, *126*(13), 134114.

[88] Granucci, G.; Persico, M.; Toniolo, A. Direct Semiclassical Simulation of Photochemical Processes with Semiempirical Wave Functions. *J. Chem. Phys.* **2001**, *114*, 10608−10615.

[89] Shakiba, M.; Akimov, A. V. Generalization of the Local Diabatization Approach for Propagating Electronic Degrees of Freedom in Nonadiabatic Dynamics. *Theor. Chem. Acc.* **2023**, *142*, 68.

[90] Akimov, A. V. Libra: An Open-Source "Methodology Discovery" Library for Quantum and Classical Dynamics Simulations. *J. Comput. Chem.* **2016**, *37*, 1626−1649.

[91] Shakiba, M.; Smith, B.; Li, W.; Dutra, M.; Jain, A.; Sun, X.; Garashchuk, S.; Akimov, A. Libra: A Modular Software Library for Quantum Nonadiabatic Dynamics. *Softw. Impacts* **2022**, *14*, 100445.

[92] Akimov, A. V. Libra: An Open-Source "Methodology Discovery" Library for Quantum and Classical Dynamics Simulations. *J. Comput. Chem.* **2016**, *37*, 1626−1649.

3 SIZE AND HYDRATION EFFECT ON GROUND STATE PROPERTIES

Chapters 3–5 present the results of this thesis, which have been divided into these three blocks based on their distinct research topics, allowing for a clearer and more structured discussion.

This first chapter focuses on the effects of size and hydration on the ground-state (GS) properties of TiO_2. It is the most extensive chapter, as it is based on three publications, related to the impact of hydroxylation and size effects on the GS properties of titania systems with varying sizes and morphologies. In this context, we have examined properties such as DFT energies, atomic local environments, and energy gaps—factors that may directly influence the photocatalytic performance of these systems.

In this and the following results chapters, we include the published papers at the end, after comprehensive summaries of the key findings. Additionally, each results' chapter begins with an introductory section that provides context to the discussed research field.

3.1 Introduction

3.1.1 Size-Dependent Crystallinity and Structural Stability

As detailed in the Introduction (first) chapter, TiO_2 nanoparticles exhibit fascinating size-dependent transformations in crystallinity, structural stability, and electronic properties**,** which define their behaviour in photocatalysis, energy storage, and environmental applications.[1-4] Recent theoretical and computational studies have provided detailed insights into the transition from amorphous nanoclusters to bulk-like anatase nanoparticles**,** highlighting a critical size range of 2–3 nm for crystallinity emergence and a bulk-like transition occurring beyond ~20 nm.[5,6] These findings, based on bottom-up global optimization, top-down Wulff construction, thermal annealing simulations, and relativistic all-electron DFT**,** converge toward a unified picture of how structure and properties evolve as a function of size in TiO_2 nanosystems.

At the smallest scales, nanoclusters with diameters below ~2 nm remain largely amorphous, lacking any long-range crystalline order.[7] Global optimization studies of small TiO_2 clusters ($n \leq 38$) consistently show that the most stable

configurations are highly distorted, quasi-spherical structures**,** deviating significantly from the bulk-like anatase lattice. Even for $(TiO_2)_n$ (n = 28, 35, and 38), where direct comparisons were made, non-crystalline structures remained energetically more favourable than their anatase-like counterparts by nearly 7.9–9.9 eV per TiO_2 unit.[5] This thermodynamic preference for amorphous-like arrangements stems from the high surface-to-volume ratio, surface stress, and the energetic penalty of maintaining bulk-like coordination at small sizes**.** Theoretical work extending up to $(TiO_2)_{84}$ (composed by 252 atoms) further demonstrated that even when bulk-cut Wulff-like anatase nanocrystals were considered, they remained metastable compared to fully relaxed amorphous clusters below 2 nm.[5] These results align well with experimental observations, where small TiO_2 nanoparticles synthesized via sol-gel or hydrothermal routes frequently exhibit amorphous or poorly ordered structures unless post-synthesis annealing is performed.[8]

The transition from amorphous to crystalline structures occurs between 2 and 3 nm, marking the critical size at which anatase-like order becomes thermodynamically stable. Initially, theoretical predictions indicate that this transition began around $n \approx 125$ (375 atoms), corresponding to a diameter of ~2.5 nm, where anatase crystallinity starts to dominate.[5] Further computational research (including DFT calculations and MD simulations) led to Figure 3.1, which confirms the 2-3 nm range for the appearance of crystallinity, but points towards a higher n = 280 titania units' number for the crystalline-amorphous crossover.[9] Such figure presents the size-dependent energetic stabilities of faceted, spherical, annealed spherical, and globally optimized TiO_2 nanoparticles NPs. The relative stability of all titania NPs is expressed per TiO_2 unit, normalized to the bulk anatase phase. Using the spherical cluster approximation (SCA),[10] the energetic stability of a $(TiO_2)_n$ NP, E_n, relative to bulk anatase, E_{bulk}, can be approximated by the scaling law:

$$E_n = E_{bulk} + a_1 n^{-\alpha} \tag{3.1}$$

where $a_1$is a fitting parameter related to NP morphology, and α is taken as 1/3, reflecting the surface-to-volume ratio. Both E_n and E_{bulk} are expressed per TiO_2 unit. Equation 3.1 is derived based on the geometric shape of NPs; however, realistic NPs are more complex, consisting of interacting aggregates of atoms/ions. As a result, additional contributions to E_n (e.g., surface stresses) may become significant and can be incorporated through higher-order terms.

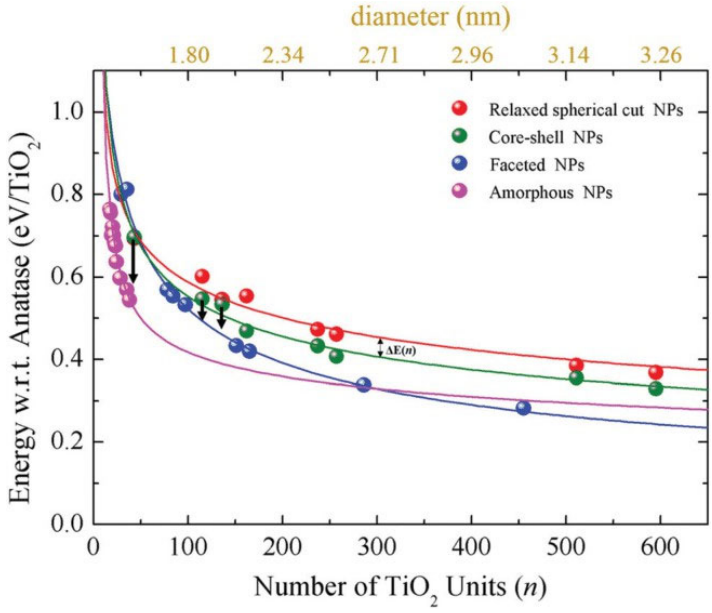

Figure 3.1: Evolution of the energy per TiO_2 unit relative to the anatase bulk phase (set to zero) of: faceted (blue), spherical cut (red), core–shell spherical (green), and amorphous (pink) TiO_2 NPs as a function of the number of TiO_2 units (n). An approximate diameter is included on the upper x-axis. Figure adapted from reference 9.

At the crystalline-amorphous crossover, particles undergo structural rearrangement, forming a crystalline core often surrounded by an amorphous shell.[11] This core-shell morphology, also observed in annealed TiO_2 nanoparticles,[9] results from the competition between bulk-driven crystallization and surface-induced disorder. Notably, thermal annealing simulations confirm that at this size range, the core adopts an anatase-like structure, whereas the outermost layers remain amorphous due to their under-coordinated atomic environment. This

anatase-core, amorphous-shell arrangement bears resemblance to black TiO_2 nanoparticles, which have been shown to exhibit enhanced optical absorption and catalytic activity.[12,13]

Figure 3.2 (also from reference 9) shows a tentative structure versus stability diagram that visually represents the relationship between NP size, morphology, and relative energetic stability. The authors constructed it using the fitted energetic tendencies from the various NP families considered in their study. The uppermost black curve represents the metastability of relaxed spherical cut NPs, which are energetically less favourable than other morphologies. As the size of the NP increases, there is a transition from amorphous structures (for very small NPs) to annealed core-shell NPs (for intermediate sizes) and finally to faceted crystalline NPs (for larger sizes). This transition is based on computed relative energies of the optimized structures and the changes observed upon thermal annealing. The shading in the figure represents the effects of annealing, which leads to structural rearrangements that stabilize the NPs. For small NPs (diameter < 2 nm), annealing results in a transition from a crystalline core-shell structure to a fully amorphized NP, suggesting that small spherical NPs cannot maintain a stable crystalline core. For intermediate-sized NPs (diameter between 2 and 2.7 nm), the most stable structure is a core-shell morphology, where a crystalline anatase core is surrounded by an amorphous shell. Beyond a diameter of 2.7 nm, the stability of faceted NPs surpasses that of the spherical core-shell NPs, making them the most energetically favourable structures.

As the size increases beyond 3 nm, TiO_2 nanoparticles progressively adopt well-defined faceted anatase structures**,** closely resembling bulk-like Wulff morphologies. Geometrically, nanoparticles in the 3–6 nm range exhibit minimal atomic relaxations, and their structural features remain largely intact after full DFT relaxation. The (101) and (001) surfaces dominate these structures**,** with octahedral and truncated octahedral morphologies emerging as energetically favourable configurations.[14] While bulk-cut anatase nanocrystals remain metastable below 3 nm**,** particles larger than 4–6 nm show increasing stability**,** signalling the transition toward a bulk-like structural regime. This trend is

consistent with experimental and theoretical studies on facet-engineered TiO_2 nanoparticles, where the relative stability of (101) versus (001) facets can be modified by synthesis conditions or surface passivation.[15,16]

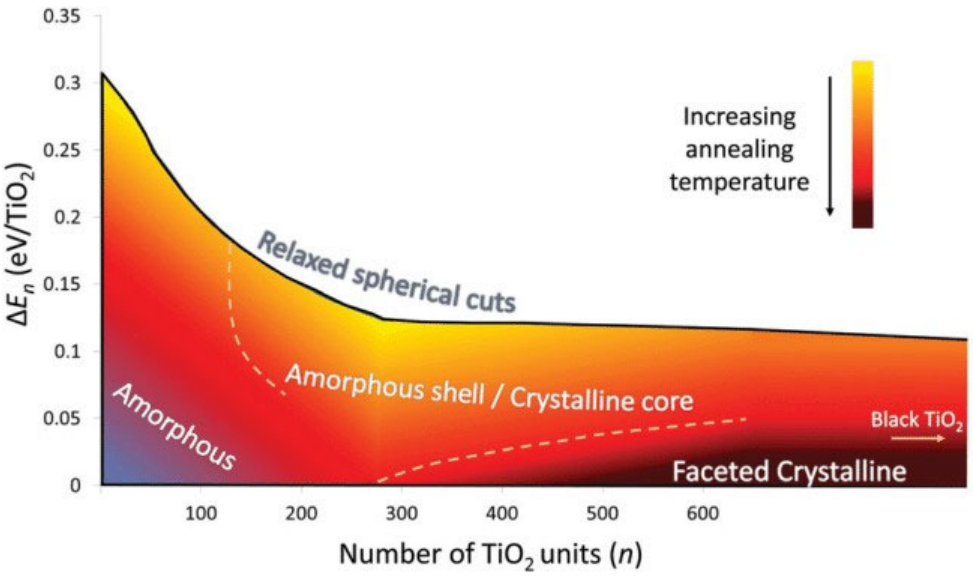

Figure 3.2: Tentative structure versus stability diagram for TiO_2 NPs with respect to the relaxed spherical cut NPs (upper black line) based on the fitted tendencies and the NP structures corresponding to the data points in Figure 3.1. Figure adapted from reference 9.

3.1.2 Electronic Properties and the Bulk-Like Transition

The transition to bulk-like electronic properties follows a more gradual path**,** strongly influenced by quantum confinement and surface effects. At small sizes (< 2 nm), quantum confinement significantly widens the band gap**,** leading to values well above the 3.2 eV bulk anatase band gap.[17-19] Theoretical studies of electronic structure predict that as size increases, the optical band gap (O_{gap}) decreases slowly**,** while the electronic energy gap (E_{gap}) drops sharply, asymptotically converging toward bulk values (see Figure 3.3).[6] This asymmetry arises from the fact that small nanoparticles exhibit strong exciton binding energies, which persist well beyond the crystallinity transition. Indeed, computational modelling suggests that for particles smaller than ~6 nm, the exciton

binding energy remains substantial, whereas it gradually diminishes as size increases, indicating a shift toward bulk-like charge carrier dynamics.[20]

Beyond ~6 nm, TiO_2 nanoparticles exhibit electronic structures nearly indistinguishable from bulk anatase, except for minor surface effects. The largest particles investigated (~6 nm, containing 1365 atoms) displayed nearly bulk-like energy gap values, confirming that quantum confinement effects are largely mitigated at this scale.[6] Extrapolating from these trends, researchers have determined that at ~20 nm, TiO_2 nanoparticles effectively become bulk-like in both electronic structure and stability. This threshold aligns with experimental findings, where photocatalytic activity, charge carrier recombination rates, and optical absorption spectra of 20 nm nanoparticles are nearly identical to those of bulk anatase.[21,22]

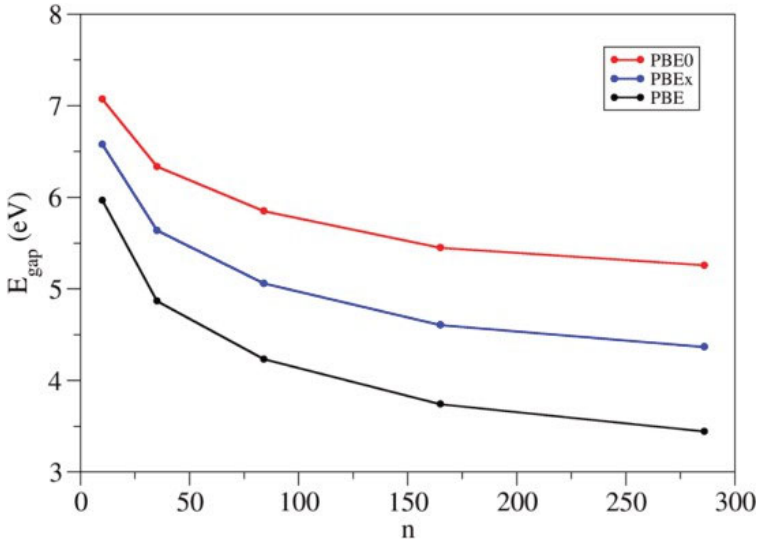

Figure 3.3: Electronic gap calculated values for the octahedral $(TiO_2)_n$ NPs as a function of *n*. Black, blue, and red correspond to PBE, PBEx, and PBE0 exchange-correlation functionals, respectively, at optimized PBE geometries. Figure adapted from reference 6.

Taken together, these findings provide a comprehensive understanding of the size-dependent properties of TiO_2 nanosystems. Below 2 nm, amorphous structures dominate, exhibiting high reactivity but poor crystallinity. Between 2 and

3 nm, the anatase-core, amorphous-shell morphology emerges**,** marking the onset of crystallinity while retaining surface disorder. In the 3–6 nm range, crystalline faceted nanoparticles become stable, and by 6 nm, electronic properties start approaching bulk values. Finally, at ~20 nm, TiO_2 nanoparticles become effectively bulk-like, with their structural, thermodynamic, and electronic properties fully converging to those of macroscopic anatase**.** These insights not only explain fundamental aspects of titania nanomaterials but also serve as guidelines for designing size-engineered TiO_2 nanoparticles with tailored properties for photocatalysis, energy applications, and surface chemistry**.**

3.1.3 Hydroxylation of TiO_2 NPs

The interaction of TiO_2 surfaces with water is fundamental to their physicochemical behaviour, particularly in applications involving photocatalysis and environmental processes.[23-28] In realistic conditions, TiO_2 nanoparticles are rarely found in an anhydrous state, as water molecules readily adsorb and react with their surfaces, leading to hydroxylation. This process, in turn, modifies the surface electronic structure, alters adsorption properties, and influences catalytic activity. The hydroxylation mechanism on TiO_2 surfaces occurs predominantly via dissociative adsorption, where water molecules split into hydroxyl groups (OH^-) and protons (H^+).[29-32] These species then bind to different sites on the surface, affecting the stability and reactivity of the material.

The distribution of hydroxyl groups across a TiO_2 surface follows a site-dependent hierarchy, with dissociation preferentially occurring at the most reactive regions. As observed in both experimental and theoretical research, highly undercoordinated Ti atoms at apical vertices and corners serve as the primary anchoring points for hydroxyl groups.[33,34] These locations provide strong adsorption sites where water dissociation is highly exothermic, leading to stable terminal hydroxyl (Ti-OH) species. Following initial hydroxylation, water molecules progressively dissociate at equatorial edge sites, which exhibit slightly lower reactivity but still stabilize hydroxyl groups through hydrogen bonding. The facet surfaces, particularly the dominant (101) plane in anatase, are the least reactive and become hydroxylated only under high water coverage conditions

The hydroxylation mechanism proceeds through a heterolytic dissociation pathway, in which a water molecule breaks into an OH fragment that binds to a fivefold-coordinated Ti (Ti^{5+}) centre, while the accompanying proton migrates to a nearby lattice oxygen, forming a bridging hydroxyl group (-OH). This pathway ensures charge neutrality at the surface and is energetically favourable at reactive sites such as undercoordinated Ti centres. Experimental infrared (IR) spectroscopy evidence studies (Figure 3.4) support this dissociative mechanism, with distinct vibrational features corresponding to both isolated and hydrogen-bonded hydroxyls.[33] In particular, terminal hydroxyl groups give rise to sharp IR bands in the 3700–3600 cm^{-1} range, characteristic of well-defined Ti-OH stretching modes. At higher hydroxyl coverages, the interaction between adjacent OH groups results in a broader spectral response extending down to 3100 cm^{-1}, indicative of extensive hydrogen bonding networks.

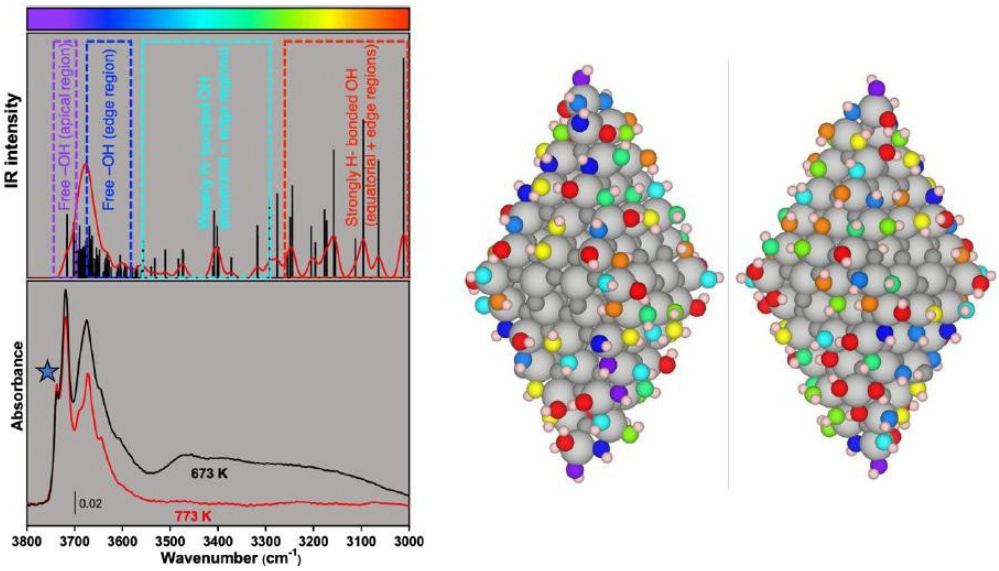

Figure 3.4: Calculated IR frequencies (top left panel) obtained from the $(TiO_2)_{84}(H_2O)_{55}$ NP model (right) compared to the FTIR spectra of the TiO_2 nano-anatase NPs (bottom left panel) after outgassing at 773 K (red curve) or 673 K (black curve).Vibration modes are distinguished by a colour scale, where the highest frequencies are found towards the purple end of the scale and the

lowest frequencies are identified by colours towards the red end of the scale. The same colour scale is used to correlate the OH groups in the $(TiO_2)_{84}(H_2O)_{55}$ NP model with their respective frequencies. Note that the Ti and O atoms that form the core of the NP are depicted with light and dark grey colours, respectively. The blue star on the FTIR spectra of the TiO_2 nano-anatase NPs indicates the frequency of a single tetrahedrally coordinated OH. Figure adapted from reference 33.

Surface hydroxylation has profound implications for TiO_2's electronic and catalytic properties. Hydroxyl groups modify the band edge positions, influencing charge transfer processes that are critical in photocatalysis. The presence of OH species also introduces Brønsted acid and Lewis base functionalities, enabling selective adsorption and activation of reactants in catalytic reactions.[35] Furthermore, hydroxylated surfaces impact charge carrier dynamics by either trapping electrons and holes or facilitating charge separation, depending on the distribution and nature of the hydroxyl species.[36] These effects become particularly evident when comparing anhydrous and hydrated TiO_2 surfaces under vacuum and ambient conditions. The evolution of hydroxyl coverage and its associated energetic stabilization across different adsorption sites is quantitatively depicted in Figure 3.5,[33] demonstrating the progressive saturation of reactive surface regions.

The degree of hydroxylation is not a fixed property but varies depending on nanoparticle size, humidity, and temperature, making environmental factors a crucial determinant of surface chemistry.[37] Hydroxyl groups not only influence fundamental photocatalytic properties but also dictate how these materials interact with external systems. In photocatalysis, hydroxylated TiO_2 plays a central role in oxidation reactions, as surface-bound OH groups can be converted into reactive hydroxyl radicals (•OH) under excitonic excitation.[24,38,39] These radicals drive many photocatalytic oxidation processes, such as organic pollutant degradation[40] and water purification.[41] It has been experimentally observed that anatase TiO_2 generates more mobile OH species than rutile, a factor that has been proposed as a key reason for anatase's superior activity in photooxidative reactions.[42] Beyond catalysis, hydroxylation also influences how TiO_2

interacts with biological systems, where photocatalytically generated hydroxyl radicals may contribute to biotoxicity effects in environmental and medical applications.[43] The reactivity of surface hydroxyl groups could thus play a dual role, acting as a beneficial catalyst in controlled environments while posing potential risks in unintended biological interactions.

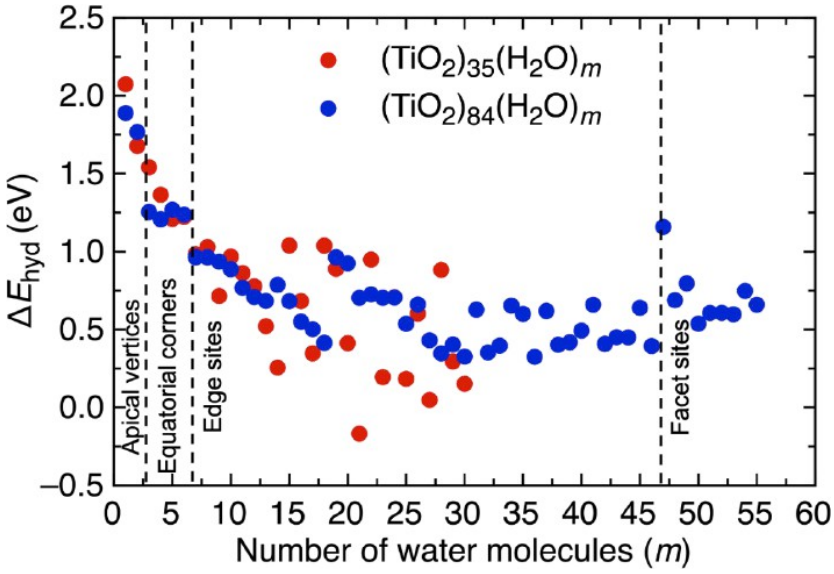

Figure 3.5: Evolution of ΔE_{hyd} (incremental hydration energy) with the number of water molecules (m) for increasingly hydrated $(TiO_2)_{35}(H_2O)_m$ and $(TiO_2)_{84}(H_2O)_m$ NPs. Coverages of different types of NP surface regions for different ranges of m are separated by vertical dashed lines. Figure adapted from reference 33. ΔE_{hyd} quantifies the energy change associated with the addition of each successive water molecule. Higher ΔE_{hyd} values reflect stronger, more favorable (exothermic) water adsorption at highly reactive sites such as apical vertices. As hydration progresses and less reactive sites are occupied, ΔE_{hyd} decreases, indicating weaker binding and a reduced thermodynamic driving force for further hydroxylation.

3.1.3.1 Impact of Hydration on the Crystallinity Transition and Morphology

As discussed earlier (3.1.1 section), TiO_2 nanoclusters smaller than ~2 nm remain predominantly amorphous, while a crystalline anatase-like core emerges around 2–3 nm. However, when hydroxylation is introduced, this transition becomes less straightforward. To investigate these effects, the Monte Carlo Basin Hopping (MCBH) algorithm[44] has been employed to explore the potential energy surface of hydrated $(TiO_2)_n(H_2O)_m$ clusters (with n = 4, 8, 12, and 16, and m values ranging respectively from 1–5, 1–5, 1–6, and 1–8).[37] Such small titania clusters tend to stabilize in hydroxylated configurations, where adsorbed water molecules passivate undercoordinated titanium and oxygen sites, reducing their tendency to reorganize into a bulk-like crystalline order.

The stabilization effect of hydroxylation is particularly significant for nanoparticles that would otherwise experience rapid structural distortions due to surface stress. As described by the general hydration reaction:

$$(TiO_2)_n + (H_2O)_m \rightleftharpoons (TiO_2)_n(H_2O)_m \tag{3.2}$$

which describes the process where water molecules bind to the surface of the TiO_2 nanoparticle. To quantify the stability imparted by hydration, we can calculate the hydration energy change ($E_{\mathrm{hyd}}(m)$), which represents the difference in energy between the hydrated nanoparticle and the isolated components (the anhydrous nanoparticle and individual water molecules). The equation for this energy change is given by:

$$E_{\mathrm{hyd}}(m) = \mathrm{E}_{(TiO_2)_m(H_2O)_n} - \mathrm{E}_{(TiO_2)_m} - nE_{H_2O} \tag{3.3}$$

where $\mathrm{E}_{(TiO_2)_n(H_2O)_m}$ and $\mathrm{E}_{(TiO_2)_n}$ are the total energies of hydrated and anhydrous nanoclusters, respectively, and E_{H_2O} is the energy of an isolated water molecule. A negative $E_{\mathrm{hyd}}(m)$ is associated to the thermodynamic favourability of water incorporation. For a more precise evaluation of the thermodynamics of hydration, free energy considerations are essential. These are discussed

in detail in Chapter 4 and will not be covered here. However, we still can introduce Figure 3.6, which presents the free energies of hydration for small nanoclusters,[37] demonstrating that hydration is highly exothermic. This confirms the strong thermodynamic preference of small nanoclusters for hydroxylated amorphous configurations. The presence of hydroxyl groups reduces internal stress, mitigating the abrupt structural reorganization that would otherwise occur in anhydrous conditions. Consequently, hydration stabilizes open, hydrated configurations rather than allowing small clusters to collapse into bulk-like Wulff morphologies. These findings suggest that the 2–3 nm crystallinity transition observed in anhydrous TiO_2 may shift toward larger sizes (~3–4 nm) when hydration is considered. This insight is critical for understanding the thermodynamics of hydrated nanoclusters and optimizing their functional properties in aqueous environments.

Hydration stabilizes five- and six-coordinated Ti centres, which are uncommon in anhydrous nanoclusters but prevalent in hydrated ones. This higher coordination environment reduces reactivity but enhances long-term stability, particularly in photocatalytic and biological applications where TiO_2 interacts with water at ambient conditions. Furthermore, highly hydrated TiO_2 nanoparticles tend to exhibit cage-like motifs, where water molecules are structurally integrated rather than simply adsorbed on the surface. This behaviour contrasts with anhydrous nanoparticles, where crystal faceting is the dominant stabilization mechanism above ~3 nm.

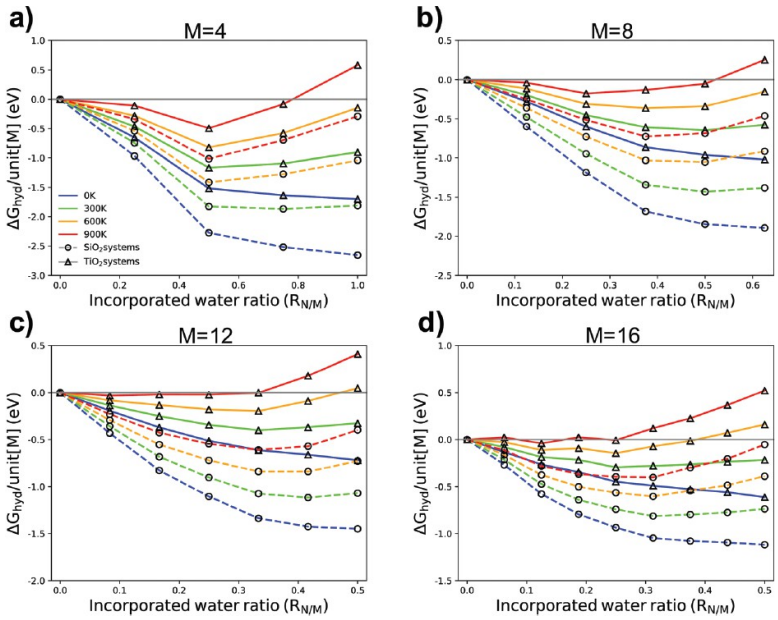

Figure 3.6: Hydration free energies of silica (dashed lines) and titania (solid lines) nanoclusters for sizes: (a) m = 4, (b) m = 8, (c) m = 12, (d) m = 16. Hydration free energies are reported at different temperatures while keeping the water partial pressure at 1 Pa which is sufficiently low to consider water as an ideal gas even at ambient conditions. Note: The figure includes SiO_2 data for comparison, as presented in Ref. 37. While SiO_2 is not discussed further in this thesis, it is noted that silica exhibits systematically more exothermic hydration and retains higher hydrophilicity than TiO_2 under comparable conditions. Figure adapted from reference 37.

3.1.3.2 Electronic and Optical Effects of Hydroxylation

The optical and electronic properties of titania nanoparticles evolve with size due to quantum confinement, but hydration introduces additional complexity. Previous discussions on energy gap trends showed that small TiO_2 nanoparticles have wider gaps (~4–5 eV) due to confinement effects, which narrow as size increases to bulk-like values (~3.2 eV at 6+ nm). For small TiO_2 nanoclusters ranging from 4 to 16 units, hydration influences the band gap in a non-monotonic manner (Figure 3.7).[37]

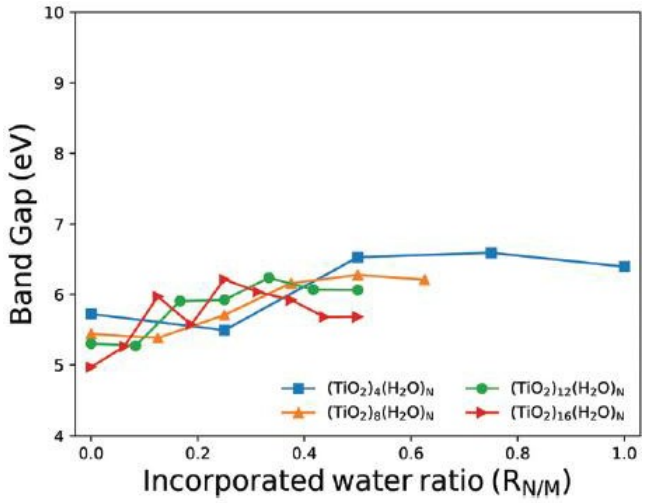

Figure 3.7: Electronic energy gaps of hydrated titania nanocluster systems with respect to the incorporated water ratio, R_n/m. Figure adapted from reference 37.

For instance, in the 12-unit titania system, the energy gap varies from a minimum of 5.3 eV at 8% hydration to a maximum of 6.2 eV at 33% hydration, after which it stabilizes or slightly declines. This trend suggests that hydration initially stabilizes the electronic structure, increasing the band gap, but excessive hydroxylation can lead to saturation effects that counteract this increase. Similar patterns are observed across other small TiO_2 clusters, though the exact gap evolution depends on their specific structural and coordination characteristics.

This behaviour arises from the structural flexibility of small titania nanoclusters, which exhibit diverse cation coordination environments (4-, 5-, and 6-coordinated Ti centres). Hydration helps heal terminal defects and stabilize the electronic state, generally leading to an increase in the band gap. However, excessive hydroxylation can lead to surface saturation, where an overabundance of hydroxyl groups diminishes mid-gap states, thereby affecting photocatalytic efficiency.

Interestingly, although hydration plays a role in modulating the electronic structure, titania nanoclusters maintain a relatively robust electronic state.

Indeed, adsorption is known to help stabilise a large bandgap.[45] In applications such as photocatalysis and photoelectrochemical water splitting, optimizing hydration levels for these small clusters is crucial to maximizing efficiency while maintaining effective charge separation and recombination dynamics.

Hydroxylation is not only a structural stabilizer but also modifies the band edges of TiO_2 surfaces via surface dipole interactions. Zhang et al. investigated hydroxylation on rutile TiO_2(110) surfaces and found that hydroxyl groups create an electric dipole effect, shifting both the valence and conduction band edges upwards.[46] This effect enhances the reducing power of rutile, making its conduction band more favourable for photocatalytic hydrogen evolution. The underlying mechanism is electrostatic in nature: hydroxyl groups induce localized dipoles, which modify the band structure at the surface level. Specifically, the total dipole moment of the hydroxylated surface arises from two contributions: the intrinsic dipole of the hydroxyl groups and the polaronic dipoles generated by structural distortion and charge redistribution. These dipoles create a local electric field that modulates the electrostatic potential near the surface, leading to a blue shift of the band edges while maintaining a nearly constant band gap. This behaviour can be approximated using a parallel-plate capacitor model, where the variation in band edges depends on the surface dipoles and the effective dielectric constant of the surface layers. The model further explains why hydroxylation stabilizes surface states and influences the photocatalytic activity of rutile TiO_2. Figure 3.8 provides a direct visualization of how the band edges shift as a function of hydroxylation.

Similar dipole effects have been observed in quantum dots, where ligand-induced surface dipoles significantly modify energy levels and electronic interactions.[47,48] Ligand attachment on semiconductor nanocrystals leads to systematic shifts in conduction and valence band positions, depending on the dipole moment of the attached species. In these studies, quantum dots exhibited band edge shifts of up to 0.9 eV, proving that surface functionalization strongly influences electronic properties. While these findings are well-established for rutile and colloidal quantum dots, they remain poorly explored for larger anatase nanoparticles, despite their superior photocatalytic activity.

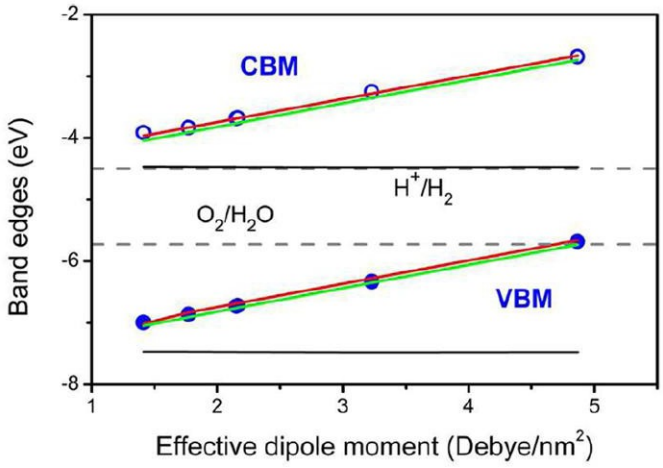

Figure 3.8: Figure 4. DFT+U energies of the conduction and valence band edges (open and solid blue symbols, respectively) of the hydroxylated TiO_2(110) surfaces as a function of effective dipole moment. The electrochemical potentials for two redox half reactions of water decomposition at pH 7, represented by dashed lines, are shown for comparison. The solid lines represent the calculated energy shifts of the band edges. Red: total contribution; Green: contributed by the hydroxyls; Black: contributed by the polaronic dipoles. Figure adapted from reference 46.

In summary, hydroxylation has a profound impact on the structural and electronic properties of TiO_2 nanostructures, but its effects vary significantly depending on size, phase, and morphology. While previous studies have extensively analysed small nanoclusters, rutile surfaces, and ligand-functionalized quantum dots, the effect of hydroxylation on larger anatase nanoparticles remains insufficiently understood. Given that anatase is the more efficient photocatalyst, a detailed exploration of hydroxylation in this regime is essential for advancing TiO_2-based photocatalytic applications. This gap in the literature motivates the research in this thesis, which focuses on elucidating the impact of hydroxylation on the band structure and stability of larger anatase nanoparticles.

3.2 Results

This section gathers the results of the three papers published regarding the effect of size and hydration degree on a selection of $(TiO_2)_n$ nanoparticles, all with diameters larger than 1.5 nm. Along the different families of NPs considered, a slab model of the anatase (101) surface is employed to compare the electronic effects observed in nanoparticles with those in an extended surface system. The anatase (101) slab model consists of a six-layer (3 × 1) supercell, where the (101) surface is symmetrically exposed on both sides. A vacuum layer of approximately 20 Å is included to prevent artificial interactions between periodic images.

3.2.1 Simulated thermal annealing

Importantly, for some of these sizes, two structural types of NPs are considered: crystalline anatase and amorphous quasi-spherical (see Figure 3.9). The crystalline anatase NPs were designed following a top-down strategy in which the bulk anatase crystal is cut to generate bipyramids with the most stable (101) surface on all exposed facets.[6,9] Their stability and properties are influenced by the preservation of specific facets, which play a role in determining their electronic and photocatalytic behaviour. In contrast, the amorphous quasi-spherical nanoparticles lack a long-range crystalline order, exhibiting a more disordered atomic structure. These amorphous NPs are generated through a thermal annealing process[49] that disrupts the crystalline framework, leading to a less rigid and more flexible atomic arrangement.

The thermal annealing procedure for NP stabilization was conducted using classical MD simulations with the NanoTiO[5] and FFTiOH[37] interatomic potentials, as implemented in the GULP code.[50] This simulated annealing (SA) approach was applied to both crystalline anatase-derived $(TiO_2)_{35}$ and $(TiO_2)_{84}$ NPs to explore their low-energy configurations. The annealing process began by heating the respective $(TiO_2)_n(H_2O)_m$ NP to ~1800 K over 1000 ps, followed by an equilibration phase at this temperature for 300 ps to ensure full disordering of the crystalline structure. The NP was then subjected to a controlled stepwise cooling process, gradually reducing the temperature to 300 K over ~4000

ps. This systematic cooling allowed for the formation of stable, low-energy amorphous or quasi-spherical configurations.

Figure 3.9: Examples of TiO_2 structures. From left to right: an amorphous annealed amorphous $(TiO_2)_{35}(H_2O)_{12}$ NP, and faceted anatase crystalline $(TiO_2)_{84}(H_2O)_{31}$ and a supercell of an extended (101) surface model of anatase with 0 water molecules.

For crystalline anatase NPs, the structural framework remained largely intact, with hydroxylation playing only a minor role in modifying their morphology. In contrast, for smaller anhydrous spherical-cut NPs, thermal annealing significantly altered their structure, leading to the loss of internal crystallinity and the adoption of quasi-spherical, amorphous-like morphologies. As indicated in the previous sections, theoretical studies have demonstrated that, for small nanoclusters, annealed, non-crystalline NPs are energetically more stable than their faceted crystalline counterparts of the same size. To further explore hydroxylation effects, dissociated water molecules were incrementally added by binding H and –OH groups to undercoordinated surface O and Ti atoms, respectively. After each hydroxylation step, the NP was annealed to identify the lowest-energy $(TiO_2)_n(H_2O)_m$ structures. This iterative process revealed that hydroxylation strongly influences atomic rearrangement, leading to distinct NP structures at different hydration levels. Unlike crystalline anatase NPs, where hydroxylation produces only local modifications, thermally annealed NPs undergo significant structural evolution as hydroxylation increases.

After the MD-based SA procedure, the lowest-energy NPs were further refined using DFT calculations at PBE level[51] to minimize residual forces and precisely determine their atomic structures. For the faceted crystalline systems, the same level of theory was applied for optimization. All reported properties correspond to the most stable configurations identified through this combined MD-DFT approach.

3.2.2 Influence of Nanoparticle Size

We first focus on the influence of size on the total energy stability of crystalline and amorphous structures and the electronic energy gap broadening due to the quantum confinement effect. Our discussion considers crystalline faceted NPs, amorphous annealed NPs, and the extended TiO_2 (101) surface as a reference, restricting our analysis in this section to the anhydrous (bare) state.

PBE total energy calculations reveal a strong dependence of stability on NP size and structure. At small sizes, amorphous NPs are energetically preferred over crystalline anatase-like structures (see first point in Figure 3.10). For instance, in the $(TiO_2)_{35}$ system, the total energy difference ($\Delta E_{tot} = E_{tot}(crystalline) - E_{tot}(amorphous)$) is −8.87 eV, while for the $(TiO_2)_{84}$ system, it is −7.49 eV. When normalized per titania unit, these values correspond respectively to −0.25 eV for $(TiO_2)_{35}$ and −0.09 eV per unit for $(TiO_2)_{84}$. This decreasing trend suggests that as NP size increases, the energetic preference for amorphization diminishes. Eventually, as described earlier in this chapter, a stability crossover occurs beyond approximately 2–3 nm, where crystalline anatase-like structures become more favourable.

The physical origin of this behaviour is the high proportion of undercoordinated surface atoms in smaller NPs, which makes highly reconstructed, amorphous-like structures more stable. As NP size increases, the bulk-like interior becomes more dominant, reducing the energy penalty for maintaining a crystalline lattice. Again, this trend is consistent with prior studies on the thermodynamic stability of TiO_2 NPs, which predict that amorphous forms are preferred at the smallest sizes but become progressively less favourable with increasing NP diameter.

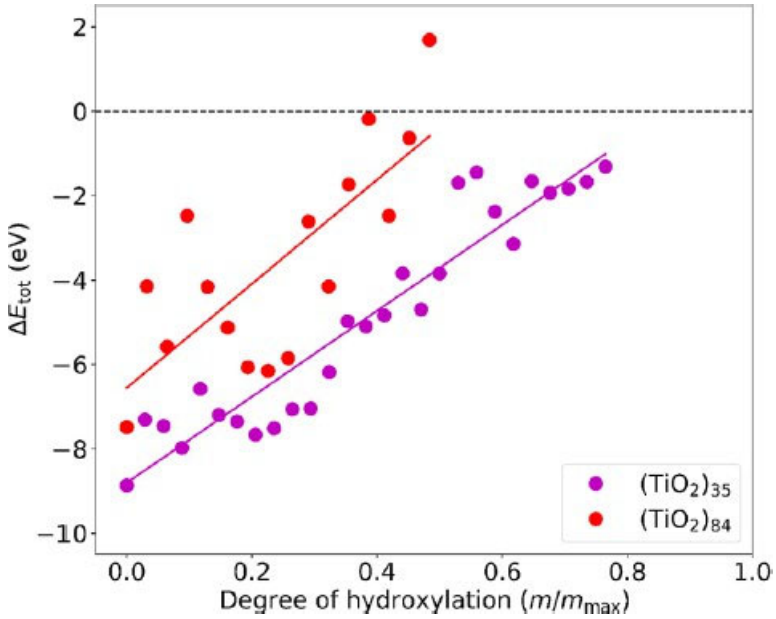

Figure 3.10: Calculated total energy differences (ΔE_{tot}) between anatase crystalline faceted NPs and amorphous annealed NPs for the $(TiO_2)_{35}(H_2O)_m$ system (purple) and the $(TiO_2)_{84}(H_2O)_m$ system (red) with respect to degree of hydroxylation (m/m_{max}). Linear fits to the data are added as rough indications of tendencies to facilitate comparison between both NP system sizes.

3.2.2.1 QC effect on Electronic Gap

While total energy trends dictate thermodynamic stability, electronic properties follow a different size-dependent behaviour. The most significant effect of decreasing NP size is the widening of the electronic gap due to Quantum Confinement. We have already introduced this effect, which occurs because, as the particle shrinks, the spatial extent of electronic wavefunctions decreases. This reduction leads to a shift in energy levels and an increased separation between the highest occupied and lowest unoccupied molecular orbitals. DFT calculations using a hybrid-inspired PBEx correction[52] to our initial PBE values clearly demonstrate this QC effect across different TiO_2 NPs. In crystalline faceted anatase structures, the E_{gap} progressively increases as size decreases (see first point in Figure 3.11). Specifically, the $(TiO_2)_{35}$ NP exhibits an E_{gap} of 3.84 eV, while for the larger $(TiO_2)_{165}$ NP, the value decreases to 3.66 eV. In

comparison, the TiO_2 (101) surface, which serves as a bulk-like reference, has a gap of 3.58 eV, slightly higher than the bulk anatase value of 3.23 eV. These results confirm the expected QC-induced shift in electronic states.

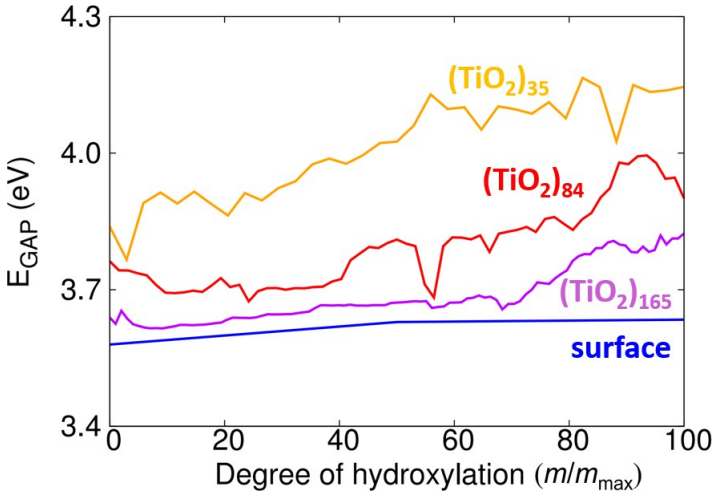

Figure 3.11: Evolution of E_{GAP} energies with degree of hydroxylation of the $(TiO_2)_n$ (n = 35, 84 and 165) anatase NPs and the extended (101) anatase surface.

Interestingly, while crystalline nanoparticles follow the expected trend of quantum confinement leading to an increase in E_{gap}, amorphous nanoparticles do not exhibit the same behaviour. For instance, the anhydrous amorphous $(TiO_2)_{35}$ nanoparticle has a lower energy gap (3.43 eV) compared to the larger anhydrous $(TiO_2)_{84}$ nanoparticle (3.58 eV). This suggests that in amorphous nanoparticles, the impact of quantum confinement is partially masked by structural effects such as defects and atomic reconstructions, which play a dominant role in determining electronic properties.

The balance between these effects determines the optimal size range for different applications. For high stability, larger crystalline anatase NPs (>3 nm) are preferable, as they have lower total energies relative to amorphous structures. For enhanced electronic properties, such as larger band gaps for photocatalysis, smaller NPs are advantageous due to QC-driven gap widening. Crystalline faceted NPs may provide additional advantages in specific scenarios due to their

slightly higher E_{gap} values compared to amorphous counterparts. Besides, their increased thermodynamic stability at larger sizes makes them more favourable compared to amorphous structures.

3.2.3 Effect of Hydroxylation

As detailed above, when exposed to aqueous environments, TiO_2 NPs undergo hydroxylation via water dissociation, leading to the formation of hydroxyl (-OH) groups on their surfaces. This process modifies the total energy landscape of both crystalline and amorphous structures, influencing the relative stability of different NP morphologies. In this section, we analyse the impact of hydroxylation on the DFT total energies of $(TiO_2)_{35}$ and $(TiO_2)_{84}$ NPs, focusing on the observed convergence between crystalline and amorphous structures. We then examine the energetics of hydration, introducing key thermodynamic quantities such as hydration energies and incremental hydration energies. These analyses provide insight into the extent to which hydroxylation stabilizes or destabilizes small TiO_2 NPs and how this effect varies with size and structural order. Throughout the chapter, we adopt a consistent definition for the degree of hydroxylation, expressed as m/m_{max}, where m is the number of water molecules dissociated on the NP surface and m_{max} is the maximum number of dissociable water molecules that can form hydroxyl (–OH) groups on the fully hydroxylated, faceted NP. Importantly, m/m_{max} depends on nanoparticle size and varies between the different TiO_2 nanosystems.

Along the chapter, a common m/m_{max} definition of the degree of hydroxylation is established. We define it as the number of water molecules (m) divided by the maximum number of water molecules that can dissociate to form hydroxyl (−OH) groups on the faceted NP surface (m_{max}). Note that this maximum value varies from one 35- to 84- systems' size.

3.2.3.1 DFT Energies

The total energy differences between crystalline faceted and amorphous annealed TiO_2 NPs exhibit a striking evolution as the degree of hydroxylation increases. In the anhydrous state, as discussed previously, amorphous structures are more stable than their crystalline counterparts at small sizes, with the energy difference ΔE_{tot} decreasing as NP size increases. However, as

hydroxylation progresses, the total energy differences between amorphous and crystalline NPs decrease, leading to an eventual convergence in energetic stability.

This trend is clearly illustrated in Figure 3.10, which shows the evolution of ΔE_{tot} as a function of hydroxylation for both $(TiO_2)_{35}$ and $(TiO_2)_{84}$ NPs. Initially, the anhydrous amorphous $(TiO_2)_{35}$ NP is significantly more stable than the faceted crystalline form (as discussed in 3.2.2), with $\Delta E_{\mathrm{tot}} \approx$ -8.87 eV. As hydroxylation increases, the energy difference gradually decreases until the two structures become nearly equivalent in total energy. For the larger $(TiO_2)_{84}$ NP, the energy difference is initially smaller and converges more rapidly, achieving comparable stability at 50% hydroxylation. For the smaller $(TiO_2)_{35}$ systems this crossover occurs at approximately 75% hydroxylation degree. The faster convergence for the larger NP suggests that hydroxylation is more effective at stabilizing crystalline structures as size increases, likely because a larger fraction of the total atoms in the system is at the surface, where hydroxylation-induced coordination effects become dominant.

The underlying mechanism driving this convergence lies in the local structural modifications induced by hydroxylation. Hydroxyl (-OH) groups interact strongly with undercoordinated Ti and O atoms, reducing structural disorder and increasing the local atomic coordination number (as shown in Figure 3.13). Hydroxylation thus leads to a marked reduction in the fraction of Ti_{4c} species and a corresponding increase in Ti_{6c} coordination. This redistribution reflects the structural healing effect induced by water dissociation and subsequent -OH binding. This effect is more pronounced in crystalline faceted NPs, where hydroxylation effectively "heals" surface distortions, making the total energy more comparable to that of amorphous structures.

3.2.3.2 Energetics of Hydration

To quantify the energetic effects of hydroxylation, we introduce the hydration energy (E_{hyd}), which measures the energy change associated with progressively increasing the degree of hydroxylation (see Equation 3.3). It is defined as:

$$E_{\mathrm{hyd}}(m) = E_{\mathrm{tot}}(m) - (E_{\mathrm{tot}}(0) + m \cdot E_{\mathrm{H_2O}}) \tag{3.4}$$

where $E_{\mathrm{tot}}(m)$ is the total energy of the NP with m hydroxyl groups, $E_{\mathrm{tot}}(0)$ is the total energy of the anhydrous NP, and $E_{\mathrm{H_2O}}$ is the energy of an isolated water molecule. A negative $E_{\mathrm{hyd}}(m)$ value indicates that hydroxylation is energetically favourable, stabilizing the NP.

Additionally, we define the incremental hydration energy, which measures the energy change associated with adding a single hydroxyl group at a given step (see Figure 3.5):

$$\Delta E_{\mathrm{hyd}}(m) = E_{\mathrm{tot}}(m) - (E_{\mathrm{tot}}(m-1) + E_{\mathrm{H_2O}}) \tag{3.5}$$

This quantity helps us understand how the energetic stabilization changes incrementally as more hydroxyl groups are added.

The hydration energy trends for crystalline and amorphous NPs are presented in Figure 3.12, showing the variation of $E_{\mathrm{hyd}}(m)$ as a function of hydroxylation for $(TiO_2)_{35}$ and the $(TiO_2)_{84}$ NPs. For the smaller $(TiO_2)_{35}$ NPs, hydroxylation is consistently exothermic, with $E_{\mathrm{hyd}}(m)$ decreasing as hydroxyl groups are added. However, the rate of stabilization slows down at higher hydroxyl coverages, reflecting diminishing returns in energy gain. This suggests that initial hydroxylation events are particularly effective at stabilizing undercoordinated surface sites, while later additions experience weaker binding due to increased steric and electrostatic interactions. This interpretation is supported by the known site-specific reactivity hierarchy of TiO_2 surfaces, where highly undercoordinated Ti atoms—such as those at apical vertices and corners—are preferentially hydroxylated at low coverage, yielding strong exothermic stabilization. As these reactive sites are progressively passivated, subsequent water molecules bind to less reactive edge and facet sites, leading to the observed reduction in stabilization energy.

A similar but more pronounced stabilization trend is observed for $(TiO_2)84$ NPs, where hydroxylation leads to a faster convergence in total energy between crystalline and amorphous forms. This aligns with the ΔE_{tot} trends in Figure 3.10, further confirming that hydroxylation promotes structural convergence by stabilizing previously unstable crystalline surfaces.

The incremental $\Delta E_{\mathrm{hyd}}(m)$ hydration energy data provide further insight into this behaviour. For crystalline anatase TiO_2 nanoparticles, hydroxylation follows a predictable stabilization pattern. The initial adsorption of water molecules leads to strong exothermic reactions, particularly at under-coordinated surface sites such as apical or edge positions. As hydroxylation progresses and these reactive sites become occupied, the incremental stabilization energy decreases and eventually fluctuates around a lower value. This orderly trend reflects the fixed atomic arrangement of the crystalline nanoparticles, where each successive hydroxylation step progressively stabilizes the system without major structural rearrangements.

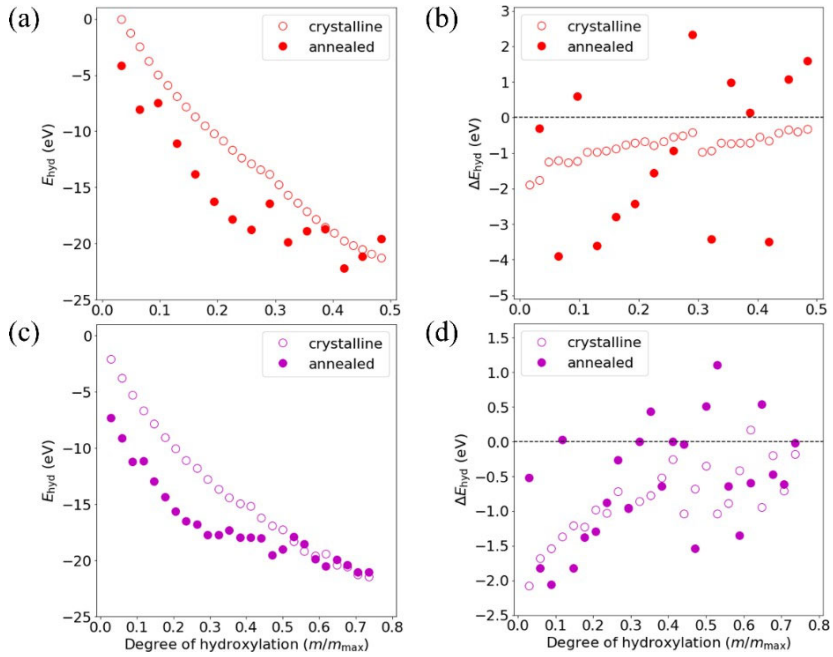

Figure 3.12: (a) Variation of $E_{\mathrm{hyd}}(m)$ with respect to the degree of hydroxylation (m/m_{max}) for increasingly hydroxylated crystalline and annealed $(TiO_2)_{84}(H_2O)_m$ NPs. The hydration energy of the faceted NP with two water molecules is set to 0 eV as an offset, with the total energy of the bare crystalline NP, $E_{\mathrm{tot}}(0)$, used as the common reference for both sets of NPs. (b) Variation of $\Delta E_{\mathrm{hyd}}(m)$ with respect to the degree of hydroxylation. Plots (c,d) correspond

to the m-dependent tendencies in $E_{\mathrm{hyd}}(m)$ and $\Delta E_{\mathrm{hyd}}(m)$ for amorphous and crystalline $(TiO_2)_{84}(H_2O)_m$ NPs.

In contrast, amorphous nanoparticles exhibit a more irregular hydroxylation pattern. These larger fluctuations likely stem from significant structural rearrangements occurring within the annealed nanoparticles at different hydroxylation levels. Unlike crystalline nanoparticles, where hydroxylation follows a predictable pattern, each hydroxylation step in the annealed NPs can lead to notable changes in both the overall structure and the positioning of hydroxyl groups, making the process inherently less predictable. In some cases, particularly in the larger $(TiO_2)_{84}$ systems, positive stabilization energy values suggest that certain hydroxylation states correspond to less favourable low-energy configurations identified by the MD-SA procedure. This indicates that, as the surface becomes increasingly hydroxylated, some structural adjustments become energetically costly. This effect is less pronounced in the smaller $(TiO_2)_{35}$ amorphous nanoparticles, where the hydroxylation-induced energy variations remain more controlled. Overall, the comparable trends in $\Delta E_{\mathrm{hyd}}(m)$ observed for both $(TiO_2)_{84}(H_2O)_m$ and $(TiO_2)_{35}(H_2O)_m$ nanoparticles suggest that the underlying stabilization mechanisms driven by hydroxylation remain consistent across different nanoparticle sizes.

3.2.3.3 Mechanistic Explanation and Crystalike concept

The observed energy convergence between crystalline faceted and amorphous annealed TiO_2 NPs upon hydroxylation is closely linked to changes in atomic coordination environments. As surface hydroxylation increases, the structural differences between these two forms become less pronounced at a local coordination level, despite the global structural order remaining distinct. This suggests that hydroxylation stabilizes surface atoms in a way that makes the amorphous structure behave more like its crystalline counterpart in terms of electronic and energetic properties.

The coordination of Ti atoms plays a crucial role in determining the energetic and electronic structure of TiO_2 NPs. In a bulk crystalline anatase structure, Ti atoms are predominantly six-fold coordinated (Ti_{6c}), forming a well-ordered octahedral network. In contrast, at the nanoscale, undercoordinated surface

atoms are common, leading to the presence of five-fold (Ti_{5c}) and four-fold (Ti_{4c}) coordinated titanium species, particularly in small or amorphous structures.

In the anhydrous state, amorphous TiO_2 NPs contain a higher fraction of undercoordinated Ti atoms compared to their crystalline counterparts. As shown in Figure 3.13, in the anhydrous $(TiO_2)_{84}$ NP:

- The fraction of Ti_{4c} is ~40%, significantly higher than in the faceted crystalline NP (~15%).
- The fraction of Ti_{5c} is ~20%, way lower than the ~50% of the crystalline NP.
- The fraction of Ti_{6c} is similar in both settings (around ~25-30%).

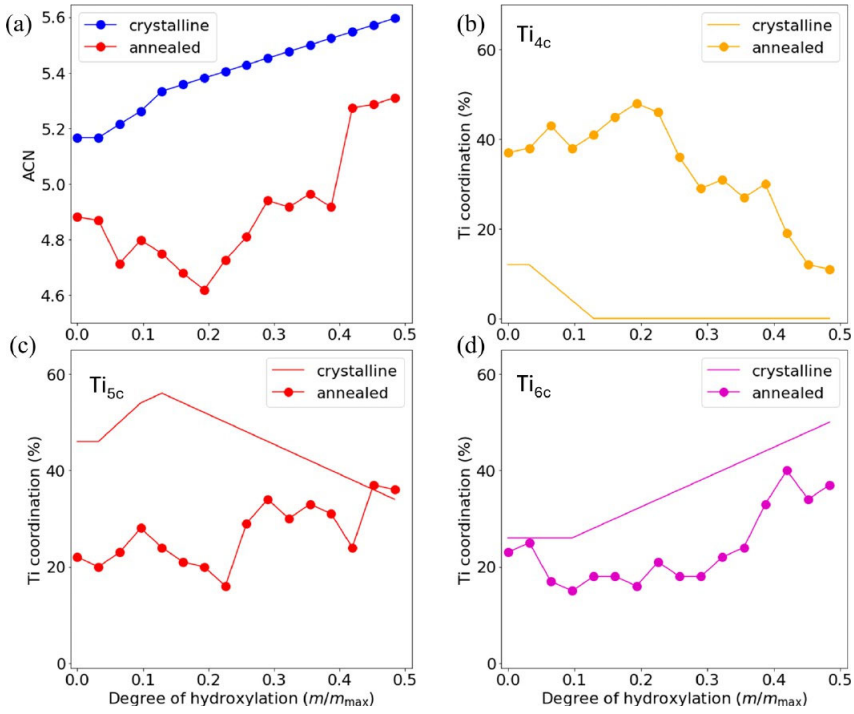

Figure 3.13: Average coordination number (ACN) of Ti centres for the annealed amorphous and crystalline anatase $(TiO_2)_{84}(H_2O)_m$ NPs with respect to the degree of hydroxylation. (b–d) Corresponding evolution of the distribution

of 4-, 5-, and 6-fold local atomic coordination environments of Ti centres (Ti_{4c}, Ti_{5c}, and Ti_{6c}) with respect to the degree of hydroxylation of both crystalline and annealed $(TiO_2)_{84}(H_2O)_m$ NPs.

These numbers clearly indicate that amorphous structures contain a higher proportion of undercoordinated Ti_{4c} contributing to their lower total energy in the anhydrous state. As hydroxylation increases, Ti atoms at the NP surface recoordinate, effectively shifting the population from undercoordinated states (Ti_{4c}, Ti_{5c}) toward higher coordination states (Ti_{6c}).

For $(TiO_2)_{84}$ annealed NPs at medium 50% hydroxylation:

- The fraction of Ti_{4c} drops from ~40% to ~15%.
- The fraction of Ti_{5c} increases from ~20% to ~40%.
- The fraction of Ti_{6c} increases from ~25% to ~40%.

These numbers indicate that hydroxylation leads to a strong increase in Ti_{6c} sites, particularly in amorphous NPs, making their local coordination environment much closer to that of crystalline anatase. This transformation helps reduce the total energy difference between the two NP forms, driving the observed energetic convergence.

The stabilization of amorphous NPs via increased local coordination does not imply a full recrystallization. The Pair Distribution Function (PDF) analysis in Figure 3.14 confirms that even at high hydroxylation levels, amorphous structures retain their disordered nature, lacking the long-range periodicity of crystalline anatase.

This supports the "crystalike" concept, where amorphous TiO_2 NPs, despite remaining structurally disordered at a global scale, exhibit electronic (see next section) and energetic properties similar to crystalline anatase due to local coordination effects. The local structure converges, but the long-range order remains distinct. This means that hydroxylated amorphous NPs can mimic the desirable electronic properties of crystalline anatase without requiring full crystallization, making them potential candidates for applications where crystalline TiO_2 is traditionally used.

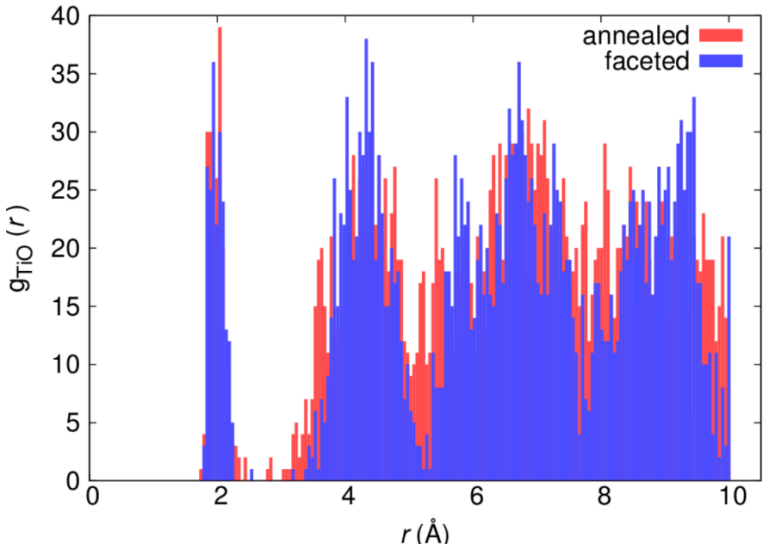

Figure 3.14: Pair distribution function (PDF) for Ti−O distances in a faceted crystalline anatase NP (blue) and thermally annealed NP (red), both with a $(TiO_2)_{84}(H_2O)_{30}$ composition. The bin size for the histogram is 0.05 A.

3.2.3.4 Evolution of the Energy Gap and HOMO-LUMO levels

The electronic structure of TiO_2 NPs undergoes significant changes upon hydroxylation, affecting both the energy gap (E_{gap}) and the individual shifts of the HOMO (highest occupied molecular orbital) and LUMO (lowest unoccupied molecular orbital) levels. In the previous subsections, we have established that hydroxylation leads to a convergence in total energy between amorphous and crystalline NPs due to local structural modifications, particularly in the titanium coordination environment. This subsection extends that discussion by examining the evolution of the energy gap with increasing hydroxylation, followed by an analysis of the separate shifts in HOMO and LUMO energies for different NP structures.

As hydroxylation progresses, the electronic energy gap of TiO_2 NPs generally increases, reflecting the passivation of surface states and a reduction in defect-induced electronic states. This behaviour is consistently observed across different NP sizes and morphologies, as evidenced by Figure 3.11. As hydroxylation increases, both crystalline and amorphous structures exhibit a progressive increase in the energy gap, with the effect being strongest for smaller NPs.

Besides, faceted NPs undergo a more progressive variation on the E_{gap} as hydroxylation proceeds. On the contrary, MD-SA generated titania systems suffer from sharp changes in the gap, as the annealing protocol implies huge transformation in the NPs' structures (see section 3.1.2). Figure 3.15 illustrates these differences in the larger $(TiO_2)_{84}$ NPs. Overall, this trend is directly related to the progressive reduction of undercoordinated Ti atoms—particularly Ti_{4c} species—through hydroxyl binding, which effectively heals electronic defects and stabilizes the local structure. A key result is the convergence of E_{gap} values between amorphous and crystalline forms at high hydroxylation levels, further supporting the convergence of properties on highly hydroxylated NPs.

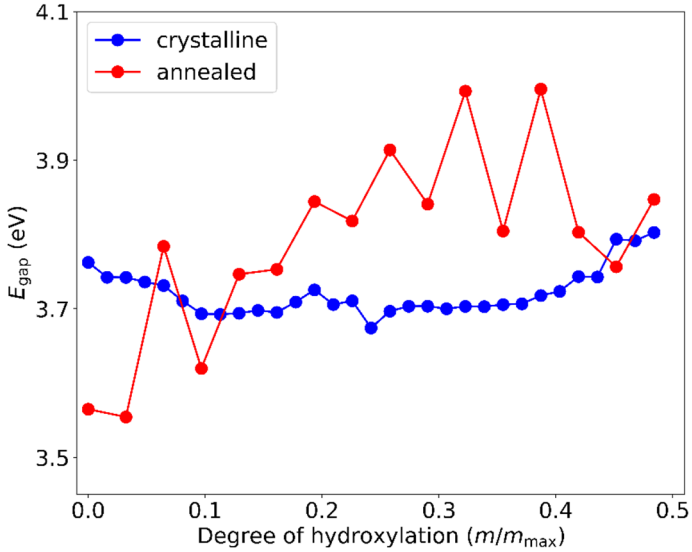

Figure 3.15: Evolution of E_{gap} with respect to the degree of hydroxylation for crystalline and annealed $(TiO_2)_{84}(H_2O)_m$ NPs.

For larger NPs such as $(TiO_2)_{165}$ and the (101) anatase surface, the impact of hydroxylation on the gap is significantly weaker. The energy gap of the (101) surface remains nearly constant (~3.6 eV) across hydroxylation levels, indicating that hydroxylation predominantly affects surface states rather than bulk-like electronic structure.

While the overall energy gap increases with hydroxylation, the individual shifts of the HOMO and LUMO levels provide deeper insight into how hydroxylation modifies the electronic structure. This effect is illustrated in Figure 3.16, where the changes in absolute energy levels (relative to vacuum) for different TiO_2 NP sizes (all crystalline anatase) are examined.

A key observation is that hydroxylation causes a nearly parallel shift of both HOMO and LUMO levels toward lower energies, rather than altering E_{gap} in an asymmetric manner. This means that while the energy gap widens, the absolute positions of the band edges are also shifted, which has important implications for photocatalytic performance. The degree of shift is strongest in smaller NPs, consistent with their greater surface-to-volume ratio and the stronger influence of surface hydroxyl groups.

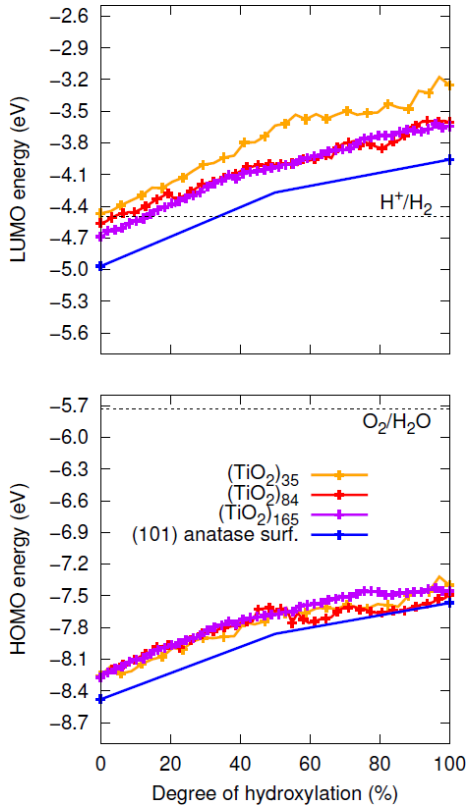

Figure 3.16: Evolution of the energies of the HOMO (lower) and LUMO (upper) with degree of hydroxylation of the $(TiO_2)_n$ (n = 35, and 165) anatase NPs

and the extended (101) anatase surface. Dotted grey lines represent the redox potentials for the HER (upper) and the OER (lower), which have the approximate values of −4.5 and −5.7 eV, respectively.

Faceted crystalline and amorphous annealed NPs display similar initial and final values with respect to the degree of hydroxylation. As in the energy gap case (Figure 3.15), the annealed setting presents larger fluctuations due to the effect of the MD-SA protocol

3.2.3.5 The Ligand-Induced Dipole Effect

A critical mechanism underlying the downward shift of electronic states with hydroxylation is the ligand-induced dipole effect (LIDE). The hydroxyl (-OH) groups on the NP surface introduce local electric fields, which create a global electrostatic potential shift across the NP. As stated in the end of 3.1 introductory section, this effect has been widely studied in semiconductor quantum dots and rutile surfaces and is now recognized as a key factor in controlling the absolute band edge positions in TiO_2 NPs.

LIDE is typically modelled as linearly proportional to ligand coverage, assuming a fixed dipole per ligand. This dipole arises from both the intrinsic dipole of the ligand and induced polarization due to ligand-surface interactions. In this thesis, a more detailed approach is taken by explicitly considering how the dipole of the –OH group is influenced by structural changes (Ti–O–H bond angle, α), inter-hydroxyl hydrogen bonding (H-bond formation), and charge redistribution:

$$\vec{p_{OH}} = \sum_{i=1}^{N} Q_{H,i} \cdot d_{OH,i} \cdot \cos(\alpha_i) \tag{3.6}$$

where N is the number of OH groups on a NP, and Q_{H} is the positive charge on the H atoms in every OH ligand. We obtained the Q_{H} charges using the Hirshfeld atomic charge partitioning scheme. Notably, the polarization of the TiO_2 surface due to hydroxylation is minimal and largely independent of OH coverage, which aligns with previous reports for rutile TiO_2 surfaces.

Using such refined model, we found that while the OH bond length (d_{OH}) remains nearly constant, the parameters α (bond angle) and QH (charge on the hydroxyl hydrogen) decrease non-linearly with increasing hydroxylation. This effect is attributed to the formation of OH···OH hydrogen bonds, which progressively bend the Ti–O–H bond closer to 90°, thereby reducing the net dipole moment ($\vec{p}_{OH}$) compared to a purely linear model. The reduction in Q_{H} suggests partial charge delocalization within the hydroxyl network, further moderating the dipole increase. Notably, for 50–100% hydroxylation of our NP systems, the observed dipole moment deviates by −15% to −22% from the expected linear model.

The effect of hydroxylation on energy levels is closely linked to LIDE. As hydroxylation increases, the energy levels shift non-linearly, deviating subtly from the expected linear trend. This behaviour is quantitatively described using an adapted LIDE model:

$$E_l = E_0 + \Delta E = E_0 + A \cdot \left(\frac{\vec{p}_{OH}}{r^2}\right) \tag{3.7}$$

where E_l is the shifted energy level, E_0 is the energy level in anhydrous TiO_2, and ΔE represents the LIDE shift, which depends on $\vec{p}_{OH}$ (the hydroxyl-induced dipole moment) and r (the effective NP radius). The parameter A is a system-dependent fitting constant.

The strong correlation between hydroxylation-induced ligand-induced dipole effects and energy level shifts is shown in Figure 3.17 and further validates the use of the refined dipole model. DFT calculations show a clear relationship between the total dipole moment from surface hydroxyl groups and shifts in the HOMO and LUMO energy levels of faceted TiO_2 nanoparticles. This supports the idea that hydroxylation systematically influences electronic structure through dipolar interactions. These findings also reveal that hydroxylation-induced hydrogen bonding and charge redistribution play a crucial role in modulating the dipole moment and energy levels of TiO_2 NPs, with implications for their electronic properties and photocatalytic performance. This nuanced

understanding provides a more accurate model of how hydroxylation affects TiO_2 surfaces beyond simple linear approximations.

3.2.3.6 Implications for Photocatalytic Applications

In photocatalysis, the alignment of the conduction band minimum (CBM) and valence band maximum (VBM) relative to the redox potentials of water dictates the efficiency of charge transfer reactions. The effects of QC and hydroxylation must be considered together when evaluating the suitability of different NP sizes and morphologies for photocatalytic applications.

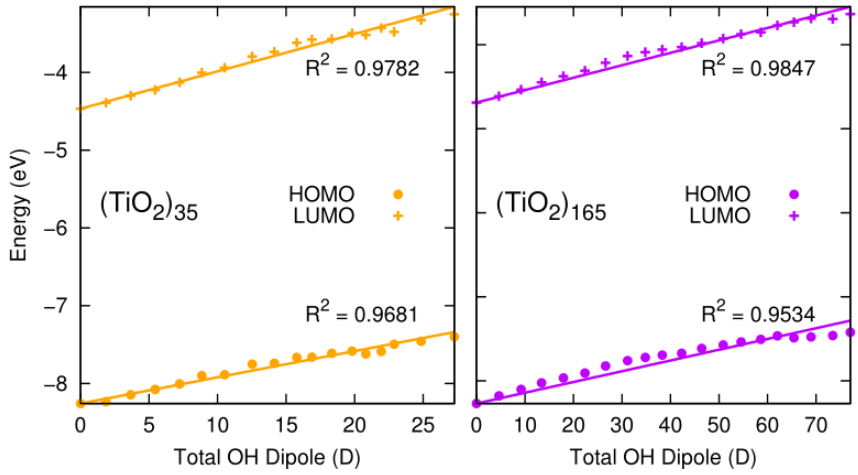

Figure 3.17: Correlation between calculated HOMO (LUMO) energies and projected total –OH dipole moment for the anatase $(TiO_2)_{35}$ and $(TiO_2)_{165}$ NPs calculated using Equation 3.6.

As seen in the top plot of Figure 3.16, the impact of hydroxylation on band edge positions varies with NP size and structural morphology. In the anhydrous state, QC dominates the electronic properties, leading to an upward shift of both the CBM and VBM as NP size decreases. This shift is particularly strong in small NPs, where the increased energy gap raises the CBM to higher energy levels. While this can enhance the oxidation potential of the valence band, it also pushes the CBM too far above the hydrogen evolution reaction (HER) potential, making electron transfer for hydrogen production inefficient. This

suggests that while QC can be beneficial in moderate amounts, excessive QC leads to unfavourable charge transfer properties.

Hydroxylation introduces an additional layer of complexity by lowering both CBM and VBM energies in a nearly parallel fashion. This effect, driven by the LIDE, ensures that hydroxylated NPs exhibit band alignments that are more suitable for water splitting. The downward shift induced by hydroxylation counteracts the QC-driven CBM rise, making hydroxylated NPs better aligned with the hydrogen redox potential.

The influence of hydroxylation on band alignment varies across different NP sizes. For very small NPs (e.g., $(TiO_2)_{35}$), the strong QC effects raise the CBM too high, even after hydroxylation, potentially making charge transfer inefficient. In contrast, larger NPs (e.g., $(TiO_2)_{165}$), which exhibit weaker QC effects, rely more on hydroxylation to lower the CBM into an optimal range. This results in a size-dependent interplay between QC and hydroxylation, where neither extreme is ideal for photocatalytic performance.

The best photocatalytic performance is expected in moderately quantum-confined NPs (~2–3 nm, such as $(TiO_2)_{84}$) with an appropriate degree of hydroxylation (~50%), ensuring that the CBM is slightly above the hydrogen evolution potential while the VBM remains low enough for oxidative reactions. This highlights the importance of coordinating both size and surface chemistry when designing TiO_2-based photocatalysts, as depicted in Figure 3.18. By tuning both the NP size and the degree of hydroxylation, it is possible to optimize the band alignment for water splitting applications. The combination of moderate QC and hydroxylation-driven band edge shifts provides a powerful approach for engineering TiO_2 photocatalysts that maximize efficiency in hydrogen evolution and oxygen reduction reactions. These findings underscore the need to consider both electronic structure modifications and surface chemistry when designing next-generation photocatalytic materials.

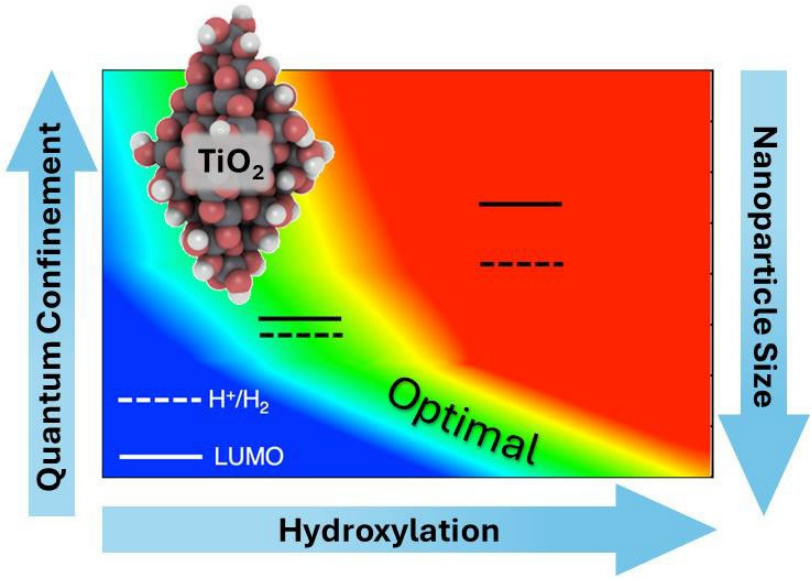

Figure 3.18: LUMO versus HER potential energy level alignment plot with respect to varying the degree of hydroxylation (x-axis), degree of QC (left y-axis) and anatase system size (right y-axis). The colours indicate the regions where the LUMO is below/above the HER potential (blue/red) and where the LUMO is between 0–0.1 eV above the redox potential of the HER (green).

3.3 Conclusions

This first results' chapter systematically explores the role of size, crystallinity, and hydroxylation in determining the energetic stability and electronic properties of TiO_2 nanoparticles using DFT-based calculations. Our findings reveal that these factors act synergistically, allowing for the controlled tuning of NP properties in a predictable manner. By analysing the effects of quantum confinement and ligand-induced dipole effects, we provide a framework for understanding how small-scale structural modifications influence macroscopic electronic behaviour, particularly in photocatalytic applications.

Our results demonstrate that hydroxylation significantly alters the energetic stability of TiO_2 NPs, leading to a convergence in total energy between crystalline faceted and amorphous annealed NPs. In the anhydrous state, amorphous structures are more stable than their crystalline counterparts due to their higher proportion of undercoordinated Ti sites. However, with increasing hydroxylation, this energetic difference diminishes, and at high hydroxylation levels, both NP morphologies exhibit similar stability. This hydroxylation-induced stabilization is not accompanied by a complete recrystallization of amorphous structures, as confirmed by Pair Distribution Function analysis. Instead, the effect is driven by a local structural transformation, where the distribution of four-fold (Ti_{4c}), five-fold (Ti_{5c}), and six-fold (Ti_{6c}) coordinated Ti sites becomes similar between amorphous and crystalline NPs. This redistribution increases the average coordination number, making hydroxylated amorphous NPs electronically behave like their crystalline counterparts—leading to the concept of crystalike NPs.

The impact of hydroxylation on the electronic structure follows a similar trend, inducing a convergence in electronic properties between crystalline and amorphous NPs. As hydroxylation increases, E_{gap} rises for both NP types, eventually reaching similar values at high hydroxyl coverage. This increase is attributed to the passivation of surface defect states, which reduces localized mid-gap states and leads to a more bulk-like band structure. A key insight from this work is that the anatase crystal structure may not be necessary to achieve anatase-like electronic properties. Instead, by tailoring hydroxylation, non-crystalline NPs can be tuned to exhibit electronic structures comparable to crystalline

anatase, expanding the potential for using amorphous titania in applications traditionally dominated by its crystalline counterpart.

Beyond the energy gap, we analyse the separate effects of hydroxylation on the HOMO and LUMO levels, revealing a nearly parallel downward shift in both energy levels due to LIDE. The absolute positions of these levels depend on the interplay between QC and hydroxylation, where the former raises electronic states due to spatial confinement, while the latter lowers them due to cumulative dipole effects from surface-bound hydroxyl groups. Our findings indicate that LIDE is not a simple linear function of hydroxyl coverage, as hydroxyl-hydroxyl hydrogen bonding interactions reduce the effective dipole moment, leading to a saturation effect at high hydroxylation levels. By leveraging the combination of QC and hydroxylation-driven LIDE, it is possible to fine-tune electronic energy levels in TiO_2 NPs, achieving a broad range of band edge alignments without requiring chemical doping or interfacing with other materials.

The implications for photocatalytic applications are substantial. The alignment of CBM and VBM relative to the water redox potentials is crucial for ensuring efficient electron and hole transfer in water splitting reactions. In highly quantum-confined NPs (e.g., $(TiO_2)_{35}$), the CBM is too high above the hydrogen evolution reaction (HER) potential, reducing the efficiency of electron transfer for H_2 production. Conversely, in larger, bulk-like structures, the CBM may lie too close to the HER potential, limiting the driving force for reaction kinetics. Hydroxylation counteracts these size effects, lowering both CBM and VBM and enabling better band alignment in mid-sized NPs (~2–3 nm, such as $(TiO_2)_{84}$). Our results indicate that an optimal degree of QC, combined with moderate hydroxylation (~50%), yields the best electronic alignment for photocatalytic water splitting. This strategy ensures that the CBM remains sufficiently high for hydrogen evolution while maintaining a low VBM for efficient hole oxidation.

Overall, this first part of the thesis provides a unified picture of how size, crystallinity, and hydroxylation influence the stability and electronic properties of TiO_2 NPs. We confirm that (i) the local structure and electronic properties of

amorphous and crystalline titania NPs converge with increasing hydroxylation, (ii) QC and hydroxylation-induced LIDE play key roles in electronic level tuning, and (iii) the combination of size-dependent QC effects and surface hydroxylation provides a highly versatile approach for engineering electronic properties in TiO_2 nanomaterials. These findings open the possibility of designing highly tunable amorphous crystalike NPs, which could serve as alternatives to crystalline anatase for photocatalysis and other optoelectronic applications. By strategically balancing QC effects and hydroxylation, it is possible to tailor TiO_2 NPs for specific electronic and photocatalytic performance criteria, providing a flexible, top-down approach for nanomaterial optimization.

3.4 Publications

Nanoscale

ROYAL SOCIETY OF CHEMISTRY

COMMUNICATION

View Article Online
View Journal

Check for updates

Cite this: DOI: 10.1039/d3nr00141e

Received 9th January 2023,
Accepted 2nd February 2023
DOI: 10.1039/d3nr00141e

rsc.li/nanoscale

Crystal properties without crystallinity? Influence of surface hydroxylation on the structure and properties of small TiO_2 nanoparticles†

Miguel Recio-Poo, [a] Ángel Morales-García, *[a] Francesc Illas [a] and Stefan T. Bromley *[a,b]

Titania (TiO_2) nanoparticles (NPs) are widely employed in applications that take advantage of their photochemical properties (*e.g.* pollutant degradation, photocatalysis). Here, we study the interrelation between crystallinity, surface hydroxylation and electronic structure in titania NPs with 1.4–2.3 nm diameters using all electron density functional theory-based calculations. We show how the distribution of local coordination environments of the atoms in thermally annealed quasi-spherical non-crystalline NPs converge to those in correspondingly sized faceted crystalline anatase NPs upon increasing hydroxylation. When highly hydroxylated, annealed NPs also possess electronic energy gaps with very similar energies and band edge orbital characters to those of the crystalline anatase NPs. We refer to the crystallite-mimicking non-crystalline annealed NPs as "crystalikes". Small stable crystalike NPs could allow for photochemical applications of titania in the size range where crystalline anatase NPs tend to become thermodynamically unfavoured (<3–5 nm). Our work implies the anatase crystal structure may not be as essential as previously assumed for TiO_2 NP applications and generally suggests that crystalikes could be possible in other nanomaterials.

Introduction

Over five decades have passed since the breakthrough discovery that the anatase crystal polymorph of titania (TiO_2) is able to split water into hydrogen and oxygen under ultraviolet light.[1] Since then, the anatase TiO_2 + water system has become a benchmark for studying the fundamental physiochemical principles underlying a range of photocatalytic processes[2,3] with relevance to numerous practical applications[4] (*e.g.* production of H_2 as green fuel,[5,6] polluted water remediation[7]). As an extended solid, titania is thermodynamically most stable in the rutile crystal phase, which shows a significantly lower photocatalytic activity than anatase. This polymorphic difference in performance has been discussed with respect to numerous possible factors but is often ascribed to the relative ease in which photo-generated excitons in anatase can reach the surface.[8] Experiments on thin films show that up to a thickness of about 2.5 nm the photoactivity of anatase and rutile are comparable, but that further thickness increase (up to 15 nm) only improves the performance of the anatase films.[9] This result demonstrates: (i) that the surface-accessible excitons in anatase can be formed further from the reactive surface than in rutile, and (ii) this difference only starts to be measurable for systems with surface-to-interior dimensions greater than 2.5 nm. In turn, this implies that the surface accessibility of excitons should not play a role in distinguishing the photoactivity of anatase and rutile nanoparticles (NPs) with diameters ≤5 nm. We note that titania NPs close to this size are often employed in photocatalytic experiments where the variation in observed photoactivity is thus most likely dependent on other factors. Herein, we study titania NPs within this size range (<2.5 nm diameters) and focus on two alternative properties of that are likely to significantly affect their photocatalytic performance: (1) surface hydroxyl (–OH) coverage and (2) crystallinity.

Nanoscale titania has a high surface to bulk ratio and possesses surface atoms with low coordination which readily react with water vapour under ambient conditions resulting in surface hydroxylation.[10] Recently, combined computational and experimental efforts have been used to identify types and locations of the hydroxyl groups on anatase NPs.[11] Generally, the degree of surface hydroxylation can vary depending on TiO_2 system size and the environment (*e.g.* humidity, temperature).[12] For many years it has been known that the density of

[a]*Departament de Ciència de Materials i Química Física & Institut de Química Teòrica i Computacional (IQTCUB), Universitat de Barcelona, c/Martí i Franquès 1-11, 08028 Barcelona, Spain. E-mail: angel.morales@ub.edu, s.bromley@ub.edu*
[b]*Institució Catalana de Recerca i Estudis Avançats (ICREA), Passeig Lluís Companys 23, 08010 Barcelona, Spain*

†Electronic supplementary information (ESI) available: MD-SA temperature profile, difference in proportion of Ti_{6c} centres and E_{gap} for crystalline and annealed NPs, comparison of the pair distribution function for Ti–O distances in highly hydroxylated crystalline and annealed NPs. See DOI: https://doi.org/10.1039/d3nr00141e

surface hydroxyls plays an important role in affecting the photoactivity of titania NPs.[13] This effect is linked to the exciton-induced conversion of surface hydroxyls to hydroxyl radicals (˙OH) which subsequently play a role in photocatalytic oxidation reactions.[3,14,15] The observation that hydroxylated anatase NPs generate more mobile OH species than rutile NPs has even been proposed as a key factor to explain the relatively higher activity of anatase NPs for many photooxidative reactions.[16] We note that surface hydroxyl groups can also facilitate the interaction of titania NPs with biosystems[17] where the photocatalytic production of hydroxyl radicals may lead to biotoxicity.[18]

Starting from the stable extended rutile crystal phase, decreasing the system size to the nanoscale decreases the relative thermodynamic stability of rutile with respect to anatase until a crossover is reached for titania NPs of approximately 14 nm diameter.[19] The exact size at which the more photoactive anatase crystal phase becomes the most stable in NPs is largely determined by surface contributions to the free energy,[20] and can thus be significantly affected by adsorbed species.[21,22] Generally, it is known that strongly bound water (*e.g.* surface hydroxyl groups) plays an essential role in determining the stability of TiO_2 NPs.[23] In the bare case, the anatase crystal phase persists in NPs down to a diameter ~2–3 nm, whereupon titania NPs are predicted to energetically favour non-crystalline structures due to the extended influence surface reconstruction from the high proportion of undercoordinated surface atoms.[24,25] In such small amorphous NPs for other materials, the effect of water strongly interacting with the surface has been shown to induce crystallinity by lowering the interfacial energy.[26] For TiO_2 NPs, water adsorption is more exothermic on rutile crystal surfaces than on anatase surfaces.[23] For small crystalline TiO_2 NPs it has been predicted that a high surface coverage of strongly bound water could make rutile NPs thermodynamically competitive with anatase NPs.[27]

For experimental studies on NPs, it is difficult to disentangle the intimate interrelation between the type and degree of crystallinity, the nature of their surfaces and their resulting physicochemical properties. Here we employ accurate and detailed computational models to understand how these interacting factors play out for two families of TiO_2 NPs (*i.e.*, crystalline faceted NPs and non-crystalline thermally annealed NPs). We focus on titania NPs with diameters ranging between 1.4–2.3 nm which is close to the non-crystalline/crystalline anatase crossover size for bare NPs.[24] The structure of NPs in this size regime is thus likely to be highly sensitive to surface adsorption. We consider both facetted crystalline anatase NPs, and thermally annealed NPs which can explore potentially lower energy non-crystalline structures. Simultaneously, we probe the effect of systematically increasing the degree of surface hydroxylation from the bare case to high –OH coverages for both types of NP. For the resulting two sets of NPs, we then compare the energetic, structural, and electronic properties. To enable a rigorous comparison, we employ the same NP size and degrees of hydroxylation for both NP types. The unique perspective provided by our controlled study allows us to discern numerous differences and similarities between crystalline and non-crystalline titania NPs with corresponding varying degrees of hydroxylation. For low and intermediate hydroxylation the two types of NP have distinct atomistic structures and electronic gaps which respond in different ways to varying hydroxylation. For higher degrees of hydroxylation, we find that the electronic energy gap of both types of NP converges to a very similar value. We also find that the distribution of local atomic coordination environments for both types of NPs become very similar at high hydroxyl coverages. However, this hydroxylation-induced electronic and local structural convergence does not appear to coincide with an increase in crystallinity in the thermally annealed NPs. Our results show that degree of surface hydroxylation can determine the electronic energy gap in nanotitania *via* induced modifications of local structural (*i.e.* coordination environments). At high –OH coverages, our results also suggest that this induced local structural effect leads to a convergence in the electronic structure, regardless of the degree of crystallinity of the NPs. This surprising result indicates that it may be possible to employ hydroxylation to induce electronic properties associated with crystalline anatase NPs in non-crystalline nanotitania.

Crystallite-mimicking non-crystalline NPs (or "crystalike" NPs) could have important implications for photochemical applications of small hydroxylated titania NPs. Synthesis of small crystalline anatase NPs is hampered by their low thermodynamic stability.[28] As crystallinity may no longer be a requirement to access the characteristic electronic structure of crystalline anatase NPs, small hydroxylated crystalike NPs may offer new opportunities for photochemical applications arising from: higher surface areas, higher energy excitons from quantum confinement (QC), lower radiationless photon transfer from quantization.[29] Overall, our study highlights the possibility of crystalike nanomaterials as a potential means to obtain the desirable properties of crystalline systems without the requirement of long-range crystalline order.

Models and computational methodology

Our study models the progressive and systematic hydroxylation of realistically structured model $(TiO_2)_{35}$ NPs. This size allows us to employ structurally stable crystalline reference NP models with a morphology and atomic ordering characteristic of larger anatase NPs, while also allowing for a computationally tractable study. We assume that hydroxylation occurs from the interaction of these initially anhydrous species with water molecules up to highly hydroxylated NPs with a $(TiO_2)_{35}(H_2O)_{25}$ chemical composition. We consider two types of NPs during this process: (i) crystalline anatase NPs with a faceted bipyramidal morphology, (ii) thermally annealed NPs with no fixed morphology (see Fig. 1).

As for all NPs, the properties of all our model NPs will be affected by the presence of undercoordinated atoms at their

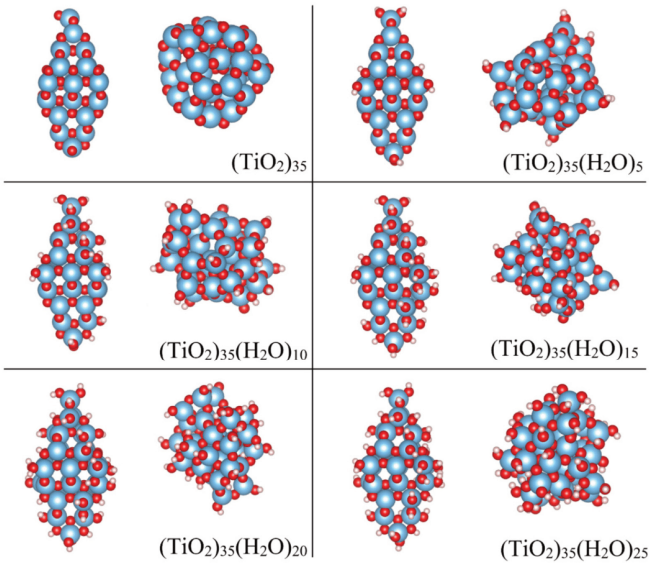

Fig. 1 DFT-optimized structures of the crystalline anatase (left) and annealed (right) $(TiO_2)_{35}(H_2O)_m$ NPs for m = 0, 5, 10, 15, 20, 25. Atom colour key: Ti – blue, O – red, H – white.

surfaces and by intrinsic QC. The effects of undercoordination are most pronounced for small anhydrous NPs which tend to energetically favour resconstructed non-crystalline structures.[24,25] Even for small faceted NPs cut from crystal structures, as used as model reference systems herein, surface relaxation can lead to a measurable decrease in the degree of atomic ordering.[30] However, hydroxylation tends to recover the bulk like coordination of surface atoms which reduces the tendency for structural reconstruction/relaxation. Thus, for increasing hydroxylation, the main size-related effect is likely to be a electronic energy gap increase (with respect to the bulk band gap) due to QC. As QC is primarily dependent on NP size, its effect is likely to result in an almost a constant electronic gap increase for all our considered NPs. We thus expect small, hydroxylated NPs to reflect most of the properties of larger hydroxylated NPs (*e.g.* bonding, structure, morphology) but with a somewhat larger electronic energy gap.

Crystalline anatase NP models

The initial anhydrous crystalline $(TiO_2)_{35}$ NP was derived from a top-down cut from the bulk anatase crystal structure following the Wulff construction, as described in previous works.[24,31,32] This procedure results in bipyramidal NPs which exhibit the thermodynamically stable (101) surface on all facets in line with experimental observations for larger anatase NPs.[33] From collaborative experimental and computational work, it is known that water molecules interact in a dissociative way with the surfaces of bipyramidal anatase NPs.[11] The resultant –H and –OH species are bound to O and Ti atoms, respectively where the energetic stability of hydroxylation depends on the coordination environment of the surface atoms (*i.e.* apical > equatorial > edge > facet).[11,27] Here we followed this energetically-determined order to progressively hydroxylate the initial faceted anatase $(TiO_2)_{35}$ NP and produce a set of crystalline anatase NPs with the composition $(TiO_2)_{35}(H_2O)_m$ with m = 0–25 (see selected NPs in Fig. 1).

Initial crystalline NP structures were pre-optimised using the NanoTiO interatomic potential (IP) which has been shown to accurately describe the structures and relative energetics of nano-titania systems with high computational efficiency.[12,31,32] The final DFT-optimised anatase NPs have maximum diameters ranging between 2.1–2.3 nm depending on the degree of hydroxylation. These optimisations lead to local energy minima NP structures in which the internal crystalline structure of the NP is largely unperturbed. We note that these anatase NPs are used only as size-appropriate reference systems to assess how crystalline the more stable thermally

annealed NPs (described below) are with respect to their calculated structural and electronic properties.

Thermally annealed NP models

To compare with the hydroxylation of an anhydrous faceted crystalline NP, we also started from a non-crystalline anhydrous $(TiO_2)_{35}$ NP. This initial NP was generated by using a molecular dynamics (MD) based method to thermally anneal the internal structure and morphology of a spherical cut $(TiO_2)_{35}$ NP from the anatase crystal structure (see details below). In previous work we have shown that thermally annealed anhydrous NPs of this size lose their internal crystalline atomic ordering and also adopt quasi-spherical morphologies.[31,32] The purpose of the thermal annealing is to search for low energy NP structures. Indeed, bare annealed $(TiO_2)_{35}$ NPs are significantly more energetically stable than bare faceted crystalline anatase NPs of the same size.[24,31] To an initially bare annealed NP structure, we first added a dissociated water molecule by binding one H and one –OH species to low coordinated surface O and Ti atoms, respectively. The interaction of NPs with water can strongly affect surface energies and overall NP stability[21,22] and even induce internal crystallisation.[26] As such, for every step of hydroxylation by a single water the NP was again thermally annealed to search for low energy $(TiO_2)_{35}(H_2O)_m$ NP structures with m = 1–25, generally leading to significant changes in all atomic positions and the NP morphology. This implies that every NP in the series of progressively hydroxylated thermally annealed NPs is structurally independent of each other, unlike in the case of the crystalline anatase NPs. In other words, the structural framework of the annealed NPs changes as hydroxylation increases due to the thermal annealing process, whereas it is relatively unaltered in the (non-annealed) locally optimised crystalline faceted counterparts. The final DFT-optimised thermally annealed NPs have maximum diameters ranging between 1.4–1.8 nm depending on the degree of hydroxylation. Structures of selected annealed NPs are shown in Fig. 1.

MD-based thermal annealing

Global optimisation searches have been previously employed to search for the lowest energy structure (global minimum) for relatively small, hydroxylated NPs.[12,34,35] As NPs get larger and more chemically complex the corresponding energy landscapes tend to have a very rapidly increasing number of low energy minima. In such cases, the global minimum structure is likely to be one of many characteristic low energy minima inhabited by the system. For our chemically complex $(TiO_2)_{35}(H_2O)_m$ systems with three atom types and up to 180 atoms we use a physically motivated simulated annealing (SA)[36] approach to guide us to characteristic low energy structures. Generally, SA involves controlled cycles of heating and cooling to guide the system into regions of energetic stability. Here, we use classical MD in the canonical NVT ensemble to control the temperature of our NPs. Specifically, we use MD runs starting at 300 K with an equilibration of 600 ps. The temperature is then increased gradually for 3500 ps with a step of 0.5 K ps^{-1}, thus reaching ~1750 K. This latter temperature is then maintained for 800 ps, after which the system is then cooled down by 300 K over a period of 1250 ps and, again, maintained for 800 ps. This stepwise cooling process is repeated till the initial temperature of 300 K is reached again, in which the system remains for the final 8000 ps. Five $(TiO_2)_{35}(H_2O)_m$ structures were selected from each MD-SA run for each NP composition (*i.e.* degree of hydroxylation) for further DFT-based refinement (see below). Fig. S1 in the ESI† illustrates the stepwise MD-SA procedure.

The interactions between atoms in the NPs during the MD-SA calculations were modelling using the NanoTiO IP.[12,31,32] We note that the internal structure of the NP (including the locations and interactions between –OH groups) and its overall morphology can freely adapt to the degree of hydroxylation during our MD-SA runs while exploring progressively lower energy states. The General Utility Lattice Program (GULP)[37] was used for all IP-based MD-SA calculations. Classical MD simulations have also been employed in other work for studying how the size of spherically cut crystalline anatase NPs affects their surface reactive response to water solvation.[38] In this latter study the anatase crystalline structure and spherical morphology of the studied NPs was relatively unperturbed and the degree of hydroxylation was determined by the solvation. In contrast, thermally annealing *via* a MD-SA approach allows us to search for low energy NP structures in a much more extensive and unbiased manner, helping us to avoid higher energy parts of the potential energy landscape. In this way, we can follow the interplay of NP crystallinity/morphology and hydroxylation by systematically comparing and varying both aspects.

DFT calculations

To obtain the electronic structure for all $(TiO_2)_{35}(H_2O)_m$ compositions the selected low energy annealed NPs and all faceted NPs were further optimised using relativistic all-electron DFT-based calculations as implemented in the FHI-aims code.[39] Structural optimisations were performed using Perdew–Burke–Ernzerhof (PBE) exchange–correlation functional[40] and electronic energy gaps were calculated using a hybrid PBEx (12.5% Fock exchange) which has been tailored to well reproduce the electronic structure of various titania systems.[41,42] All calculations employed a light tier-1 numerical atom-centred orbital basis set, which has an accuracy comparable to a TZVP Gaussian-type orbital basis set for TiO_2.[43] The convergence thresholds for atomic forces and total energy during the relaxation of the structure of the NPs were set to 10^{-5} eV $Å^{-1}$ and 10^{-6} eV, respectively. Relativistic effects were included using the zero order regular approximation.[44]

Results and discussion

Below, we report the calculated energetic, structural and electronic properties of our $(TiO_2)_{35}(H_2O)_m$ NPs. In particular, we compare how these characteristics are affected by the degree of

hydroxylation and by the underlying crystallinity of the respective NP.

NP energetics with respect to hydroxylation

As our two types of NP have the same range of compositions, we can directly compare their respective energetic stabilities for all degrees of hydroxylation. In Fig. 2 we show how the difference in total energy between faceted and annealed $(TiO_2)_{35}(H_2O)_m$ NPs ($\Delta E_{tot}(m) = E_{tot\text{-}anneal}(m) - E_{tot\text{-}cryst}(m)$) varies with m. The plot shows that ΔE_{tot} is always negative, showing that annealed $(TiO_2)_{35}(H_2O)_m$ NPs are more energetically stable than crystalline faceted NPs for the full range of hydroxylation considered. The largest magnitude of ΔE_{tot} occurs for the anhydrous case. This observation is in line with previous work, where we show that for small NP sizes anhydrous non-crystalline NPs are energetically more favourable than faceted crystalline NPs.[24,31] Upon increasing hydroxylation, the magnitude of ΔE_{tot} remains fairly constant and high ($|\Delta E_{tot}|$ = 7.5 ± 1.4 eV) for $m \leq 10$. When increasing hydroxylation beyond this point in the range $11 \leq m \leq 17$, the annealed NPs are progressively destabilized with respect to the faceted anatase NPs by approximately 5 eV. For the highest considered hydroxylations ($17 < m \leq 25$) the magnitude of ΔE_{tot} is relatively low and again fairly constant ($|\Delta E_{tot}|$ = 2.0 ± 1.1 eV). We note that this energy difference translates to 0.06 ± 0.03 eV per TiO_2 unit, which is comparable to typical energy differences between crystalline bulk titania polymorphs.[45] The convergence of the energetic stability of faceted anatase NPs and thermally annealed NPs with increasing m suggests that hydroxylation could be inducing a structural homogenisation.

It is important to note that this stability convergence is rather asymmetric with respect to crystallinity. The faceted crystalline NPs are used as a reference system in which the degree of crystallinity is relatively fixed. Increasing hydroxylation only acts to reduce the undercoordination of the surface atoms of these NPs, which, in a sense, only increases the crystallinity. In fact, for their size, our crystalline NPs can be taken as maximally crystalline reference NPs for their size.[24,31] In contrast, the annealed NPs are free to adopt a new energy-lowering structure and morphology for each degree of hydroxylation. As such any convergence of properties in the two NP types implies that the annealed NPs are becoming more like the reference crystalline NPs rather than the other way around.

To follow the induced energetic changes due to gradually increasing the degree of hydroxylation for each of our two types of $(TiO_2)_{35}(H_2O)_m$ NP, we use two quantities:

(1) the total hydration energy:

$$E_{hyd}(m) = E_{tot}(m) - (E_{tot}(0) + m \cdot E_{H_2O})$$

and

(2) the incremental hydration energy:

$$\Delta E_{hyd}(m) = E_{tot}(m) - (E_{tot}(m-1) + E_{H_2O})$$

where $E_{tot}(m)$ is the total energy of a NP with m dissociatively adsorbed water molecules and E_{H_2O} is the total energy of a water molecule. As such, $E_{tot}(0)$ is the total energy of a bare titania NP. In Fig. 3 the plot of $E_{hyd}(m)$ *versus* m shows a tendency to become progressively more negative for both NP types with increasing hydroxylation. Here, we use a common reference $E_{tot}(0)$ value for the bare crystalline NP in both curves. Overall, the $E_{hyd}(m)$ plot shows that dissociative reaction with water molecules is energetically stabilising for all –OH coverages considered for both crystalline and annealed NPs. We note that the stabilising effect of water addition is slightly less effective for the annealed NPs than for the crystalline NPs for higher degrees of hydroxylation. This tendency is in line with the energetics of hydroxylation for smaller globally optimised titania nanoclusters.[12]

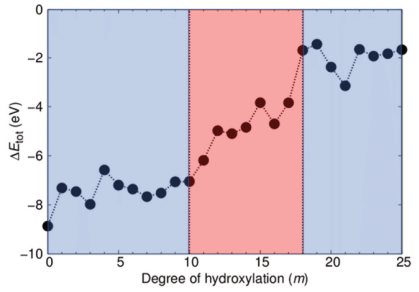

Fig. 2 Total energy difference (ΔE_{tot}) between the faceted and annealed $(TiO_2)_{35}(H_2O)_m$ NPs with respect to degree of hydroxylation induced by the number of dissociatively adsorbed water molecules (m). The coloured regions indicate two regions of relatively constant energetic stability (blue) and a transitional region (light red).

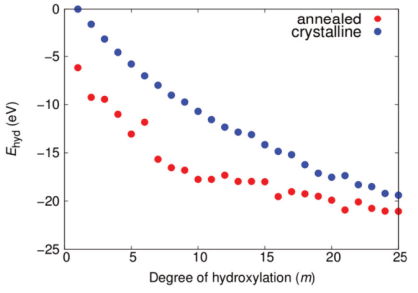

Fig. 3 Variation of $E_{hyd}(m)$ with the number of water molecules (m) for increasingly hydroxylated crystalline and annealed $(TiO_2)_{35}(H_2O)_m$ NPs. The $E_{tot}(0)$ reference energy is taken to be that of the anhydrous crystalline NP in both cases leading to a corresponding energetic stabilisation downshift in the data for the annealed NPs.

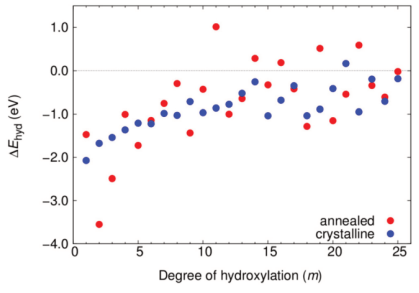

Fig. 4 Variation of $\Delta E_{hyd}(m)$ with the number of water molecules (m) for increasingly hydroxylated crystalline (blue) and annealed (red) $(TiO_2)_{35}(H_2O)_m$ NPs.

In Fig. 4 we show the evolution of $\Delta E_{hyd}(m)$ with respect to the degree of hydroxylation for both NP types. Here, the $E_{tot}(0)$ value in each case is taken to be that of the corresponding NP type. For the crystalline NPs with their structurally persistent anatase NP core, the resulting series of energies indicates how the dissociative reaction energy of adding each successive H_2O water molecule varies with –OH coverage. Here, we see that our chosen sequence of anatase NP hydration, depending on increasing surface coordination of adsorption sites (*i.e.* apical > equatorial > edge > facet), results in nearly every individual H_2O addition reaction being exothermic. Only for m = 21 do we see a small endothermic adsorption energy for incremental hydroxylation. This is likely to be simply due to the specific adsorption sequence chosen, of which there are a huge number, and does not imply that there is anything unusual for this degree of hydroxylation. Overall, the magnitude of $\Delta E_{hyd}(m)$ is highest for the lowest hydroxylation (approx. −2.0 eV) and then steadily decreases until about m = 14. This reflects the progressive adsorption of surface sites with increasing coordination. For the highest hydroxylation, $\Delta E_{hyd}(m)$ fluctuates around a value of about −0.5 eV.

For the annealed NPs, $\Delta E_{hyd}(m)$ is not open to such a simple interpretation (*i.e.* sequential H_2O adsorption reaction energy) as for the crystalline anatase NPs. For each degree of hydroxylation, each annealed NP is produced from a new MD-based stochastic search and all such NPs are thus structurally independent from each other. Going from m to m + 1, for example, typically involves a change in the both underlying $(TiO_2)_{35}$ NP structure and the locations of the m –OH groups. In general, the trend of $\Delta E_{hyd}(m)$ for the annealed NPs with increasing m, is quite similar to that for the anatase NP, but with significantly larger fluctuations. These large changes in $\Delta E_{hyd}(m)$ for small changes in m reflects the corresponding larger structural changes for the annealed NPs. The positive values of $\Delta E_{hyd}(m)$ for some values of m could indicate the difficulty of finding low energy NPs for these degrees of hydroxylation using our MD-SA approach. We note that these positive incremental changes do not affect the fact that the corresponding degrees of hydroxylation are energetically stabilising overall, as shown in Fig. 3. Such behaviour could indicate that energetically costly changes in NP structure are necessary to dissociatively adsorb water in the most energetically favourable way with increasing hydroxylation. Below we analyse the change in NP structure with increasing hydroxylation.

Structure of hydroxylated $(TiO_2)_{35}$ NPs

To compare the local structure of each type of NP throughout the considered hydroxylation range we follow the change in the local bonding coordination of Ti atoms. To do so we count the number of O atoms around each Ti centre in each NP within a maximum Ti–O cut-off distance of 2.4 Å. Summing the coordination values of each Ti centre within a given NP and then dividing by the total number of Ti centres gives the average coordination number (ACN). Fig. 5 shows the variation in the ACN for crystalline anatase NPs and thermally annealed NPs with respect to hydroxylation, and the respective difference in ACN between both NP types (ΔACN). We note that the ACN values for the annealed NPs for each degree of hydroxylation are averaged from values obtained for the five low energy NPs from the respective thermal annealing run.

For the crystalline anatase NPs, the ACN tends to steadily increase with increasing hydroxylation from 4.8 for the bare case to 5.6 for the highest hydroxylation considered. This increasing tendency is due to new Ti–OH bonds being formed the surface. The small observed fluctuations in the ACN are the result of surface relaxation upon hydroxylation which can sometimes lead to a localised reduction in Ti coordination. In the case of the annealed NPs, the bare NP has a relatively lower ACN value of 4.65. Unlike for the anatase NPs, increasing

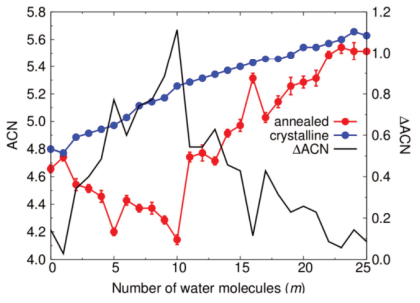

Fig. 5 Average coordination number (ACN) of Ti centres for the annealed and crystalline anatase NPs with respect to hydroxylation (left hand axis). The "error bars" for the annealed NP data indicate the maximum and minimum ACN values found in a sample of five low energy NPs from each respective annealing run. The black line follows the difference between the ACN values of the annealed and crystalline NPs (ΔACN) with respect to m (right hand axis).

the degree of hydroxylation of the annealed NPs from this point initially tends decrease the ACN until a minimum of about 4.15 is reached at m = 10. Afterwards, for $m \geq 11$, the ACN tends to increase and approach the ACN of the respective hydroxylated anatase NPs. This rate of ACN increase with respect to m is fastest in the range $11 \leq m \leq 17$. This range of hydroxylation coincides with that in which rapid energetic destabilisation of the annealed NPs occurs with respect to the anatase crystalline NPs (see Fig. 2). In the range $17 < m \leq 25$, the ACN values are very similar for both annealed and crystalline NPs. This is also the hydroxylation regime for which the energetic stabilities of annealed and crystalline NPs are found to be most similar (see Fig. 2). The correspondence between the hydroxylation dependence of both ACN and ΔE_{tot} values suggests that annealed NPs become structurally more anatase-like with increasing hydroxylation.

To better understand the m-dependent ACN trends and differences we follow a more detailed analysis whereby we breakdown the ACN values into contributing proportions of 4-, 5-, and 6-coordinated Ti atoms (denoted as Ti_{4c}, Ti_{5c}, and Ti_{6c}). Fig. 6 (left) displays the evolution of the proportion of Ti_{4c}, Ti_{5c}, and Ti_{6c} centres with respect to hydroxylation. Starting with the Ti_{6c} centres, we see that they follow a very similar m-dependence for both annealed and crystalline anatase NPs. In the hydroxylation range $0 \leq m \leq 6$ for both NP types, Ti_{6c} centres make up 15–20% of the total number of Ti centres. In the anatase NP, for $m > 6$ the number of these centres increases at steady rate with further hydroxylation until they constitute ~65% of the total number of Ti centres for m = 25. For this progressively OH-covered crystalline NP this two-stage m-dependence can be understood by: (i) the initial energetic preference to hydroxylate low coordinated Ti_{4c} centres for small m (reducing the number of Ti_{4c} centres and increasing the number of Ti_{5c} centres), and (ii) after the exhaustion of Ti_{4c} centres, the gradual hydroxylation of Ti_{5c} centres for larger m producing Ti_{6c} centres. This explanation is corroborated by following the corresponding tendencies in the proportions of Ti_{4c}, Ti_{5c} and Ti_{6c} centres in the anatase NPs in Fig. 6 (left).

For the annealed NPs, after initially possessing a similarly constant proportion of Ti_{6c} centres as for the anatase NPs for low hydroxylation, this value then drops to 0% going from m = 7–10. Thereafter, for m = 11–25, the proportion of Ti_{6c} centres progressively increases in a very similar way as for the crystalline anatase NPs towards a maximum of ~60% at the highest hydroxylation. In this later range of hydroxylation the proportions of Ti_{4c} and Ti_{5c} centres in the annealed NPs also gradually approach those found in the anatase NPs in line with the corresponding change in ACN. Although we see a convergence for the ACN and its individual components for both types of NP we find no evidence of significant increases in crystallinity or faceting in the annealed NPs with increasing hydroxylation. In the case of highest hydroxylation, we extract

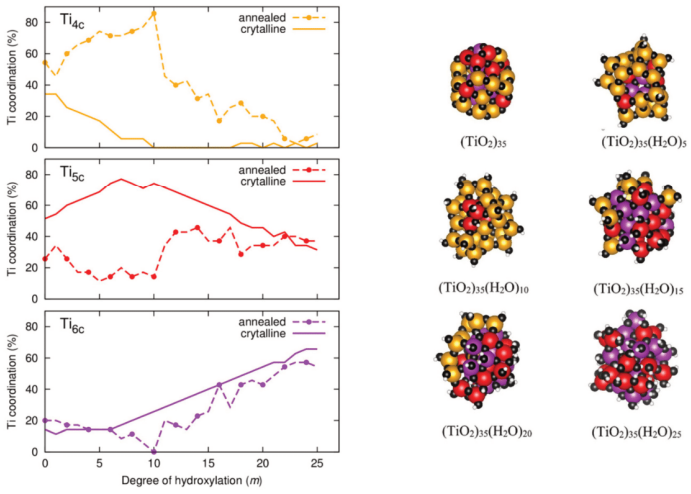

Fig. 6 Left: Evolution of the distribution of 4-, 5- and 6-fold local atomic coordination environments of Ti centres (Ti_{4c}, Ti_{5c}, and Ti_{6c}) with respect to the degree of hydroxylation (m) of both crystalline and annealed $(TiO_2)_{35}$ NPs. Right: location of Ti_{4c}, Ti_{5c}, and Ti_{6c} centres depicted by dark yellow, red, and purple spheres respectively in the thermally annealed NPs for m = 0, 5, 10, 15, 20 and 25.

the pair distribution function for Ti–O distances for each type of NP (see Fig. S2 in the ESI†) to provide an approximate measure of crystallinity.[24,25] This shows that the local Ti–O distance distribution is similarly sharp in both types of highly hydroxylated NPs, but for larger Ti–O distances the distributions are broader for the annealed NPs, indicating less longer range order (*i.e.* lower crystallinity). Generally, the highly hydroxylated annealed NPs tend to structurally mimic the highly hydroxylated anatase NPs on a local scale, but both have distinct overall NP structures and morphologies.

For the initial stages of hydroxylation from m = 0–10, where we see distinct tendencies in the ACN for both NP types, the proportions of Ti_{4c} and Ti_{5c} centres are correspondingly also very different. Overall, the proportion of Ti_{5c} centres in the annealed NPs is fairly constant and relatively low (approx. 10–30%) in this initial range of hydroxylation low. This is in contrast to the corresponding high and increasing proportions of Ti_{5c} centres in the crystalline anatase NPs. In the same hydroxylation range, we also find a high (approx. 50–90%) and increasing proportion of Ti_{4c} centres. Considering that the m = 0–10 range is where the annealed NPs are most energetically stable with respect to the anatase NPs, it thus appears that Ti_{4c} centres are helping to stabilise the annealed NPs for low/moderate hydroxylation. NPs have a high proportion of surface atoms and, as noted above, their energetic stability is highly sensitive to changes in surface stress.[20,21] Ti_{4c} centres have a tetrahedral structure which tend to lead to more open lower density networks with respect to the octahedral Ti_{6c} centres. We suggest that the density-lowering effect of Ti_{4c} centres helps to lower the surface stress in the annealed NPs. Inspecting the structure of a low energy annealed $(TiO_2)_{35}(H_2O)_{10}$ NP, we indeed see that the Ti_{4c} centres are associated with surface hydroxyls (*i.e.* ≡Ti–OH), see Fig. 6 (right). With the increasing number of oxygen atoms in the system due to hydroxylation it appears that the stabilising effect of these surface Ti_{4c} species reaches a limit at around m = 10. After this degree of hydroxylation, we see is a sudden significant decrease in the proportion of surface Ti_{4c} centres (see Fig. 6). We note that Ti_{4c} species have also been found near the surface of relatively large anhydrous TiO_2 NPs after simulated annealing. Here, the centres were not hydroxylated, and their main observed effect was to reduce the band gap of the NP.[31] Below, we examine the effect of hydroxylation and the associated structural changes on the electronic structure of both annealed and crystalline NPs.

Electronic structure of hydroxylated $(TiO_2)_{35}$ NPs

In Fig. 7 we show the evolution of the electronic energy gap (E_{gap}), as estimated by the difference in the highest occupied and lowest unoccupied orbital energies, of both annealed and crystalline NPs with respect to hydroxylation. A hybrid density functional that contains 12.5% Fock exchange and which accurately reproduces the band gap of stoichiometric and reduced anatase and rutile bulk crystals[41] was used to calculate the electronic structure. We note that the E_{gap} in both systems is higher than that for the bulk anatase phase due to the effect of

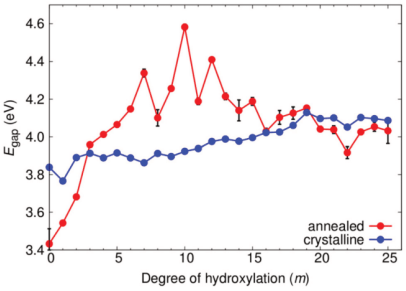

Fig. 7 Evolution of E_{gap} with respect to degree of hydroxylation for crystalline and annealed $(TiO_2)_{35}(H_2O)_m$ NPs. For the annealed NPs, the data points indicate a mean value of E_{gap} from considering five low energy NPs. The "error bars" indicate the range of E_{gap} values for five low energy NPs from the respective MD-SA run.

QC in our small NPs.[43,46] From previous work on smaller titania nanoclusters, it is expected that increasing hydroxylation would tend to only slightly and gradually increase the magnitude of E_{gap}.[12] This tendency is in line with the overall effect of hydroxylation to stabilise low coordinated surface sites. For the crystalline anatase NPs we indeed see this type of behaviour, whereby increasing hydroxylation from the anhydrous state to the highest hydroxylation tends to progressively raise the E_{gap} value by ~0.25 eV from 3.84 eV to 4.11 eV. However, for the annealed NPs we observe a stark contrast in the hydroxylation dependent E_{gap} behaviour. Initially, the anhydrous annealed NP has a E_{gap} of 3.45 eV, which is ~0.4 eV lower than that of the corresponding anatase NP. With increasing hydroxylation up to m = 10 the value of E_{gap} rises by 1 eV to a maximum of 4.6 eV. Thereafter, for further increases in m, the value of E_{gap} falls towards that of the highly hydroxylated anatase NPs. We note that in the region $7 \leq m \leq 13$ the E_{gap} value exhibits its largest fluctuations (4.3 ± 0.3 eV). This hydroxylation range overlaps with that at which the ACN and local coordination environments (see Fig. 5 and 6) show their largest change with respect to hydroxylation. These competing structural variations in the annealed NPs in this transitional hydroxylation range will significantly affect the electronic structure and are thus the likely reason for the observed larger fluctuations in E_{gap}. In contrast, for the highest degrees of hydroxylation considered the E_{gap} values for the crystalline anatase and annealed NPs are relatively stable and almost identical. In this converged E_{gap} value range for $m \geq 19$ the electronically perturbing effects of low-coordinated surface sites is minimal and we can assume that the E_{gap} value of ~4.05 eV (*i.e.* +0.85 eV with respect to the bulk anatase band gap) is mainly influenced by QC.

To help understand the overall E_{gap} trends we have extracted the projected density of states (pDOS) with respect to the coordination of the atoms making up the NPs (see Fig. 8

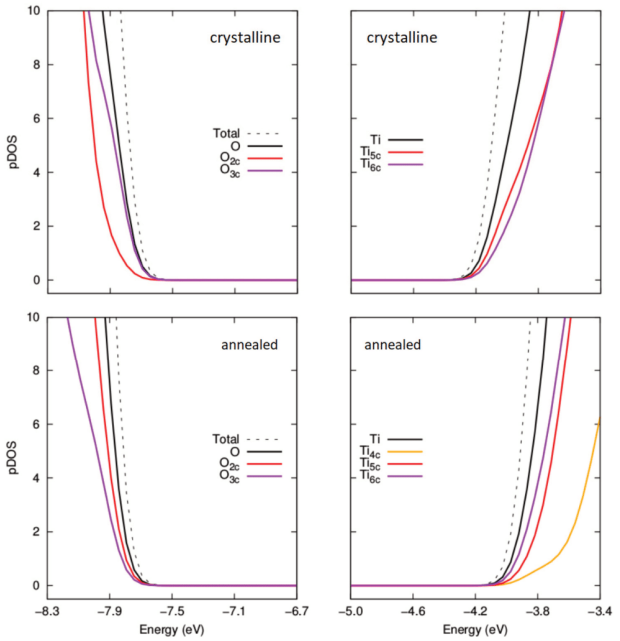

Fig. 8 Comparison of projected density of states (pDOS) for the VBM and CBM for crystalline anatase NPs (upper) and thermally annealed NPs (lower) with composition $(TiO_2)_{35}(H_2O)_{11}$.

and 9). Generally, in bulk titania the valence band maximum (VBM) is dominated by contributions from O centres, while the conduction band minimum (CBM) is dominated by contributions from Ti centres. Although reference to electronic bands is only strictly valid for extended systems, for convenience we also use VBM and CBM when describing the electronic structure of our NPs below. For anhydrous NPs and very low degrees of hydroxylation the relatively smaller E_{gap} values found for the annealed NPs is due to surface 2-coordinated oxygen (O_{2c}) 2p contributions to the VBM, as found in previous work on anhydrous NPs.[30] For increasing hydroxylation of the surface of the annealed NPs this O_{2c}-induced E_{gap} decrease is rapidly quenched.

In Fig. 8, we compare the pDOS for both types of NP for m = 11, where the E_{gap} value for the annealed NP is larger than the corresponding anatase NP. Here we see that both NPs have a VBM with main contributions from O_{2c} and O_{3c} centres and a CBM made up from contributions from Ti_{5c} and Ti_{6c} centres. The Ti_{4c} centres in the annealed NP contribute to the pDOS only at higher energies. We note that the anatase NP for m = 11 has no Ti_{4c} centres. The VBM in both these cases is found at a similar energy. However, the CBM for the crystalline anatase NP is found at a lower energy than in the annealed NP indicating an electronic destabilisation of the Ti 3d states in its Ti_{5c} and Ti_{6c} centres. This destabilisation could be due to the relatively high proportion of Ti_{4c} centres which tend to disrupt higher density structures made from highly co-ordinated centres. The relative difference in the energy of the CBM seems to be the main contributing factor for the observed difference in the E_{gap} value for annealed and crystalline anatase NPs at this degree of hydroxylation. We note that this link between E_{gap} differences and the stability of Ti 3d states in Ti_{5c}/Ti_{6c} centres seems to be reflected in the difference in the proportion of Ti_{6c} centres in each type of NP (see Fig. S3 in the ESI†).

In Fig. 9 we show the pDOS for both types of NP for m = 20. Here, it seems that the unoccupied 3d states associated with the increasing number of Ti_{5c} and Ti_{6c} centres contributing to the CBM tend to become energetically similar in both types of NP with increasing m. In fact, we now see that both the charac-

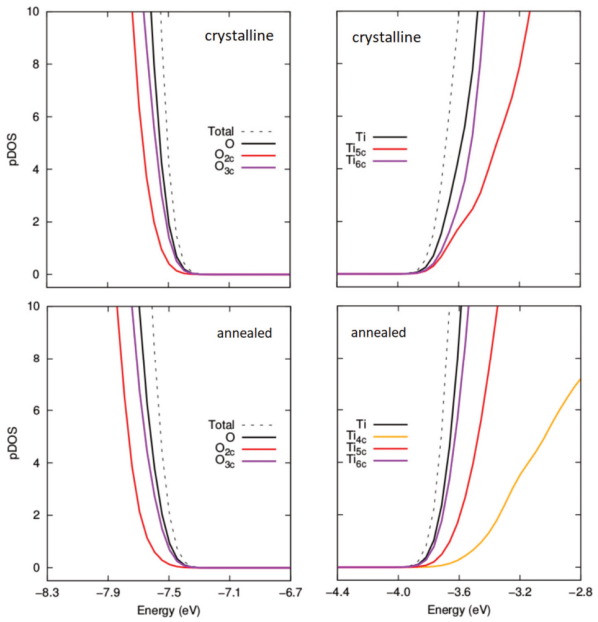

Fig. 9 Comparison of projected density of states (pDOS) for the VBM and CBM for crystalline anatase NPs (upper) and thermally annealed NPs (lower) with composition $(TiO_2)_{35}(H_2O)_{20}$.

ter and energies of the VBM and CBM are very similar for both annealed and anatase NPs. For higher degrees of hydroxylation, the convergence in E_{gap} values between annealed and crystalline NPs is also found to follow a convergence of the VBM and CBM. This implies that annealed and crystalline NPs should become electronically very similar with higher degrees of hydroxylation, in spite of the evident differences in atomic structure.

In summary, the above results show that the gap/edge electronic structure of small hydroxylated anatase NPs can be accurately mimicked by NPs of the same chemical composition and the same distribution of local atomic coordination environments but with a different overall (non-crystalline) structure and morphology. In particular, such crystalike NPs could be electronically indistinguishable from anatase NPs. Considering that surface accessibility of photogenerated excitons is unlikely to vary significantly in small NPs (*i.e.* $\lesssim$5 nm diameter),[9] it would be interesting to examine photoactivity of crystalike NPs with respect to that of small hydroxylated anatase NPs. Generally, smaller NPs offer potential photochemical performance improvements over larger NPs due to their higher surface areas, higher energy photo-generated carriers due to QC and lower radiationless photon transfer due to increased quantization of electronic levels.[29] However, the anatase-like electronic structure of small crystalike NPs does not necessarily imply a corresponding anatase-like photoactivity as there could be differences in the nature of the photoactivated reactions at crystalike and anatase NP surfaces. Nevertheless, our results suggest that, as far as small unsupported and undoped titania NPs are concerned, the anatase crystal structure may not be as important as previously thought for achieving an electronic structure that could be favourable for NP-based photocatalytic applications. The highly sensitive response of such crystalike NPs to hydroxylation could also offer more tunability with respect to crystalline titania NP applications.

Conclusions

We have employed DFT-based calculations to analyse and compare the effect of hydroxylation by dissociative water

addition on the on the properties of thermally annealed and crystalline $(TiO_2)_{35}$ NPs with diameters between 1.4–2.3 nm. In both cases the hydroxylation is energetically favourable for $(TiO_2)_{35}(H_2O)_m$ NPs up to the considered upper limit with m = 25. For lower values of m in this range, the thermally annealed NPs are significantly more energetically stable than the crystalline NPs. With increasing m there is a rapid convergence in the stability of both types of NP resulting in annealed and crystalline NPs having comparable energetic stabilities for high hydroxylation. This hydroxylation-induced convergence in stability in not reflected in a convergence of NP morphology or crystallinity. However, for high hydroxylation both quasi-spherical non-crystalline NPs and faceted crystalline anatase NPs are found to converge with respect to their local structure. Specifically, the distributions of local atom coordination environments are found to become almost the same in both types of NP for high hydroxylation. This local structural similarity for high hydroxylation is found to also be accompanied with a convergence in the electronic properties of both NP types. Here, we find that both the magnitude of the electronic energy gap and the energies and orbital character of the band edges become almost the same in both types of highly hydroxylated NP.

Overall, we show that, for small NPs, one can use hydroxylation to induce the characteristic electronic structure of faceted crystalline NPs in compositionally equivalent but non-faceted non-crystalline NPs (*i.e.* crystalike NPs). The key to this effect is the surface-induced change in the distribution of local atom coordination environments throughout the annealed hydroxylated crystalike NP structures. Our study thus suggests that the anatase crystal structure may not be as essential as previously assumed for obtaining an electronic structure that could be favourable for NP-based photocatalytic applications. In turn, this opens the possibility to employ highly tunable crystalike NPs in a size range where obtaining anatase crystalline samples becomes thermodynamically disfavoured (*i.e.* diameters <3–5 nm). As the realisation of crystalike NPs in titania appears to rely only on mimicking the local coordination environment distribution of a correspondingly crystalline NP, we speculate that it may also be possible to form crystalike NPs of other materials.

Conflicts of interest

There are no conflicts to declare.

Acknowledgements

We acknowledge financial support from MCIN/AEI/10.13039/501100011033 through projects PID2020-115293RJ-I00, PID2021-126076NB-I00, TED2021-129506B-C22, TED2021-132550B-C21 and the María de Maeztu CEX2021-001202-M projects; the fund from FEDER Una manera de hacer Europa also supports the former project. The reported research is involved in the COST Action CA18234 (CompNanoEnergy), supported by European Cooperation in Science and Technology (COST). S. T. B. acknowledge support from grant 2021SGR00354 funded by the Generalitat de Catalunya. M. R.-P. acknowledges the Ministerio de Ciencia e Innovación for a Formación Personal Investigador (FPI) fellowship (PRE2019-087627). We also acknowledge the Red Espanola de Supercomputación (RES) for the provision of supercomputing time.

References

1 A. Fujishima and K. Honda, *Nature*, 1972, **238**, 37–38.
2 J. Schneider, M. Matsuoka, M. Takeuchi, J. Zhang, Y. Horiuchi, M. Anpo and D. W. Bahnemann, *Chem. Rev.*, 2014, **114**, 9919–9986.
3 A. Fujishima, X. Zhang and D. A. Tryk, *Surf. Sci. Rep.*, 2008, **63**, 515–582.
4 X. Chen and S. S. Mao, *Chem. Rev.*, 2007, **107**, 2891–2959.
5 A. Kudo and Y. Miseki, *Chem. Soc. Rev.*, 2009, **38**, 253–278.
6 H. Idriss, *Curr. Opin. Chem. Eng.*, 2020, **29**, 74–82.
7 J. Ryu and W. Choi, *Environ. Sci. Technol.*, 2008, **42**, 294–300.
8 B. Samanta, Á. Morales-García, F. Illas, N. Goga, J. A. Anta, S. Calero, A. Bieberle-Hütter, F. Libisch, A. B. Muñoz-García, M. Pavone and M. C. Toroker, *Chem. Soc. Rev.*, 2022, **51**, 3794–3818.
9 T. Luttrell, S. Halpegamage, J. Tao, A. Kramer, E. Sutter and M. Batzill, *Sci. Rep.*, 2014, **4**, 4043.
10 C. Deiana, E. Fois, S. Coluccia and G. Martra, *J. Phys. Chem.*, 2010, **114**, 21531–21538.
11 L. Mino, Á. Morales-García, S. T. Bromley and F. Illas, *Nanoscale*, 2021, **13**, 6577–6585.
12 A. Cuko, A. M. Escatllar, M. Calatayud and S. T. Bromley, *Nanoscale*, 2018, **10**, 21518–21532.
13 K. Kobayakawa, Y. Nakazawa, M. Ikeda, Y. Sato and A. Fujishima, *Ber. Bilnsenges. Phys. Chern.*, 1990, **94**, 1439–1443.
14 A. Di Paola, M. Bellardita, L. Palmisanoa, Z. Barbierikovác and V. Brezovác, *J. Photochem. Photobiol., A*, 2014, **273**, 59–67.
15 J. Wang, X. Liu, R. Li, P. Qiao, L. Xiao and J. Fan, *Catal. Commun.*, 2012, **19**, 96–99.
16 W. Kim, T. Tachikawa, G.-H. Moon, T. Majima and W. Choi, *Angew. Chem., Int. Ed.*, 2014, **53**, 14036–14041.
17 M. J. Limo, A. Sola-Rababa, E. Boix, V. Thota, Z. C. Westcott, V. Puddu and C. C. Perry, *Chem. Rev.*, 2018, **118**, 11118–11193.
18 Y. Tanga, R. Caia, D. Caob, X. Konga and Y. Luc, *Toxicology*, 2018, **406–407**, 1–8.
19 H. Zhang and J. F. Banfield, *Chem. Rev.*, 2014, **114**, 9613–9644.
20 H. Zhang and J. F. Banfield, *J. Mater. Chem.*, 1998, **8**, 2073–2076.

21 A. S. Barnard and P. Zapol, *Phys. Rev. B: Condens. Matter.*, 2004, **70**, 235403.
22 M. P. Finnegan, H. Zhang and J. F. Banfield, *J. Phys. Chem. C*, 2007, **111**(5), 1962–1968.
23 A. A. Levchenko, G. Li, J. Boerio-Goates, B. F. Woodfield and A. Navrotsky, *Chem. Mater.*, 2006, **18**, 6324–6332.
24 O. Lamiel-García, A. Cuko, M. Calatayud, F. Illas and S. T. Bromley, *Nanoscale*, 2017, **9**, 1049–1058.
25 H. Zhang, B. Chen, J. F. Banfield and G. A. Waychunas, *Phys. Rev. B: Condens. Matter*, 2008, **78**, 214106.
26 H. Zhang, B. Gilbert, F. Huang and J. F. Banfield, *Nature*, 2003, **424**, 1025–1029.
27 D. R. Hummer, J. D. Kubicki, P. R. C. Kent and P. J. Heaney, *J. Phys. Chem. C*, 2013, **117**, 26084–26090.
28 E. Scolan and C. Sanchez, *Chem. Mater.*, 1998, **10**, 3217–3223.
29 M. Anpo, T. Shima, S. Kodama and Y. Kubokawa, *J. Phys. Chem.*, 1987, **91**, 4305–4310.
30 L. Zamirri, A. Macia Escatller, J. Mariñoso Guiu, P. Ugliengo and S. T. Bromley, *ACS Earth Space Chem.*, 2019, **3**, 2323–2338.
31 Á. Morales, A. Macia-Escatllar, F. Illas and S. T. Bromley, *Nanoscale*, 2019, **11**, 9032–9041.
32 A. Macia Escatllar, Á. Morales-García, F. Illas and S. T. Bromley, *J. Chem. Phys.*, 2019, **150**, 214305.
33 S. Pigeot-Rémy, F. Dufour, A. Herissan, V. Ruaux, F. Maugé, R. Hazime, C. Foronato, C. Guillard, C. Chaneac, O. Durupthy, C. Colbeau-Justin and S. Cassaignon, *Appl. Catal., B*, 2017, **203**, 324–334.
34 K. E. Jelfs, E. Flikkema and S. T. Bromley, *Phys. Chem. Chem. Phys.*, 2013, **15**, 20438–20443.
35 A. Cuko, A. Macià, M. Calatayud and S. T. Bromley, *Comput. Theor. Chem.*, 2017, **1102**, 38–43.
36 S. Kirkpatrick, C. D. Gelatt and M. P. Vecchi, *Science*, 1983, **220**, 671–680.
37 J. D. Gale and A. L. Rohl, *Mol. Simul.*, 2003, **29**, 291–341.
38 F. A. Soria and C. Di Valentin, *Nanoscale*, 2021, **13**, 4151–4166.
39 V. Blum, R. Gehre, F. Hanke, P. Havu, V. Havu, X. Ren, K. Reuter and M. Scheffler, *Comput. Phys. Commun.*, 2009, **180**, 2175–2196.
40 J. Perdew, K. Burke and M. Ernzerhof, *Phys. Rev. Lett.*, 1996, **77**, 3865–3868.
41 K. C. Ko, O. Lamiel-García, J. Y. Lee and F. Illas, *Phys. Chem. Chem. Phys.*, 2016, **18**, 12357–12367.
42 Á. Morales-García, R. Valero and F. Illas, *Phys. Chem. Chem. Phys.*, 2018, **20**, 18907.
43 O. Lamiel-García, K. C. Ko, J. Y. Lee, S. T. Bromley and F. Illas, *J. Chem. Theory Comput.*, 2017, **13**, 1785–1793.
44 E. van Lenthe, E. J. Baerends and J. G. Snijders, *J. Chem. Phys.*, 1993, **99**, 4597–4610.
45 T. Zhu and S.-P. Gao, *J. Phys. Chem. C*, 2014, **118**(21), 11385.
46 K. C. Ko, S. T. Bromley, J. Y. Lee, F. Illas and J. Phys, *Chem. Lett.*, 2017, **8**, 5593–5598.

Nanoscale

PAPER

View Article Online
View Journal | View Issue

Check for updates

Cite this: *Nanoscale*, 2024, **16**, 8975

Tuning electronic levels in photoactive hydroxylated titania nanosystems: combining the ligand dipole effect and quantum confinement†

Miguel Recio-Poo, [a] Ángel Morales-García, *[a] Francesc Illas [a] and Stefan T. Bromley *[a,b]

Received 4th December 2023,
Accepted 1st April 2024

DOI: 10.1039/d3nr06189b

rsc.li/nanoscale

Reducing the size of titania (TiO_2) to the nanoscale promotes the photoactive anatase phase for use in a range of applications from industrial catalysis to environment remediation. The nanoscale dimensions of these systems affect the magnitude of the electronic energy gap by quantum confinement. Upon interaction with aqueous environments or water vapour, the surfaces of these systems will also be hydroxylated to some degree. In turn, this affects the electronic energy levels due to the cumulative electrostatic effect of the dipolar hydroxyl (–OH) ligands (*i.e.* the ligand dipole effect). Using accurate density functional calculations, we investigate the combined effects of quantum confinement and the hydration-induced ligand dipole effect on a set of realistic titania nanosystems over a wide range of hydroxylation. Our detailed investigation reveals that, contrary to previous models, the ligand dipole effect does not-linearly depend on the ligand coverage due to the formation of inter-ligand OH···OH hydrogen bonds. To account for the resulting effects, we propose a refined model, which describes the ligand dipole effect more accurately in our systems. We show that both hydroxylation (by the ligand dipole effect) and size (by quantum confinement) have significant but distinct impacts on the electronic energy levels in nanotitania. As an example, we discuss how variations in these effects can be used to tune the highest unoccupied energy level in nanotitania for enhancing the efficiency of the hydrogen evolution reaction. Overall, we show that any specific energy shift can be achieved by a range of different combinations of nanosystem size and degree of hydroxylation, thus providing options for energy-level tuning while also allowing consideration of practical constraints (*e.g.* synthetic limitations, operating conditions) for photochemical applications.

Introduction

Nanoparticles (NPs) of the photoactive anatase polymorph of titania (TiO_2) are widely studied and used for a range of photochemical uses such as photocatalytic H_2 production,[1] or remediation of polluted water.[2] In such applications, titania NPs are expected to be significantly hydroxylated due to interaction with their aqueous working environment.[3] The photochemical importance of surface OH groups in these systems due to their role in hydroxyl radical formation ($^{\bullet}OH$) is well established.[4–6] Surface hydroxyls and adsorbed water can also help to stabilise surface hole centres in photocatalytic processes.[7] Herein, we show that hydroxylation can have a surprisingly significant further effect on the energetic positions of the frontier orbital energy levels that eventually define the band edges in sufficiently large titania NPs. Band edge positions play an essential role in determining the utility and performance of semiconducting materials for photocatalytic applications.[8,9] Generally, the degree and type of alignment of a material's band edge energies with the energy levels of species interacting with its surfaces can strongly influence the transfer of photo-generated charge carriers for reduction/oxidation reactions. For photocatalytic water splitting, for example, the band edges of the system in question should lie above and below the redox potentials for H_2 and O_2 respectively.[10] Understanding and controlling factors that significantly affect band edge positions are thus critical for developing and advancing photoelectrochemical technologies.

The band edge positions of the bulk anatase phase have been widely studied with respect to those of the less photoactive rutile polymorph due to a proposed staggered alignment

[a]*Departament de Ciència de Materials i Química Física & Institut de Química Teòrica i Computacional (IQTCUB), Universitat de Barcelona, c/Martí i Franquès 1-11, 08028 Barcelona, Spain. E-mail: angel.morales@ub.edu, s.bromley@ub.edu*
[b]*Institució Catalana de recerca i Estudis Avançats (ICREA), Passeig Lluis Companys 23, 08010 Barcelona, Spain*

† Electronic supplementary information (ESI) available. See DOI: https://doi.org/10.1039/d3nr06189b

having a synergistic role in photocatalytic water splitting.[11] The energy gap in titania NPs is highly affected by size-dependent quantum confinement (QC),[12] which, in turn, can thus affect the rutile-anatase energy edge alignment.[13] The main effect of QC upon decreasing NP size is to increase the spacing between those discrete energy levels that define the band gap in the corresponding extended system. Attempts to more finely tune band edge positions in titania NPs without varying their size have followed a number of different strategies such as: engineering morphology and/or crystallinity,[14–17] chemical doping,[18,19] and creation of heterostructures with other materials.[20–22] These approaches require significant control of the detailed chemical structure of the NPs and, once employed, cannot be easily and/or dynamically changed by external means. In this work we examine the influence on band edge positions in nanotitania by ever-present surface hydroxyls, whose surface coverage can be controlled by external conditions (*e.g.* water vapour partial pressure).[3,23]

For small anhydrous titania nanoclusters, hydration leads to progressive increasing the coverage of surface –OH species which in turn leads to a gradual fluctuating increase in the electronic gap magnitude.[23] This gap increase is ascribed to the stabilisation of the electronic structure of the nanoparticle as a result of hydroxylation-induced healing of local under-coordinated atoms/defects. For the relatively large titania NPs considered herein, we also find a similar hydroxylation-induced moderate energy gap increase. However, we find that the main effect of hydroxylation is to significantly shift both band edge positions in a similar parallel manner. This phenomenon can be ascribed to the ligand-induced Stark effect in which the cumulative electric field from the dipoles of surface ligands act to uniformly shift all the electronic energy levels of the NP with a linear dependence on ligand coverage. This effect was first observed, and has been subsequently mainly explored, for controlling the band edge positions of quantum dots by organic ligands for increasing solar cell efficiencies.[24–26] In the field of photocatalysis, there have also been a few studies using dipolar fields of organic ligands to improve catalytic performance,[27,28] where the effect is usually referred to as the ligand-induced dipole effect (LIDE).[29] In the following, we will use the acronym LIDE to be consistent with the practice in the photocatalytic literature.

Herein, we focus on LIDE in hydroxylated anatase titania NPs using realistic models developed in previous works[16,30] which have been used to rationalise experimental results on hydroxylated anatase NPs.[3] As far as we are aware, hydroxylation induced LIDE for titania has only been previously studied using periodic slab models of ideal surfaces with small numbers of hydrogen atoms placed on oxygen atoms (*i.e.* hydrogenation) on regular surface sites.[31,32] In contrast, our NP based approach allows for a highly detailed examination of hydroxylation from dissociated water at various different sites such as corners, edges and facets. In addition, with the absence of periodic boundary constraints in our NP models, we can follow a gradual and progressive hydroxylation over a wide range of –OH coverages. Thereby, we show that LIDE in our systems has an unexpected non-linear –OH ligand coverage dependence that detailed analysis of the results shows to be due to effects of OH···OH interactions. Using our versatile NP models, we are also able to examine the additional effect of QC by considering hydroxylated NPs with different sizes. We note that as our models are discrete, they also allow us to use the true vacuum level as a natural unambiguous reference for all band edge energies for all NP systems considered.[13] To provide further context for our work, we compare our results for anatase NPs with analogous calculations on a non-crystalline anatase-mimicking NP,[30] and on an extended anatase surface slab model.

Overall, our study provides a highly detailed and systematic description of the combined effects of hydroxylation (through LIDE, electronic stabilisation and inter-ligand interactions) and system size (governing QC) on the electronic band edge positions in titania nanosystems. Due to the versatility of our modelling approach, we can accurately assess the relative influence of each effect and thereby provide guidance on how to combine these factors to optimise band edge positions for photocatalytic applications. Specifically, we show how the band edges in our considered systems vary relative to the standard potentials for the hydrogen evolution reaction (HER) and the oxygen evolution reaction (OER) involved in water splitting. The valence band maximum (VBM) is always found to be lower than the potential for the OER. In contrast, by following level-alignment with respect to hydroxylation and system size, we show that the conduction band minimum (CBM) can be sensitively tuned to be above or below the potential for the HER. We highlight that any particular level alignment can be achieved using a range of different choices of size and hydroxylation degree. Unlike many other level-tuning approaches such as chemical doping or interfacing with other materials, these system variables are not dependent on chemically detailed interventions. As such, varying size and hydroxylation degree provides a top-down approach to tuning electronic energy levels, whose versatility means that it can accommodate different practical constraints when designing and/or operating photochemical nanosystems.

Models and computational strategy

We employ three previously reported realistic titania NP models with different sizes and crystalinities.[3,16,30] Two of these $(TiO_2)_n$ NPs, with sizes n = 35, 165, possess the anatase crystal structure with bipyramidal faceted morphologies. We also consider one amorphous $(TiO_2)_{35}$ NP with a roughly spherical morphology. All NP structures are shown in Fig. 1a. The anatase titania NPs were designed following a top-down strategy in which the bulk anatase crystal is cut to generate bipyramids with the most stable (101) surface on all exposed facets.[12,16] The bare anatase titania NPs were progressively hydroxylated considering the relative reactivity of different surface sites (*e.g.*, apical, edge, facet).[3] The amorphous $(TiO_2)_{35}$ NP was generated by a simulated annealing process[33]

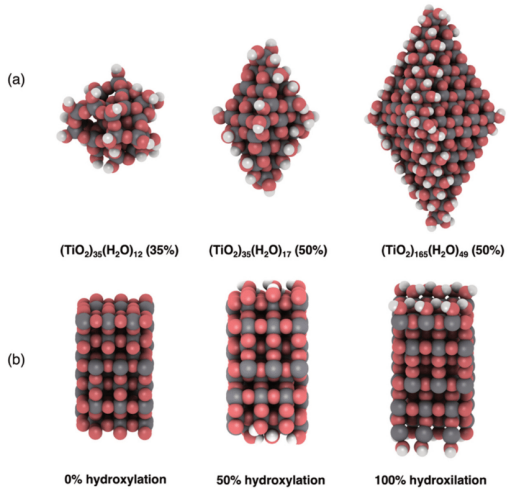

Fig. 1 (a) Examples of hydroxylated NP structures. From left to right: an annealed amorphous $(TiO_2)_{35}(H_2O)_{12}$ NP, and faceted anatase crystalline $(TiO_2)_{35}(H_2O)_{17}$ and $(TiO_2)_{165}(H_2O)_{49}$ NPs. The percentages in parentheses indicate the degree of hydroxylation. (b) Supercell of an extended (101) surface model of anatase with 0 (left), 50% (middle) and 100% (right) degrees of hydroxylation. Atom key: O – red, Ti – grey, H – white.

in which the faceted $(TiO_2)_{35}$ NP was heated up to 3000 K, followed by sequential cooling steps.[30] The simulated annealing was performed using the NanoTiO interatomic potential (IP)[34] and the GULP code.[35] The structures of the hydroxylated amorphous $(TiO_2)_{35}$ NPs were generated by separate simulated annealing runs for each degree of hydroxylation.[30]

To compare with our NP based results we also considered a periodic slab model of the (101) anatase surface (see Fig. 1b). This model consists of six layers of a (3 × 1) anatase supercell in which the (101) surface is symmetrically exposed on either side of slab. Periodically repeated slabs in the out-of-plane direction were separated by approximately 20 Å of vacuum space to avoid artificial inter-slab interactions. For each degree of hydroxylation considered we symmetrically hydroxylated both top and bottom surfaces of the slab to avoid the build-up of anisotropic electric fields. In these models, the averaged electrostatic potential over the mid-plane in the vacuum space was used to define a zero reference for evaluating the changes in band edge positions with respect to hydroxylation. Note that in the discrete NP systems the real vacuum level could be used as an absolute energy reference. In both the slab and NP systems we define the degree of hydroxylation with respect to the maximum hydroxylation we could achieve (*i.e.*, defined to be 100%).

All the anhydrous $(TiO_2)_n$ and hydrated $(TiO_2)_n(H_2O)_m$ nanostructures and surface models were relaxed using all-electron DFT-based calculations as implemented in the FHI-aims code.[36] The Perdew–Burke–Ernzerhof (PBE) exchange–correlation density functional[37] was selected to perform the structural optimizations. A light tier-1 numerical atom-centred orbital basis set was employed. Such a basis set is comparable in accuracy to a TZVP Gaussian-type orbital basis set for TiO_2.[12] The convergence thresholds for atomic forces and total energy during the optimization were set to 10^{-5} eV Å^{-1} and 10^{-6} eV, respectively. A 1 × 1 × 1 **k**-point grid (*i.e.* Γ-point) was used in the (101) surface model. We verified that **Γ**-point calculations provide sufficiently converged energies for the relatively large periodic supercell employed (see ESI†).

DFT calculations employing the PBE functional are generally reliable in providing a good structural description of materials. However, generalised gradient approximation (GGA) functionals such as PBE tend to be relatively poor when describing electronic properties such as the energy gap and band edge positions.[38] Hybrid density functionals which mix in a percentage of Hartree–Fock exchange into GGA functionals can help to overcome this systematic drawback.[39] A hybrid PBEx (12.5% Hartree-Fock exchange) functional has previously been shown to significantly improve the description of the electronic structure of titania systems.[40,41] A systematic PBEx-inspired correction of our computed PBE-based energy gaps and band edge positions was employed throughout.[41]

Results and discussion

We divide the discussion of our results into three parts. We first discuss the evolution of the electronic energy gap (E_g) values and how they are influenced by system size and hydroxylation. Afterwards, we focus on the effect of hydroxylation-induced LIDE on the band edges in our considered systems. Finally, we relate our results to water splitting though comparison of band edge energies with the potentials for the HER and OER and suggest how hydroxylation, and system size could be used to optimise photocatalytic performance. As our NP models are discrete systems, the VBM and CBM are formally associated with the highest occupied molecular orbital (HOMO) energy and the lowest unoccupied molecular orbital (LUMO) energy, respectively. As such we will tend to refer to HOMO and LUMO values when discussing our NP-based results.

Electronic energy gaps

We first consider the E_g values of the (101) anatase surface slab and the faceted titania NPs with respect to degree of hydroxylation (see Fig. 2). For the anhydrous anatase slab, we obtain an E_g value of 3.58 eV, which is 0.25 eV larger than the experimental band gap of bulk anatase (3.23 eV).[42] As our approach provides an accurate E_g value for bulk anatase,[40] this is likely due to the finite thickness of our slab model and the associated band-opening effect of QC. Upon reducing the size and dimension of the anatase slab to anatase NPs of progressively decreasing size (*i.e.*, $(TiO_2)_{165} > (TiO_2)_{35}$) both the HOMO and LUMO are shifted up in energy, but with the LUMO upshift being more pronounced. In the smallest anhydrous anatase $(TiO_2)_{35}$ NP considered, this QC-induced effect raises the value of E_g to 3.84 eV, which is 0.26 eV higher than for the anhydrous slab. With hydroxylation, the main influence of QC is maintained with the E_g values being smaller in the hydroxylated slabs with respect to those in the correspondingly hydroxylated NPs. However, increasing hydroxylation also leads to a differential small increase in E_g values for different system sizes. For the anatase slab, the magnitude of E_g increases by 0.05 eV from 0%–100% hydroxylation. In contrast, for the corresponding increase in hydroxylation, the increase in E_g is of 0.18 and 0.31 eV for $(TiO_2)_{165}$ and for $(TiO_2)_{35}$, respectively. This increase in E_g is likely due to hydroxylation-induced healing of local undercoordinated atoms/defects and a concomitant stabilisation of the electronic structure, as noted in previous work on hydroxylated titania nanoclusters.[23] The relative increase in the magnitude of this effect with reducing system size is probably due to the increasing proportion of low-coordinated surface sites (especially at corners and edges) going from the planar surface slab to progressively smaller discrete NPs. For the smallest NP, this overall increase in E_g with hydroxylation is also accompanied by relatively large energy fluctuations with respect to small changes in hydroxylation as also observed in small titania nanoclusters.[23] However, this effect seems to diminish with increasing system size, where the hydroxylation-induced E_g increase becomes smaller and more gradual.

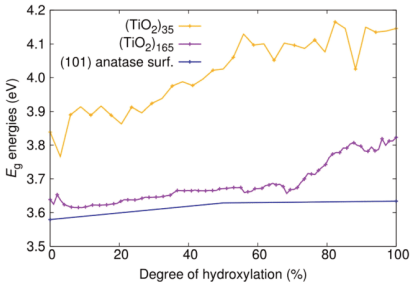

Fig. 2 Evolution of E_g energies with degree of hydroxylation of the $(TiO_2)_n$ (n = 35, and 165) anatase NPs and the extended (101) anatase surface as depicted in Fig. 1.

Band edge positions

For the anhydrous anatase slab, the VBM energy is found to be −8.4 eV and the CBM energy to be −4.9 eV. These values correspond well to other calculated band edge energies reported for bulk anatase (−8.3 eV and −4.9 eV).[43] We note that these latter values were obtained by a method which, similar to our approach, uses an absolute vacuum reference and hybrid functionals, and which has been confirmed to be quite reliable as compared with experiment.[11] As noted above, both the corresponding HOMO and LUMO of the anhydrous NPs are higher in energy due to QC. The resultant HOMOs of both the largest $(TiO_2)_{165}$ and smallest $(TiO_2)_{35}$ NPs are upshifted by approximately 0.3 eV. In the case of the LUMOs, the upshift is also about 0.3 eV for $(TiO_2)_{165}$, but almost 0.5 eV for $(TiO_2)_{35}$. Upon hydroxylation, all initial band edge/orbital energies appear to initially increase in a fairly parallel linear manner with respect to the degree of hydroxylation. With increasing hydroxylation, the rate of increase in these energies slows down gradually. Overall, the total upshift in the edge/orbital energies is >1 eV in all cases from 0–100% hydroxylation. These data are summarised in Fig. 3. We note that this hydroxylation-induced orbital energy up-shift is not only observed for the HOMO and LUMO in our systems but is a general effect that effects all orbital energies. In Fig. S1 and S2 of the ESI† we show, for example, the hydroxylation dependent energies of ten energy levels ranged between LUMO+5 and HOMO−5 and for a significantly deeper lying energy level.

We also note that the magnitude of this effect does not strongly depend on the underlying anatase crystal structure. To show this, we compare the hydroxylation dependence of the HOMO and LUMO of the faceted anatase $(TiO_2)_{35}$ NP with that of an amorphous $(TiO_2)_{35}$ NP where the structure of the titania core of the NP and the positions of all hydroxyls are optimised for each degree of hydroxylation *via* simulated annealing[30]

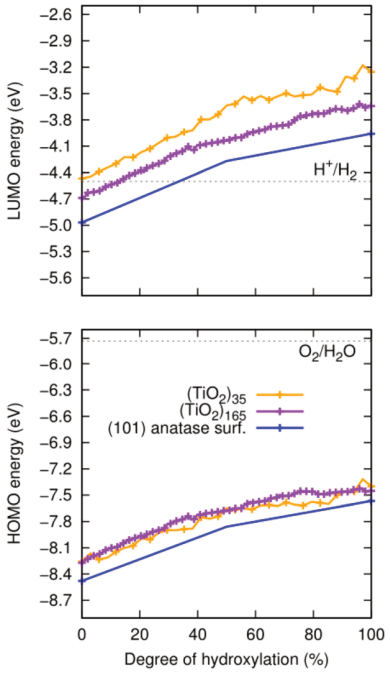

Fig. 3 Evolution of the energies of the HOMO (lower) and LUMO (upper) with degree of hydroxylation of the $(TiO_2)_n$ (n = 35, and 165) anatase NPs and the extended (101) anatase surface as depicted in Fig. 1. Dotted grey lines represent the redox potentials for the HER (upper) and the OER (lower), which have the approximate values of −4.5 and −5.7 eV, respectively.[44,45]

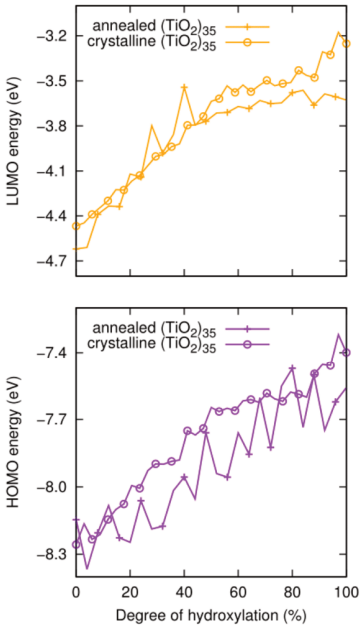

Fig. 4 Evolution of the HOMO (lower) and LUMO (upper) energies with respect to the degree of hydroxylation for annealed amorphous and faceted anatase $(TiO_2)_{35}$ NPs as depicted in Fig. 1.

(see Fig. 4). The annealed NP clearly shows relatively larger fluctuations in the energies of the frontier orbitals. These variations are related to both the structure of the titania NP core structure and the hydroxylation configuration, which are re-calculated for each degree of hydroxylation through the annealing process. However, generally, we see that the average values of both the HOMO and LUMO in both NP types increase systematically in a similar way and over very similar energy ranges.

From the above, we propose that the general hydroxylation-dependent upshift in all orbital energies in all our systems is most likely due to the LIDE coming from the cumulative electrostatic field of the surrounding dipolar –OH groups. To quantify the total –OH-induced dipole moment acting on the NP, the sum of the components of each –OH dipole vector in the direction of the centre of the NP should be calculated. To obtain the effective radial O–H distances, we use the angle α between Ti–O–H atoms and project the O–H bond distance (d_{OH}) along Ti–O bond direction, which taken to be approximately in-line with the radial direction to the NP centre (see Fig. 5). Rather than assuming that the charge separation in each –OH group is constant, we also measure possible $H^{\delta+}$ and $O^{\delta-}$ variations. Taking the above considerations into account, we use the following expression for the total magnitude of the –OH dipole contribution ($\vec{p}_{OH}$) for each degree of hydroxylation:

$$\vec{p}_{OH} = \sum_{i=1}^{N} Q_{H,i} \cdot d_{OH,i} \cdot \cos(\alpha_i) \quad (1)$$

where N is the number of OH groups on a NP, and Q_H is the positive charge on the H atoms in every OH ligand. We obtain the Q_H charges using the Hirshfeld atomic charge partitioning scheme.[46] Unlike dipoles, atomically partitioned charges are not observables, and their accuracy cannot be directly assessed. Here, we scale the magnitude of all partitioned

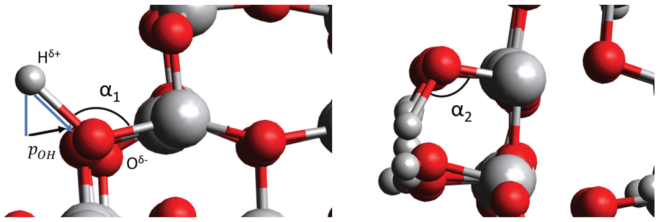

Fig. 5 Left: Radial component of the dipole moment vector acting towards the centre of a titania NP ($\vec{p}_{OH}$) associated with a single hydroxyl group. Right: A relatively higher hydroxylation regime in which OH···OH H-bonding leads to $\alpha_2 < \alpha_1$, and a reduced value of ($\vec{p}_{OH}$). Large grey, red, and small grey spheres correspond to Ti, O and H atoms, respectively.

charges by a constant factor of ~0.7, such that the scaled atomic charges in a calculation of the water molecule reproduces the experimental H_2O dipole moment. We note that this constant scaling does not affect any of our reported trends, but just provides OH dipole magnitudes that are more reasonably in line with the OH bond moment in the water molecule.[47] In the context of dissociative water adsorption, H and OH constituents interact, respectively, with under-coordinated O and Ti surface atoms. In this way, the hydration process leads to two kinds of hydroxyls which both can lead to an added dipole. We estimate the total dipole using the calculated charge on the H atoms and assuming that the deficit of electrons is only taken by the neighbouring O atom in each case. Lastly, for each –OH group, the factor $\cos(\alpha_i)$ projects out the component of the dipole vector along the Ti–O bond direction (*i.e.* approximately the radial direction leading towards the centre of the NP).

We note that LIDE is usually modelled as being linearly proportional to ligand coverage with a fixed dipole per ligand.[26,29,31,32] This dipole is typically assumed to arise from the intrinsic dipole of the ligand and from the induced polarisation due to the ligand-surface interaction. In our expression, the dipole of the –OH group and how it is affected by structural change (*via* d_{OH} and α) and polarisation (*via* Q_H) due to the interaction with the surface is taken into account. We note that the contributions to the overall dipole through polarisation of the TiO_2 surface due to interaction with the –OH groups has been reported to be very small and largely independent of OH coverage on rutile surfaces.[31] The small variation in the partial charges of the surface Ti (and O) atoms with respect to hydroxylation in our systems also confirms this conclusion.

Here, we use eqn (1) to estimate how the total hydroxylation-induced polarisation varies with –OH coverage. In all studied systems, we find that d_{OH} has an almost constant value, and thus has a linear effect on the total dipole with respect to changes in degree of hydroxylation. In contrast, with varying hydroxylation we find non-linear contributions to the total dipole for α and Q_H. Specifically, we find that both α and Q_H decrease with increasing hydroxylation, which tends to moderate the overall dipole increase. The reason for the decrease in both α and Q_H is the formation of OH···OH inter-hydroxyl H-bonds which becomes more and more prevalent with higher –OH coverages. These H-bond interactions trigger an increased bending of the Ti–O–H bond angles, making α increasingly closer to 90° and thus causing a $\vec{p}_{OH}$ decrease. Fig. 5 shows this ligand bending effect by comparing α for low and high hydroxylation. Similarly, with increasing H-bonding, we find that the OH···OH, H-bonded network promotes a partial delocalisation/polarisation leading to a reduction in the absolute values of the atomically partitioned charges on the hydroxyl groups, and a dipole reduction. The change in both the average value of α and Q_H with respect to the degree of hydroxylation for the $(TiO_2)_n$ (n = 35, 165) anatase NPs is provided in the ESI (Fig. S3†). In Fig. 6 we show evolution of $\vec{p}_{OH}$ given by eqn (1) with respect to hydroxylation for our n = 35 and n = 165 $(TiO_2)_n$ anatase NPs. For reference we also show the typically assumed model in which the total dipole is linearly dependent on ligand coverage.

Clearly, the H-bonding induced α variation and charge delocalisation tends to increasingly moderate the increase in $\vec{p}_{OH}$ with increasing hydroxylation. For 50–100% hydroxylation for the $(TiO_2)_{165}$ NP, for example, the magnitude of $\vec{p}_{OH}$ varies from −15% to −22% with respect to a linear model. This tendency is very similar to that we report for the variation of energy levels with respect to degree of hydroxylation (see Fig. 2 and 3). The link between these two phenomena is likely to be LIDE whose effect on energy levels can be estimated using our calculated values of $\vec{p}_{OH}$ for each degree of hydroxylation for each of our systems using eqn (2):[26]

$$E_l = E_0 + \Delta E = E_0 + A \cdot \left(\frac{\vec{p}_{OH}}{r^2}\right) \quad (2)$$

where the energy of a level, E_l is given by the energy of the level in the anhydrous TiO_2 system (E_0) plus the LIDE shift (ΔE) which depends mainly on $\vec{p}_{OH}$ (where we use the dipole moment evaluated using eqn (1)), and r, an effective radius of

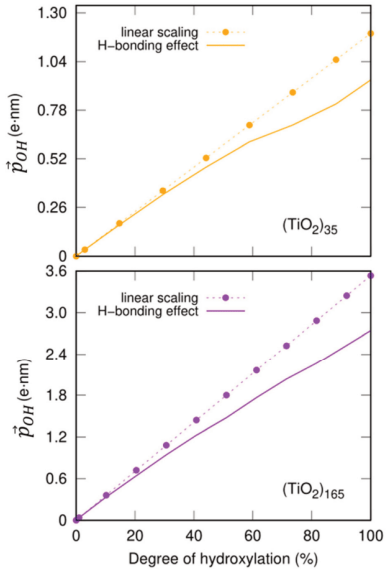

Fig. 6 Total –OH dipole moment ($\vec{p}_{OH}$) *versus* degree of hydroxylation for the faceted $(TiO_2)_{35}$ $(TiO_2)_{35}$ (upper) and $(TiO_2)_{165}$ (lower) NPs. The dashed line shows the case in which all –OH dipoles contribute equally irrespective of hydroxylation, while the solid line incorporates the variability of α and Q_H following eqn (1).

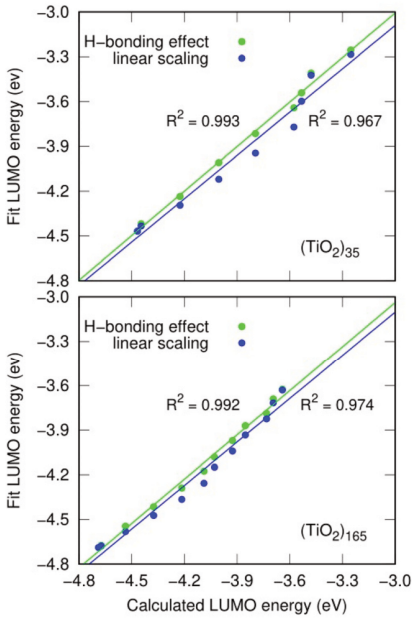

Fig. 7 Correlation between DFT-calculated LUMO energy values and model-estimated-values for different degrees of hydroxylation for the $(TiO_2)_{35}$ and $(TiO_2)_{165}$ NPs incorporating effects of inter-OH H-bonding (green), and by using a simple linear model (blue).

the system in question (which, for NPs, is taken to be the radius of a spherical NP with the same volume as the corresponding NP). Finally, A is a system dependent fitting constant.

As an example, we use the LIDE dependent shifting in the LUMO with respect to hydroxylation in the $(TiO_2)_n$ (n = 35, 165) NPs. In Fig. 7 we compare the DFT-calculated hydroxylation dependent variation in the LUMO energy levels of these two systems with predictions using eqn (2) from using: (i) constant dipoles for each hydroxyl, (ii) OH dipoles calculated using eqn (1). In both systems both models (i) and (ii) provide a good fit to the variation in LUMO energies indicating that the main effect on the energy change is due to LIDE. Comparing the models, we can also see that in both systems, using the dipoles from eqn (1) provides a non-negligible improvement over the linear dipole model.

We can further justify the use of our new detailed model for fitting the variation in energy levels with respect to the total dipole moment from surface –OH groups. In Fig. 8 we show the evolution in the HOMO and LUMO energies of our faceted NPs directly from DFT calculations with respect to $\vec{p}_{OH}$ calculated using eqn (1). In all cases we observe a very good correlation, which again supports the link between energy level shifting and hydroxylation-induced LIDE. The correlation between total dipole and energy shift is slightly less strong for the HOMO in the larger NP (R^2 = 0.95) than in the other cases examined (R^2 = 0.99). This lower correlation is related to a levelling of the $(TiO_2)_{165}$ HOMO level for high hydroxylation (>70%) which also results in an abrupt upshift in the E_g value (see Fig. 2). This may be related to specific surface sites being stabilised through chemical bonding and thus not purely a dipolar effect.

Relevance to water splitting and extrapolation to larger NP sizes

The position of the absolute redox potential for the OER is always significantly higher than the HOMO energies in our considered systems (see Fig. 3). As such, photo-generated holes in the HOMO would easily drive the OER for all systems for all degrees of hydroxylation. However, for solar-induced water splitting, the low HOMO energy would entail a relatively large E_g. With respect to capturing the maximum amount of useful energy from available sunlight, this would be detrimen-

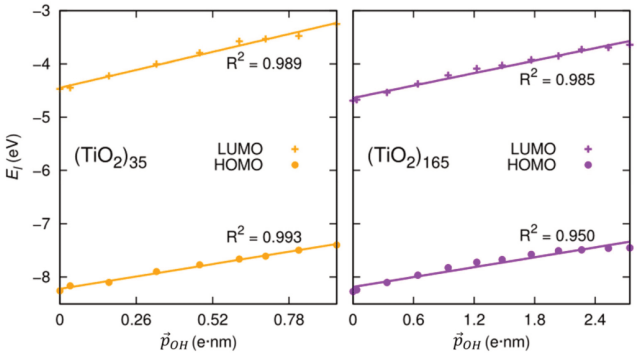

Fig. 8 Correlation between calculated HOMO (LUMO) energies and projected total –OH dipole moment for the anatase $(TiO_2)_{35}$ and $(TiO_2)_{165}$ NPs calculated using eqn (1).

tal. Minimising E_g under the conditions that: (i) the HOMO lies just below the redox potential for the OER, and (ii) the LUMO lies just above the redox potential for the HER, would help maximise the solar efficiency of water splitting photocatalysts. In the following, we focus on tuning the LUMO for the HER, assuming that the OER potential could be matched by employing other strategies (*e.g.*, alternative materials,[48] doping[49]).

For low hydroxylation degrees, the high QC of the smallest $(TiO_2)_{35}$ anatase NP causes it to have a LUMO which is optimally placed just above the HER redox potential. We note, however, that the anatase NPs of this size are metastable with respect to amorphous NPs[16,30] which tend to have lower lying LUMO levels for the lowest hydroxylation (see Fig. 3). We also note that it would be practically very difficult to prepare populations of NPs that are confined to such a small size range while also restricting their natural tendency to be hydroxylated through reaction with water. In larger NPs, the lower QC leads to a decrease in the LUMO. However, this effect can be compensated by increased hydroxylation and thus higher LIDE which causes a LUMO energy increase. Moving to higher hydroxylation in larger anatase NPs thus allows for more practically viable NPs to have an optimally tuned LUMO energy. As such an approach is linked only to the controllable working conditions of as-synthesised NPs, it also avoids the use of extra level-tuning measures (*e.g.* doping, interfacing with other materials). We note that very recently reported experiments have indicated that the induced dipole effect of deliberately grafted –OH ligands can enhance of photocatalytic activity of $BiPO_4$.[50]

More generally, the combination of LIDE and QC allows one to tune the energy levels for a particular application. Our results show how orbital energies vary with the degree of hydroxylation for three sizes of NPs and for the infinite-sized limiting case of the extended anatase (101) surface. By interpolating between these results, we can provide approximate maps of how hydroxylation affects any chosen orbital level(s) for arbitrary system sizes. As an example, in Fig. 9 we show how the LUMO in anatase NPs can be tuned by combinations of hydroxylation and size to be either above or below the HER redox potential. For LUMO energies well above the HER (red region in Fig. 9) the reducing power of hydroxylated titania NPs is relatively enhanced. We specifically highlight the hydroxylation/size-tuning of the LUMO for efficient E_g matching (*i.e.* to be just above the HER redox potential – see green region in Fig. 9). Overall, Fig. 9 shows that many titania systems of different sizes and degree of hydroxylation can achieve specified electronic level alignments.

We note that in Fig. 9 we assume that only –OH groups from dissociated water causes the LIDE effect at all sizes. This scenario is most probable for non-crystalline NPs for which the surfaces tend to be more irregular and reactive. For more crystalline bipyramidal anatase NPs, a low-to-moderate degree of hydroxylation will readily occur through dissociative water adsorption on lower-coordinated edges and corner sites.[3] Larger anatase bipyramidal NPs will have a higher proportion of their surfaces terminated by regular (101) facets. For the extended (101) surface, it is likely that there is a competition between molecular and dissociative water adsorption and that the balance between these two is temperature dependent.[51] Recent work using a combination of surface X-ray spectroscopy and DFT calculations has reported a 3 : 1 ratio of dissociative *versus* molecular water on the (101) anatase surface at room temperature.[52] For suitably high water coverages, having such a mixture of molecular H_2O (25%) and –OH (75%) bound to (101) NP facets would be more than sufficient to reach the higher degrees of hydroxylation considered in Fig. 9.

In future work it would also be interesting to consider influence of the accompanying molecularly adsorbed water on the

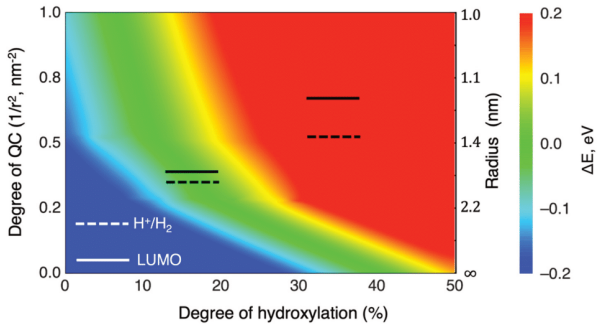

Fig. 9 LUMO *versus* HER potential energy level alignment plot with respect to varying the degree of hydroxylation (*x*-axis), degree of QC (left *y*-axis) and anatase system size (right *y*-axis). The colours indicate the regions where the LUMO is below/above the HER potential (blue/red) and where the LUMO is between 0–0.1 eV above the redox potential of the HER (green).

(101) facets of larger bipyramidal NPs at higher water coverages. Molecularly adsorbed water has a high dipole (similar in magnitude to that of –OH) and is thus also expected produce a dipolar Stark effect in titania NPs. However, for the effect to be cumulative and vary systematically with changes in coverage, the dipoles should be radially aligned. For low temperatures a coherent ordering of molecularly adsorbed water may indeed be possible and could induce a very similar effect to that we describe for –OH groups. However, we would expect molecular adsorption to be more susceptible to disordering (*e.g. via* H-bond network rearrangements) at higher temperatures, thus diminishing any effect.

Conclusions

Employing accurate DFT based calculations, we have carefully analysed the influence of system size and hydroxylation on the electronic energy levels in a set of titania nanosystems, including realistic NP models and an extended anatase surface slab. Reducing system size increases the spacings between energy levels in a non-linear manner due to QC. Conversely, the cumulative electrostatic dipole of surface –OH ligands shifts all the energy levels by a uniform amount due to the LIDE. The magnitude of this latter shift is found not to be linearly dependent on the degree of ligand coverage, as is usually assumed in LIDE models. Instead, we show that inter-ligand interactions, in this case OH···OH H-bonds, can lead to a non-negligible coverage-dependent dipole reduction, due to ligand bending and charge delocalisation.

We show that size-induced QC and hydroxylation-driven LIDE can have significant, but distinct impacts on the electronic energy levels in nanotitania systems. As a highlighted example, we show how combined variations in QC and LIDE can be used to tune the highest unoccupied energy level in anatase NPs with respect to the HER redox potential. Here, we show that any specific energy shift can be achieved by a range of different combinations of system size and degree of hydroxylation. This flexibility means that one can achieve level-tuning (*e.g.*, to enhance the HER) while taking into account different practical constraints (*e.g.*, synthetic NP size limitations, degrees of hydroxylation due to operating conditions). We also note that, unlike many other proposed level-tuning approaches (*e.g.*, chemical doping, interfacing with other materials), LIDE and QC do not require chemically detailed interventions. In summary, we show that combining QC and LIDE provides a highly versatile top-down approach to tuning electronic energy levels in photoactive nanomaterials.

Conflicts of interest

There are no conflicts to declare.

Acknowledgements

We thank the financial support from MCIN/AEI/10.13039/501100011033 through projects PID2020-115293RJ-I00, PID2021-126076NB-I00, PID2021-127957NB-100, TED2021-129506B-C22, TED2021-132550B-C22 and the María de Maeztu CEX2021-001202-M project and from the Generalitat de Catalunya through the projects 2021-SGR-00079 and 2021-SGR-00354. Red de investigación RED2022-134295-T (FOTOFUEL) is also partly acknowledged. The reported research is also involved in the European Cooperation in Science and Technology (COST) Actions: CA18234 (CompNanoEnergy) and CA21101 (COSY). M. R.-P. acknowledges the Ministerio de Ciencia e Innovación (MICIN) for a Formación Personal Investigador (FPI) fellowship (PRE2019-087627). We also thank

the Red Española de Supercomputación (RES) for the provision of supercomputing time.

References

1 H. Idriss, *Curr. Opin. Chem. Eng.*, 2020, **29**, 74–82.
2 J. Ryu and W. Choi, *Environ. Sci. Technol.*, 2008, **42**, 294–300.
3 L. Mino, Á. Morales-García, S. T. Bromley and F. Illas, *Nanoscale*, 2021, **13**, 6577–6585.
4 K. Kobayakawa, Y. Nakazawa, M. Ikeda, Y. Sato and A. Fujishima, *Ber. Bunsenges Phys. Chem.*, 1990, **94**, 1439–1443.
5 J. Wang, X. Liu, R. Li, P. Qiao, L. Xiao and J. Fan, *Catal. Commun.*, 2012, **19**, 96–99.
6 A. Di Paola, M. Bellardita, L. Palmisanoa, Z. Barbierikovác and V. Brezovác, *J. Photochem. Photobiol., A*, 2014, **273**, 59–67.
7 E. G. Panarelli, S. Livraghi, S. Maurelli, V. Polliotto, M. Chiesa and E. Giamello, *J. Photochem. Photobiol., A*, 2016, **322**, 27–34.
8 E. A. Abdullah, *Eur. J. Chem.*, 2019, **10**, 82–94.
9 H. L. Tan, F. F. Abdi and Y. H. Ng, *Chem. Soc. Rev.*, 2019, **48**, 1255–1271.
10 M. G. Walter, E. L. Warren, J. R. McKone, S. W. Boettcher, Q. Mi, E. A. Santori and N. S. Lewis, *Chem. Rev.*, 2010, **110**, 6446–6473.
11 D. O. Scanlon, C. W. Dunnill, J. Buckeridge, S. A. Shevlin, A. J. Logsdail, S. M. Woodley, C. R. A. Catlow, M. J. Powell, R. G. Palgrave, I. P. Parkin, G. W. Watson, T. W. Keal, P. Sherwood, A. Walsh and A. Sokol, *Nat. Mater.*, 2013, **12**, 798–801.
12 O. Lamiel-Garcia, K. C. Ko, J. Y. Lee, S. T. Bromley and F. Illas, *J. Chem. Theory Comput.*, 2017, **13**, 1785–1793.
13 K. C. Ko, S. T. Bromley, J. Y. Lee and F. Illas, *J. Phys. Chem. Lett.*, 2017, **8**, 5593–5598.
14 X. Chen and S. S. Mao, *Chem. Rev.*, 2007, **107**, 2891–2959.
15 M. Maeda and T. Watanabe, *Surf. Coat. Technol.*, 2007, **201**(22–23), 9309–9312.
16 Á. Morales-García, A. M. Escatllar, F. Illas and S. T. Bromley, *Nanoscale*, 2019, **11**, 9032–9041.
17 Y.-H. Wang, K. H. Rahman, C.-C. Wu and K.-C. Chen, *Catalysts*, 2020, **10**(6), 598.
18 A. Fuerte, M. D. Hernández-Alonso, A. J. Maira, A. Martinez-Arias, M. Fernandez-Garcia, J. C. Conesa and J. Soria, *Chem. Commun.*, 2001, **24**, 2718–2719.
19 E. R. Remesal and Á. Morales-García, *Phys. Chem. Chem. Phys.*, 2022, **24**, 21381–21387.
20 O. Fontelles-Carceller, M. J. Muñoz-Batista, E. Rodríguez-Castellón, J. C. Conesa, M. Fernández-García and A. Kubacka, *J. Catal.*, 2007, **347**, 157–169.
21 H. I. Elsaeedy, A. Qasem, H. A. Yakout and M. Mahmoud, *J. Alloys Compd.*, 2021, **867**, 159150.
22 M. Allès, E. R. Remesal, F. Illas and Á. Morales-García, *Adv. Theory Simul.*, 2022, **6**(10), 2200670.
23 A. Cuko, A. M. Escatllar, M. Calatayud and S. T. Bromley, *Nanoscale*, 2018, **10**, 21518–21532.
24 N. Yaacobi-Gross, M. Soreni-Harari, M. Zimin, S. Kababya, A. Schmidt and N. Tessler, *Nat. Mater.*, 2011, **10**, 974.
25 P. R. Brown, D. Kim, R. R. Lunt, N. Zhao, M. G. Bawendi, J. C. Grossman and V. Bulovic, *ACS Nano*, 2014, **8**, 5863–5872.
26 D. M. Kroupa, M. Vörös, N. P. Brawand, B. W. McNichols, E. M. Miller, J. Gu, A. J. Nozik, A. Sellinger, G. Galli and M. C. Beard, *Nat. Commun.*, 2017, **8**, 15257.
27 R. Wick-Joliat, T. Musso, R. R. Prabhakar, J. Löckinger, S. Siol, W. Cui, L. Sévery, T. Moehl, J. Suh, J. Hutter, M. Iannuzzi and S. D. Tilley, *Energy Environ. Sci.*, 2019, **12**, 1901.
28 F.-Y. Fu, I. Shown, C.-S. Li, P. Raghunath, T.-Y. Lin, T. Billo, H.-L. Wu, C.-I. Wu, P.-W. Chung, M.-C. Lin, L.-C. Chen and K.-H. Chen, *ACS Appl. Mater. Interfaces*, 2019, **11**, 25186.
29 S. Yang, D. Prendergast and J. B. Neaton, *Nano Lett.*, 2012, **12**, 383–388.
30 M. Reeio-Poo, Á. Morales-García, F. Illas and S. T. Bromley, *Nanoscale*, 2023, **15**, 4809–4820.
31 D. Zhang, M. Yang and S. Dong, *J. Phys. Chem. C*, 2015, **119**, 1451.
32 D. Zhang, M. Yang and S. Dong, *Phys. Chem. Chem. Phys.*, 2015, **17**, 29079–29084.
33 S. Kirkpatrick, C. D. Gelatt Jr and M. P. Vecchi, *Science*, 1983, **220**, 671–680.
34 A. Macià Escatllar, Á. Morales-García, F. Illas and S. T. Bromley, *J. Chem. Phys.*, 2019, **150**, 214305.
35 J. D. Gale and A. L. Rohl, *Mol. Simul.*, 2003, **29**, 291–341.
36 V. Blum, R. Gehre, F. Hanke, P. Havu, V. Havu, X. Ren, K. Reuter and M. Scheffler, *Comput. Phys. Commun.*, 2009, **180**, 2175–2196.
37 J. Perdew, K. Burke and M. Ernzerhof, *Phys. Rev. Lett.*, 1996, **77**, 3865–3868.
38 Á. Morales-García, R. Valero and F. Illas, *J. Phys. Chem. C*, 2017, **121**, 18862–18866.
39 I. de P. R. Moreira, F. Illas and R. L. Martin, *Phys. Rev. B: Condens. Matter Mater. Phys.*, 2002, **65**, 155102.
40 K. C. Ko, O. Lamiel-García, J. Y. Lee and F. Illas, *Phys. Chem. Chem. Phys.*, 2016, **18**, 12357–12367.
41 Á. Morales-García, R. Valero and F. Illas, *Phys. Chem. Chem. Phys.*, 2018, **20**, 18907.
42 B. Kraeutler and A. J. Bard, *J. Am. Chem. Soc.*, 1978, **100**, 5985–5992.
43 J. Buckeridge, K. T. Butler, C. R. A. Catlow, A. J. Logsdail, D. O. Scanlon, S. A. Shevlin, S. M. Woodley, A. A. Sokol and A. Walsh, *Chem. Mater.*, 2015, **27**(11), 3844–3851.
44 D. Cho, K. C. Ko, O. Lamiel-Garcia, S. T. Bromley, J. Y. Lee and F. Illas, *J. Chem. Theory Comput.*, 2016, **12**(8), 3751–3763.
45 S. Trasatti, *Pure Appl. Chem.*, 1986, **58**, 955.
46 F. Hirshfeld, *Theor. Chim. Acta*, 1977, **44**, 129–138.
47 L. Burnelle and C. A. Coulson, *Trans. Faraday Soc.*, 1957, **53**, 403–405.
48 L. Zhao, Q. Cao, A. Wang, J. Duan, W. Zhou, Y. Sang and H. Liu, *Nano Energy*, 2018, **45**, 118.
49 M. Abbas, T. ul Haq, S. N. Arshad and M. Zaheer, *Mol. Catal.*, 2020, **488**, 110894.

50 Z. Yang, Z. Qiang, J. Wang, Y. Wang and W. Yao, *Small Struct.*, 2024, **5**, 2300339.
51 L. E. Walle, A. Borg, E. M. J. Johansson, S. Plogmaker, H. Rensmo, P. Uvdal and A. Sandell, *J. Phys. Chem. C*, 2011, **115**(19), 9545–9550.
52 I. M. Nadeem, J. P. Treacy, S. Selcuk, X. Torrelles, H. Hussain, A. Wilson, D. C. Grinter, G. Cabailh, O. Bikondoa, C. Nicklin, A. Selloni, J. Zegenhagen, R. Lindsay and G. Thornton, *J. Phys. Chem. Lett.*, 2018, **9**(11), 3131–3136.

THE JOURNAL OF PHYSICAL CHEMISTRY C
A JOURNAL OF THE AMERICAN CHEMICAL SOCIETY
pubs.acs.org/JPCC Article

Impact of Surface Hydroxylation on the Structural and Electronic Properties of 2−3.5 nm Diameter Crystalline and Amorphous Titania Nanoparticles

Published as part of The Journal of Physical Chemistry C special issue "Francesc Illas and Gianfranco Pacchioni Festschrift".

Miguel Recio-Poo, Ángel Morales-García,* and Stefan T. Bromley*

Cite This: J. Phys. Chem. C 2025, 129, 3299−3309 Read Online

ABSTRACT: We investigate how surface hydroxylation affects the energetic stability and electronic properties of 2−3 nm diameter titania (TiO_2) nanoparticles (NPs) using density functional theory based calculations. Specifically, crystalline anatase NPs with faceted morphologies are compared to quasi-spherical amorphous NPs in their anhydrous $(TiO_2)_{84}$ and hydroxylated $(TiO_2)_{84}(H_2O)_m$ states. In the anhydrous case, amorphous NPs are more energetically stable than anatase NPs. Surface hydroxylation is energetically favorable for both of the NP types. However, at higher −OH coverages, the stabilization from hydroxylation is less for amorphous NPs relative to crystalline NPs, leading to a convergence in energetic stability. Eventually, for high hydroxylation, a crossover in energetic stability occurs, where hydroxylated anatase NPs become more stable than hydroxylated amorphous NPs. This stability crossover occurs at a lower degree of hydroxylation for $(TiO_2)_{84}$ NPs than previously predicted for smaller $(TiO_2)_{35}$ systems. Hydroxylation also affects electronic properties due to the cumulative effect of the bound OH groups, leading to a ligand-induced dipole effect. In addition to energetic stability convergence, we also find a convergence in electronic properties (e.g., band gaps and band edge energies) with increasing hydroxylation for both NP types. Our results further underscore how small amorphous TiO_2 NPs can be tuned by surface functionalization (e.g., hydroxylation in aqueous environments) to behave as crystalline mimicking "crystalike" systems. These insights help provide a pathway for optimizing TiO_2 NPs for photocatalytic applications, where controlling the electronic structure is crucial.

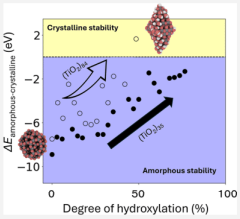

■ INTRODUCTION

Titanium dioxide (TiO_2), commonly referred to as titania, is a highly studied wide band gap semiconductor material with applications ranging across various fields, such as photocatalysis,[1−3] photovoltaics,[4] and environmental remediation.[5] Titania's remarkable properties, such as strong oxidizing power, chemical stability, and nontoxicity, have made it a material of choice for catalyzing reactions like water splitting[6,7] and degradation of organic pollutants,[5,8] and for use in dye-sensitized solar cells.[9] Among the polymorphs of TiO_2, anatase has attracted the most attention due to its superior photocatalytic activity compared with the rutile and brookite phases. This advantage is primarily attributed to the higher capacity of anatase to efficiently generate and transport charge carriers when irradiated with UV light.[10,11]

The properties of TiO_2 can be further affected when its size is reduced to the nanoscale. Titania nanoparticles (NPs) are affected by size-dependent quantum confinement (QC) effects which significantly influence the electronic band gap energy,[12] which in turn affects photocatalytic performance. QC is particularly prominent in NPs with diameters below 10 nm, where it leads to significantly increased gaps between electronic energy levels compared to bulk titania.[13] Decrease in size also leads to changes in structural stability, where in contrast to bulk titania, the anatase polymorph becomes more thermodynamically stable than rutile for NPs with diameters less than approximately 14 nm.[14] For smaller NPs, with diameters less than ∼2 to 3 nm, amorphous noncrystalline structures become more favored.[15,16]

The stability and electronic properties of nano-TiO_2 systems can also be affected by interactions with their environment. Here, water can play a crucial role in tuning structural and electronic properties.[17,18] When bare TiO_2 NPs are exposed to aqueous environments, water molecules dissociate to form

Received: November 29, 2024
Revised: January 22, 2025
Accepted: January 23, 2025
Published: February 4, 2025

https://doi.org/10.1021/acs.jpcc.4c08070
J. Phys. Chem. C 2025, 129, 3299−3309

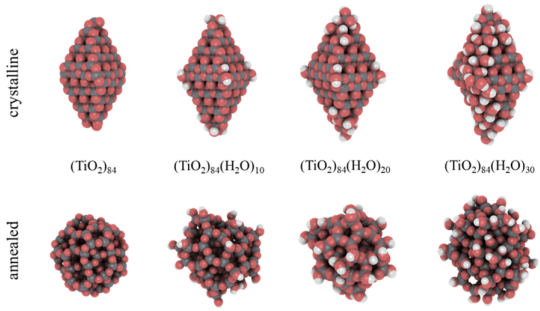

Figure 1. DFT-optimized structures of the crystalline anatase (top) and annealed amorphous (bottom) $(TiO_2)_{84}(H_2O)_m$ NPs for m = 0, 10, 20, and 30. Atom color key: Ti—gray, O—red, H—white.

hydroxyl (−OH) groups on the NP surface.[19,20] This hydroxylation can stabilize the NPs by passivating undercoordinated surface defects, which are prevalent due to the high surface-to-volume ratio in nanoscale materials. In addition to affecting the stability of TiO_2 NPs,[21] strongly bound water (e.g., surface hydroxyl groups) can have a significant impact on the electronic and structural properties of TiO_2 nanostructures. In this way, previous work has shown that hydroxylation can be employed to tune electronic and structural properties of $(TiO_2)_{35}$ NPs.[22] The influence of hydroxylation can be so strong that at high −OH coverages, the energetic stability and electronic properties of small crystalline anatase NPs and amorphous NPs converge. This energetic and electronic convergence is linked to an −OH-induced local structural convergence, whereby, regardless of crystallinity, the distributions of local atomic coordination environments become similar in both types of NPs. Hydroxylation can therefore be used to induce the characteristic electronic structure of crystalline anatase in thermodynamically preferred amorphous NPs. We refer to such crystalline-mimicking amorphous NPs as crystalike NPs.[22] In this way, we have previously proposed that, in the ∼1−2 nm NP size regime, the anatase crystal structure may not be as essential as previously assumed for achieving an electronic structure that is favorable for photocatalytic applications.

Surface hydroxylation of NPs also introduces an additional layer of complexity through the ligand-induced dipole effect (LIDE).[23] As demonstrated in previous studies,[24−26] the intrinsic dipolar nature of the hydroxyl groups leads to a cumulative electrostatic effect that shifts the electronic energy levels, including the highest occupied molecular orbital (HOMO) and the lowest unoccupied molecular orbital (LUMO). This shift mainly depends on the hydroxyl coverage, but is also affected by the formation of hydrogen bonds between hydroxyl groups, which can moderate the extent of the shift.[20,24] The LIDE becomes particularly relevant in systems where controlling the electronic properties are essential for optimizing photocatalytic performance, as it allows for fine-tuning the band edges without significantly altering the band gap magnitude.

In this work, we build upon our previous studies[22,24] to explore the properties of $(TiO_2)_{84}$ NPs, focusing on two distinct structural families: faceted crystalline anatase and noncrystalline amorphous NPs. These NPs have diameters in the range of 1.9−3.4 nm, striking a balance between a size where QC effects are significant and which starts to become relevant for practical applications. In line with our previous work on the smaller $(TiO_2)_{35}$ NP system, we find a convergence in different properties (e.g., stability, local coordination environments, and electronic energy gaps) for amorphous and crystalline $(TiO_2)_{84}$ NPs when reaching high degrees of hydroxylation. Interestingly, for the $(TiO_2)_{84}$ NPs, we find a faster convergence of all considered properties with respect to the degree of hydroxylation, suggesting that surface hydroxylation is more efficient at promoting this convergence in stability in larger NPs. Analogously to the $(TiO_2)_{35}$ NP case, this hydroxylation-induced convergence is not related to crystallinity or morphology but is associated with the degree of similarity in the distribution of local atomic coordination environments. Lastly, we also analyze the effect of LIDE in these systems to rationalize the observed shifts in the HOMO and LUMO energy levels for both faceted and annealed NPs as a function of surface hydroxylation. By analyzing the differences between the two structural families of NPs, we further confirm that the structural and energetic differences between crystalline and noncrystalline titania NPs can be minimized through surface hydroxylation. In this way, this study aims to extend our understanding of how to optimize the properties of TiO_2 NPs for applications, particularly in environments in which water plays a significant role in determining their functionality.

■ COMPUTATIONAL DETAILS AND MODELS

NP Models. Our study provides a systematic analysis of several structural, energetic, and electronic properties of two families of $(TiO_2)_{84}(H_2O)_m$ NPs, covering a wide range of degrees of hydroxylation. We consider both anatase crystalline faceted NPs and amorphous quasi-spherical NPs (see Figure 1). The hydroxylation of the NPs is assumed to occur in a dissociative manner by water molecules, where for every chemisorbed H_2O molecule −OH and −H groups are attached to undercoordinated Ti and O surface atoms, respectively.[19] Herein, we consider progressive hydroxylation of the respective anhydrous NPs by adding two water molecules at each step. We define the degree of hydroxylation as the number of water

https://doi.org/10.1021/acs.jpcc.4c08070
J. Phys. Chem. C 2025, 129, 3299−3309

molecules (m) divided by the maximum number of water molecules that can dissociate to form hydroxyl (−OH) groups on the faceted NP surface (m_{max}). Note that for the present $(TiO_2)_{84}(H_2O)_m$ NP system, we find a m_{max} value of 62.

As described in previous works,[12,15,27,28] the initially anhydrous faceted NP is obtained from a top-down cut from bulk anatase crystal structure following the Wulff construction.[29] This procedure leads to bipyramidal NPs exhibiting the thermodynamically stable (101) surface on all facets, as corroborated in experiments.[30] The energetic stability of hydroxylation in these NPs depends on the coordination environment of the surface atoms. In this way, hydroxylation was performed manually, considering the varying reactivity of the different NP surface sites (i.e. apical > equatorial > edge > facet).[19,31] Apical sites, having the lowest coordination, are the most reactive, followed by equatorial corners, edges, and finally facets, which are the least reactive. Subsequently, the hydroxylated NPs were fully optimized using density functional theory (DFT)-based calculations (see details below). This process was repeated iteratively, hydroxylating the NPs step by step and generating a series of crystalline anatase NPs with the composition $(TiO_2)_{84}(H_2O)_m$, for m = 0−62 (see Figure 1 top panel). These increasingly hydroxylated faceted NPs have a corresponding range of diameters between 2.9 and 3.3 nm.

The second set of non-crystalline (amorphous) $(TiO_2)_{84}$ NPs were generated through a simulated annealing (SA) procedure.[32] Following a SA protocol established in previous work,[22] we began with the crystalline $(TiO_2)_{84}(H_2O)_m$ NP, which was then subjected to a progressive temperature-dependent annealing process using classical molecular dynamics (MD) simulations (see details below). For every step of hydroxylation consisting of adding two water molecules, the NP was again thermally annealed to search for low energy $(TiO_2)_{84}(H_2O)_m$ NP structures with m = 0−30, generally leading to significant changes in all atomic positions and the NP morphology. This implies that every NP in the series of progressively hydroxylated thermally annealed NPs is structurally independent of each other, unlike in the case of the crystalline anatase NPs. The thermally annealed NPs were then optimized using DFT-based calculations (see below). The maximum diameters of these NPs range between 1.9 and 2.3 nm depending on the degree of hydroxylation (see selected NP structures in the Figure 1 bottom panel).

MD-Based SA Procedure. The simulated thermal annealing procedure was carried out using classical MD simulations using the NanoTiO interatomic potential,[28,33] as implemented in the GULP code.[34] Following our previous work,[22] the MD-SA process begins by heating the respective crystalline anatase $(TiO_2)_{84}(H_2O)_m$ NP to ∼1800 K over a period of 1000 ps. Once the target temperature is achieved, the NP is maintained at this maximum temperature for 300 ps to ensure full disordering of the crystalline structure. After this equilibration phase, the NP undergoes a controlled cooling process. The temperature is gradually reduced from 1800 to 1550 K over 125 ps, then maintained at 1550 K for another 300 ps. This reduce-and-maintain stepwise process is repeated until the NP is cooled to 300 K over an additional ∼4000 ps, ensuring the formation of a stable, low-energy amorphous configuration. Figure S1 of the Supporting Information shows the temperature evolution profile throughout the whole MD−SA runs. Contrary to the relatively unaltered crystalline faceted counterparts, the structural framework of the annealed NPs changes as hydroxylation increases due to the thermal annealing process. After the MD-SA procedure, a selection of low energy amorphous NP structures are then optimized using DFT to refine the atomic positions and minimize residual forces. All reported calculated properties pertain to the lowest energy NPs resulting from this procedure.

DFT Calculations. All structural optimizations and electronic property calculations were performed using DFT based calculations as implemented in the FHI-aims code.[35] The Perdew−Burke−Ernzerhof (PBE)[36] exchange−correlation functional was used for geometry optimization, while a hybrid functional (PBEx) with 12.5% Fock exchange was employed to calculate electronic properties such as the HOMO−LUMO gap.[37,38] All calculations utilized a light tier-1 numerical atom-centered orbital basis set, providing accuracy comparable to a TZVP Gaussian-type orbital basis set for TiO_2.[12] The convergence criteria for atomic forces and total energy during the relaxation of the NP structures were set at 10^{-5} eV Å^{-1} and 10^{-6} eV, respectively.

RESULTS AND DISCUSSION

Energetic Stability with Increasing Hydroxylation. Throughout our results for the $(TiO_2)_{84}(H_2O)_m$ NPs, we compare our findings with those of our previous work on the smaller $(TiO_2)_{35}(H_2O)_m$ NP system. We evaluate the energetic stability of the amorphous and crystalline $(TiO_2)_{84}(H_2O)_m$ NPs with respect to the degree of hydroxylation by first analyzing ΔE_{tot}, defined as the difference in the total energy between the two types of NP for the same degree of hydroxylation. Using this quantity, Figure 2 shows that the annealed $(TiO_2)_{84}(H_2O)_m$ NPs are energetically more stable than their crystalline counterparts for most of the considered degrees of hydroxylation. Comparing with the corresponding data for the $(TiO_2)_{35}(H_2O)_m$ system, we see that the ΔE_{tot} dependence on hydroxylation for both NP sizes displays several similarities. For instance, in both NP systems, ΔE_{tot} tends to be negative and have the largest magnitude (i.e., greatest excess stability of amorphous NPs) for the anhydrous NPs. Also, in both systems, at a hydroxylation degree of ∼25% only a slight overall decrease in the magnitude of ΔE_{tot} is

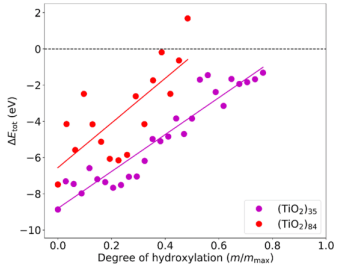

Figure 2. Calculated total energy differences (ΔE_{tot}) between anatase crystalline faceted NPs and amorphous annealed NPs for the $(TiO_2)_{35}(H_2O)_m$ system (purple) and the $(TiO_2)_{84}(H_2O)_m$ system (red) with respect to degree of hydroxylation (m/m_{max}). Linear fits to the data are added as rough indications of tendencies to facilitate comparison between both NP system sizes. Data for the $(TiO_2)_{35}$ based NP system are from ref 22.

https://doi.org/10.1021/acs.jpcc.4c08070
J. Phys. Chem. C 2025, 129, 3299−3309

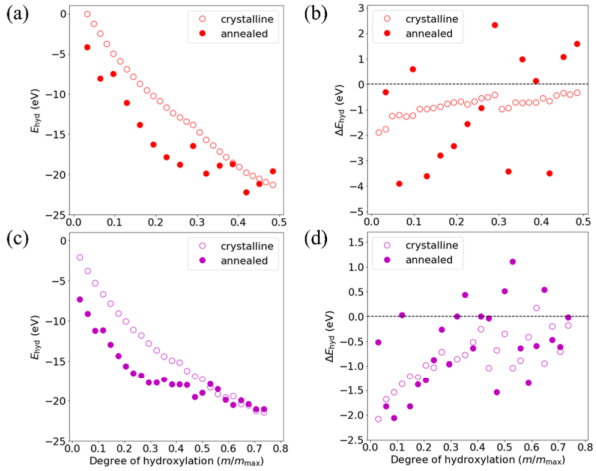

Figure 3. (a) Variation of $E_{hyd}(m)$ with respect to the degree of hydroxylation (m/m_{max}) for increasingly hydroxylated crystalline and annealed $(TiO_2)_{84}(H_2O)_m$ NPs. The hydration energy of the faceted NP with two water molecules is set to 0 eV as an offset, with the total energy of the bare crystalline NP [$E_{tot}(0)$] used as the common reference for both sets of NPs. (b) Variation of $\Delta E_{hyd}(m)$ with the number of water molecules (m). Plots (c,d) correspond to the m-dependent tendencies in $E_{hyd}(m)$ and $\Delta E_{hyd}(m)$ for amorphous and crystalline $(TiO_2)_{35}(H_2O)_m$ NPs, respectively.[22]

observed. However, above this degree of hydroxylation, the magnitude ΔE_{tot} in both systems tends to decrease more rapidly. For the $(TiO_2)_{84}(H_2O)_m$ system, we observe that the energetic stability of the annealed amorphous NPs becomes comparable to that of the faceted crystalline NPs for 50% hydroxylation. This convergence is achieved for a lower degree of hydroxylation than for the $(TiO_2)_{35}$-based NP system, where such a situation is achieved at 75% hydroxylation.

These findings reinforce our prediction that upon increasing the degree of hydroxylation titania NPs with different morphologies become comparable in terms of their energetic stability. A plausible explanation for the difference in the degree of hydroxylation required to induce this convergence in the two considered NP system sizes lies in the respective difference in ΔE_{tot} for the anhydrous case. In the anhydrous $(TiO_2)_{84}$ NP case, ΔE_{tot} is −7.49 eV, which is smaller in magnitude than the corresponding value for the $(TiO_2)_{35}$ NP system (−8.87 eV). Normalizing each value by the number of respective TiO_2 units, we obtain ∼−0.09 eV/TiO_2 for the $(TiO_2)_{84}$ NP system, and ∼−0.25 eV/TiO_2 for the $(TiO_2)_{35}$ NP system. These values are in very good agreement with a previous study analyzing the size-dependent emergence of crystallinity in anhydrous titania NPs.[15] This work predicts that anhydrous amorphous titania NPs are energetically more favorable than anhydrous crystalline NPs up to a diameter of approximately 2−3 nm, whereupon a stability crossover occurs. Following this finding, we predict that with increasing system size, fewer and fewer water molecules will be required to achieve a competitive energetic situation between crystalline and amorphous NPs. Finally, we note that, compared to the $(TiO_2)_{35}(H_2O)_m$ NP system, the larger number of atoms in the $(TiO_2)_{84}(H_2O)_m$ NPs leads to a significantly larger configurational space for the MD-SA runs to explore. This makes it much more challenging to identify low energy $(TiO_2)_{84}(H_2O)_m$ NP structures, particularly in the hydroxylated cases. For this reason, the ΔE_{tot} data in Figure 2 is more scattered for the $(TiO_2)_{84}(H_2O)_m$ NP system than for the $(TiO_2)_{35}(H_2O)_m$ NP system. However, the clear similarity in the overall tendencies in each case gives us confidence in the reliability and consistency of our findings.

In Figure 3, we compare the hydroxylation-dependent total hydration energies (E_{hyd}) for faceted crystalline and annealed amorphous NPs for the $(TiO_2)_{84}(H_2O)_m$ and $(TiO_2)_{35}(H_2O)_m$ systems. E_{hyd} is defined as

$$E_{hyd}(m) = E_{tot}(m) - (E_{tot}(0) + m \cdot E_{H_2O}) \quad (1)$$

where $E_{tot}(m)$ corresponds to the total energy of a NP with a m chemisorbed water molecules, $E_{tot}(0)$ corresponds to the total energy of the reference anhydrous NP, and E_{H_2O} is the total energy of a water molecule.

Figure 3a shows the evolution of E_{hyd} with respect to the degree of hydroxylation for annealed and crystalline $(TiO_2)_{84}(H_2O)_m$ NPs. Here, the reference energy is taken to be that of the anhydrous crystalline NP in both cases, leading to an initial energetic downshift in the data corresponding to the comparatively more stable amorphous NPs for lower degrees of hydroxylation (see Figure 2). As hydroxylation increases, higher degrees of hydroxylation entail a less effective stabilizing effect for the amorphous NPs compared to the faceted crystalline NPs.[22,33] For $(TiO_2)_{84}(H_2O)_{28}$, which corresponds to ∼45% hydroxylation, the total hydration energies of the two types of NP converge to −21.14 eV

https://doi.org/10.1021/acs.jpcc.4c08070
J. Phys. Chem. C 2025, 129, 3299−3309

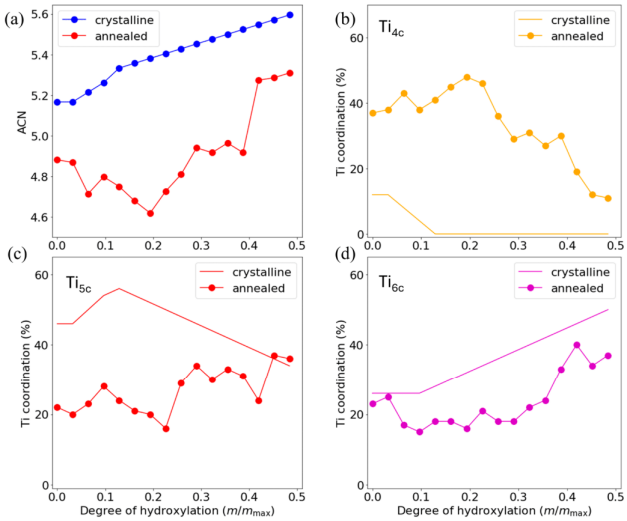

Figure 4. (a) Average coordination number (ACN) of Ti centers for the annealed amorphous and crystalline anatase $(TiO_2)_{84}(H_2O)_m$ NPs with respect to the degree of hydroxylation. (b–d) Corresponding evolution of the distribution of 4-, 5-, and 6-fold local atomic coordination environments of Ti centers (Ti_{4c}, Ti_{5c}, and Ti_{6c}) with respect to the degree of hydroxylation of both crystalline and annealed $(TiO_2)_{84}(H_2O)_m$ NPs.

(annealed) and −20.51 eV (faceted), indicating that the amorphous NPs have reached a comparable energetic stability to the crystalline NPs. When further water molecules are dissociatively adsorbed, a crossover in hydration energies occurs, where crystalline NPs become energetically more stable than amorphous NPs. For comparison, we also include the analogous E_{hyd} results for the $(TiO_2)_{35}(H_2O)_m$ NP system, which shows tendencies very similar to those of the $(TiO_2)_{84}(H_2O)_m$ system.

To get further insight into the hydroxylation energetics of the $(TiO_2)_{84}(H_2O)_m$ NPs, we also compute the incremental hydration energies defined as

$$\Delta E_{hyd}(m) = E_{tot}(m) - (E_{tot}(m-1) + E_{H_2O}) \quad (2)$$

This value quantifies the energy change associated with the addition of each successive water molecule. For the faceted crystalline $(TiO_2)_{84}(H_2O)_m$ NP, which retains a persistent anatase core structure throughout hydroxylation, the incremental hydration energies follow a pattern of progressive energetic stabilization, with all H_2O additions having negative $\Delta E_{hyd}(m)$ values (see Figure 3b). In this system, the magnitude of $\Delta E_{hyd}(m)$ is highest for the lowest degrees of hydroxylation, starting at ∼−1.8 eV for the first two water molecules. This strong initial stabilization reflects the dissociative adsorption of water on highly under-coordinated surface sites, such as apical or edge positions. As hydroxylation proceeds and these more reactive sites become saturated, the magnitude of $\Delta E_{hyd}(m)$ decreases, reaching approximately −0.55 eV at 16 water molecules and fluctuates around this value for higher hydroxylation levels. This trend mirrors observations made for the smaller $(TiO_2)_{35}(H_2O)_m$ NP system (Figure 3d), where the dissociative reaction energy magnitude of each successive H_2O molecule diminishes as surface coordination increases. This predictable, stepwise hydration behavior reflects the orderly fixed atomic arrangement of the faceted NPs.

In contrast, the amorphous NPs, which are generated through thermal annealing and thus lack a fixed core structure, display larger fluctuations in $\Delta E_{hyd}(m)$. For instance, after an initial stabilization of −0.31 eV with the first two water molecules, the incremental hydration energies vary significantly, reaching as high as +2.32 eV at 18 water molecules (∼30% degree of hydroxylation). These larger fluctuations likely reflect significant structural reconfigurations within the annealed NPs for different degrees of hydroxylation. Unlike the crystalline NPs, each degree of hydroxylation in the annealed NPs may result in substantial changes in both the overall structure of the NP and the location of the hydroxyl groups, making the process less predictable. The positive values of $\Delta E_{hyd}(m)$ observed at certain degrees of hydroxylation (e.g., 18 and 30 water molecules) indicates that suboptimal low-energy NP structures were found by the MD−SA procedure in these cases. This behavior indicates that some energetically costly structural adjustments are required to accommodate additional water molecules as the NP surface becomes more saturated. As such, the overall hydroxylation-induced stabilization trend for amorphous $(TiO_2)_{84}(H_2O)_m$ NPs is less orderly than that of crystalline NPs. This more stochastic convergence of $\Delta E_{hyd}(m)$ values is also seen for the amorphous $(TiO_2)_{35}(H_2O)_m$ NP system (Figure 3d). Overall, the similarities in the general trends of $\Delta E_{hyd}(m)$ observed for the $(TiO_2)_{84}(H_2O)_m$ and

https://doi.org/10.1021/acs.jpcc.4c08070
J. Phys. Chem. C 2025, 129, 3299−3309

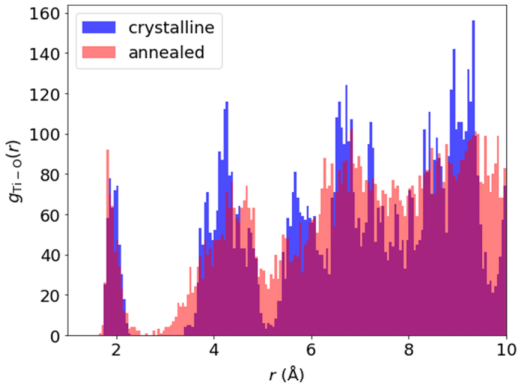

Figure 5. Pair distribution function (PDF) for Ti−O distances in a faceted crystalline anatase NP (blue) and thermally annealed NP (red), both with a $(TiO_2)_{84}(H_2O)_{30}$ composition. The bin size for the histogram is 0.05 Å.

$(TiO_2)_{35}(H_2O)_m$ NP systems indicate that the fundamental mechanisms of stabilization through hydroxylation are consistent for both NP sizes.

Local Structural Analysis. We examine the local structure of both the faceted and annealed amorphous $(TiO_2)_{84}(H_2O)_m$ NPs throughout the range of considered hydroxylation by analyzing the coordination environments of Ti atoms. By counting the number of oxygen atoms around each Ti center within a cutoff distance of 2.5 Å (slightly larger than the average Ti−O bond distance in the anatase bulk crystalline structure), we obtain the number of 4-, 5-, and 6-coordinated Ti centers. The average coordination number (ACN) for a NP is calculated by summing the coordination values for each Ti atom in the NP and dividing by the total number of Ti centers.

For the crystalline faceted $(TiO_2)_{84}(H_2O)_m$ NPs, the ACN steadily increases with hydroxylation (see Figure 4a), ranging from 5.17 for the bare anhydrous NP to approximately 5.60 at higher degrees of hydroxylation. This increase is primarily due to the formation of new Ti−OH bonds on the surface. For this reason, compared to the evolution of the ACN when hydroxylating a smaller $(TiO_2)_{35}$ crystalline NP,[22] we get a proportionally smaller ACN increase. Minor fluctuations in the ACN values are attributed to localized surface relaxation processes upon hydroxylation. These fluctuations tend to slightly reduce Ti coordination in certain areas while increasing it in others, reflecting a subtle restructuring of the NP surface.

In contrast, the annealed amorphous $(TiO_2)_{84}(H_2O)_m$ NPs exhibit a lower initial ACN value of 4.89, which, unlike the crystalline NPs, decreases in the early stages of hydroxylation, reaching a minimum of 4.62 for around a 20% degree of hydroxylation. This initial decrease suggests a more substantial restructuring of the annealed NPs, due to the surface hydroxyl groups. However, as hydroxylation increases, the ACN increases and approaches that of the faceted NPs at higher hydroxylation levels. By the time 26 water molecule are added (∼42% degree of hydroxylation), the ACN for annealed NPs reaches around 5.27, which is similar to that of the faceted NP at this degree of hydroxylation (5.55).

This trend indicates that the local structural environments of annealed amorphous NPs become similar to that of crystalline faceted NPs as hydroxylation increases, as also observed in the $(TiO_2)_{35}(H_2O)_m$ NP system.[22] However, the hydroxylation-induced convergence of the coordination numbers in the $(TiO_2)_{84}(H_2O)_m$ NP system is somewhat slower than that observed for the smaller $(TiO_2)_{35}(H_2O)_m$ NP system. This difference lies in contrast with the relatively more rapid energetic stability convergence of crystalline and amorphous NPs in the $(TiO_2)_{84}(H_2O)_m$ NP system compared to that of the $(TiO_2)_{84}(H_2O)_m$ NP system (see Figure 2). This mismatch between structural and energetic convergence tendencies could indicate that only a subset of NP atoms is mainly responsible for energetic stability, whereas all are taken into account in the ACN.

Further analyses were carried out by examining the separate ACN values for 4-, 5-, and 6-coordinated Ti atoms (denoted as Ti_{4c}, Ti_{5c}, and Ti_{6c}), as shown in Figure 4b−d. For both NP types, the evolution of Ti_{6c} atoms follows a similar trend as for the total ACN, with the proportion of Ti_{6c} centers increasing with hydroxylation. Initially, both crystalline and amorphous $(TiO_2)_{84}(H_2O)_m$ NPs contain approximately 25% Ti_{6c} atoms. As hydroxylation proceeds, the proportion of Ti_{6c} atoms increases steadily, reaching around 50% in the crystalline NPs and 40% in the amorphous NPs by the time the highest degree of hydroxylation is achieved.

The proportion of Ti_{5c} centers provides further insight into the structural changes induced by hydroxylation. In the crystalline NPs, the number of Ti_{5c} centers increase sharply in the initial stages of hydroxylation as low-coordinated Ti_{4c} atoms become hydroxylated. This is followed by a more gradual decrease in the proportion of Ti_{5c} centers, which tends to around 40% for the highest hydroxylation. For annealed NPs, the trend in the proportion of Ti_{5c} centers with hydroxylation is more irregular. Here, the initial proportion of Ti_{5c} atoms remains relatively low and constant before increasing more significantly for higher hydroxylation levels. However, the final proportion of Ti_{5c} centers in the annealed

https://doi.org/10.1021/acs.jpcc.4c08070
J. Phys. Chem. C 2025, 129, 3299−3309

amorphous NPs becomes almost identical to that in the crystalline NPs for high hydroxylation, reflecting again the hydroxylation-induced convergence in local structural environments in the two NP systems.

The Ti_{4c} centers, which correspond to undercoordinated surface Ti sites, decrease with increasing hydroxylation in both NP types. However, the annealed amorphous NPs exhibit a consistently higher proportion of Ti_{4c} centers than the crystalline NPs for all degrees of hydroxylation. This higher proportion of Ti_{4c} surface sites in amorphous NPs seems to be correlated to their relatively higher stability at lower hydroxylation levels (lower than 20%). As hydroxylation progresses, the proportion of Ti_{4c} centers decreases in both NP types, reflecting the saturation of these undercoordinated sites with hydroxyl groups.

To provide an additional measure of the degree of crystallinity, the Ti−O pair distribution function (PDF) for both NP types was analyzed, as shown in Figure 5. The PDF, $g_{Ti-O}(r)$, was calculated as the number of Ti−O pairs at a given distance r, grouped into spherical shells of width Δr. This analysis was performed on the $(TiO_2)_{84}(H_2O)_{30}$ NPs, the most strongly hydroxylated system analyzed in this study for which both crystalline faceted and annealed NPs were available. These NPs serve as a critical case study to test whether hydroxylation of annealed NPs leads to a degree of crystallinity comparable to that in the faceted NPs.

The sharper first peak in the Ti−O PDF for the annealed system compared to the crystalline system is likely a consequence of the MD−SA procedure, which tends to lead to low energy disordered structures. The resulting NP structures appear to achieve their stability via their well-relaxed local Ti−O bonds. In contrast, the crystalline faceted NPs display slightly more deviations in their Ti−O bond lengths due to the constraints imposed by the anatase lattice structure. However, for larger Ti−O distances, the PDF distributions for the annealed NPs exhibit broader and less pronounced peaks compared to those of the crystalline faceted NPs. This broadening highlights the lower long-range order (i.e., crystallinity) of the annealed NPs, which persists even at the highest hydroxylation levels.

Electronic Properties. Here, we investigate the effect of hydroxylation on the electronic HOMO−LUMO energy gap (E_{gap}) and gap edges for both crystalline and annealed amorphous $(TiO_2)_{84}(H_2O)_m$ NPs. Although E_{gap} values based on HOMO−LUMO energy differences do not directly represent experimental observed electronic gap, they serve as an accessible computational metric for analyzing trends in electronic properties. As depicted in Figure 6, the HOMO−LUMO energy gap for the anhydrous crystalline NP is approximately 3.76 eV, which is larger than the electronic energy gap of bulk anatase (around 3.2 eV) due to QC effects.[13] This is in line with the of the anhydrous crystalline $(TiO_2)_{35}$ NP (3.83 eV), where QC is even more pronounced due to the smaller size. Conversely, we do not observe the same trend in the respectively sized anhydrous amorphous NP, where the $(TiO_2)_{35}$ NP exhibits an E_{gap} of 3.43 eV, which is slightly lower than that of the anhydrous $(TiO_2)_{84}$ NP (3.75 eV). This implies that the effect of specific structural features (e.g., defects and reconstruction) dominates over the effect of QC in these irregular anhydrous amorphous NPs.

As the degree of hydroxylation increases, the E_{gap} of the crystalline NPs slightly decreases, reaching a minimum of 3.69 eV when around 15 water molecules are adsorbed. However,

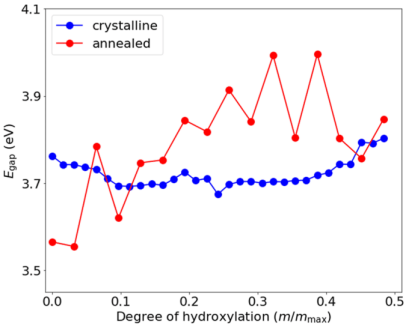

Figure 6. Evolution of E_{gap} with respect to the degree of hydroxylation for crystalline and annealed $(TiO_2)_{84}(H_2O)_m$ NPs.

with further hydroxylation, the E_{gap} begins to increase again, eventually reaching 3.80 eV with 30 water molecules (∼50% hydroxylation). The increase in the energy gap with higher degrees of hydroxylation can be attributed to the healing of undercoordinated sites and the elimination of midgap states, which contribute to stabilizing the electronic structure. The LUMO and HOMO levels (Figure 7) shift upward from −4.56 to −4.0 eV and −8.27 to −7.73 eV, respectively, as hydroxylation increases.

The annealed amorphous NPs exhibit a more complex and fluctuating electronic response to hydroxylation. Such larger fluctuations are due to the correspondingly larger changes to the NP core structure, which is re-evaluated at each hydroxylation step by means of the MD−SA procedure. For the anhydrous amorphous NP, the E_{gap} of 3.5 eV is lower than that of the crystalline NP. As hydroxylation progresses, the E_{gap} decreases slightly but then increases more dramatically, peaking at 4.00 eV with 20 (and 24) water molecules. Despite the fluctuations, the E_{gap} of the annealed NPs reaches a final value of around 3.81 eV with 30 water molecules (ca. 50% hydration degree), which is remarkably close to the final E_{gap} value of the highly hydroxylated crystalline NPs (3.80 eV). The increase in E_{gap} with increasing hydroxylation in the annealed system can also be linked to the healing of undercoordinated surface atoms and the reduction of midgap states. Again, both HOMO and LUMO levels exhibit a larger fluctuating character for the annealed NPs compared with the faceted crystalline NPs.

A key observation from this analysis is that although the crystalline and annealed NPs evolve in distinctly different ways with respect to hydroxylation, their E_{gap} values at high hydroxylation are strikingly similar (∼3.80 eV). This E_{gap} convergence underscores the potential for amorphous annealed NPs to exhibit electronic properties that closely resemble those of their crystalline counterparts.

The energetic alignment of the HOMO and LUMO levels with redox potentials is particularly relevant for photo-excitation applications. For example, the position of the LUMO relative to the hydrogen evolution reaction (HER) redox potential is critical for determining the efficiency of this reaction.[24] Our results show that hydroxylation can tune the position of the LUMO, allowing for better alignment with the

https://doi.org/10.1021/acs.jpcc.4c08070
J. Phys. Chem. C 2025, 129, 3299−3309

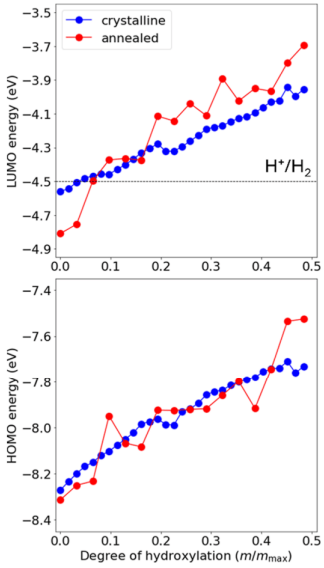

Figure 7. Evolution of the HOMO (lower) and LUMO (upper) energies with respect to the degree of hydroxylation for annealed amorphous and faceted anatase $(TiO_2)_{84}(H_2O)_m$ NPs. The dotted gray line in the upper plot shows the redox potential for the hydrogen evolution reaction, which has an approximate value of −4.5 eV.[39,40]

HER redox potential, which is an essential process in photocatalytic water splitting (see Figure 7, upper panel). Here, we see that by increasing the degree of hydroxylation above aproximately 0.1 would enhance the reducing power of our hydroxylated titania NPs.

Finally, we employ the ligand dipole effect (LIDE) model to rationalize the electronic shifts in the HOMO and LUMO levels as a function of hydroxylation. Previous studies introduced a linear LIDE model describing how the dipoles from chemisorbed ligands at semiconductor surfaces affect the electronic states.[23,25,26,41−43] This model partitions the total dipole moment into two components: the intrinsic dipole of the ligand, which depends on its molecular structure and orientation, and the induced dipole, which arises from structural distortions and charge rearrangement at the interface. The energy shift of the semiconductor's electronic states relative to the vacuum level is proportional to the surface area per ligand and the dielectric constant of the ligand layer. This relationship can be leveraged to tune band edge positions (e.g. modifying ligand dipoles and/orr surface coverage) offering a strategy to optimize the electronic properties of semiconductors for applications such as photocatalysis and optoelectronics.

In the present case, following our previous study,[24] we model the LIDE in our titania NPs by calculating the dipolar contributions of the surface hydroxyl groups. The dipoles in each −OH group arise from the charge separation between the hydrogen and oxygen atoms. For each considered hydroxylated system, we calculate the total dipole pointing toward the NP center by projecting the dipole vector of each −OH group on the NP surface along the radial direction (estimated as the Ti−OH bond direction). Here we use the bond distance (d_{OH}) and angle (α) between the Ti−O−H atoms. The partial charges of the various atoms are determined using the Hirshfeld charge partitioning scheme,[44] and, as in our previous study, are scaled by a constant factor of ∼0.7 to match the experimental dipole moment of a water molecule.[45] The −OH dipole moments depend on the position and magnitude of the positive H charge (Q_H) relative to that of oxygen. The variability of the Ti−O−H angles due to inter-OH hydrogen bonding and the resulting changes in charge distribution, leads to a modulation of the net −OH dipole effect with respct to the degree of hydroxylation. The total dipole moment ($\vec{p}_{OH}$) is then computed as the sum of the contributions from all hydroxyl groups, considering both their charge distribution and geometry

$$\vec{p}_{OH} = \sum_{i=1}^{N} Q_{H,i} \cdot d_{OH,i} \cdot \cos(\alpha_i) \tag{3}$$

where i iterates over the total number (N) of OH groups.

Importantly, the increase in dipole moment with hydroxylation is nonlinear due to the formation of hydrogen bonds (OH···OH) between neighboring hydroxyl groups. These interactions cause a reduction in the Ti−O−H bond angles (α_i) and changes in the partitioned hydrogen atomic charges ($Q_{H,i}$) due to partial delocalization, which both act to moderate the overall dipole contribution as the hydroxyl coverage increases. The induced TiO_2 surface polarization due to the ligand−surface interactions is found to be negligible, in line with previous studies on rutile surfaces.[46]

Overall, the model defined in eq 3 accounts for both the geometric and electrostatic H-bonding effects of hydroxylation, offering a more accurate representation of the LIDE in NPs than in typically employed linear models cited above. In Figure 8 we show how our refined LIDE model and the linear LIDE model give rise to a different $\vec{p}_{OH}$ evolution with respect to the degree of hydroxylation for both crystalline faceted and annealed amorphous NPs. The addition of H-bonding effects via our refined model clearly introduces a stabilizing effect to the linear scaling evolution provided by the simpler linear model. Comparing both types of $(TiO_2)_{84}(H_2O)_m$ NP, we find slightly larger total dipole values for the annealed amorphous case, regardless of the LIDE model employed. This can be attributed to the effect of the less regular surfaces of the amorpous NPs, which results in less efficient OH···OH interactions. Consequently, we find that the respective Ti−O−H angles tend to be less bent, leading to larger dipole moments. The the evolution of $\vec{p}_{OH}$ as we increase the degree of hydroxylation is very similar in both families of NPs, with a slightly larger deviation from the linear trend in the amorphous NP system. This is likely due to the structural disorder inherent to the amorphous NPs, where surface defects and irregularities allow for more variable interactions between hydroxyl groups, resulting in localized changes in the dipole moments. We note that for the highest degrees of hydroxylation, the total cumulative −OH dipole maximum

https://doi.org/10.1021/acs.jpcc.4c08070
J. Phys. Chem. C 2025, 129, 3299−3309

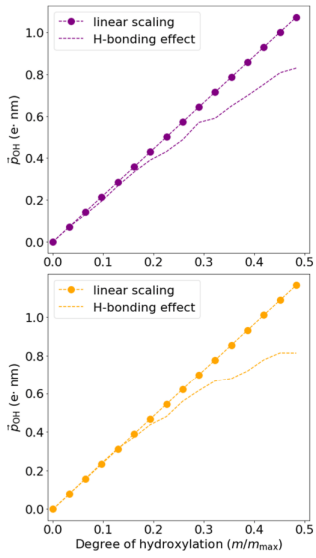

Figure 8. Total −OH dipole moment versus degree of hydroxylation for the crystalline (upper) and amorphous (lower) $(TiO_2)_{84}(H_2O)_m$ NPs with both linear scaling and H-bonding effect LIDE models.

reaches around 55 and 40 debyes for the linear and refined LIDE models, respectively.

Working with our refined LIDE model, one can correlate the evolution of HOMO and LUMO electronic energy levels with respect to hydroxylation-induced $\vec{p}_{OH}$ values obtained with eq 3. In this way, Figure 9 provides insights into the morphology and structural effects on the electronic properties of $(TiO_2)_{84}(H_2O)_m$ NP systems. Both the amorphous and crystalline NPs display strong correlations between the dipole moments and their respective energy levels, although with distinct differences that highlight the role of NP structure and morphology on their electronic response to hydroxylation. In the annealed amorphous $(TiO_2)_{84}(H_2O)_m$ system, the correlation between the total dipole moment and the HOMO energy shows a linear regression coefficient R^2 value of approximately 0.84. This reasonable correlation suggests that the irregular and disordered structure of the amorphous NPs introduces a relatively high variability in the energy levels as the surface hydroxylation evolves (see Figure 7). This may be related to specific surface sites being stabilized through chemical bonding and thus not purely a dipolar effect. The correlation with the LUMO energy is stronger, with an R^2 value of 0.94, indicating that the LUMO is more stable and consistently affected by LIDE in amorphous NPs.

In contrast, the faceted crystalline $(TiO_2)_{84}(H_2O)_m$ NP system exhibits near−perfect correlations between the dipole moment and both the HOMO and LUMO energies. The R^2 value for the HOMO energy is 0.99 and, for the LUMO energy, 0.98. This indicates a remarkably linear and predictable relationship between the dipole moment and the energy levels in crystalline NPs. The highly ordered and regular atomic structure of the crystalline faceted NP system likely contributes to the strong correlation, as the dipole moments of hydroxyl groups on well-defined facets and edges lead to consistent electronic level shifts with minimal variability.

CONCLUSIONS

This study further demonstrates the significant role of surface hydroxylation in energetically stabilizing both crystalline and amorphous $(TiO_2)_{84}(H_2O)_m$ NPs and its influence on their electronic properties. Increased hydroxylation is found to lead to a convergence of structural and electronic properties of

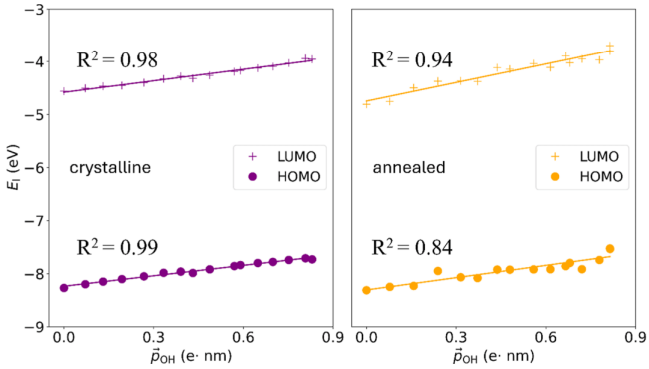

Figure 9. Correlation between calculated HOMO (LUMO) energies and projected total −OH dipole moment for the crystalline anatase (left) and annealed amorphous (right) $(TiO_2)_{84}(H_2O)_m$ NPs.

https://doi.org/10.1021/acs.jpcc.4c08070
J. Phys. Chem. C 2025, 129, 3299−3309

crystalline anatase and annealed amorphous $(TiO_2)_{84}(H_2O)_m$ NPs. Comparing with our previous findings on significantly smaller $(TiO_2)_{35}(H_2O)_m$ NPs, the present results suggest that hydroxylation minimizes energetic stability differences between crystalline and amorphous structures more efficiently in larger NPs, making it a crucial factor in tuning NP stability. In all NP systems, this energetic stabilization is associated with a hydroxylation-induced convergence in the distribution of local atomic coordination environments, regardless of the degree of crystallinity.

Our study also highlights that surface hydroxylation allows non-crystalline NPs to achieve electronic properties comparable to those of crystalline NPs (i.e., for amorphous NPs to act as crystalikes).[22] As hydroxylation progresses, both types of NPs show similar E_{gap} values, suggesting that hydroxylated amorphous NPs could be viable alternatives to crystalline anatase NPs in applications, such as photocatalysis.

The strong LIDE-based correlations between the dipole moment and HOMO and LUMO energy levels found for $(TiO_2)_{84}(H_2O)_m$ NPs confirm the potential of hydroxylation for precise tuning of electronic levels. For photocatalytic systems, the ability to predictably adjust HOMO and LUMO levels through controlled hydroxylation enables selection of energy level alignments for optimizing performance.

Overall, our results reinforce and generalize our previous findings on titania nanosystems, confirming that (i) the local structure and electronic properties of amorphous and crystalline titania NPs converge with increasing hydroxylation[22] and (ii) both size-dependent QC and hydroxylation-induced LIDE can play significant roles in determining the electronic properties of hydroxylated titania NPs.[24]

■ ASSOCIATED CONTENT

Supporting Information

The Supporting Information is available free of charge at https://pubs.acs.org/doi/10.1021/acs.jpcc.4c08070.

DFT-optimized Cartesian coordinates of atoms of all NP models used (ZIP)

Temperature evolution profile in the SA procedure (PDF)

■ AUTHOR INFORMATION

Corresponding Authors

Ángel Morales-García − *Departament de Ciència de Materials i Química Física & Institut de Química Teòrica i Computacional (IQTCUB), Universitat de Barcelona, 08028 Barcelona, Spain;* orcid.org/0000-0003-0491-1234; Email: angel.morales@ub.edu

Stefan T. Bromley − *Departament de Ciència de Materials i Química Física & Institut de Química Teòrica i Computacional (IQTCUB), Universitat de Barcelona, 08028 Barcelona, Spain; Institució Catalana de Recerca i Estudis Avançats (ICREA), 08010 Barcelona, Spain;* orcid.org/0000-0002-7037-0475; Email: s.bromley@ub.edu

Author

Miguel Recio-Poo − *Departament de Ciència de Materials i Química Física & Institut de Química Teòrica i Computacional (IQTCUB), Universitat de Barcelona, 08028 Barcelona, Spain*

Complete contact information is available at: https://pubs.acs.org/10.1021/acs.jpcc.4c08070

Notes

The authors declare no competing financial interest.

■ ACKNOWLEDGMENTS

S.T.B. acknowledges support from the by the Spanish Ministerio de Ciencia e Innovación and Agencia Estatal de Investigación (AEI) MCIN/AEI/10.13039/501100011033 through projects PID2021-127957NB-I00 and TED2021-132550B-C21 and the Maria de Maeztu program for Spanish Structures of Excellence (CEX2021-001202-M) and project grants 2021SGR00354 and 2023CLIMA00064 funded by the Generalitat de Catalunya M.R.-P. acknowledges the Ministerio de Ciencia e Innovación (MICIN) for a Formación de Personal Investigador (FPI) fellowship (PRE2019-087627). A.M.-G. thanks the support by the Spanish Ministerio de Ciencia e Innovación and Agencia Estatal de Investigación (AEI) MCIN/AEI/10.13039/501100011033 through projects PID2020-115293RJ-I00, PID2021-126076NB-I00, TED2021-129506B-C22, la Unidad de Excelencia María de Maeztu CEX2021-001202-M granted to the IQTCUB and, in part, from Generalitat de Catalunya 2021SGR00079. All authors thank the Red Española de Supercomputación (RES) for the provision of supercomputing time on the FinisTerrae3 supercomputer.

■ REFERENCES

(1) Fox, M. A.; Dulay, M. T. Heterogeneous Photocatalysis. *Chem. Rev.* **1993**, *93*, 341−357.

(2) Hashimoto, K.; Irie, H.; Fujishima, A. TiO_2 Photocatalysis: A Historical Overview and Future Prospects. *Jpn. J. Appl. Phys.* **2005**, *44*, 8269−8285.

(3) Valero, R.; Morales-Garcia, A.; Illas, F. Theoretical modeling of electronic excitations of gas-phase and solvated TiO_2 nanoclusters and nanoparticles of interest in photocatalysis. *J. Chem. Theory Comput.* **2018**, *14* (8), 4391−4404.

(4) Bai, Y.; Mora-Seró, I.; De Angelis, F.; Bisquert, J.; Wang, P. Titanium dioxide nanomaterials for photovoltaic applications. *Chem. Rev.* **2014**, *114* (19), 10095−10130.

(5) Hoffmann, M. R.; Martin, S. T.; Choi, W.; Bahnemann, D. W. Environmental applications of semiconductor photocatalysis. *Chem. Rev.* **1995**, *95* (1), 69−96.

(6) Fujishima, A.; Honda, K. Electrochemical photolysis of water at a semiconductor electrode. *Nature* **1972**, *238* (5358), 37−38.

(7) Ma, Y.; Wang, X.; Jia, Y.; Chen, X.; Han, H.; Li, C. Titanium dioxide-based nanomaterials for photocatalytic fuel generations. *Chem. Rev.* **2014**, *114* (19), 9987−10043.

(8) El Sharkawy, H. M.; Shawky, A. M.; Elshypany, R.; Selim, H. Efficient photocatalytic degradation of organic pollutants over TiO_2 nanoparticles modified with nitrogen and MoS_2 under visible light irradiation. *Sci. Rep.* **2023**, *13* (1), 8845.

(9) Pagliaro, M.; Palmisano, G.; Ciriminna, R.; Loddo, V. Nanochemistry aspects of titania in dye-sensitized solar cells. *Energy Environ. Sci.* **2009**, *2* (8), 838−844.

(10) Scanlon, D. O.; Dunnill, C. W.; Buckeridge, J.; Shevlin, S. A.; Logsdail, A. J.; Woodley, S. M.; Catlow, C. R. A.; Powell, M. J.; Palgrave, R. G.; Parkin, I. P.; Watson, G. W.; Keal, T. W.; Sherwood, P.; Walsh, A.; Sokol, A. A. Band alignment of rutile and anatase TiO_2. *Nat. Mater.* **2013**, *12* (9), 798−801.

(11) Samanta, B.; Morales-García, Á.; Illas, F.; Goga, N.; Anta, J. A.; Calero, S.; Bieberle-Hütter, A.; Libisch, F.; Muñoz-García, A. B.; Pavone, M.; Toroker, M. C. Challenges of modeling nanostructured materials for photocatalytic water splitting. *Chem. Soc. Rev.* **2022**, *51* (9), 3794−3818.

(12) Lamiel-Garcia, O.; Ko, K. C.; Lee, J. Y.; Bromley, S. T.; Illas, F. When anatase nanoparticles become bulklike: properties of realistic TiO_2 nanoparticles in the 1−6 nm size range from all electron

relativistic density functional theory based calculations. *J. Chem. Theory Comput.* **2017**, *13* (4), 1785−1793.
(13) Ramalingam, G.; Kathirgamanathan, P.; Ravi, G.; Elangovan, T.; kumar, B. A.; Manivanna, N.; Kasinathan, K. QuantumConfinement Effect of 2D Nanomaterials. In *Quantum Dots−Fundamental and Applications*; IntechOpen, 2020.
(14) Zhang, H.; Banfield, J. F. Structural characteristics and mechanical and thermodynamic properties of nanocrystalline TiO_2. *Chem. Rev.* **2014**, *114* (19), 9613−9644.
(15) Lamiel-Garcia, O.; Cuko, A.; Calatayud, M.; Illas, F.; Bromley, S. T. Predicting size-dependent emergence of crystallinity in nanomaterials: titania nanoclusters versus nanocrystals. *Nanoscale* **2017**, *9* (3), 1049−1058.
(16) Zhang, H.; Chen, B.; Banfield, J. F.; Waychunas, G. A. Atomic structure of nanometer-sized amorphous TiO_2. *Phys. Rev. B Condens. Matter* **2008**, *78* (21), 214106.
(17) Kobayakawa, K.; Nakazawa, Y.; Ikeda, M.; Sato, Y.; Fujishima, A. Influence of the density of surface hydroxyl groups on TiO_2 photocatalytic activities. *Bunsenges. Phys. Chem.* **1990**, *94* (12), 1439−1443.
(18) Di Paola, A.; Bellardita, M.; Palmisano, L.; Barbieriková, Z.; Brezová, V. Influence of crystallinity and OH surface density on the photocatalytic activity of TiO_2 powders. *J. Photochem. Photobiol., A* **2014**, *273*, 59−67.
(19) Mino, L.; Morales-García, Á.; Bromley, S. T.; Illas, F. Understanding the nature and location of hydroxyl groups on hydrated titania nanoparticles. *Nanoscale* **2021**, *13* (13), 6577−6585.
(20) Deiana, C.; Fois, E.; Coluccia, S.; Martra, G. Surface structure of TiO_2 P25 nanoparticles: infrared study of hydroxy groups on coordinative defect sites. *J. Phys. Chem. C* **2010**, *114* (49), 21531−21538.
(21) Levchenko, A. A.; Li, G.; Boerio-Goates, J.; Woodfield, B. F.; Navrotsky, A. TiO_2 stability landscape: Polymorphism, surface energy, and bound water energetics. *Chem. Mater.* **2006**, *18* (26), 6324−6332.
(22) Recio-Poo, M.; Morales-García, Á.; Illas, F.; Bromley, S. T. Crystal properties without crystallinity? Influence of surface hydroxylation on the structure and properties of small TiO_2 nanoparticles. *Nanoscale* **2023**, *15*, 4809−4820.
(23) Yang, S.; Prendergast, D.; Neaton, J. B. Tuning semiconductor band edge energies for solar photocatalysis via surface ligand passivation. *Nano Lett.* **2012**, *12* (1), 383−388.
(24) Recio-Poo, M.; Morales-García, Á.; Illas, F.; Bromley, S. T. Tuning electronic levels in photoactive hydroxylated titania nanosystems: combining the ligand dipole effect and quantum confinement. *Nanoscale* **2024**, *16* (18), 8975−8985.
(25) Wick-Joliat, R.; Musso, T.; Prabhakar, R. R.; Löckinger, J.; Siol, S.; Cui, W.; Sévery, L.; Moehl, T.; Suh, J.; Hutter, J.; Iannuzzi, M.; Tilley, S. D. Stable and tunable phosphonic acid dipole layer for band edge engineering of photoelectrochemical and photovoltaic heterojunction devices. *Energy Environ. Sci.* **2019**, *12* (6), 1901−1909.
(26) Fu, F. Y.; Shown, I.; Li, C. S.; Raghunath, P.; Lin, T. Y.; Billo, T.; Wu, H. L.; Wu, C. I.; Chung, P. W.; Lin, M. C.; Chen, L. C.; Chen, K. H. KSCN-induced interfacial dipole in black TiO_2 for enhanced photocatalytic CO_2 reduction. *ACS Appl. Mater. Interfaces* **2019**, *11* (28), 25186−25194.
(27) Morales-García, Á.; Escatllar, A. M.; Illas, F.; Bromley, S. T. Understanding the interplay between size, morphology and energy gap in photoactive TiO_2 nanoparticles. *Nanoscale* **2019**, *11* (18), 9032−9041.
(28) Escatllar, A. M.; Morales-García, Á.; Illas, F.; Bromley, S. T. Efficient preparation of TiO_2 nanoparticle models using interatomic potentials. *J. Chem. Phys.* **2019**, *150* (21), 214305.
(29) Wulff, G. Xxv. zur frage der geschwindigkeit des wachsthums und der auflösung der krystallflächen. *Z. für Kristallogr. - Cryst. Mater.* **1901**, *34* (1−6), 449−530.
(30) Pigeot-Rémy, S.; Dufour, F.; Herissan, A.; Ruaux, V.; Maugé, F.; Hazime, R.; Foronato, C.; Guillard, C.; Chaneac, C.; Duruptthy, O.; Colbeau-Justin, C.; Cassaignon, S. Bipyramidal anatase TiO_2 nanoparticles, a highly efficient photocatalyst? Towards a better understanding of the reactivity. *Appl. Catal. B Environ.* **2017**, *203*, 324−334.
(31) Hummer, D. R.; Kubicki, J. D.; Kent, P. R.; Heaney, P. J. Single-site and monolayer surface hydration energy of anatase and rutile nanoparticles using density functional theory. *J. Phys. Chem. C* **2013**, *117* (49), 26084−26090.
(32) Kirkpatrick, S.; Gelatt, C. D.; Vecchi, M. P. Optimization by simulated annealing. *Science* **1983**, *220* (4598), 671−680.
(33) Cuko, A.; Escatllar, A. M.; Calatayud, M.; Bromley, S. T. Properties of hydrated TiO_2 and SiO_2 nanoclusters: dependence on size, temperature and water vapour pressure. *Nanoscale* **2018**, *10* (45), 21518−21532.
(34) Gale, J. D.; Rohl, A. L. The general utility lattice program (GULP). *Mol. Simul.* **2003**, *29* (5), 291−341.
(35) Blum, V.; Gehrke, R.; Hanke, F.; Havu, P.; Havu, V.; Ren, X.; Reuter, K.; Scheffler, M. Ab initio molecular simulations with numeric atom-centered orbitals. *Comput. Phys. Commun.* **2009**, *180* (11), 2175−2196.
(36) Perdew, J. P.; Burke, K.; Ernzerhof, M. Generalized gradient approximation made simple. *Phys. Rev. Lett.* **1996**, *77* (18), 3865.
(37) Ko, K. C.; Lamiel-García, O.; Lee, J. Y.; Illas, F. Performance of a modified hybrid functional in the simultaneous description of stoichiometric and reduced TiO_2 polymorphs. *Phys. Chem. Chem. Phys.* **2016**, *18* (17), 12357−12367.
(38) Morales-García, Á.; Valero, R.; Illas, F. Reliable and computationally affordable prediction of the energy gap of $(TiO_2)_n$ ($10 \leq n \leq 563$) nanoparticles from density functional theory. *Phys. Chem. Chem. Phys.* **2018**, *20* (28), 18907−18911.
(39) Cho, D.; Ko, K. C.; Lamiel-Garcia, O.; Bromley, S. T.; Lee, J. Y.; Illas, F. Effect of Size and Structure on the Ground-State and Excited-State Electronic Structure of TiO_2 Nanoparticles. *J. Chem. Theory Comput.* **2016**, *12* (8), 3751−3763.
(40) Trasatti, S. The absolute electrode potential: an explanatory note (Recommendations 1986). *Pure Appl. Chem.* **1986**, *58*, 955.
(41) Yaacobi-Gross, N.; Soreni-Harari, M.; Zimin, M.; Kababya, S.; Schmidt, A.; Tessler, N. Molecular control of quantum-dot internal electric field and its application to CdSe-based solar cells. *Nat. Mater.* **2011**, *10* (12), 974−979.
(42) Brown, P. R.; Kim, D.; Lunt, R. R.; Zhao, N.; Bawendi, M. G.; Grossman, J. C.; Bulovic, V. Energy level modification in lead sulfide quantum dot thin films through ligand exchange. *ACS Nano* **2014**, *8* (6), 5863−5872.
(43) Kroupa, D. M.; Vörös, M.; Brawand, N. P.; McNichols, B. W.; Miller, E. M.; Gu, J.; Nozik, A. J.; Sellinger, A.; Galli, G.; Beard, M. C. Tuning colloidal quantum dot band edge positions through solution-phase surface chemistry modification. *Nat. Commun.* **2017**, *8* (1), 15257.
(44) Hirshfeld, F. L. Bonded-atom fragments for describing molecular charge densities. *Theor. Chim. Acta* **1977**, *44*, 129−138.
(45) Burnelle, L.; Coulson, C. A. Bond dipole moments in water and ammonia. *Trans. Faraday Soc.* **1957**, *53*, 403−405.
(46) Zhang, D.; Yang, M.; Dong, S. Hydroxylation of the rutile TiO_2 (110) surface enhancing its reducing power for photocatalysis. *J. Phys. Chem. C* **2015**, *119* (3), 1451−1456.

https://doi.org/10.1021/acs.jpcc.4c08070
J. Phys. Chem. C 2025, 129, 3299−3309

3.5 References

[1] Chen, X.; Mao, S. S. Titanium dioxide nanomaterials: synthesis, properties, modifications, and applications. *Chem. Rev.* **2007**, *107*(7), 2891-2959.

[2] Chen, X.; Li, C.; Grätzel, M.; Kostecki, R.; Mao, S. S. Nanomaterials for renewable energy production and storage. *Chem. Soc. Rev.* **2012**, *41*(23), 7909-7937.

[3] Selli, D.; Fazio, G.; Di Valentin, C. Using density functional theory to model realistic TiO_2 nanoparticles, their photoactivation and interaction with water. *Catalysts* **2017**, *7*(12), 357.

[4] Li, Y. F.; Liu, Z. P. Particle size, shape and activity for photocatalysis on titania anatase nanoparticles in aqueous surroundings. *J. Am. Chem. Socc.* **2011**, *133*(39), 15743-15752.

[5] Lamiel-Garcia, O.; Cuko, A.; Calatayud, M.; Illas, F.; Bromley, S.T. Predicting Size-Dependent Emergence of Crystallinity in Nanomaterials: Titania Nanoclusters Versus Nanocrystals. *Nanoscale* **2017**, 9, 1049−1058.

[6] Lamiel-Garcia, O.; Ko, K. C.; Lee, J. Y.; Bromley, S. T.; Illas, F. When anatase nanoparticles become bulklike: properties of realistic TiO_2 nanoparticles in the 1–6 nm size range from all electron relativistic density functional theory based calculations. *J. Chem. Theory Comput.* **2017**, *13*(4), 1785-1793.

[7] Zhang, H.; Chen, B.; Banfield, J. F.; Waychunas, G. A. Atomic structure of nanometer-sized amorphous TiO_2. *Phys. Rev. B* **2008**, *78*(21), 214106.

[8] Zhang, H.; Finnegan, M.; Banfield, J. F. Preparing single-phase nanocrystalline anatase from amorphous titania with particle sizes tailored by temperature. *Nano Lett.* **2001**, *1*(2), 81-85.

[9] Morales-García, Á.; Escatllar, A. M.; Illas, F.; Bromley, S. T. Understanding the interplay between size, morphology and energy gap in photoactive TiO_2 nanoparticles. *Nanoscale* **2019**, *11*(18), 9032-9041.

[10] Johnston, R. L. *Atomic and molecular clusters*. CRC Press Taylor & Francis, London, **2002**.

[11] Banfield, J. F.; Zhang, H. Nanoparticles in the environment. *Rev. Mineral. Geochem.* **2001**, *44*(1), 1-58.

[12] Chen, X.; Liu, L.; Yu, P. Y.; Mao, S. S. Increasing solar absorption for photocatalysis with black hydrogenated titanium dioxide nanocrystals. *Science* **2011**, *331*(6018), 746-750.

[13] Zhou, X.; Wierzbicka, E.; Liu, N.; Schmuki, P. Black and white anatase, rutile and mixed forms: band-edges and photocatalytic activity. *Chem. Commun.* **2019**, *55*(4), 533-536.

[14] Nunzi, F.; Storchi, L.; Manca, M.; Giannuzzi, R.; Gigli, G.; De Angelis, F. Shape and Morphology Effects on the Electronic Structure of TiO_2 Nanostructures: From Nanocrystals to Nanorods. *ACS Appl. Mater. Interfaces* **2014**, *6*(4), 2471-2478.

[15] Liu, G.; Yang, H. G.; Pan, J.; Yang, Y. Q.; Lu, G. Q.; Cheng, H. M. Titanium dioxide crystals with tailored facets. *Chem. Rev.* **2014***, 114*(19), 9559-9612.

[16] Barnard, A. S.; Curtiss, L. A. Prediction of TiO_2 nanoparticle phase and shape transitions controlled by surface chemistry. *Nano Lett.* **2005**, *5*(7), 1261-1266.

[17] Baldini, E.; Chiodo, L.; Dominguez, A.; Palummo, M.; Moser, S.; Yazdi-Rizi, M.; Auböck, G.; Mallett, B. P. P.; Berger, H.; Magrez, A.; Bernhard, C.; Grioni, M.; Rubio, A.; Chergui, M. Strongly bound excitons in anatase TiO_2 single crystals and nanoparticles. *Nat. Commun.* **2017**, *8*(1), 13.

[18] Ramalingam, G.; Kathirgamanathan, P. Quantum Confinement Effect of. *Quantum Dots: Fundamental and Applications* **2020**, 11.

[19] Ko, K. C.; Bromley, S. T.; Lee, J. Y.; Illas, F. Size-dependent level alignment between rutile and anatase TiO_2 nanoparticles: implications for photocatalysis. *J. Phys. Chem. Lett.* **2017**, *8*(22), 5593-5598.

[20] Cho, D.; Ko, K. C.; Lamiel García, O.; Bromley, S. T.; Lee, J. Y.; Illas, F. Effect of Size and Structure on the Ground and Excited State Electronic Structure of TiO_2 Nanoparticles. *J. Chem. Theory Comput.* **2016**, 12, 3751−3763.

[21] Luttrell, T.; Halpegamage, S.; Tao, J.; Kramer, A.; Sutter, E.; Batzill, M. Why is anatase a better photocatalyst than rutile?-Model studies on epitaxial TiO_2 films. *Sci. Rep.* **2014**, *4*(1), 4043.

[22] Lettieri, S.; Pavone, M.; Fioravanti, A.; Santamaria Amato, L.; Maddalena, P. Charge carrier processes and optical properties in TiO_2 and TiO_2-based heterojunction photocatalysts: A review. *Mater.* **2021**, *14*(7), 1645.

[23] Hoffmann, M. R.; Martin, S. T.; Choi, W.; Bahnemann, D. W. Environmental applications of semiconductor photocatalysis. *Chem. Rev.* **1995**, *95*(1), 69-96.

[24] Fujishima, A.; Zhang, X.; Tryk, D. A. TiO_2 photocatalysis and related surface phenomena. *Surf. Sci. Rep.* **2008**, *63*(12), 515-582.

[25] Ma, Y.; Wang, X.; Jia, Y.; Chen, X.; Han, H.; Li, C. Titanium dioxide-based nanomaterials for photocatalytic fuel generations. *Chem. Rev.* **2014**, *114*(19), 9987-10043.

[26] Panarelli, E. G.; Livraghi, S.; Maurelli, S.; Polliotto, V.; Chiesa, M.; Giamello, E. Role of surface water molecules in stabilizing trapped hole centres in titanium dioxide (anatase) as monitored by electron paramagnetic resonance. *J. Photochem. Photobiol. A* **2016**, *322*, 27-34.

[27] Levchenko, A. A.; Li, G.; Boerio-Goates, J.; Woodfield, B. F.; Navrotsky, A. TiO_2 stability landscape: Polymorphism, surface energy, and bound water energetics. *Chem. Mater.* **2006**, *18*(26), 6324-6332.

[28] Kobayakawa, K.; Nakazawa, Y.; Ikeda, M.; Sato, Y.; Fujishima, A. Influence of the density of surface hydroxyl groups on TiO_2 photocatalytic activities. *Ber. Bunsenges. Phys. Chem.* **1990**, *94*(12), 1439-1443.

[29] Walle, L. E.; Borg, A.; Johansson, E. M. J.; Plogmaker, S.; Rensmo, H.; Uvdal, P.; Sandell, A. Mixed dissociative and molecular water adsorption on anatase TiO_2 (101). *J. Phys. Chem. C* **2011**, *115*(19), 9545-9550.

[30] Martinez-Casado, R.; Mallia, G.; Harrison, N. M.; Pérez, R. First-principles study of the water adsorption on anatase (101) as a function of the coverage. *J. Phys. Chem. C* **2018**, *122*(36), 20736-20744.

[31] Nadeem, I. M.; Treacy, J. P.; Selcuk, S.; Torrelles, X., Hussain, H., Wilson, A., Grinter, D. C.; Cabailh, G.; Bikondoa, O.; Nicklin, C.; Selloni, A.; Zegenhagen, J.; Lindsay, R.; Thornton, G. Water dissociates at the aqueous interface with reduced anatase TiO_2 (101). *J. Phys. Chem. Lett.* **2018**, *9*(11), 3131-3136.

[32] Fisicaro, G., Filice, S., Scalese, S., Compagnini, G., Reitano, R., Genovese, L., Goedecker, S.; Deretzis, I.; La Magna, A. Wet environment effects for ethanol and water adsorption on anatase TiO_2 (101) surfaces. *J. Phys. Chem. C* **2019**, *124*(4), 2406-2419.

[33] Mino, L.; Morales-Garcia, Á.; Bromley, S. T.; Illas, F. Understanding the nature and location of hydroxyl groups on hydrated titania nanoparticles. *Nanoscale* **2021**, *13* (13), 6577−6585.

[34] Deiana, C.; Fois, E.; Coluccia, S.; Martra, G. Surface structure of TiO_2 P25 nanoparticles: infrared study of hydroxy groups on coordinative defect sites. *J. Phys. Chem. C* **2010**, *114* (49), 21531−21538.

[35] Henderson, M. A. A surface science perspective on TiO_2 photocatalysis. *Surf. Sci. Rep.* **2011**, *66*(6-7), 185-297.

[36] Sun, C.; Liu, L. M.; Selloni, A.; Lu, G. Q. M.; Smith, S. C. Titania-water interactions: a review of theoretical studies. *J. Mater. Chem.* **2010**, *20*(46), 10319-10334.

[37] Cuko, A.; Escatllar, A. M.; Calatayud, M.; Bromley, S. T. Properties of hydrated TiO_2 and SiO_2 nanoclusters: dependence on size, temperature and water vapour pressure. *Nanoscale* **2018**, *10*(45), 21518-21532.

[38] Di Paola, A.; Bellardita, M.; Palmisano, L.; Barbieriková, Z.; Brezová, V. Influence of crystallinity and OH surface density on the photocatalytic activity of TiO_2 powders. *J. Photochem. Photobiol. A* **2014**, *273*, 59-67.

[39] Wang, J.; Liu, X.; Li, R.; Qiao, P.; Xiao, L.; Fan, J. TiO_2 nanoparticles with increased surface hydroxyl groups and their improved photocatalytic activity. *Catal. Commun.* **2012**, *19*, 96-99.

[40] Senff, L.; Tobaldi, D. M.; Lucas, S.; Hotza, D.; Ferreira, V. M.; Labrincha, J. A. Formulation of mortars with nano-SiO_2 and nano-TiO_2 for degradation of pollutants in buildings. *Compos. B Eng.* **2013**, *44*(1), 40-47.

[41] Mills, A.; Davies, R. H.; Worsley, D. Water-Purification by Semiconductor Photocatalysis. *Chem. Soc. Rev.* **1993**, *22*, 417−425.

[42] Kim, W.; Tachikawa, T.; Moon, G. H.; Majima, T.; Choi, W. Molecular-level understanding of the photocatalytic activity difference between anatase and rutile nanoparticles. *Angew. Chem.* **2014**, *126*(51), 14260-14265.

[43] Adams, L. K.; Lyon, D. Y.; Alvarez, P. J. Comparative eco-toxicity of nanoscale TiO_2, SiO_2, and ZnO water suspensions. *Water Res.* **2006**, *40*, 3527.

[44] Wales, D. J.; Doye, J. P. Global optimization by basin-hopping and the lowest energy structures of Lennard-Jones clusters containing up to 110 atoms. *J. Phys. Chem. A* **1997**, *101*(28), 5111-5116.

[45] Calatayud, M.; Markovits, A.; Minot, C. Electron-count control on adsorption upon reducible and irreducible clean metal-oxide surfaces. *Catal. Today* **2004**, *89*(3), 269-278.

[46] Zhang, D.; Yang, M.; Dong, S. Hydroxylation of the rutile TiO_2 (110) surface enhancing its reducing power for photocatalysis. *J. Phys. Chem. C* **2015**, *119*(3), 1451-1456.

[47] Brown, P. R.; Kim, D.; Lunt, R. R.; Zhao, N.; Bawendi, M. G.; Grossman, J. C.; Bulovic, V. Energy level modification in lead sulfide quantum dot thin films through ligand exchange. *ACS Nano* **2014**, *8*(6), 5863-5872.

[48] Kroupa, D. M.; Vörös, M.; Brawand, N. P.; McNichols, B. W.; Miller, E. M.; Gu, J.; Nozik, A. J.; Sellinger, A; Galli, G.; Beard, M. C. Tuning colloidal quantum dot band edge positions through solution-phase surface chemistry modification. *Nat. Commun.* **2017**, *8*(1), 15257.

[49] Kirkpatrick, S.; Gelatt Jr, C. D.; Vecchi, M. P. Optimization by simulated annealing. *Science* **1983**, *220*(4598), 671-680.

[50] Gale, J. D.; Rohl, A. L. The general utility lattice program (GULP). *Mol. Simul.* **2003**, *29*(5), 291-341.

[51] Perdew, J. P.; Burke, K.; Ernzerhof, M. Generalized gradient approximation made simple. *Phys. Rev. Lett.* **1996**, *77*, 3865.

[52] Morales-García, Á.; Valero, R.; Illas, F. Reliable and computationally affordable prediction of the energy gap of $(TiO_2)_n$ ($10 \leq n \leq 563$) nanoparticles from density functional theory. *Phys. Chem. Chem. Phys.* **2018**, *20*(28), 18907-18911.

4 REVISING SIZE-DEPENDENT *AB INITIO* ATOMISTIC THERMODYNAMICS

4.1 Introduction

The fundamental thermodynamic property governing material stability is the Gibbs free energy of formation, $\Delta G_f(T, p)$, which quantifies the energy difference between the initial and final states of a synthesis process at temperature T and pressure p. A negative $\Delta G_f(T, p)$ indicates thermodynamic favourability, serving as a guiding metric for material stability under realistic conditions. $\Delta G_f(T, p)$ is composed of the enthalpy of formation $\Delta H_f(T, p)$ and an entropic term $-T\Delta S_f(T, p)$, both of which depend on the heat capacity of the compounds involved. Experimentally, calorimetry is used to determine these properties for bulk materials, but such measurements become increasingly complex for nanomaterials.[1,2] Theoretical predictions of $\Delta G_f(T, p)$ are thus highly valuable, especially when explicit vibrational and configurational contributions become computationally prohibitive. While the internal energy at 0 K contributes the largest portion to $\Delta G_f(T, p)$, the remaining terms—although smaller—can be crucial in determining stability differences between competing phases.

The *Ab Initio* Atomistic Thermodynamics (AIAT) framework has proven to be a powerful tool for predicting the stability of surfaces and interfaces under varying environmental conditions.[3,4] However, its application to nanoscale materials, particularly hydrated titania nanoparticles, introduces new challenges that require a more refined approach. The conventional AIAT method for solids (hereafter called $\text{AIAT}_{\text{solid}}$) assumes that, for changes of coverage, the vibrational contributions (all gathered in a F^{vib} function as in Equation 2.34) to $\Delta G_f(T, p)$ for the surfaces cancel out and the configurational entropic changes are negligible (more details were included in section 2.4.2 of the Methodology chapter). While this approximation holds for bulk-like surfaces, it becomes increasingly unreliable for small nanoparticles. For much smaller systems composed of up to a few tens of atoms interacting with a gaseous environment, 0 K DFT calculations combined with standard statistical thermodynamics can be used to directly calculate all relevant thermodynamic contributions.[5-7] An AIAT description of such a system ($\text{AIAT}_{\text{explicit}}$) avoids the simplifying assumptions of solid surface treatments by explicitly computing all partition

function contributions, including translational, rotational, vibrational, and zero-point energy (ZPE) effects. At the nanoscale, size-dependent vibrational and configurational factors play a crucial role in determining hydration stability, necessitating explicit corrections for accurate thermodynamic predictions.

Between molecular-scale clusters and extended macroscopic solids lie nanosized systems, which include catalytic nanoparticles, biological colloids, and nanoparticulate pollutants. These systems interact strongly with their environments and are often too large for direct $AIAT_{explicit}$ calculations yet not large enough to justify the approximations inherent in $AIAT_{solid}$. To address these limitations, we introduce $AIAT_{nano}$, a refined computational framework that systematically incorporates size-dependent vibrational free energy corrections (within a f^{vib} analytical function) into $\Delta G_f(T, p)$ expression of $AIAT_{solid}$. In this way, $AIAT_{nano}$ provides a more accurate description of hydration thermodynamics in nanoparticles by capturing the intricate interplay between vibrational entropy and surface hydration energetics. By applying this approach to TiO_2 NPs across various sizes, we demonstrate that $AIAT_{nano}$ yields significantly improved hydration phase diagrams compared to the standard bulk-based AIAT approach. This refined framework facilitates a continuous thermodynamic description across size scales, bridging the gap between small clusters and extended surfaces. Therefore, the main nature of this chapter is computational, as we have derived a simple yet effective function to address vibrational calculations in systems where computing all atomic vibrations is computationally prohibitive. Figure 4.1 summarizes the three regimes in terms of system size, together with the various followed approaches to derive the $\Delta G_f(T, p)$ expression

4.1.1 AIAT to Surfaces and Extended Systems

The AIAT approach has been instrumental in understanding surface stability, catalytic activity, and oxidation mechanisms across a variety of material systems. By incorporating DFT-calculated total energies into thermodynamic models, $AIAT_{solid}$ provides a predictive framework for determining the Gibbs free energy of bulk models and surfaces under varying T and p conditions. As already indicated, with such an AIAT approach, one typically assumes that (i) the vibrational entropy contribution from surface atoms is the same for the

clean and covered surface, and (ii) each system is dominated by very few low energy configurations. Then, for changes of coverage, the vibrational contributions to $\Delta G_f(T, p)$ for the surfaces cancel out and the configurational entropic changes are negligible. The vibrational contribution of the adsorbates (typically the zero point energy− ZPE) can also be included in such calculations for a moderate extra computational cost. Here, the $\Delta G_f(T,\ p)$ values become changes in enthalpies of the solid phase plus relevant changes due to gas phase (and sometimes adsorbed) species. Thus, $\Delta G_f(T, p)$ values become accessible based on standard 0 K DFT calculations including normal modes of molecular species. This approach has been applied successfully to a broad range of materials, from transition metal oxides[3] to nanostructured catalysts,[8] demonstrating its versatility in materials science, catalysis, and surface chemistry.

	$AIAT_{explicit}$	$AIAT_{nano}$	$AIAT_{solid}$
System size	Small clusters, molecules (< 2nm)	Nanoscale structures	Extended surfaces, solids (>100 nm)
Treatment of $\Delta G_f(T,p)$	Bottom-up statistical mechanics	System + size dependent interpolation	Generally applied fixed approximations
Contribution of frequencies	Explicit calculation of $F^{vib}(T, \Theta_{v,k})$	Approximated by $f^{vib}(N)$	None or adsorbate related

Figure 4.1: Scheme indicating three different system size regimes with respect to the respective AIAT-based computation of $\Delta G_f(T, p)$. Blue and red, respectively, relate to the small and large regimes for which $AIAT_{explicit}$ and $AIAT_{solid}$ have been extensively applied. Our bridging interpolation approach for nanosized systems ($AIAT_{nano}$) replaces the explicit computation of vibrational frequencies with the use of a temperature-dependent and N-dependent parametrized function, $f^{vib}(T,N)$, where N represents a generic system size variable. Figure adapted from reference 9.

One of the most foundational applications of $AIAT_{solid}$ was in $RuO_2(110)$ surfaces,[3] a system widely studied for its catalytic oxidation properties. In their seminal work, Reuter and Scheffler used $AIAT_{solid}$ to construct a thermodynamic phase diagram for $RuO_2(110)$ under oxygen-rich conditions, identifying

stable and metastable surface terminations that depend on the oxygen chemical potential. This study challenged conventional ultrahigh vacuum (UHV) surface science models, which typically assumed a stoichiometric $RuO_2(110)$ surface, and instead demonstrated that under realistic oxygen pressures, the surface adopts nonstoichiometric, oxygen-rich terminations. This was a major breakthrough, as it provided quantitative predictions about the dominant surface structures in catalytically relevant environments, rather than relying on idealized, UHV-based assumptions.

Building on this foundation, $AIAT_{solid}$ has been extensively applied to catalytic systems, particularly in the context of oxidation reactions. In Reuter and Scheffler's 2003 study,[10] AIAT was used to construct surface phase diagrams for CO oxidation over $RuO_2(110)$, revealing how the competition between CO and oxygen adsorption dictates catalytic performance. By mapping out the stability regions of different surface structures, they demonstrated that the most active catalytic phase lies at the phase boundary between oxygen-covered and CO-covered surfaces, where reactive intermediates dynamically exchange. This insight has had profound implications for the design of oxidation catalysts, as it suggests that catalytic activity is maximized at regions of dynamic phase coexistence, rather than at any single static surface configuration.

Another important application of $AIAT_{solid}$ was in the study of In_2O_3 surfaces,[8] which play a crucial role in CO_2 hydrogenation to methanol. Here, AIAT was employed to investigate the relative stabilities of different In_2O_3 facets under varying oxygen chemical potentials, revealing that the (100) facet is more stable under oxygen-poor conditions, whereas the (111) facet dominates in oxygen-rich environments. These findings were crucial for optimizing catalytic selectivity, as they demonstrated that controlling the surrounding chemical potential can effectively tune the exposed surface facets, thereby enhancing the efficiency of methanol synthesis.

4.1.2 AIAT Applied to Small NPs

While AIAT has been extensively and successfully applied to extended surfaces, its extension to NPs and small clusters introduces additional complexities. At the nanoscale, finite-size effects, surface relaxations, and vibrational

contributions play a much more significant role than in bulk materials. This is particularly relevant for hydration processes, where the free energy of water adsorption and incorporation into the NP environment is strongly dependent on vibrational contributions.

In recent years, AIAT has been extended to study small metal and metal-oxide NPs, aiming to capture size-dependent trends in stability and reactivity. A key challenge that emerges in this regime is the accurate treatment of vibrational free energy contributions, which become non-negligible as particle size decreases. Unlike extended surfaces, where vibrational modes are often approximated using bulk phonon DOS, small clusters exhibit quantized vibrational spectra and low-frequency phonon softening, which significantly modify their thermodynamic stability.

Several studies have applied AIAT to supported metal NPs to predict their stability, morphology, and adsorption behaviour. For instance, the equilibrium shape of Ag NPs supported on α-Al_2O_3(0001) was determined using a first-principles thermodynamics approach, incorporating surface energy, oxygen adsorption, and support interactions.[11] This study combined DFT calculations with the Wulff–Kaichew construction, showing that truncated octahedral shapes are energetically preferred, but with notable contact angle variations depending on the support termination. While this study successfully extended AIAT to supported NPs, it did not explicitly account for vibrational entropy contributions, which become crucial for hydration thermodynamics.

A more comprehensive treatment of vibrational effects in AIAT-based NP studies is provided in investigations on Pt NPs of varying sizes.[12] Using a combination of EXAFS (Extended X-ray Absorption Fine Structure) experiments, transmission electron microscopy (TEM), and DFT modelling, this study revealed that vibrational properties vary significantly with NP size, affecting free energy corrections. Notably, the work demonstrated that the Debye temperature (Θ_D) increases non-monotonically with decreasing NP size, leading to enhanced vibrational entropy contributions in small clusters. This highlights the necessity of incorporating explicit vibrational corrections when applying AIAT to hydration processes in sub-nanometer titania clusters.

A successful example of AIAT with explicit vibrational frequency treatment in hydration thermodynamics is the study of hydrated TiO_2 and SiO_2 nanoclusters.[7] This study has been already cited when discussing electronic/energetics in the previous chapter and is closely linked to this thesis—as it examines n = 4, 8, 12, 16 titania nanoclusters. In the context of thermodynamics, this work used $AIAT_{explicit}$ framework to investigate how hydration affects the structure and stability of nanoclusters, incorporating vibrational contributions explicitly within a statistical thermodynamics' framework. By computing Gibbs free energies as a function of temperature and water vapor pressure, the study captured size-dependent hydration trends, showing that vibrational entropy significantly influences hydration thermodynamics at elevated temperatures.

The Gibbs free energy for hydration was computed using:

$$\Delta G_{\mathrm{hyd}}(T, p) = G(\mathrm{TiO_2})_n(\mathrm{H_2O})_m(T) - G(\mathrm{TiO_2})_n(T) - n\mu_{\mathrm{H_2O}}(T, P) \qquad (4.1)$$

where $G(\mathrm{TiO_2})_n(\mathrm{H_2O})_m(T)$ and $G(\mathrm{TiO_2})_n(T)$ are the free energies of the hydrated and anhydrous nanoclusters, respectively, and $\mu_{\mathrm{H_2O}}(T, p)$ is the chemical potential of water vapor, which depends on both temperature and pressure. The free energy contributions were explicitly obtained from the molecular partition function, considering translational, rotational, vibrational, and symmetry components, where the vibrational contribution, explicitly included, was derived from the harmonic frequencies (ν_i):

$$F_{\mathrm{vib}}(T) = \sum_i \frac{h\nu_i}{2} + \sum_i k_B T \ln(1 - e^{-h\nu_i/k_B T}) \qquad (4.2)$$

A key result of this study was the construction of hydration pressure-temperature phase diagrams, which map the most thermodynamically stable hydration states as a function of temperature and water vapor pressure. These diagrams revealed that at ambient conditions (e.g., 300 K, 1 kPa H_2O vapor pressure), hydrated nanoclusters are favoured, but at higher temperatures, dehydration becomes more probable. Interestingly, the hydration stability decreases with increasing cluster size, indicating that smaller nanoclusters tend to be more

hydrophilic. Additionally, SiO_2 nanoclusters remain hydrated at higher temperatures than TiO_2, suggesting a stronger water affinity.

The phase diagrams also confirmed that hydration occurs exclusively via dissociative adsorption of water, with no molecular adsorption observed under equilibrium conditions. Furthermore, they highlighted the importance of including vibrational entropy, as hydration free energies calculated without vibrational contributions overestimate hydration stability, especially at elevated temperatures.

4.1.3 Limitations and Challenges of AIAT

Despite its broad applicability, AIAT has certain fundamental limitations, particularly when applied to complex, nanoscale systems. One of the most notable drawbacks is its assumption of thermodynamic equilibrium, which means it does not account for kinetic barriers, reaction pathways, or metastable states.[13] In real catalytic or electrochemical environments, surface transformations often occur under non-equilibrium conditions, where kinetic effects dominate over purely thermodynamic predictions. To address this, AIAT is often coupled with microkinetic models[4,14] or kinetic Monte Carlo simulations to provide a more comprehensive picture.

As already discussed, another significant challenge arises from vibrational contributions to Gibbs free energy. In bulk and extended surfaces, vibrational effects are often minor and cancel out in energy differences, making AIAT predictions reliable. However, for small clusters and NPs, the phonon DOS can deviate significantly from bulk-like behaviour, necessitating explicit vibrational free energy corrections. For example, studies on Li_2O NPs have shown that neglecting phonon contributions can lead to significant errors in phase transition temperatures, highlighting the importance of size-dependent vibrational corrections.[15]

Configurational entropy presents another challenge in AIAT. The method is typically applied to ordered surfaces with well-defined configurations, but in NPs, amorphous materials, or highly defective surfaces, multiple metastable structures contribute to the overall free energy.[16,17] This means that entropy arising from structural disorder is often neglected, which can lead to

discrepancies between AIAT predictions and experimental observations. To overcome this, techniques such as Monte Carlo sampling and cluster expansion models have been employed,[18,19] though they require extensive computational resources.

Finally, AIAT was originally formulated for gas-phase environments, making its direct extension to solvent-mediated and electrochemical systems non-trivial. Recent advancements have incorporated continuum solvation models (PCM),[20] explicit water adsorption calculations, and computational hydrogen electrode (CHE) models,[21] but these techniques add complexity and computational cost. For oxides and catalysts, where surface charge and pH-dependent stability play crucial roles, additional corrections such as Poisson-Boltzmann solvation models or explicit molecular dynamics simulations may be required.

4.2 Results

The $AIAT_{nano}$ approach was developed to overcome the limitations of traditional AIAT methods in nanoscale systems. By integrating DFT-derived energies with a size-dependent interpolation of vibrational contributions, $AIAT_{nano}$ provides a computationally efficient framework for estimating Gibbs free energy changes in nanosystems interacting with gas-phase species. As a case study, we applied this method to photoactive titania and its interaction with water molecules.

For the small system size limit, we primarily considered a $(TiO_2)_{16}(H_2O)_m$ nanoparticle,[7] constructed using a $(TiO_2)_{16}$ core derived from bulk anatase and progressively hydrated while minimizing structural perturbations. This approach maintains the bulk-like stability of larger anatase NPs, providing a natural reference point while allowing for explicit calculation of all contributions to $\Delta G_{\mathrm{hyd}}(T, p)$. This method leads to slight deviations from results obtained using globally optimized $(TiO_2)_{16}(H_2O)_m$ structures. For the large system size limit, we model an extended anatase TiO_2 (101) surface with varying hydration levels. The surface is represented by a periodically repeated slab (six atomic layers of a (3 × 1) supercell),[22] exposing the (101) facets on both sides, as shown in the previous chapter.

To benchmark our approach against the standard solid-surface $AIAT_{solid}$ method, we analysed bipyramidal titania NPs containing up to 500 atoms, specifically $(TiO_2)_{35}(H_2O)_m$, $(TiO_2)_{84}(H_2O)_m$, and $(TiO_2)_{165}(H_2O)_m$. As previously described, these NP systems were derived from top-down cuts of bulk anatase to expose the most stable (101) facets.[23,24] To standardize NP sizes, we define diameters based on a sphere enclosing n TiO_2 units, with unit volume taken from bulk anatase. This results in diameters ranging from ~2 nm for $(TiO_2)_{35}$ to ~4.3 nm for fully hydrated $(TiO_2)_{165}$. These systems fall within a size range where direct DFT-based frequency calculations become computationally prohibitive. Across all titania systems, we assume hydration follows a mechanism in which H_2O dissociates upon adsorption**,** with H and OH species interacting with surface O and Ti atoms, respectively**.**

4.2.1 $f^{vib}(T, N)$ analytical function

The vibrational contributions to the Gibbs free energy of hydration were approximated using an analytical function, $f^{vib}(T, N)$, which was derived to reproduce the vibrational free energy (F^{vib}) for a reference $(TiO_2)_{16}(H_2O)_m$ NP system. The vibrational contribution to Gibbs free energy, F^{vib}, can be expressed as the sum of three terms:

$$F^{vib}(T, \Theta_k) = E^{ZPE}(\Theta_k) + U^{vib}(T, \Theta_k) - TS^{vib}(T, \Theta_k) \qquad (4.3)$$

where $U^{vib}$and S^{vib} are the vibrational contributions to the internal energy and entropy and E^{ZPE} corresponds to the zero-point energy contribution. Θ_k is the vibrational temperature, which depends on the frequencies (ν_k). Using our $(TiO_2)_{16}(H_2O)_8$ NP as an example, we explicitly compute the harmonic vibrational frequencies of the system and evaluate the $F^{vib}(T, \Theta_k)$. In Figure 4.2 we show $F^{vib}(T, \Theta_k)$ with respect to vibration frequency and temperature (T).

Two distinct contributions to $F^{vib}(T, \Theta_k)$ are clearly seen. The first one at lower frequencies is almost totally defined by the temperature dependent terms and relates to the modes of the bonded Ti-O titania framework. The second contribution for higher frequencies, mainly corresponding to the temperature-independent ZPE term, is dominated by the vibrational modes of the pendant -OH groups.

The f^{vib} function was parameterized using second-order polynomial expressions, allowing for the estimation of vibrational contributions without the need for explicit calculation of all vibrational frequencies. This approach significantly reduces computational costs while maintaining accuracy, as demonstrated by the close agreement between $AIAT_{nano}$ and explicitly calculated phase diagrams for the $(TiO_2)_{16}(H_2O)_m$ system (see Figure 4.3).

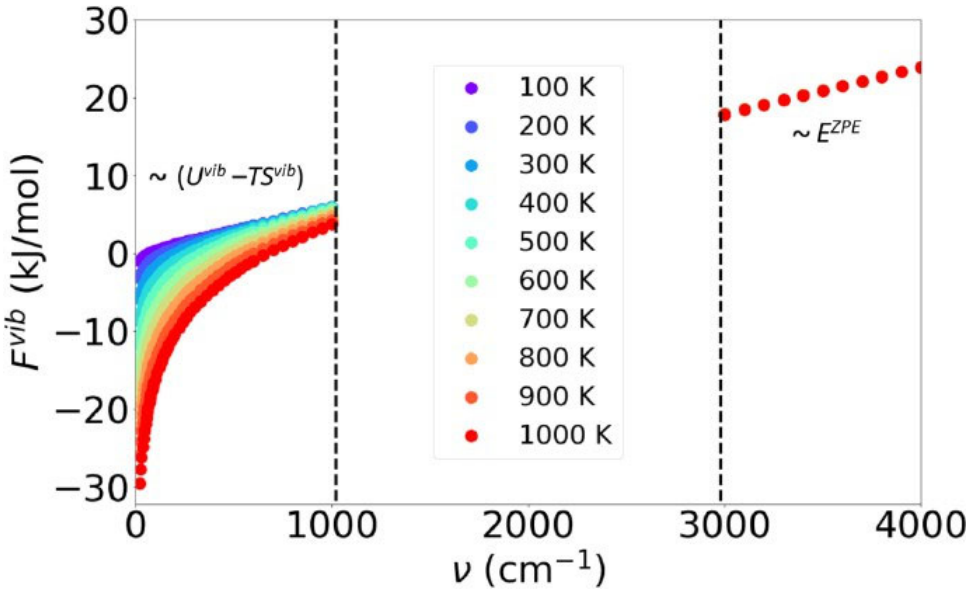

Figure 4.2: F^{vib} variation respect to vibrational frequency (ν_k) at different temperatures calculated for the $(TiO_2)_{16}(H_2O)_8$ NP. The dominant influence of the temperature-dependent terms (lower frequencies) and the ZPE term (higher frequencies) are clearly differentiated.

4.2.2 Size-Dependent Hydration Energetics

The $AIAT_{nano}$ approach was then applied to the series of titania NPs with increasing sizes ($(TiO_2)_{35}(H_2O)_m$, $(TiO_2)_{84}(H_2O)_m$, $(TiO_2)_{165}(H_2O)_m$). We construct thermodynamics phase diagrams for the hydroxylation of such titania NPs under varying temperature and pressure conditions. Given the presumed applicability of Boltzmann statistics and the harmonic nature of molecular vibrations, we limited our temperature range to 100–1000 K, as in previous

studies.[5,7] We considered water partial pressures not exceeding 1×10^5 Pa (approximately 1 atm). This allows us to consider water as an ideal gas from around 450–500 K and above. Treating water as an ideal gas at lower temperatures and higher pressures is a more severe approximation but its impact is confined to a small region of these phase diagrams, thus minimally impacting most of the considered p versus T range. Such phase diagrams show an increasing preference for hydration as the temperature decreases, consistent with the exothermic nature of water adsorption on titania surfaces. However, the specific temperatures and pressures at which hydration becomes thermodynamically favourable vary significantly with NP size, highlighting the importance of size-dependent effects in nanoscale thermodynamics. In this way, the 35-size titania NP exhibited the largest deviations from the predictions of the traditional $\mathrm{AIAT_{solid}}$ approach, with differences in both the qualitative progression of hydration and the temperatures and pressures at which hydration is favoured (see Figure 4.4).

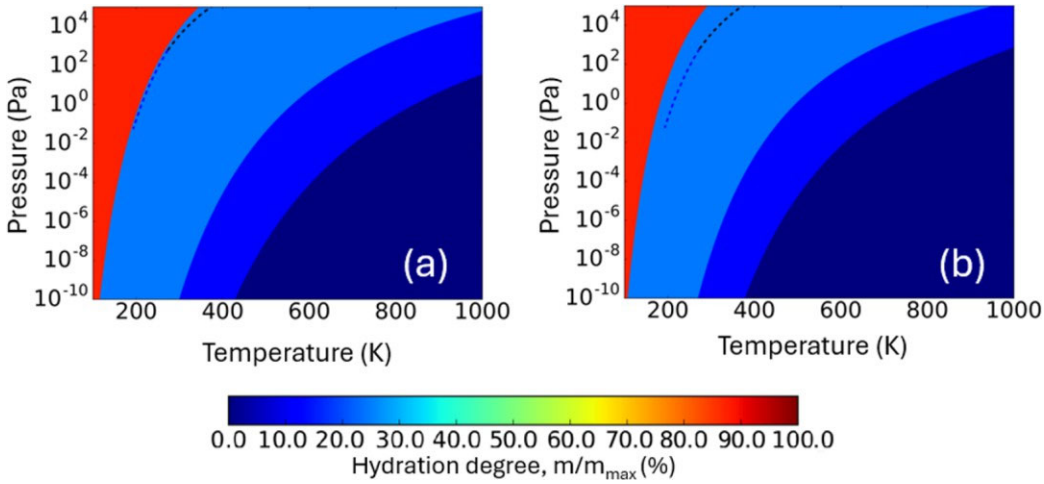

Figure 4.3: Thermodynamic p–T phase diagrams for the DFT-optimized $(TiO_2)_{16}(H_2O)_m$ NPs using different approaches to calculate differences in $\Delta G_f(T, p)$: (a) $\mathrm{AIAT_{explicit}}$, (b) $\mathrm{AIAT_{nano}}$.

As the NP size increases, the differences between $\mathrm{AIAT_{nano}}$ and $\mathrm{AIAT_{solid}}$ predictions diminish, converging toward the bulk limit. However, even for larger NPs ($(TiO_2)_{165}(H_2O)_m$), the inclusion of size-dependent vibrational

contributions in nano AIAT approach leads to quantitatively distinct phase diagrams, particularly at higher pressures and lower temperatures.

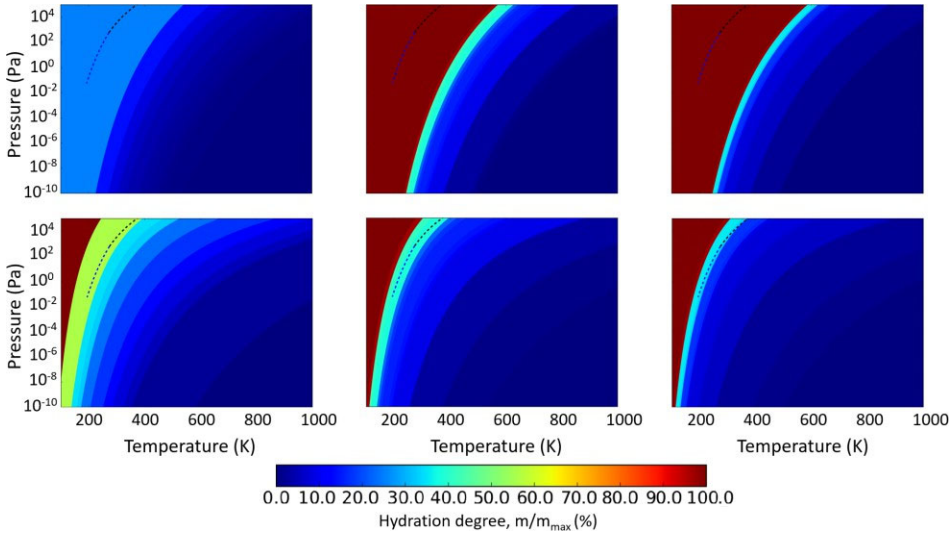

Figure 4.4: From left to right: predicted $\Delta G_{\mathrm{hyd}}(T, p)$ phase diagrams for the hydration of $(TiO_2)_{35}(H_2O)_m$ (left), $(TiO_2)_{84}(H_2O)_m$ (middle), and $(TiO_2)_{165}(H_2O)_m$ (right) obtained by using $AIAT_{solid}$ (top) and $AIAT_{nano}$ (bottom). Blue and black dashed lines indicate the equilibrium vapor pressure with ice and liquid water, respectively. Within each phase diagram, each shaded region represents the most thermodynamically stable titania NP for a certain degree of hydration.

4.2.3 Phase Diagrams and Hydration Stability

To emphasize the practical utility of the $AIAT_{nano}$ approach, we constructed a size-temperature-pressure diagram (Figure 4.5) to predict the thermodynamic conditions under which anhydrous anatase NPs initially become hydroxylated. This diagram provides a comprehensive depiction of the crossover conditions, specifically identifying the temperature and pressure thresholds at which hydration begins. The analysis focuses on the first $\Delta G_{\mathrm{hyd}}(T, p)$ crossover contour, which demarcates the transition between the anhydrous state and the onset of hydroxylation, where a single water molecule becomes adsorbed onto the NP surface. Notably, this contour is a fundamental thermodynamic feature

common to all titania systems and is consistently associated with the lowest pressure and highest temperature crossover point in $\Delta G_{\mathrm{hyd}}(T, p)$.

By employing $\mathrm{AIAT_{nano}}$-predicted crossover contours for model our three set of NPs, as well as the bulk $\mathrm{AIAT_{solid}}$-derived limiting contour for the anatase $TiO_2(101)$ surface model, we establish a systematic framework for understanding hydration behaviour across different NP sizes. Specifically, the analysis highlights selected nanostructure diameters: (i) 1 nm, where global optimization studies indicate that non-crystalline, quasi-spherical NPs are energetically favoured;[25] (ii) 5 nm, representing the upper size limit for TiO_2 NPs to maintain spherical-like morphologies;[24] and (iii) 20 nm, which approaches the stability threshold where anatase remains thermodynamically favourable over rutile.[26]

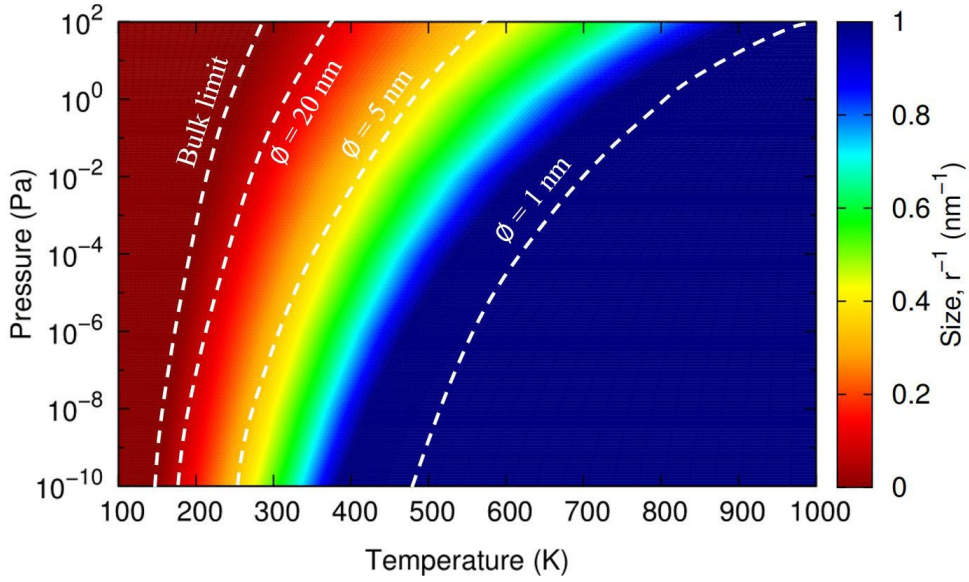

Figure 4.5: Size-dependency of the $\Delta G_{\mathrm{hyd}}(T, p)$ crossover contour for the initial hydration of an anhydrous anatase titania system by one water molecule. The coloured regions correspond to different titania NP sizes. White dashed contours highlight selected NP sizes.

The results reveal a strong size dependence in the crossover temperatures for hydration onset. Smaller NPs, such as those with a 1 nm diameter, exhibit

significantly larger crossover temperatures compared to their larger counterparts, such as 20 nm NPs. Furthermore, our analysis confirms that even for crystalline anatase NPs with diameters approaching 20 nm, the crossover temperature remains noticeably distinct from the bulk case, with differences ranging from 20 to 90 K.

Importantly, these findings have significant implications for the rational design and synthesis of titania NPs for targeted applications. By leveraging the $AIAT_{nano}$ approach, we establish a predictive model that enables control over hydration behaviour under realistic environmental conditions. The $AIAT_{nano}$ framework serves as a bridge between the computationally demanding $AIAT_{explicit}$ approach, which is suitable for small clusters (diameters < 2 nm), and the $AIAT_{solid}$ approximation, which is most effective for extended surfaces and bulk materials. By incorporating vibrational contributions through the analytical function f^{vib}, we provide a computationally efficient method for estimating $\Delta G_{\mathrm{hyd}}(T,\ p)$ without the need for explicit frequency calculations, thereby facilitating accurate thermodynamic predictions across a wide range of NP sizes.

4.3 Conclusions

This chapter has introduced $AIAT_{nano}$, a computational framework designed to bridge the gap between $AIAT_{explicit}$, which is limited to small molecular-scale clusters, and $AIAT_{solid}$, which relies on bulk-like approximations. The key advancement of $AIAT_{nano}$ is the incorporation of a size-dependent vibrational free energy correction, allowing for a more accurate and computationally feasible estimation of Gibbs free energy in nanoscale systems. By parameterizing vibrational contributions through an analytical function, $f^{vib}(T, N)$, this approach enables the study of hydration thermodynamics in systems where explicit phonon calculations are impractical due to their prohibitive computational cost.

The results demonstrate that hydration stability in TiO_2 nanoparticles is strongly influenced by size-dependent vibrational effects, which are often neglected in traditional $AIAT_{solid}$ treatments. $AIAT_{nano}$ provides an improved thermodynamic description, particularly for nanosized titania clusters (2–5 nm range), where explicit vibrational calculations are computationally infeasible, yet bulk approximations fail to capture key finite-size effects. The application of $AIAT_{nano}$ to hydrated TiO_2 nanoparticles reveals that smaller systems exhibit enhanced hydration stability due to vibrational entropy contributions, an effect that is progressively diminished as system size increases.

From a methodological perspective, this work underscores the power of computational modelling in materials chemistry, particularly in developing thermodynamic models that remain accurate across different length scales. The $AIAT_{nano}$ framework significantly reduces computational costs while maintaining predictive accuracy, making it a valuable tool for exploring the thermodynamics of nanoscale hydration. By systematically refining the AIAT approach to include parametric vibrational corrections, this work demonstrates how efficient computational methodologies can overcome the limitations of direct DFT-based phonon calculations in complex nanoscale systems.

Beyond its fundamental thermodynamic implications, the $AIAT_{nano}$ model has broad applications in computational materials chemistry, particularly in catalysis, electrochemistry, and environmental nanoscience, where hydration

processes are critical. The insights gained from this study contribute to the broader effort of developing computationally efficient first-principles based thermodynamic models applicable to nanoscale materials, reinforcing the role of theoretical and computational chemistry in advancing our understanding of material stability and reactivity under realistic conditions.

4.4 Publications

THE JOURNAL OF PHYSICAL CHEMISTRY LETTERS
A JOURNAL OF THE AMERICAN CHEMICAL SOCIETY

pubs.acs.org/JPCL
Letter

Size-Dependent Ab Initio Atomistic Thermodynamics from Cluster to Bulk: Application to Hydration of Titania Nanoparticles

Miguel Recio-Poo, Ángel Morales-García,* Francesc Illas, and Stefan T. Bromley*

Cite This: J. Phys. Chem. Lett. 2024, 15, 8240−8247
Read Online
ACCESS | Metrics & More | Article Recommendations | Supporting Information

ABSTRACT: Ab initio atomistic thermodynamics (AIAT) has become an indispensable tool to estimate Gibbs free energy changes for solid surfaces interacting with gaseous species relative to pressure (p) and temperature (T). For such systems, AIAT assumes that solid vibrational contributions to Gibbs free energy differences cancel out. However, the validity of this assumption is unclear for nanoscale systems. Using hydrated titania nanoparticles (NPs) as an example, we estimate the vibrational contributions to the Gibbs free energy of hydration ($\Delta G_{hyd}(T,p)$) for arbitrary NP size and degree of hydration. Comparing $\Delta G_{hyd}(T,p)$ phase diagrams for NPs when considering these contributions ($AIAT_{nano}$) relative to a standard AIAT approach reveals significant qualitative and quantitative differences, which only become negligible for large systems. By constructing a size-dependent $\Delta G_{hyd}(T,p)$ phase diagram, we illustrate how our approach can provide deeper insights into how nanosytems interact with their environments, with many potential applications (e.g., catalytic nanoparticles, biological colloids, nanoparticulate pollutants).

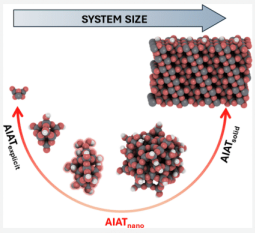

Computational modeling is increasingly playing a central role in the discovery and development of new materials that underly many technological advances. Here, approaches based on density functional theory (DFT) are widely employed due their capacity to calculate properties of materials accurately and rapidly. Formation of data sets of DFT-based calculations of thousands of compounds, and subsequent exploration using machine learning methods, can be employed to propose candidate materials with desirable characteristics for a class of applications.[1,2] Still, however, the deliberate theoretical design of materials with structures and properties that are tailored for specific real life technological uses remains a significant challenge. To better address this problem, DFT-based models should account for the interaction of a material with its environment. This more realistic situation can be approximately captured for extended solid systems interacting with a gaseous phase by the *ab initio* atomistic thermodynamics (AIAT) approach.[3,4] For such systems, AIAT makes simplifying assumptions (see below) that permit the application of standard DFT calculations. Decreasing system sizes to the nanoscale magnifies the complexity due to the emergence of a strong dependence of structures and properties on size and surface area. For nanosystems, the AIAT approximations used when modeling extended solids become more questionable. Accurately modeling the huge variety of important nanomaterials in realistic scenarios has thus been hindered by the theoretical challenges involved. Herein, to help address this issue, we propose a straightforward approach to estimate the thermodynamic stability of nanoscale structures in the presence of an interacting environment of gas-phase species.

Viable materials, irrespective of their size, should not only possess desirable characteristics but should also be synthesisable and sufficiently stable once made.[5] These latter conditions are determined by both kinetics and thermodynamics. Kinetics can be studied to compare the rates of different synthetic routes followed to obtain a material from a given starting point. Thermodynamics is more fundamental as it pertains to whether such a synthesis is plausible under given conditions, regardless of the rate or route taken. The Gibbs free energy of formation, $\Delta G_f(T,p)$, (i.e., the difference in Gibbs free energy between start and end points of a material's synthesis at temperature T and pressure p) determines the favorability of the process. Phase diagrams derived from $\Delta G_f(T,p)$ can thus serve as useful guides for predicting the stability of materials under realistic conditions.

From an experimental point of view, $\Delta G_f(T,p)$ is typically viewed as being composed from the enthalpy of formation $\Delta H_f(T,p)$ and an entropic term $\Delta S_f(T,p)$, which are both functions of the heat capacity of the compounds involved in a formation reaction. The calorimetry experiments needed to accurately measure heat capacities of bulk materials are intricate and time-consuming,[6] and become even more challenging for nanomaterials.[7] The possibility to theoretically

Received: May 24, 2024
Revised: July 22, 2024
Accepted: July 25, 2024
Published: August 6, 2024

https://doi.org/10.1021/acs.jpclett.4c01531
J. Phys. Chem. Lett. 2024, 15, 8240−8247

The Journal of Physical Chemistry Letters pubs.acs.org/JPCL

predict *8.Gf_T,p)* values for materials of arbitrary size with reasonable accuracy is thus very attractive. Prom. a computational view, a standard DFT calculation of the interna! energy of a chemical system at O K typically pro\lides by far the most significant contribution to *.ó..Gi{T,p*). In contrast, explicitly calculating contributions to *f::i.G*$\hat{\phi}$*T,p)* which depend on all relevant degrees of freedom *(* e.g., vibrations and atomic configurations) before and after a formation process, is relatively highly cornputationally demanding. For systems composed of hundreds ar thousands of atoms explicit calculations of these contributions quickly become practically intractable. Although these contributions are typically rnuch srnaller than the O K interna! energy, irnportantly, they can often be the deciding factor when assessing differences in *.ó.Gi(T,p)* for two competing processes.

For eitended surfaces, DFT cakulations have thus mainly been used to predict properties at O K in vacuum due to the high computational cost of explicitly evaluating all terms in *.ó.G/T,p)* for more rcalistic scenarios. Howcver, under certain simplifying circumstances, *t:.G/T,p)* values for extended solid surfaces interacting with a gaseous environment can be reasunably estimateJ by O K r.::akulateJ t!nergy Jifferenr.::es uf the solids plus therrnodynamical properties of the gas phase molecules assurned to behave asan ideal gas.RHere, *ó.Gi(T,p)* values relate to the formation energies of systems where different proportions of gaseous molecules have adsorbed on the salid surface. VVith such an AIAT approach, one typically assurnes that (i) the vibrational entropy contribution from surface atoms is the same for the dean and covered surface, and (ii) each systern is dorninated by very few low energy configurations. Then, for changes of coverage, the vibrational contributions to *.D..G/T,p)* for the surfaces cancel out and the configurational entropic changes are negligible. The vibrational contribution of the adsorbates (typically the zero point energy - ZPE) can ako he included in snch calcnlations fnr a moderate extra computational cost. Here, the *.ó.G/T,p)* values become changes in enthalpies of the solid phase plus relevant changes due to gas phase (and sometimes adsorbed) species. Thus, *.D..Gi(T,p)* values become accessible based on standard O K DFT calculations induding normal modes of molecular species.

This general AIAT approach to extended solids {hereafter referred to as AIATsolid) has been widely used to predict the state of single-crystal metal surfaces in contact with a gaseous phase far a range of values of *T* and p.[3,1,9,10] Generally, the AlAT approach relates to the use of O K calculated results to estimate *.D..G_/T,p)* values for solid systems in the presence of a reservoir of interacting chemical species.

For much smaller systems composed of up to a few tens of atoms interacting with a gaseous environment, one can use O K DFT calculations and standard statistical thermodynamics to directly calculate ali relevant terrns that contribute to *.ó.Gi(T,p).* An AIAT description of such a system does not rely on the simplifying asswnptions used in the treatment of solid surfaces; hnt is derived from explicit calculation of all relevant contributions to the partition function far ali parts of the system (e.g., translational, rotational, vibrational, ZPE). This AIATexphct methodology has been applied to calculate *.ó.G_/T,p)* for numerous clusters reacting with gaseous environments (e.g., Mg_nO_n clusters with oxygen,[11] Au_n clusters with CO and $(H_2O)_n$, and $(SiO_2)_n$ clusters with water vapor).

Between small molecular scale clusters and extended macroscopic solids lie nanosized systems. 1-Iere, we find severa! imporlant dasses of objects which can strongly interact with their envirunmenb: (e.g., 1.:atalytir.:: nanopartides, biulugiul colloids, nanoparticulate pollutants) for which a *.ó.G/T,p)*-based characterization could be highly instructive. These systems are generally too large to be computationally tractable using an AIATexplicit approach. It is also often unclear if such systerns are sufficiently large such that one can use the approximations inherent in an AIATmlid. approach. Herein, we propose a simple method to estimate *t:.Gf(T,p)* values for nanosysterns interacting with gas phase species. We thus provide a general AIAT approach (hereafter referred to as $AIAT_{nl_{110}}$) that is tailored for the bridging system size regi.me between the molecular scale and extended solids. In this way, we demonstrate how to exploit the powerful AIAT method for a significantly extended range of system sizes. Our work also highlights the size-dependent limitations of the approxirnations used in the standard AlAT• ..Jid approach to solid surfaces. As our approach does not rely on any system specific properties, it should be straightforward to apply it generally to many nanosystems. By doing so, we hope that our ATATonano ;ipproach wil.l yield new insights into how n;inoparticulrtte systems interact v.::ith their environments with potentially wide-ranging implications.

As a specific example of our approach, we consider photoactive tifania (TiO_2) and its interaction with water molecules. Such a system is relevant to severa! technological applications (e.g., water purification, photoreduction of CO_2, water splitting).[14−16] Key to the $AIAT_{nano}$ approach is the choice of reference system.s. Ideally, for the lower size lim.it, these systems should be small enough to permit a AlAT explicit trealm!!nl ami large enough tu exhibit typir.::al nano$\hat{\phi}$r.::alt! characteristics. Here, as an example, we mainly consider a NP system based on a 48 atom $(TiO_2)_{16}$ core structure cut from the bulk anatase crystal structure which we progressively hydrate while minimizing perturbations to its core structure. This systern possesses the bulk-like stability and structure of larger anatase NPs (thus providing a natural limiting case for such systems) while allowing far an explicit calculation of ali contributions to *t:.Ghi T,p)* (i.e., the Gibbs free energy of hydration). We note that constraining the core structure ofthe NP to maintain a characteristic anatase-like structure leads to slightly different results in the final AIAT nano approximation compared to the use of globally optimized $(TiO_2)_{16}(H_2O)_n$ structures[13] (see Sl in the Supporting Information (SI)). Asan example of a molecular scale system, we also consider a $(TiO_2)_4(H_2O)_{10}$ system for which globally optimized structures were used. ;)

For the large size limit, we use an extended anatase TiO_2 (1O1) surface with different degrees of hydration. The surface model was represented hy a periodically repeated slah consisting of six atomic layers of a (3 x 1) snpercell, exposing the (101) surface on either side of the slab. Reciproca! space sampling at r point only was found to be sufficiently accurate.[17] A 20 Å vacuum spJ.ce between repeated sbbs in the direction perpendicular to the surface was uscd avoid the artificial interslab interactions.

To compare our $AIAT_{nmo}$ approach with the standard AlATsolid method, we considera set of bipyramidal titania NP systems sontaining up to 500 atoms, namely $(TiO_2)_{33}(H_2O)_{38}$ (TiO_2 nH O)nn, and $(TiO_2)_{165}(H_2O)_{82}$. The titania r.::ore$\hat{\phi}$ uf these NPs were obtained from top-down cuts of the bulk

htt)\$://doi.org/1O.1 021/acs.jp:lettAcO1531
J. Phys. Chrm. Lett.1024, 15, 8240-3247

anatase crystal structure to expose facets of the most stable (101) surface[18,20] To standardize our reported $(TiO_2)_N$ NP sizesi we use the diameter of a sphere containing N TiO_2 unitsi wht:=re the volume uf a single unit is taken frum that in bulk anatase. This leads to diameters ranging from ~2 nm (for the $(TiO_2)_5$ NP) to ~4.3 nm (for the fully hydrated $(TiO_2)_{165}$ NP). These NPs are in the size regime for which direct DFT-based calculation of their vibrational frequencies would be extremely computationally expensive.

We assume that the hydration of all considered titania systems follows a mechanism where H_2O dissociates upon adsorption and H and OH species interact with surface O and Ti atoms, respectively. This picture is supported by experiments on anatase NPs[21] where progressive hydration proceeds from more reactive to less reactive regions (i.e.i apicali equatoriali edge, and facet sites) until ali coordinatively unsaturated atoms are covered. For extended (101) facets (e.g., on large crystalline anatase NPs) sorne molecular water adsorption will likely also occur along with dissociation.[22,23] We note that molecular water adsorption is not likely to be prevalent on the relatively small NPs in our test set. Such a regime is also not relevant to the reported size-dependent example of our method where we focus only on the initial hydration step. The maximum degree of dissociative hydration in our $(TiO_2)_{35}(H,O)m$, $(TiO_2)_{84}(H,O)w$ $(TiO_2)_{..}(H,O)m$ NPs corresponds to m = 34, 62, and 98i respectively (i.e.i $(TiO_2)_{35}(H,0)_{3.}$- $(TiO_2)_{84}(H,0)_{6b}$ and $(TiO_{,})_{165}(H,0)_{98)}$. For thc $(TiO_{,})_1$,(H,olm and $(TiO_{,})_{,}$(H,Olm systems, full dissociative hydration is reached with eight and four water moleculesi respectively. Lastlyi we considered a range of different degrees of hydration of our (101) anatase surface model. Figure 1 shows examples of titania systems consideredi fur: Zl!fo_1 minimal (i.e.$_1$ une water moler.::ule) an<l maximal degrees of hydration.

The structures of ali as-cut anatase-based $(TiO_2)(H_2O)_{111}$ nanostructures and the (101) surface model were optimized using DFT-based calculations with the Perdew-Burke-Ernzerhof (PBE) exchange-correlation functional[/1] as implemented in the FHI-aims code.[25] A light-tier-1 numerical atom-centered orbital basis set was utilized in all cases¡ which provide results of triple-(plus polarization quality.[19] The energy and force thresholds far the energy minimization and geometry optimization were fix.ed at 10^{-5} eV and 10^{-4} eV/Ái respectively.

The most computationally expensive part of explicitly evaluating $.ó..G_{1,,}(T,p)$ involves the calculation of the vibrational degrees of freedom of the system. As this rapidly becomes intractable with increasing system size, we take $(TiO_2)_1H_2O)_{.,}$ as a reference system for which it is practical to explicitly calculate data to parametrize a temperature- and size-dependentf'ib(T,N) function that consider'> contributions frnm all atoms of the sy.,:;tem. A,;; noted ahove, the SÍ7.e and properties ofthis reference system (e.g., anatase-like strncture) are also chosen so that $_{i}wb(T,N)$ should provide a reasonable estímate of the vibrational contributions to $8.Ghya(Tip)$ for brger anatase-structured NPs. Although we expect that our $(TiO_2)_{1}iH_2O)_m$ NP system is a reasonablc choice of an example to illustrate the expected type and magnitudes of eiected contributions to $.6.G1i>iT,p)_{1}$ how the specific form of $J^{1}(T,N)$ depends on the chosen reference system will be studied in more detail in future work. We note thati ideally, the dmsen rdl!rl:!111.:e system(s) for Jerivingf"b(T,N) shuulJ have structural/vibrational properties that are representative of NPs

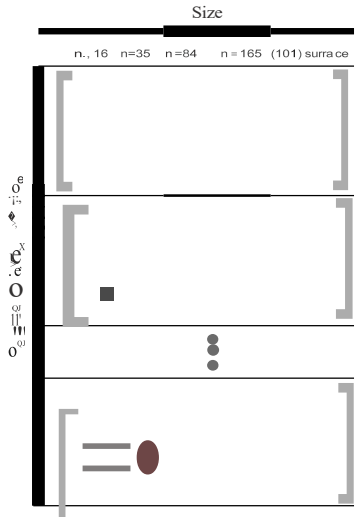

Figure 1. Examples of $(Ti0_2)"(H_2O)_{111}$NP models and the anatase (101) surfact' supercell moJel used. Whik, gray, and red splm·es denote H, Ti,. and O atoms, respectively.

in the scalable regime (i.e., where NP properties scale in a regular manner with size).[26]

Figure 2 schematically compares our AIAT nano approach with AIATexplicit and AIATsolid approaches used for smaller and larger systems, respectively.

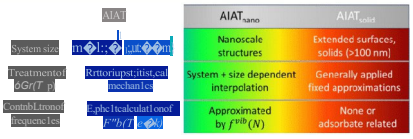

Figure 2. Scheme indicating three ditferent system size regimes with respect to the respective AIAT-based computation of $8.Gf(\_T,p)$. Bine and red, respectively, relate to the small and large regimes far which AIATexplicit and AIATsolid have been extensivdy applied. Our bridging interpolation approach for nanosized systems (AIATnmo) replaces the cxplicit computation of vibrational frcqucncies with thc use of a tempcrature-dependent and N-dependent parametrized function, $rb(T,N)$, where N rcpresents a generic system size variable.

To estímate $D..G1i_{p}JCTip)$ for a given hydrated tita.nía nanostructure at a temperature (T) and partial pressure of water vapor (p) at equilibrium we use:

$$iiG_{i,y,}(T,\ p) = G(Tiü,),(H,O),(T)- \quad G(Tiü,),(T) - \ m_i1_{8,}0(T,\ p) \qquad (1)$$

where $\mu_{H_2O}(T,\ p)$ i$\hat{\Omega}$ the chemical potential of the gas-phase water molecule as a function of T and p. In this way,

https://do;.o,g/10.1021/acs.jp:lett4c01531
J. Phys. Chrm. Lett.2024, 15, 8240-3247

6.G1iyiT1p) estimates the free energy of hydration relative to the respective nonhydrated system. Once we have obtained the most stable degree of hydroxylation of a system under a range of conditionsi the thermodynamic p versus T phase diagram can be derived. The vibrational contribution to Gibbs free energy, *p;h,* can be expressed as the sum of three terrns:

$$F^{1}{}'(r,e,) - EZPE(e,) + U^{r1}{}'(T, e,) - TS^{''1}{}'(T, e,) \quad (2)$$

where *U"ib* and S";t are the vibrational contributions to the interna! energy and entropy and *EZPE* corresponds to the zero-point energy (ZPE) contribution. *8k* is the vibrational temperature, which depends on the normal mode frequencies (v1;). The standard analytical expressions for each term for a molecular system can be found in ref 27. *u•ib* and *5vib* are dependent on T and ;ue mainly iniluenced by lower frequencies, whereas *EZPE* is mainly governed by higher frequencies and is independent of *T.* In Figure S2 in the SI, we show how the explicitly calculated *pib(T,0k)* at different temperatures varies with respect to frequency, *vicJ* for the $(TiO_2)_6O(H,0)_8$ system.

To circumvcnt thc nced for calculating ali vibrational frequencies, we define an analytical expression, *pib(N,T),* to approximate *pib_ J"ib(N T)* is derived to reproduce both contributions to *pb* for the hydrated $(TiO_2)_{16}(l\text{-}1_20)$m NP system for different temperatures. We partitionrb(N,T) into two terms: *[fih•ZPE* (combining temperature-dependent terrns and ZPE) af Proximately accounting for energetic contributions and *S"* , which estimares the entropic contributions:

$$f_{viO} = U_{vib}\text{-}ZPE \_ TS_{vib} \quad (3)$$

We approximate these contributions using the fol\owing second order polynomial expression_.:::

$$U'ib\text{-}ZPE = (a_O + a,T + a_2T^2)N,, + (b_O + b,T + b_2T^2)m,, \quad (4)$$

$$S^{vib} = (c_0 + c_1T + c_2T^2)N_v \quad (5)$$

where $Nv = 3(3n + m)$ - 6ı which is total number of vibrations from ali Ti and O atoms in a $(TiO_2)_t(H_2O)_m$ NP. Similarly1 *mv* = *lm* gives the total number of vibrations from the -0-H groups. The values of al\ coefficients are provided in the SI. The first term of *U"ib-ZPE* mainly captures the contribution from the low-frequency Ti-O vibrational rnodes connected to the temperature-dependent part, while the second term is mainly associated with the higher frequency vibrations (-OH) from the ZPE contribution. Although formally the ZPE contribution is ternperature independent there is also a small contribution from the intemal energy term from high -OH frequencies at high temperatures, which leads to a weak. temperature dependence of the second term in eq 4. The *svib(T)* term is only determined by lower frequency Ti-O vibrational modes. Fiaure S3 in the SI shows the evolution of both *r_jvib-ZPE/* and *T-svi* contributions to the Gibbs free energy for our $\{Ti0_2)_1t_1(H_2O)_8$ NP with respect to *T.* As our simple derivation of fib is quite general with respect the types of vibrations expected in any $(TiO_2)n(H_2O)$": *NP1*we assume that it provides a reasonable account of the vibrational contributions to the *Gi:ya(T1p)* for NPs of this type for any ıı and *m.* We also note that the thennodynamical terrns involved in fitting *f";h(N,T)* are general to ali nanoparticulate-adsorbate systems. We thus anticipate that fits like that used in eqs 4 and 5ı with parameters adjusted to reflect the respective number/types of atoms and number/frequendes of vibrational modes, could be used for m.any nanosystems. We also note that although a simple polynomial fit was found to be adequate for this example systemı other types of fit may be more appropriate for other nanosystems.

Using ɾ;ı, toestimare ali the vibrational contributions to *.ó.GnriT1p),* along ·with all other nonvibrational contributions calculated explicitly (e.g., O K interna! energy, rotational translational entropic terms) we construct a AIATnano phase diagram showing the most stable $(TiO_2)_{11}iH_2O)"'$ compositions with for a range of temperatures and partial pressures of water vapor (see Figure 3b). Given the presumed applicability

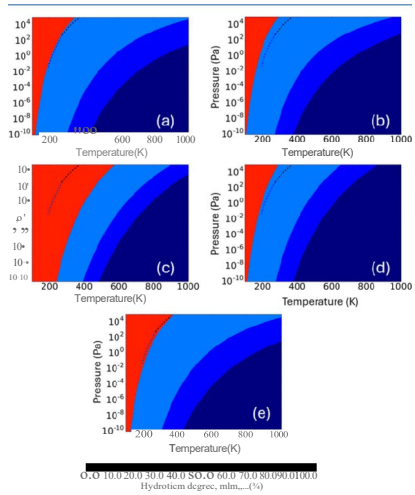

Figure 3. Thermodynamic *p-T* phase diagrams for the DFT-optimized $(TiO_2)_{11}iH_2O)$m NPs using different approaches to calculate differences in *i1Gn;iT,p):* (a) AIAT•xrlicitl (b) AIATnano• (c) AIATsoliJ, (d) AlAT$_{ls}$l,J + i1Gzr& and (e) AIATro'id + i1G,,;b• Blue and black dashed lines indicate the equilibrium vapor pressure with ice and liquid water, respectively. Within each phase diagram, each shaded region represents the most thermodynamically stable titania NP Íor a cerlain degree of hyd1alion.

of Boltzmann statistics and the harmonic nature of molecular vibrations, we limit our temperature range to 100-1000 K_I as in previous studies.[13,2] B We consider water partial pressures less than ı x 10^5 Pa allowing us to consider water as an ideal gas from around 450-500 K and above. For lower temperatures and higher pressures this is a more severe approximationı but its impact is confined to a small region of the phase diagrams only. Comparing the AIATnano phase diagram with one derived using AIATcxplict (see Figure 3a) we can see a reasonably good qualitative and quantitative match. In contrastı for the corresponding phase diagram derived by employing AlATs<Jlid (see Figure 3c), the agreement with the explicitly calculated phase diagram significantly worsens. Including explicitly calculated ZPE contributions (mainly

https://doi.o,g/10.1021/acs.jpdett4c01531
J. Phys. Chrm. lett.2024, 15,8240-3247

The Journal of Physical Chemistry Letters pubs.acs.org/JPCL Letter

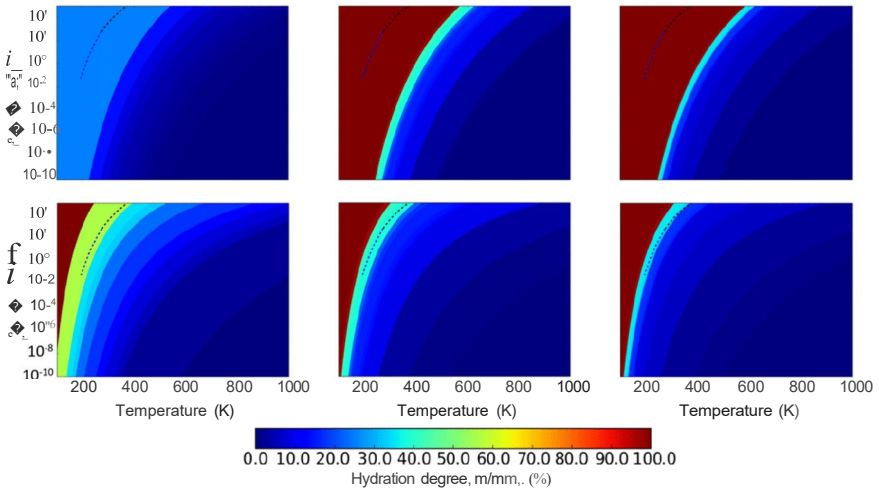

Figure 4. From left to right: predicted *j.Ghyd(T,p)* phase diagrams for the hydration of $(TiO_2h_5(H_2O)$,..(left), $(TiO_{2)8}iH_2O)$,.,(middle), and $(TiO_{2)16}S\{H_2O)$.., (right) obtained by using AIATsobJ (top) and AL'\T:iano (bottom). Blue and black dashed lines indicate the equilibrium vapor pressure with ice and liquid water, respectively. Within each phase diagram, each shaded region represents the most thermodynamically stable titania NP for a certain degree of hydration.

from adsorbate vibrations) within an AIATsolid approach (i.e.,1 AIATtolid + ZPEadsi see Figure 3d) only moderately improves the phase diagram with respect to the AIATexplicit description. Conversely, including explicitly calculated non-ZPE temperature-dependent vibrational contributions to an AIATsolid approach (see Figure 3e) significantly irnproves the phase diagram compared to the AIATexrlicit reference phase diagram. This comparison indicates that the temperature-dependent vihrational terms are the main reason for the differences between an AIATsolid approach and a reference AIATexplidt description.

Usingfibi wc can now estimatc thc vibrational contributions to *6.G11ya(T,p)* for larger NPs in the scalable regime. We note that lhe size-dependency of *6.G11ya(T,p)* values are largely dominated by O K energy differences which are considered in both AIAT nano and AIAT solid approaches. Generally, these energy differences are more pronounced for smaller systems than for larger systems, as hydration tends to perturb the former more than latter. From the definition of F'''' (see eqs 4 and 5), *◆rtb* values far a specific change in hydration degree do not explicitly depend on the size of the underlying titania system (N). This also implies that the differences in predictions of *◆GhyiTip)* between AIATnano and AIAT,olid approaches, for any fixed conditions and for a specific hydration change, wil.l not be size-dependent. However, such fixed shifts can still have a larger or smaller impact on thermodynamic crossovers for differcnt NP sizes. To illustrate this, in Figure S4 in thc SI, wc show thc tcmpcraturc evolution of *6.Gh1a(T,p)* as predicted by AIATnano and AlATsolid for system sizes of $(TiO_2)iH_2O)$mand $(TiO_2)u;_5(H_2O)_{1111}$ far the hydration of the anhydrous systems by a single water molecule (far a water partial pressure of 1000 Pa). As expected, the temperature-dependent difference between the predicted variation in *L)..GhyiT,p)* by AIATsolid and AIATnano is the same for both systern sizes. However, for each fixed systern size, the predicted ternperature at which *aG,,YiT,p)* changes sign (i.e., crosses the x-axis) is different for a AIATsohl and AIATn•no approaches. This change in sign signifies a change in the relative stability of the system with respect to hydration and is a key factor in defining the *.ó.G1iyiT,p)* phase diagrams. lmportantly, the size-dependency of the *T* and *p* conditions at which the predicted values of *.ó.G11yiT,p)* change sign will gcncrally be diffcrcnt for a AIATnano approach with respect to a AIATsolid approach. Consequently, the corresponding pre-Jir.::teJ *6.G1i1JCT,p)* pha◆e <liagrams fur butli approad1t:s will bt: distinct and size-dependent.

In Figure 4, we show the predictions frorn an Al.ATnano approach as compared to AIATsolid for *.ó.Gh1iT,p)* phase diagrams for increasingly sized $(Ti_2Ls(H_2ü)m$, $(TiO_2)s_4(H_2O)$mand $(TiO_2)_1dH_2O)$mmodel NPs. We note that for these systerns explicit DFT-based calculation of ali vibrational modes would be computationally very expensive, as compared to our $(Ti0_{2)16}(H_20)$,., reference system. For both considered AlAT approaches and ali three NP sizes, ali phase diagrams show an increasing preference for hydration as the temperature decreases far the full pressure range. Of the three considered NPs, as expected, the phase diagram far the smallest $(Ti0i\}_{.35}(Hz0)$,,,NP shows the largest difference ,vith rcspect to thc two AIAT approaches. Por this sizc, differenccs in both the qualitative progression of the preferred degrees of hydration and the tem.peratures and pressures at which they are favored are seen. Slightly less dramatic differences between

https://doi.org/10.1021/acs.jpdett-1c01531
J. Phys. Chrm. Lett.2024, 15, 8240-3247

the two approaches are also observed for the larger two NPs. Here the qualitative description of the predicted *.ó.G1i₁a(T₁p)* phase diagrams is similar, but the quantitative agreement is often quite poor. This is particularly clear for higher pressures where, in line with Figure *S4₁* we see that *.ó.G1i,i T₁p)* crossovers are predicted to occur at significantly higher temperatures in an AlAT nano approach as compared to AIAT!olid· Considering the similar comparison in Figure 3₁ these differences are likely mainly due to the inclusion of estimates of temperature-dependent vibrational contributions to *�GhyJ(T.,p)* in the AIAT$_{n;no}$ approach, rather than the effect of ZPE contributions.

As our AIATnano description is based on estimating total *�G,,yiT,p)* values from first-principles, it is independent of the approximations made in AIATsolid. and thus, does not necessarily converge to a AIATsuliJ description with increasing size. However, we see in Figure 4 that the differences behveen the predicted *ilGhyiT,p)* phase diagrams from AIAT$_{nano}$ and AIATtolid appcar to converge with incrcasing sizc. In Figure SS we track the size-dependent ALI\.Tnano versus AIATsolid differences in the predicted crossover temperature for the initial hydration onset. Here we can see that the highest sensitivity occurs for smaller system sizes (of a few hundred atoms) where the ternperature difference can vary over more than 200 K for relatively srnall changes in system size. With increasing system size, we indeed see that this difference starts to converge to a constant value for which the large system size AlAT$_{1}$iano predictions can range above and below the corresponding AIATsolid predictions. We may expect that such differences should approach zero if the assumptions of AIAT$_{s011;d}$ are taken to hold for the infinite sized limiting system. In such a case, we can use an AIAT,olid description of *�G,,yiT,p)* for an anatase bulk surface modelas a size-limiting description for ATATnarn,· U..:;ing this limit and an ATATnano· based *ilG$_{1}$,y.i(T₁p)* description for a set of finite systems$_{i}$ such as shown in Figure 4, we can interpolate between these two regimes (i.e., Al.ATt1ano· AIATsohd) to estimate the arbitraty size dependency any particular crossovcr.

Pinally$_{i}$ to highlight a practica! example of an AIATnano--;. AIATiolid approach, in Figure 5 we show a size-temperature-pressure-<lepen<l1::nt <liagram pre<liding thr.= thermo<lynamir.:: conditions at which anatase NPs initially becornes hydroxy-lated (see section S6 of the S1). Again, we focus on the

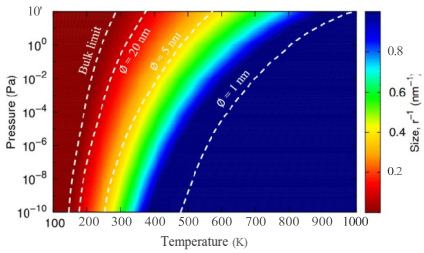

Figure 5. Size-dependency of the *8G^{1},yiT p)* crossover contour for the initial hydration of an anhydrous anatase titania system by one water molecule. The colored regions correspond to different titania NP sizes. White dashed contours highlight selected NP sizes.

8Ghya(T₁p) crossover contour dividing the anhydrous system and the systern with a single water rnolecule adsorbed on it. Following a similar strategy to that described above (see also SI}¡ we use the AIATnan$_{o}$ -predicted crossover contours from our $(TiO,)_{35}(H_2O)$., $(TiO_2)_{84}(H,0)$., and $(TiO_2)_{11}dH_2O)$. model NPs and the corresponding bulk AlATsolid-derived limiting contour derived for our anatase TiOi{101) surface model. In Figure 5 we highlight the contours corresponding to sorne selected NP diameters: (i) 1 nrni a size at which global optimization searches have established that noncrystalline anhydrous TiO_2 NPs with quasi-spherical morphologies are the most energetically stable,[18] (ii) S nm, which corresponds to the upper limit for TiO_2 NPs to exhibit spherical-like NP morphologies[9] and (iii) 20 *nm* ,which is close to the upper limiting NP size for rclative thermodynamic stability of anatasc with respect to rutile.[3] Far the 1 nm diameter crossover 1.::untuur *wr.*= arr.= duse in <izr.= lo the bulk-mimi1.::kin $(TiO_2)_{i6}(H,0)$. NP that we employed to derive our *f"* function. Generally, below 5 nm in diarneter, fully crystalline NPs tend to be less stable than amorphous quasi-spherical NPs, and thus we expect our predictions to tend to be more reliable for larger system sizes. We note that even for the crossover contour corresponding to crystalline anatase NPs with 20 nm diameters, the differences in *T* with respect to the bulk limiting case are still significant (20-90 K).

Overall, using the hydration of titania nanostructures as an example we derive an analytical fünction *fib* to ;ipproximate the *8G^{1},ylT,p)* values with respect to NP size and degree of hydration. *f^{lh}* accounts far the vibrational contributions to *ll.GnyiTip)* which avoids the explicit and computationally prohibitive calculation of system frequencies. *As such, f'ib* can be used to correct predicted differences in *ll.G,,yiT,p)* based on DFT-calculated O K total energies. The etfect of *f"b* on differences in *.ó.G1,yiT,p)* diminishes with increasing system size but is still significant for nanostructures up to IUs of nm in diameter. In this way, the AlAT nano approach can be used to calculate *ll.G/T,p)* phase diagrams for nanosystems that are too large to use AlATexplicit and too small to reliably employ AIATnli<l. Our AIATMnn approach thus bridges the gap between the small cluster size regime (diameters <2 run) and extended surfaces and solids. As the AIATnano approach is not dependent on any system specific properties it is quite general and opens the door to a computationally efficient DFT-based treatment of nanoscale structures when interacting with their environment.

■ ASSOCIATED CONTENT

t, Supporting Information

The Supporting Information is available free of charge at hllps:/ /pubs.ar.:s.org/ <loi/10.1021/ au.jpdr.=ll.41.::01531.

Comparison of a AIATcx¡,li<.il 8G¡, *,¡(T,p)* phase diagram far the globally optimized (TiO_2)iiH$_2$O)mNP system compared with an AIATnano approach¡ vibrational cc mtributions to *ll.G1iyAT,p)i* fitting parameters for *f^{lh}(N,T);* temperature dependence of vibrational tenns in *.ó.Ghya(T,p*)¡ size-dependence of the initial hydration *.ó.C1,ya(T,p)* crossover contour¡ general size-dependency of AIAT^{nno} (PDF)

Transparent Peer Review report availahle (PDF)

https://doi.org/10.1021/acs.jpclettc01531
J. Phys. Chrm. Lett.2024, 15, 8240-3247

AUTHOR INFORMATION

Corresponding Authors

Stefan T. Bromley - *Departament de Ciencia de Materials* i *Química Física & Institut de Química TeOrica i Computacional (IQTCUB), Universitat de Barcelona, 08028 Barcelona, Spain; Institució Catalana de Recerca* i *Estudis Avanfats (ICREAj, Passeig Lluis Companys* 23, *08010 Barcelona, Spain;* • orcid.org/0000-0002-7037-0475¡ , Email: s.bromley(@)ub.edu

Angel Morales-Garáa - *Deparfoment de Ciencia de Materiak i Química Física & Institut de Química Te0rica* i *Computacional (IQTCUB), Universitat de Barcelona, 08028 Barcelona, Spain;* • orcid.org/0000-0003-0491-1234¡ Email: angel.morales@ub.edu

Authors

Miguel Recio-Poo - *Departament de Ci'encia de Materials* i *Química Fi.�ica & Tmtitut de Química Te0r"ica* i *Computaciot1al (IQTCUBJ Universitat de Barcelona, 08028 Barcelona, Spain*

Francesc Illas - *Departament de Ci'encia de Materials* i *Química Física & Institut de Química Te0rica i Computacional (IQTCUB), Univcrsitat de Barcelona, 08028 Barcelona, Spain;* • ordd.org/0000-0003-2104-6123

Complete contact information is available at: https/ /pubs.acs.org/ 10.1021/ acs.jpclett.4c01531

Notes

The authors declare no competing financia! interest.

ACKNOWLEDGMENTS

We are thankful for the financia! support from MCIN/AEI/ 10.13039/501100011033 through projects PID2020-l 1 5293RJ-100, PID2021-126076NB-JO0, PID2021-127957NB-100, TED2021-l 29506B-C22, TED2021-132550B-C22 and the *María de Macztu* CEX2021-001202-M project, and from the *Gerieralitat de Catalunya* tluough prujects 2021-SGR-00079 and 2021-SGR-00354. Partial support form *Red de Investigación* RED2022-134295-T (FOTOFUEL) is also acknowledged. The reported research is also involved in the European Cooperation in Science and Technology (COST) Actions, CA18234 (CompNanoEnergy) and CA21101 (COSY). M.R.-P. acknowledges the *Ministerio de Ciencia e Innovación* (MICIN) for a *Formación Personal Investigador* (FPl) fellowship (PRE20l9-087627). We thank the *Red Española de Supercomputación* (RES) for the provision of supercomputing time. We also thank Dr. Albert Bruix for useful discussions.

REFERENCES

(1) Jain, A.; Ong. S. P.; Hautier, G.; Chen, W.; Richards, W. D.; Dacek, *S.;* Cholia, S.; Gunter, D.; Skinner, D.; Ceder, G.; Persson, K. A. Commentary: The Materials Project: A materials genome approach to accelerating materials innovation. *APL materials* 2013, *1,* 011002.

(2) Draxl, C.; Scheffler, M. The NOMAD laboratory: from data sharing to artificial intelligence. *J. Phys. Mater.* 2019, *2,* 036001.

(3) Reuter, K.; Scheffler, M. First-Principles Atomistic Thermodynamics for 0::ddation Catalysis: Smface Phase Diagrams and Catalytically Interesting Regions. *Phys. Rev. Lett.* 2003, 90, 046103.

(4) Reuter, K.; Scheftler, M. Composition, structure, and stability of as a function of KuO2 (Jl0) oxygen pressure. *Phys.* Rei•. *B* 2001, 65, 035406.

(5) Jansen, M.; Sebón, J. C. Design" in chemical synthesis-An illusion? *Angew. Chem.,* fot. *Ed.* 2006, *45,* 3406-3412.

(6) Sabbah, R; Xu-vro, A.; Chickos, J. S.; Planas Leitilo, M. L.; Roux, r-.1. V.; Torres, L. A. Reference materials for calorimetry and diffrcntial thcrmal analysis. *Thcrmochim. Acta* 1999, *331,* 93-204.

(7) Navrotsky, A Calorimetry of nanoparticles, surfaces, interfaces, thin films, and multilayers. *J. Chem. Thermodyn.* 2007, 39, 1-9.

(8) Rogal, J.; Reuter, K. *Ab initio Atomistic Thennodynamics for Surjaces: A Primer;* Defense Technical Information Center: Berlín, 2006.

(9) 7.hang, M.; W:mg. W.; Chen Y Insight of OPT and ah initio atomistic thermodynamics on the surface stability and morphology of ln,O,. *Appl. Surj Sci.* 2018, 434, 1344-1352.

(10) Lee, T.; Soon, A The rise of ab initio surface thennodynamics. *Nat. Cata/.* 2024, 7, 4-6.

(II) Bhattacharya, S.; Levchenko, S.; Ghiringhelli, L. M.; Scheffler, M. Stability and Metastability of Clusters in a Reactive Atmosphere: Theoretical Evidence for Unexpected Stoichiometries of $MgMO_3$. *Phys. Rev. Lett.* 2013, *111,* 135501.

(12) Beret, E. C.; Ghiringhelli, L. M.; Scheffler, M. Free gold clusters: Beyond the static, monostructure description. *Faraday Discuss.* 2011, *152,* 153-167.

(13) Cuko, A; Escatllar, A. M.; Calatayud, M.; Bromley, S. T. Properties of hydrated TiO_2 and SiO_2 nanoclusters: dependence on size, temperature and water vapour pressure. *Nanoscale* 2018, *10,* 21518-21532.

(14) Habisreutinger, S. N.; Schmidt-Mende, L.; Molarczyk, J. K. JJhotocatalytic Keduction of CO_2 on TiO_2 and üther Semi· conductors. *Angew. Chem., Int. Ed.* 2013, 52, 7372-7408.

(15) Kumaravel, V.; Mathew, S.; Bartlett, J.; Pillai, S. C. Photocatalytic hydrogen production using metal doped TiO_2: A review ofrecent advances. *Appl. Cata/. B: Environ.* 2019, *244,* 1021-1064.

(16) Rafique, M.; Hajra, S.; Irshad, M.; Usman, M.; Imran, M.; Assiri, M. *A.;* Muhammad Ashraf, VV. Hydrogen Production Using TiO!-Dased Photocatalysts: A Comprehensive Review. *ACS Omega* 2023, *8,* 25640-25648.

(17) Rccio-Poo, M.; Morales-Carcia, A.; lilas, F.; Bromlcy, S. T. Tuning clcctronic lcvcls in photoactivc hydroxylatcd titania nano-systcms: combining thc ligand dipolc cffcct and quantum confinc-mcnt. *Nanoscalc* 2024, *16,* 8975-8985.

(18) Lamiel-Garcia, O.; Cuko, A; Calatayud, M.; lilas, F.; Bromley, S. T. Predicting size-dependent emergence of crystallinity in nanomaterials: titania nanoclusters versus nanocrystals. *Nmwscalc* 2017, *9,* 1049-1058.

(19) Lamiel-C.arcia, O.; Ko, K. *C.;* Lee,J. Y.; Bromley, S. T.; lilas, P. When Anatase Kanoparticles Become Bulklik.e: Properties of Realistic TiO_2 Nanoparticles in the 1-6 nm Size Range from Ali Electron Relativistic Density Functional Theory Based Calculations. *J. CJiem. Theory Comput.* 2017, *l},* 1785-1793.

(20) Morales-García, A; Lamiel-García, O.; Valero, R.; lilas, F. Properties of Single Oxygen Vacancies on a Realistic ($TiO_{1\%4}$ Nanopartide: A Challenge for Density Functionals. /. *Phys. Chem.* C **2018,** *122,* 2413-2411.

(21) Mino, L; Morales-García, Á.; Bromley, S. T.; lilas, F. Understanding the nature and location of hydroxyl groups on hydrated titania nanoparticles. *Nanoscale* 2021, *13,* 6S77-6585.

(22) Vittadini, A.; Selloni, A; Rotzinger, F. P.; Gratzel, M. Structure and Energetics of Water Adsorbed at TiO_2 Anatase 101 and 001 Surfaces. *Phys. Rev. Lett.* 1998, *81,* 2954-2957.

(23) Walle, L. E.¡ Borg, A.; Johansson, E. M. J.; Plogmaker, S.¡ Rensmo, H.; Uvdal, P..: Sandell, A. Mixed Dissociative and Molecular Water Adsorption on Anatase Tiüi(I0J). *J. Ph)'s. Chem.* C 2011, *115,* 9545-9550.

(24) Perdew, J. P.; Burke, K; Ernzerhof, M. Generalized gradient approximation made simple. *Phys.* Rei•. *Lett.* 1996, 77, 3865.

(25) Blum, V.; Gehre, R.; Hanke, F.; Havu, P.; Havu, V.¡ Ren, X.¡ Reuter, K.; Scheffler, M. Ab initio molecular simulations with numeric atom-centered orbitals. *Comput. Phys. Commun.* 2009, *180,* 2175-2196.

(26) Bromley, S. T.; Moreira, I. d. P. R.; Neyman, K M.; Iilas, P. Approaching nanoscale oxides: models and theoretical methods. *Chem. Soc. Rev.* 2009, *38,* 26Si-2670.
(27) McQuarrie, D. A. *Statistical Mechanics;* Harper & Row: New York, 1973.
(28) Bhattacharya, S.; Levchenko, S. *V.;* Ghiringhelli, L. M.; Scheffler, M. Efficient *ab initio* schemes for finding thermodynamically stable and metastable atomic structures: benchmark of cascade genetic algorithms. *New J. Phys.* 2014, *16,* 123016.
(29) Morales-García, Á.; Escatllar, A. M. _: Iilas, F. _: Bromley, S. T. Understanding the interplay between size, morphology and energy gap in photoactive $Ti0_2$ nanoparticles. *Nanoscale* 2019, *11,* 9032-9041.
(30) Zhang, H.; Banfield, J. F. Structural Characteristics and Mechanical and Thermodynamic Properties of Nanocrystalline $Ti0_2$. *Chem. Rev.* 2014, *114,* 9613-9644.

https://doi.org/10.1021/acs.jpclett4c01531
J. Phys. Chrm. Lett.2024, 15, 8240-3247

4.5 References

[1] Sabbah, R.; Xu-wu, A.; Chickos, J. S.; Planas Leitão, M. L.; Roux, M. V.; Torres, L. A. Reference materials for calorimetry and differential thermal analysis. *Thermochim. Acta* **1999**, *331*, 93−204.

[2] Navrotsky, A. Calorimetry of nanoparticles, surfaces, interfaces, thin films, and multilayers. *J. Chem. Thermodyn.* **2007**, *39*, 1−9.

[3] Reuter, K.; Scheffler, M. Composition, structure, and stability of as a function of RuO_2 (110) oxygen pressure. *Phys. Rev. B* **2001**, *65*, 035406.

[4] Reuter, K.; Scheffler, M. First-Principles Atomistic Thermodynamics for Oxidation Catalysis: Surface Phase Diagrams and Catalytically Interesting Regions. *Phys. Rev. Lett.* **2003**, *90*, 046103.

[5] Bhattacharya, S.; Levchenko, S.; Ghiringhelli, L. M.; Scheffler, M. Stability and Metastability of Clusters in a Reactive Atmosphere: Theoretical Evidence for Unexpected Stoichiometries of MgMOx. *Phys. Rev. Lett.* **2013**, *111*, 135501.

[6] Beret, E. C.; Ghiringhelli, L. M.; Scheffler, M. Free gold clusters: Beyond the static, monostructure description. *Faraday Discuss.* **2011**, *152*, 153−167.

[7] Cuko, A.; Escatllar, A. M.; Calatayud, M.; Bromley, S. T. Properties of hydrated TiO_2 and SiO_2 nanoclusters: dependence on size, temperature and water vapour pressure. *Nanoscale* **2018**, *10*, 21518−21532.

[8] Zhang, M.; Wang, W.; Chen, Y. Insight of DFT and ab initio atomistic thermodynamics on the surface stability and morphology of In_2O_3. *Appl. Surf. Sci.* **2018**, *434*, 1344−1352.

[9] Recio-Poo, M.; Morales-García, Á.; Illas, F.; Bromley, S. T. Size-Dependent *Ab Initio* Atomistic Thermodynamics from Cluster to Bulk: Application to Hydration of Titania Nanoparticles. *J. Phys. Chem. Lett.* **2024**, *15*(32), 8240-8247.

[10] Reuter, K.; Scheffler, M. First-Principles Atomistic Thermodynamics for Oxidation Catalysis: Surface Phase Diagrams and Catalytically Interesting Regions. *Phys. Rev. Lett.* **2003**, *90*, 046103.

[11] García-Mota, M.; Rieger, M.; Reuter, K. *Ab initio* prediction of the equilibrium shape of supported Ag nanoparticles on α-Al_2O_3 (0 0 0 1). *J. Catal.* **2015**, *321*, 1-6.

[12] Roldan Cuenya, B.; Alcántara Ortigoza, M.; Ono, L. K.; Behafarid, F.; Mostafa, S.; Croy, J. R.; Paredis, K.; Shafai, G.; Rahman, T. S.; Li, L.; Zhang, Z.; Yang, J. C. Thermodynamic properties of Pt nanoparticles: Size, shape, support, and adsorbate effects. *Phys. Rev. B* **2011**, *84*(24), 245438.

[13] Lee, T.; Soon, A. The rise of ab initio surface thermodynamics. *Nat. Catal.* **2024**, *7*(1), 4-6.

[14] Nørskov, J. K.; Bligaard, T.; Rossmeisl, J.; Christensen, C. H. Towards the computational design of solid catalysts. *Nat. Chem.* **2009**, *1*(1), 37-46.

[15] Seriani, N. *Ab initio* thermodynamics of lithium oxides: from bulk phases to nanoparticles. *Nanotechnol.* **2009**, *20*(44), 445703.

[16] Barnard, A. S.; Curtiss, L. A. Prediction of TiO_2 nanoparticle phase and shape transitions controlled by surface chemistry. *Nano Lett.* **2005**, *5*(7), 1261-1266.

[17] Mauro, J. C.; Yue, Y.; Ellison, A. J.; Gupta, P. K.; Allan, D. C. Viscosity of glass-forming liquids. *Proc. Natl. Acad. Sci. U. S. A.* **2009**, *106*(47), 19780-19784.

[18] Frenkel, D.; Smit, B. Understanding molecular simulation. *Academic Press, San Diego* **2002**, *2*(2.2), 2-5.

[19] Landau, D.; Binder, K. *A guide to Monte Carlo simulations in statistical physics* **2021**. Cambridge university press.

[20] Tomasi, J.; Mennucci, B.; Cammi, R. Quantum mechanical continuum solvation models. *Chem. Rev.* **2005**, *105*(8), 2999-3094.

[21] Nørskov, J. K.; Rossmeisl, J.; Logadottir, A.; Lindqvist, L. R. K. J.; Kitchin, J. R.; Bligaard, T.; Jonsson, H. Origin of the overpotential for oxygen reduction at a fuel-cell cathode. *J. Phys. Chem. B* **2004**, *108*(46), 17886-17892.

[22] Recio-Poo, M.; Morales-Garcia, Á.; Illas, F.; Bromley, S. T. Tuning electronic levels in photoactive hydroxylated titania nanosystems: combining the ligand dipole effect and quantum confinement. *Nanoscale* **2024**, *16* (18), 8975−8985.

[23] Lamiel-Garcia, O.; Ko, K. C.; Lee, J. Y.; Bromley, S. T.; Illas, F. When anatase nanoparticles become bulklike: properties of realistic TiO_2 nanoparticles in the 1–6 nm size range from all electron relativistic density functional theory based calculations. *J. Chem. Theory Comput.* **2017**, *13*(4), 1785-1793.

[24] Morales-García, Á.; Escatllar, A. M.; Illas, F.; Bromley, S. T. Understanding the interplay between size, morphology and energy gap in photoactive TiO_2 nanoparticles. *Nanoscale* **2019**, *11*(18), 9032-9041.

[25] Lamiel-Garcia, O.; Cuko, A.; Calatayud, M.; Illas, F.; Bromley, S. T. Predicting size-dependent emergence of crystallinity in nanomaterials: titania nanoclusters versus nanocrystals. *Nanoscale* **2017**, *9*, 1049−1058.

[26] Zhang, H.; Banfield, J. F. Structural Characteristics and Mechanical and Thermodynamic Properties of Nanocrystalline TiO_2. *Chem. Rev.* **2014**, *114*, 9613−9644.

5 EXPLORING THE EXCITED STATE DYNAMICS

5.1 Introduction

Understanding excited-state dynamics in TiO_2 is fundamental for advancing applications in photocatalysis,[1-3] photovoltaics,[4] and energy storage technologies. The efficiency of these processes is largely determined by how photoexcited charge carriers behave, specifically how electrons and holes are generated, transported, and recombined. While TiO_2 is widely employed as a photoactive material, its performance is limited by ultrafast recombination events that reduce charge carrier lifetimes and lower overall efficiency. Therefore, characterizing and controlling these excited-state processes is critical for designing more efficient energy-harvesting devices and photocatalytic systems.

Excited-state phenomena in TiO_2 include a complex interplay of light absorption, exciton formation, charge trapping, electron-hole recombination, and energy dissipation.[5-7] These processes occur over multiple time and energy scales, ranging from femtoseconds to microseconds, making their theoretical and experimental study particularly challenging. Nonradiative recombination, which leads to the loss of absorbed photon energy as heat, is a major limiting factor in TiO_2-based solar energy applications. By contrast, extending charge carrier lifetimes through surface modification, defect engineering, or hydration can enhance performance in photocatalysis and optoelectronic applications.

A comprehensive understanding of excited-state relaxation mechanisms is particularly necessary for nanoscale TiO_2 clusters, where quantum confinement effects further alter carrier lifetimes and recombination pathways. Unlike bulk TiO_2, where extended delocalized electronic states enable efficient charge separation, small nanoclusters exhibit strong carrier localization, which often leads to rapid recombination. Hydration, defect formation, and surface functionalization further modulate these dynamics, introducing new pathways for electron and hole relaxation. Recent developments in ultrafast spectroscopy,[8,9] time-resolved photoluminescence,[10] and nonadiabatic molecular dynamics (NA-MD)[11,12] have provided powerful means to investigate and model these ultrafast processes.

This chapter focuses on excited-state dynamics in TiO_2 nanostructures, emphasizing the impact of hydration degrees on charge recombination times. We first

review key experimental and theoretical studies that have shaped our understanding of photoexcited charge carrier behaviour, before presenting our own findings using NA-MD simulations. Our results provide insight into how hydration modifies electron-hole recombination rates, with implications for the design of functionalized TiO_2-based materials for solar energy conversion and catalysis.

5.1.1.1 Exciton Formation and Charge Carrier Trapping in TiO_2-Based Systems

The ability of a photocatalyst to drive chemical transformations under light illumination depends fundamentally on its capacity to generate, separate, and transport photoexcited charge carriers.[13,14] In titania systems, these processes are strongly influenced by intrinsic properties such as particle size, crystal structure, and surface termination. Among the key challenges limiting photocatalytic efficiency is the tendency of charge carriers to become trapped or recombine before they can reach reactive surface sites.

A substantial body of theoretical and computational work has addressed the formation of excitons and the localization of charge carriers in TiO_2-based nanomaterials. Size- and structure-dependent effects on ground- and excited-state electronic structure have been investigating, showing that smaller TiO_2 nanoparticles exhibit larger energy gaps and stronger electron-hole Coulomb interactions, which lead to reduced free carrier formation.[15] Such findings suggest that as TiO_2 NPs become smaller, the charge carriers tend to localize more strongly, preventing long-range transport —an important consideration for applications requiring efficient charge separation, such as in photocatalytic and photovoltaic devices.

Exciton binding energies in TiO_2 nanoparticles up to 20 units in size have been studied, revealing that Frenkel excitons dominate at the nanoscale and significantly impact charge separation efficiency.[16] The results indicate that exciton binding energy follows an inverse power law with size, posing a fundamental limitation for ultrasmall titania NPs used as photocatalysts. This observation aligns with previous studies showing that quantum confinement effects

increase exciton binding energy in small systems, hindering free carrier formation.[17,18]

TD-DFT calculations using hybrid functionals have been employed to analyse static charge separation properties in anatase-derived bipyramidal TiO_2 nanoparticles.[19] This computational study emphasizes that structural anisotropy can lead to significant variations in charge recombination rates, as different crystal facets exhibit distinct electron-hole overlap characteristics. Surface states have also been shown to play a major role in defining excited-state lifetimes,[20,21] highlighting the importance of considering surface modifications when designing functional TiO_2 nanomaterials. However, theoretical insights into excited-state electronic properties in photocatalytic materials have highlighted the limitations of static calculations (as in the reference 19) for describing ultrafast carrier relaxation processes.[22] This body of work underscores the necessity of employing dynamic simulation methods, such as non-adiabatic molecular dynamics, to accurately capture charge carrier dynamics in TiO_2 nanostructures

Besides theoretical and computational efforts, experimental confirmation of size- and structure-dependent excited-state dynamics has also emerged. Ultrafast pump-probe spectroscopy measurements on $(TiO_2)_n$ clusters with sub-nanometer dimensions revealed that even-numbered clusters exhibit longer recombination lifetimes, a behaviour attributed to enhanced structural rigidity and stronger polaron formation tendencies.[23] In related work, femtosecond transient absorption studies on 1 nm molecular polyoxotitanate clusters showed pronounced exciton binding energies and complex recombination kinetics ranging from sub-picosecond to hundreds of picoseconds. These dynamics were found to be influenced by coordination geometry, surface states, and quantum confinement effects.[24]

Further insight into charge carrier localization was provided by femtosecond time-resolved X-ray absorption spectroscopy on anatase TiO_2 nanoparticles. These measurements captured an ultrafast red-shift in the Ti K-edge within ~100 fs, signalling the rapid formation of self-trapped polarons and structural distortion near the surface.[25] Additionally, experiments on catechol-functionalized Ti_{17} clusters demonstrated that photoinduced hole migration across ligand

sites occurs on sub-100 fs timescales, underscoring the critical role of interfacial electronic coupling in modulating carrier mobility.[26]

5.1.2 Nonadiabatic Dynamics and Charge Recombination Pathways

While TD-DFT and wavefunction-based methods have provided valuable insights into TiO_2 excited-state properties, their ability to predict real-time charge carrier evolution remains inherently limited by the Born-Oppenheimer approximation. To address this limitation, NA-MD approaches, which explicitly include electron-nuclear coupling and decoherence effects, have emerged as a powerful tool for modelling photoexcited carrier dynamics in TiO_2 nanostructures. Several studies have used real-time TD-DFT combined with nonadiabatic surface hopping approaches to investigate excited state dynamics titania-related systems.

For instance, Nam *et al.* demonstrated that both NP size and shape affect nonradiative recombination rates, with larger TiO_2 clusters exhibiting slower relaxation due to reduced nonadiabatic coupling (NAC) strengths.[11] Their work illustrated how excitonic localization within differently shaped TiO_2 NPs affects carrier lifetimes, confirming that morphology-driven variations in electronic structure influence recombination behaviour. Their computational results were further corroborated by time-resolved photoluminescence experiments, which directly measured the impact of shape anisotropy on recombination times.

A particularly important factor influencing charge recombination is the presence of oxygen vacancies (O) in TiO_2 NPs. Another research conducted by the same group explored how oxygen vacancy location alters electron-hole recombination pathways, revealing that subsurface O sites can actually slow down recombination by stabilizing charge-separated states, while surface O sites promote rapid carrier relaxation.[12] Their study emphasized the importance of defect engineering, showing that precise control over vacancy distributions could lead to improved photocatalytic performance.

Another notable example of NA-MD applied to a TiO_2-based system involves a study that combined ab initio and nonadiabatic molecular dynamics to investigate charge carrier dynamics on reduced rutile TiO_2(110) surfaces in the

presence of a CO adsorbate.[27] Their simulations revealed that the CO molecule not only enhances surface polaron stability by attracting subsurface polarons to the surface, but also suppresses polaron hopping and alters the orbital character of the electron trap state. This interaction led to a reduction in nonadiabatic coupling and shortened decoherence times, which in turn slowed down electron–hole recombination, as confirmed by their NA-MD results.

Importantly, the study highlights that surface adsorbates can serve as dynamic modulators of charge carrier lifetimes, not simply by introducing new reaction pathways, but by altering the fundamental nonadiabatic recombination mechanisms through electronic structure changes and vibrational coupling. These insights underline the necessity of incorporating surface chemistry effects into time-resolved simulations for an accurate description of photocatalytic activity in TiO_2-based systems.

In this context, this thesis applies NA-MD methodologies to hydrated TiO_2 nanoclusters, addressing how (surface) hydration accelerates radiative and nonradiative recombination pathways. Apart from the previous work of Muuronen *et al.* who examined the mechanism of water oxidation on the surface of a $(TiO_2)_4$ cluster,[28] we are not aware of other studies of the influence of chemisorbed water on excited-state dynamics in hydrated TiO_2 nanostructures. Considering that in realistic photocatalytic systems, the surfaces of photocatalytic TiO_2-based materials are most often covered with water, understanding the impact of water on the photoinduced dynamics of excited states of hydrated titania nanostructures is essential for providing a better understanding of the photocatalytic systems.

5.1.3 Many-Body Effects in Nonadiabatic Dynamics

The accurate simulation of excited-state dynamics in TiO_2 nanoclusters requires a framework that properly accounts for electron-electron interactions, excitonic effects, and strong nonadiabatic couplings. Conventional studies based on single-particle (SP) approximations within density functional theory have provided significant insights into the electronic and optical properties of nanostructures.[15,29] However, SP-based descriptions fail to capture the full complexity of electronic excitations, often neglecting important many-body

(MB) effects that arise from electron-hole interactions and multiconfigurational character. Recent research has demonstrated that accounting for MB effects via a more rigorous linear-response (LR) TD-DFT framework leads to significantly stronger NACs and, consequently, faster excited-state dynamics.[30-32]

SP-based DFT methods treat excited states as independent particle-hole excitations, ignoring the correlated electron-hole interactions that govern real-world exciton dynamics. This simplification is reasonable in weakly interacting systems but breaks down in quantum-confined systems such as TiO_2 nanoclusters, where the Coulomb interaction significantly influences the character of the excited states. SP methods also lead to underestimation or even incorrect description of nonradiative decay rates, as they fail to include configuration mixing, which is critical for enabling electronic state transitions,

One fundamental issue with SP-based TD-DFT is that the choice of exchange-correlation functional strongly affects the computed excited-state properties.[33] Generalized gradient approximation (GGA) functionals, such as PBE, suffer from self-interaction errors and cannot properly capture charge-transfer excitations, leading to spurious energy levels and artificial stabilization of excited states. Moreover, GGA-based functionals often underestimate exciton binding energies and provide incorrect energy ordering of excited states, limiting their predictive power for ultrafast charge dynamics.[34]

To address these deficiencies, many-body corrections within a linear-response TD-DFT formalism enable a proper treatment of electronic correlations and nonadiabatic interactions. The MB approach allows for state mixing, which enhances nonadiabatic coupling strengths and accelerates excited-state relaxation processes. This has been demonstrated in various nanomaterial systems, including CdSe and Si nanoclusters, where MB-based simulations showed a 2-4× acceleration in excited-state lifetimes compared to SP approximations.[31]

One of the key advantages of MB-based approaches is the incorporation of range-separated hybrid functionals (RSF), which provide a balanced treatment of short- and long-range exchange interactions. Unlike pure hybrid functionals, RSF functionals dynamically tune the fraction of Hartree-Fock exchange,

significantly improving the description of excitonic effects. Studies using optimally tuned RSF functionals have shown that they yield more accurate nonadiabatic couplings, leading to an improved prediction of carrier relaxation times.

This strong coupling between states also explains why MB methodologies result in faster excited-state decay in TiO_2 nanoclusters compared to SP methods. When NACs are weak, charge carriers remain trapped in long-lived excited states, reducing photocatalytic efficiency. By enhancing state mixing, MB frameworks allow for faster and more realistic excited-state relaxation dynamics, making them a superior tool for studying ultrafast photophysical processes in TiO_2 systems.

Despite their advantages, many-body approaches remain computationally more expensive than SP-based methodologies. Hybrid functionals, particularly range-separated hybrids, increase the cost of TD-DFT calculations, making large-scale simulations challenging. However, the trade-off in computational expense is justified by the significant improvement in accuracy, as evidenced by recent studies comparing RSF-TD-DFT against wavefunction-based methods. Furthermore, efficient numerical integration techniques and reduced dynamical basis sets have been implemented to ensure feasibility for realistic nanocluster sizes.

By accounting for many-body effects, state mixing, and enhanced NACs, MB-based methodologies bridge the gap between single-particle-based simulations and experimental ultrafast spectroscopy measurements. This methodological advancement not only improves the reliability of charge carrier dynamics predictions but also provides deeper insights into the fundamental mechanisms governing nonradiative recombination in nanoscale systems. The growing body of research applying these methods to semiconductors, quantum dots, and metal oxides has demonstrated their superior accuracy and predictive power in describing ultrafast relaxation processes.

5.2 Results

Our study investigates how surface hydration influences the excited-state properties of small TiO_2 nanoclusters using nonadiabatic molecular dynamics. Based on the titania/water (m/n) ratio, our selection covers 0% as for the

anhydrous $(TiO_2)_4$ and $(TiO_2)_8$ clusters, ~25% for $(TiO_2)_8(H_2O)_2$, ~50% for $(TiO_2)_4(H_2O)_2$, ~60% for $(TiO_2)_8(H_2O)_5$, and ~100% for $(TiO_2)_4(H_2O)_4$ hydration degrees. While prior research has explored size-dependent trends in charge carrier relaxation,[11,15,23] a detailed understanding of how water adsorption modifies radiative and nonradiative recombination remains an open question. By explicitly including many-body interactions within our TD-DFT-based NA-MD framework, we assess how hydration alters electronic structures, vibrational properties, excitonic effects, and nonadiabatic couplings to ultimately influence charge carrier lifetimes. We focus on determining the electron-hole recombination dynamics to compute the ground state (S_0) population recovery kinetics starting from the first excited singlet state (S_1). The S_1 state represents an important stage in the relaxation process, as it is typically well separated from S_0 by an energy gap. The $S_1 \rightarrow S_0$ transition becomes the bottleneck of the excited state relaxation process and largely determines the overall efficiencies of photovoltaic materials.[35]

We also conduct a systematic assessment of various components of our computational methodology. In particular, we investigate the applicability of the classical force fields to NA-MD calculations as a computationally feasible alternative to AIMD. We explore the role of hybrid density functional in such simulations. Finally, we conduct a comparative analysis of several trajectory surface hopping and decoherence correction methodologies as applied to modelling nonradiative recombination in this class of systems.

5.2.1 Power and influence spectra

To comprehensively capture these effects, we employed a multistep computational workflow (see Figure 2.2), beginning with the generation of nuclear trajectories using both force-field molecular dynamics (FFMD) and AIMD approaches. FFMD was used to efficiently explore larger configurational space, while AIMD provided more accurate descriptions of anharmonic vibrational motion. The vibrational properties of the clusters were analysed by computing the power spectra of atomic motions, as in Figure 5.1, allowing us to track hydration-induced shifts in vibrational modes. Hydrated clusters displayed softened vibrational frequencies compared to their anhydrous counterparts, with prominent shifts in low-frequency Ti-O stretching modes and bending

vibrations of surface hydroxyl groups, indicating stronger electron-phonon coupling in the presence of water molecules.

The systematically lower frequencies in the AIMD spectra with respect to the FF-based one may be attributed to a better description of anharmonic effects in the former approach. The anharmonicities also realize the cross-coupling of vibrational modes and vibrational energy redistribution between them. Thus, vibrational energy is more likely to diffuse between different modes and activate them, in addition to resonances of vibrational modes. As a result of these two effects, the AIMD approach generates denser vibrational densities of states compared to the FFMD dynamics. Despite the noted differences, the high degree of resemblance between spectra computed with FFMD or DFT-based AIMD points out that the tested FFs are sufficiently accurate to act as computationally-efficient counterparts to DFT calculations in potential studies of larger titania-derived systems, where the AIMD based approaches become significantly almost unattainable.

Figure 5.1 also shows the influence spectra and the energy evolution of the first excited state (insets) computed for $(TiO_2)_8$-based clusters using TD-DFT calculations with three density functionals: PBE (blue), PBE0 (red) and B3LYP (green). All spectra indicate that the $S_1 \rightarrow S_0$ transition is driven by the Ti-O-Ti angle bending modes that are in the 500-1000 cm^{-1} range.[36-38] In particular, the mode at around 1000 cm^{-1} is present for all methods and in all systems. Notably, the mode appears to be split when DFT is used for computing the guiding trajectory (e.g., the peaks in the 500 to 1400 cm^{-1} range), while it consists of only one strong peak at around 1000 cm^{-1} when the FF is used for producing the guiding trajectory. The splitting observed in AIMD DFT-based spectra is likely due to the activation of different modes due to the anharmonic effects enabling the vibrational energy transfer between the modes and hence their appearance in the spectrum. This effect is rather general since the AIMD influence spectra show a larger number of modes coupled to the electronic transition of interest than the FF-based influence spectra. The Ti-O stretching modes in the 100 to 200 cm^{-1} range[39] do not show strong coupling to the electronic transition of interest in neither bare nor weakly hydrated clusters (Figures 5.1 a-d). However, these modes are present in the strongly hydrated system and only

when DFT is used for producing the guiding trajectory (Figure 5.1 e). Importantly, despite all methods show the hydroxyl vibrational modes around 3000 cm^{-1} in the power spectra, this mode is not coupled to the $S_1 \rightarrow S_0$ transition as it is not present in the influence spectrum.

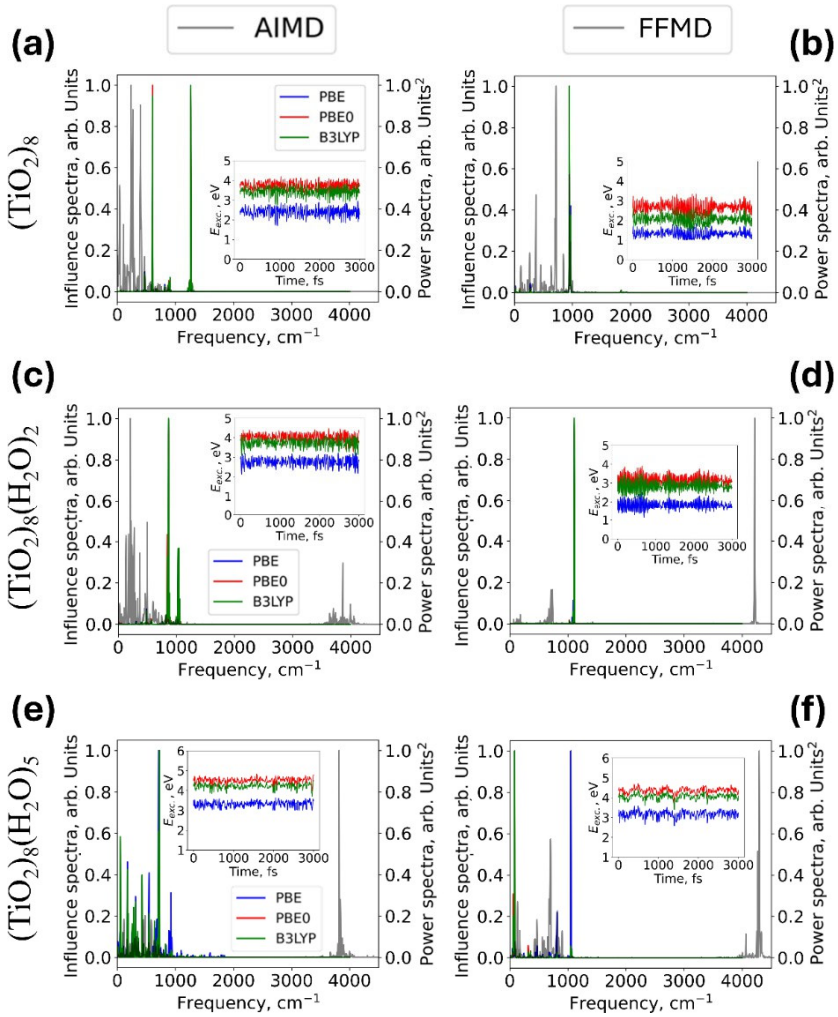

Figure 5.1: Normalized (squared) power and influence spectra for $(TiO_2)_8$ (a, b), $(TiO_2)_8(H_2O)_2$ (c, d) and $(TiO_2)_8(H_2O)_5$ (e, f) systems. The power spectra are computed using nuclear trajectories obtained with AIMD (a, c, e) or classical FFMD (b, d, f) methods. The influence spectra characterize the vibrational modes that drive the transition between the ground state and first excited state. The insets show the evolution of the ground-to-first-excited-state energy gap

in corresponding calculations. Color codes: grey – power spectra, blue, red and green –influence spectra. For the influence spectra, TD-DFT-calculated excitation energies are computed with B3LYP (green lines), PBE0 (red lines) and PBE (blue lines) functionals.

5.2.2 TD-DFT excited state energies and NACs

To rationalize the contributions from different vibrational modes as shown in the influence spectra, we analyse the electronic densities corresponding to the highest occupied molecular orbital and the lowest unoccupied molecular orbital of the $(TiO_2)_4(H_2O)_m$ (m = 0, 2, and 4), and $(TiO_2)_8(H_2O)_m$ (m = 0, 2, and 5 nanoclusters). For all considered functionals, we find that the composition of the lowest excited TD-DFT state, S_1, is dominated by the HOMO→LUMO excitation, as can be quantified by the squares of the CI coefficients with which they mix in the TD-DFT "wavefunctions"

We thus only focus on the frontier orbitals to rationalize the observed features of the influence spectra. Regardless of the hydration degree, the larger electronic densities are located around the Ti-O bonds. Thus, the Ti-O bond stretching as well as O-Ti-O or Ti-O-Ti angle bending modes can affect the corresponding MOs and excited states the most and hence reveal themselves in the influence spectrum.

The analysis of the trajectory-averaged first excited state energy computed with different methods reveals that the hydration of titania nanoclusters induces a systematic increase of the trajectory-averaged vertical excited state energies, $\bar{\bar{E}}_{\bar{\bar{e}}\bar{\bar{x}}\bar{\bar{c}}}$ (see Figure 5.2 a-b and insets of Figure 5.1We rationalize this effect by two factors, (i) energy gap opening due to the removal of defect states (i.e., uncoordinated O and Ti sites), and (ii) weaker stabilization of charge transfer excitations in hydrated systems. First, the hydration of titania nanoclusters promotes the electronic energy gap opening, as estimated by the HOMO−LUMO difference by passivating defect midgap states originated due to under-coordinated (O_{1c} and Ti_{4c}) surface atoms in the bare or weakly hydrated $(TiO_2)_4$ systems. By increasing the hydration of titania nanoclusters, the "defect" states are removed more completely thus opening the energy gap. This mechanism was already reported in previous works[40-42] and detailed in chapter 3 of this thesis.

Second, excited states exhibit more isotropic charge distributions in strongly hydrated systems, leading to smaller excited-state dipole moments and, consequently, reduced Coulombic stabilization of these states. This effect contributes to an increase in the excitation energy of the strongly hydrated clusters

The latter effect can be explained by means of the analysis of the orbitals involved in the excitations. The analysis of the CI amplitudes suggests that the S_1 states of nearly all considered clusters are dominated by the HOMO→LUMO excitation. For the bare $(TiO_2)_8$ nanocluster, such a transition is a longer-distance charge transfer that creates a strong dipole moment. The resulting charge-separated state has a notable Coulombic interaction between electron and hole which lowers the energy of the corresponding excited state to a larger extent than in smaller $(TiO_2)_4$ nanocluster. With the increased degree of hydration, both HOMO and LUMO involved in the excitation exhibit higher symmetry and are more delocalized. The corresponding HOMO→LUMO transition thus results in a shorter-distance charge transfer, smaller S_1 dipole moment, smaller Coulombic stabilization and hence in higher excitation energy of the S_1 excited state

5.2.3 NACs

The next step in our analysis involved computing nonadiabatic couplings (NACs), which dictate the efficiency of nonradiative recombination, as in Equation 2.40. We focused on the analysis of the trajectory-averaged nonadiabatic coupling ($\bar{N}\bar{A}\bar{C}$) between S_0 and S_1 states as computed with each TD-DFT methodology (Figure 5.2 c-d). With a few exceptions, the average NAC values obtained for FF-based trajectories are somewhat higher than those for the AIMD-based trajectories, although the values lie within each other's error margin, for each selected combination of system and density functional. Thus, the use of the FF-based trajectories appears to be a reasonable approach for computing NACs when computational demands do not allow using DFT-based AIMD trajectories.

The $\bar{N}\bar{A}\bar{C}$ values gradually increase with the increase of the degree of hydroxylation. This effect is, in principle, counterintuitive because the NAC between a pair of states should be inversely proportional to the energy gap between such

states. However, the NACs can be regarded as a quantification of the wave-function change upon a nuclear perturbation. Thus, for NACs to be large, it is important that: i) the vibrations that couple to the pair of states of interest are activated, and ii) the wavefunction changes with the symmetries different to the symmetries of the corresponding vibrational modes. As we alluded to above, the addition of water molecules to the $(TiO_2)_n$ clusters triggers some nuclear disorder. Thus, additional vibrations efficiently coupling the $S_0 \rightarrow S_1$ electronic transition can be activated leading to large average NACs.

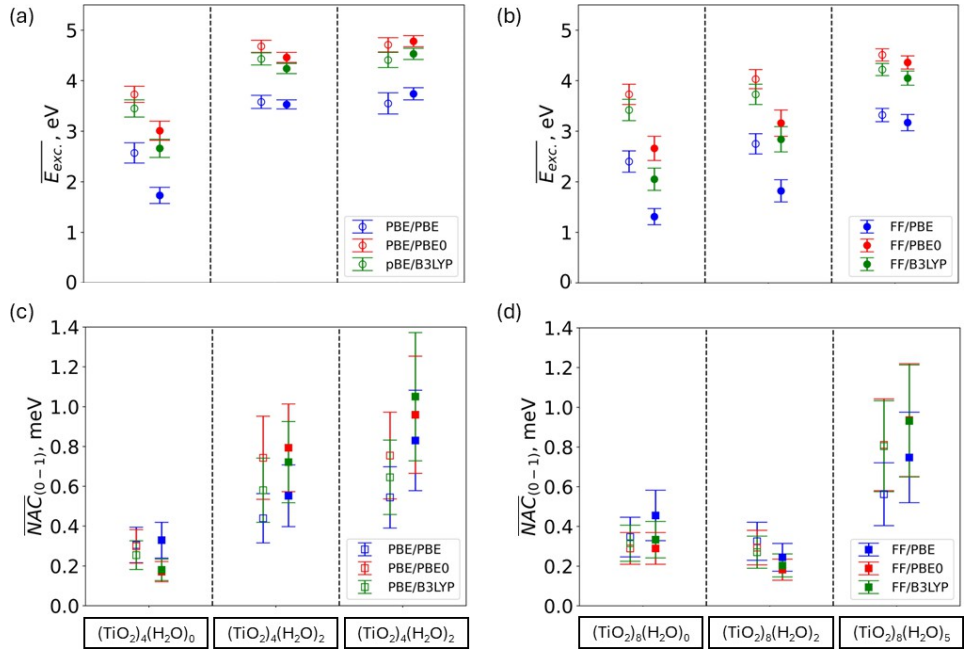

Figure 5.2: (a-b) Trajectory-averaged values of the first excited state energies (obtained with three DFT functionals) for each of the six clusters. Color codes: blue, red and green – PBE, PBE0, and B3LYP functionals. Empty and solid circles correspond respectively to DFT-based and FF-based nuclear trajectories. (c-d) Trajectory-averaged values of the trajectory-averaged nonadiabatic couplings between ground (S_0) and first excited state (S_1) obtained with three DFT functionals for each of the six clusters. Color codes: blue, red and green – PBE, PBE0, and B3LYP functionals. Empty and solid squares correspond

respectively to DFT-based and FF-based nuclear trajectories. Error bars represent the standard deviation for each of the calculations.

This explanation is also consistent with the presence of an apparent threshold of switching between NACs being sensitive or not sensitive to the amount of water chemisorbed on titania nanoclusters. Indeed, in the small $(TiO_2)_4(H_2O)_m$ nanoclusters, the surface/volume ratio is larger than in the larger $(TiO_2)_8(H_2O)_m$ ones. Thus, the surface water molecules cause more significant disorder in the former systems leading to immediate nearly linear dependence of $\bar{N}\bar{A}\bar{C}$ on the number of water molecules (Figure 5.2 c). In the $(TiO_2)_8(H_2O)_m$ systems, we first observe a plateau suggesting no dependence of $\bar{N}\bar{A}\bar{C}$ on the number of surface water molecules. As this number increases, the disorder caused by the surface hydroxylation becomes sufficient to affect the wavefunctions and increase the $\bar{N}\bar{A}\bar{C}$ values (Figure 5.2 d).

5.2.4 Recombination

We conducted nonadiabatic molecular dynamics (NA-MD) simulations to investigate the nonradiative recombination rates in titania (TiO_2) nanoclusters. Our primary focus was on understanding how recombination times varied based on several factors: the molecular dynamics approach used to generate nuclear trajectories (AIMD vs. FF), the DFT employed to compute nonadiabatic couplings, the trajectory surface hopping scheme used to model nonadiabatic dynamics (FSSH, DISH, mSDM, IDA), and the size and hydration level of the titania nanoclusters.

We first examined the role of the MD approach and the choice of DFT functional. When we used the PBE functional to compute NACs, the recombination occurred faster in FF trajectories than in AIMD trajectories, except in the case of $(TiO_2)_4$ clusters. However, this trend reversed when we employed the hybrid B3LYP functional, which generally increased NAC values. These differences were most pronounced in fast recombination scenarios modelled with FSSH, where the dynamics were strongly influenced by NAC values and nuclear motion details. In contrast, when we applied methods incorporating decoherence, such as mSDM, we observed that recombination was primarily controlled by

fluctuations in the energy gap, making the results less sensitive to nuclear trajectories.

We also investigated the impact of the density functional on recombination rates. Our results showed that hybrid functionals (PBE0, B3LYP) generally yielded faster recombination than the semilocal PBE functional. This effect stemmed from the distribution of NAC values, where smaller NAC values were more frequently sampled in PBE-based simulations, while hybrid functionals favoured larger NAC magnitudes. Consequently, the computed recombination times followed the order $\tau_{PBE} > \tau_{PBE0} \approx \tau_{B3LYP}$ across all TSH methodologies.

Next, we analysed the effect of different TSH approaches on recombination times in Figure 5.3. In nearly all systems, we observed the order $\tau_{mSDM} \geq \tau_{IDA} > \tau_{DISH(rev2023)} > \tau_{FSSH}$, consistent with the previous assessments.[31,32,43,44] The mSDM method, which incorporated strong decoherence corrections, produced the longest recombination times, with values reaching 900-1100 ps for $(TiO_2)_4$. The IDA method generally resulted in slightly shorter recombination times than mSDM, as it introduced decoherence corrections via wavefunction collapse on the active state. Meanwhile, the 2023 revision of the DISH algorithm partially accounted for decoherence, yielding results closer to FSSH but with slightly longer timescales.

We further explored how hydration influenced recombination dynamics (see Figure 5.3). Our results demonstrated that increasing hydration accelerated recombination across nearly all nanoclusters, density functionals, and TSH methods. This acceleration correlated with trends in NAC values, which increased as more water molecules adsorbed onto the cluster surface. Consequently, carrier lifetimes decreased as the degree of hydration increased. However, we noted an exception in the $(TiO_2)_8(H_2O)_2$ system with FF trajectories, which exhibited unexpectedly slow recombination dynamics. This anomaly could be attributed to the low water coverage (~25%), which made the system behave similarly to the anhydrous $(TiO_2)_8$ cluster. These findings suggested that weakly hydroxylated titania nanoclusters could be more suitable for water-splitting applications, as they promoted longer electron-hole separation times, enhancing photocatalytic efficiency.

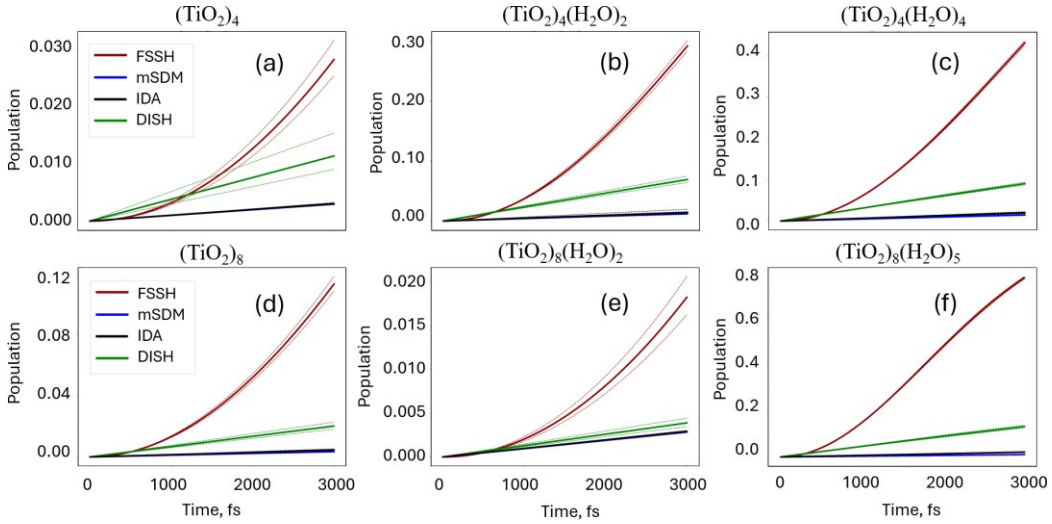

Figure 5.3: Evolution of the ground state S_0 population for classical FFMD and AIMD nuclear trajectories and fixed PBE functional as the underlying functional for computing the TD-DFT excitations. (a-c) and (d-f) panels illustrate $(TiO_2)_4$ and $(TiO_2)_8$ cluster in their anhydrous and hydrated counterparts. Red, blue, green, and black colored lines represent FSSH, mSDM, DISH and IDA TSH schemes, respectively. The average population for each case is shown in bold lines, whereas dashed lines account for the error bars at each NA-MD timestep.

When comparing our computational results with experimental data, we found discrepancies in reported recombination times. Prior time-resolved photoelectron spectroscopy (TRPES) experiments estimated recombination times on the order of nanoseconds,[45] which aligned with our results for anhydrous clusters when using IDA or mSDM schemes. However, recent pump-probe spectroscopy studies reported sub-picosecond recombination times,[9] which differed by orders of magnitude from our computed values. We proposed an alternative interpretation of these measurements, suggesting that the experimentally observed ultrafast decay times could reflect relaxation to optically dark states rather than direct charge carrier recombination between the first excited and ground states.

5.3 Conclusions

In this last chapter of the thesis' results, we investigated the impact of hydration on the excited-state properties of small titania nanoclusters using nonadiabatic molecular dynamics. Our results demonstrate that hydration plays a crucial role in modulating charge recombination rates and electronic structure. Specifically, we found that increasing hydration accelerates nonradiative recombination due to greater isotropy and delocalization of the charge distribution in hydrated nanoclusters. As hydration levels rise, the spatial symmetry of the system increases, promoting orbital degeneracies that facilitate stronger nonadiabatic couplings. This effect is particularly pronounced in smaller clusters, where NACs increase approximately linearly with hydration, while in larger clusters, an initial plateau is followed by a slower linear rise—suggesting a diminishing influence of hydration as system size increases. These hydration-induced changes lead to shorter charge carrier lifetimes, which can either enhance or hinder the efficiency of TiO_2-based photocatalytic and optoelectronic applications, depending on the specific requirements.

We also observed that hydration systematically increases the vertical excitation energies of TiO_2 clusters. This energy gap widening results from three primary factors: the removal of under-coordinated defect states, the introduction of electric field effects by hydroxyl (−OH) groups, and a weaker stabilization of charge-transfer excitations in hydrated systems. These findings suggest that the electronic properties of TiO_2 nanoclusters can be fine-tuned through controlled hydration, offering a strategy to optimize their performance in energy conversion applications.

Our analysis of nonadiabatic couplings revealed that NAC values generally increase with hydration, leading to faster nonradiative recombination. While this might seem counterintuitive given the expected inverse relationship between NACs and energy gap size, we interpret this behaviour as arising from hydration-induced increases in spatial isotropy and orbital degeneracy, which override the influence of the energy gap. The threshold behaviour observed in larger clusters highlights the nuanced interplay between structural and electronic factors in defining recombination behaviour.

To ensure the robustness of our findings, we systematically assessed different computational methodologies. Our results confirm that classical force-field molecular dynamics can serve as a reasonable alternative to AIMD for modelling excited-state dynamics, although AIMD provides a more accurate representation of anharmonic vibrational effects. Additionally, our comparison of density functionals revealed that hybrid functionals, such as PBE0 and B3LYP, predict faster recombination than the semilocal PBE functional. This suggests that a more accurate treatment of electronic structure is essential for reliable charge relaxation simulations. Furthermore, our evaluation of trajectory surface hopping methods indicated that different approaches yield varying recombination times, with mSDM and IDA producing longer lifetimes due to their inclusion of decoherence corrections, whereas FSSH predicted the fastest recombination**.**

From an application perspective, our findings indicate that weakly hydrated TiO_2 nanoclusters exhibit longer charge carrier lifetimes, making them more suitable for photocatalytic processes such as water splitting. In contrast, strongly hydrated clusters experience rapid recombination, which may limit their effectiveness in photovoltaic and photocatalytic applications. These insights highlight the potential of tailoring hydration levels and surface modifications to optimize the performance of TiO_2-based materials in energy conversion technologies.

Finally, our results provide new perspectives on the discrepancies between computational and experimental charge recombination times. While some experimental studies report recombination times on the nanosecond scale, others suggest ultrafast sub-picosecond dynamics. We propose that these ultrafast decay times may correspond to relaxation into optically dark states rather than direct charge carrier recombination. Ongoing research aims to develop predictive capabilities for the ultrafast relaxation and recombination photodynamics of small anhydrous titania clusters by integrating theoretical and experimental approaches.

Although the primary focus of this study was **on** nonradiative recombination, our calculations also provide insight into radiative pathways, which are

discussed in the publication attached at the end of the chapter. Notably, we observe that radiative recombination is faster in more highly hydrated systems, due to the increased excitation energies and corresponding transition dipole moments. Interestingly, among the bare clusters, the larger $(TiO_2)_8$ system exhibits faster radiative decay than $(TiO_2)_4$, a result we attribute to the greater electron–hole separation and enhanced dipole strength in the former.

In conclusion, our study advances the understanding of charge carrier relaxation mechanisms in TiO_2 nanoclusters, demonstrating that hydration significantly influences excited-state lifetimes and nonradiative recombination. By leveraging these insights—particularly the roles of electronic isotropy**,** charge delocalization, and surface chemistry—we can guide the design of more efficient TiO_2-based materials for applications in solar energy conversion, photocatalysis, and optoelectronics.

5.4 Publications

THE JOURNAL OF PHYSICAL CHEMISTRY C
A JOURNAL OF THE AMERICAN CHEMICAL SOCIETY
pubs.acs.org/JPCC Article

Hydration Accelerates Radiative and Nonradiative Recombination in Small TiO_2 Nanoclusters

Published as part of The Journal of Physical Chemistry C special issue "Alec Wodtke Festschrift."

Miguel Recio-Poo, Mohammad Shakiba, Francesc Illas, Stefan T. Bromley,* Alexey V. Akimov,* and Ángel Morales-García*

Cite This: https://doi.org/10.1021/acs.jpcc.4c07180 Read Online

ABSTRACT: We report a nonadiabatic molecular dynamics (NA-MD) study on radiative and nonradiative recombination dynamics in small bare and hydrated titania nanoclusters, $(TiO_2)_4(H_2O)_m$ (m = 0, 2, 4) and $(TiO_2)_8(H_2O)_m$ (m = 0, 2, 5). Our findings indicate that increased hydration raises excitation energies and nonadiabatic couplings, accelerating both radiative and nonradiative recombination. We test the robustness of this predicted trend with respect to several important choices in our NA-MD methodology. We find that nuclear trajectories from classical force fields closely match those from density functional theory (DFT) calculations, with recombination time scales weakly dependent on the choice of pure or hybrid functionals. Additionally, decoherence corrections yield longer nonradiative recombination times than the overcoherent fewest switches algorithm. Overall, our predicted hydration-induced recombination acceleration in titania nanoclusters is found to be independent of the main choices in our NA-MD approach, thus giving us confidence in our results.

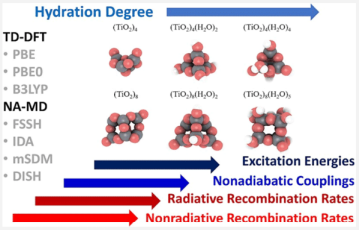

1. INTRODUCTION

As the global demand for energy continues to grow, the need for more efficient, environmentally friendly, and sustainable energy sources has become increasingly urgent. The ongoing development of heterogeneously photocatalyzed processes for solar energy conversion and sustainable energy production promises significant advancements in the quest for renewable energy solutions.[1,2] Heterogeneous photocatalysis involves the absorption of electromagnetic radiation by a solid catalyst to drive chemical reactions. This can be described as a physical phenomenon where an electron−hole pair is generated upon exposing a semiconducting material to light.[3−6] Light-harvesting constitutes the first step in heterogeneous photocatalysis and determines the capacity of a photocatalytic system to absorb incident photons and generate sufficient electron−hole pairs for the subsequent catalytic reactions.[7,8]

Among the wide variety of photoactive semiconductor materials, titanium dioxide (TiO_2), usually referred to as titania, stands out for its versatility in various photovoltaic and photocatalytic applications.[9−13] Many photoactive composite materials and heterostructures contain TiO_2 as a common ingredient, often functionalized with a metalorganic dye or quantum dots.[14,15] The onset for light absorption ranges from ∼3.0 eV for the rutile polymorph to 3.2 eV for the anatase one. Hence, the minimum energy required to generate electron−hole pairs lies in the ultraviolet (UV) region. This large energy coupled with the high recombination rate of electron−hole pairs are the two important drawbacks causing low photoefficiency. To successfully overcome these limitations, several strategies have been explored. These involve dye- and quantum-dot-sensitization approaches,[16−18] nonmetal doping,[19−21] formation of nanostructured metal/semiconductor heterostructures,[22] or crystal facet engineering.[23−25] The ground state electronic structure derived properties of photoactive titania nanostructures can be tuned by tailoring the size, shape, composition, and degree of hydration,[26−32] making heterogeneous photocatalysis more efficient.

Understanding the dynamics of photoinduced processes is of fundamental interest for engineering titania-derived materials for practical photovoltaic or photocatalytic applications.[33] Indeed, several experimental and computational studies have been carried out to date to explore the nature and dynamics of excitons[34] and charge-carriers[35] in systems such as poly-

Received: October 22, 2024
Revised: December 31, 2024
Accepted: January 2, 2025

https://doi.org/10.1021/acs.jpcc.4c07180
J. Phys. Chem. C XXXX, XXX, XXX−XXX

oxotitanates and anatase TiO_2 nanostructures using X-ray free electron lasers and pump−probe spectroscopy techniques.[36,37] Studies based on density functional theory (DFT) have been extensively employed to estimate the properties of excited electronic states in TiO_2 nanoparticles[38−42] and related systems.[43−45] Many of these studies rely on the single-particle (SP) description of electronic excited states and therefore may overlook multiconfigurational effects present in realistic excited states of such systems. Accounting for excitonic or multiconfigurational many-body (MB) effects via a more rigorous linear-response (LR) time-dependent DFT (TD-DFT) framework was shown to lead to stronger nonadiabatic couplings (NACs) between electronic states and thus to faster excited states dynamics in many other systems compared to single-particle-based simulations.[46−48] However, simply employing the conceptually solid framework of LR-TD-DFT does not guarantee a quantitative description of the excitonic effects,[49,50] as the choice of the underlying density functional strongly affects the outcomes of such calculations. As such, the choice of a suitable exchange−correlation functional remains an open question.[51] For instance, widely used generalized gradient approximation (GGA) density functionals such as Perdew−Burke−Ernzerhoff (PBE)[52] are not capable of capturing the excitonic effects and may yield negative energies of the charge-transfer excitation within the TD-DFT framework.[53] On the other hand, the use of hybrid density functionals, especially range-separated, or even better−optimally tuned range-separated− is a common solution to overcome the limitations of GGA functionals.[54] However, the computational time scaling of DFT-based calculations is more expensive with hybrid functionals than with GGA functionals, especially at the TD-DFT level, making such calculations practically prohibitive for large systems. To the best of our knowledge, no excited state dynamics simulations based on TD-DFT description of electronic excitations, especially using hybrid density functionals, have been carried out for titania clusters so far.

Relying on the computed TD-DFT excitation energies and NACs connecting the states involved in the excitation, Non-Adiabatic Molecular Dynamics (NA-MD) is *de facto* trusted as the most comprehensive computational technique to investigate the excited state dynamics.[55−59] Recently, the electron injection,[60] photoexcited polaron dynamics,[61] and the effect of size/shape in bare TiO_2 nanostructures have been investigated through the NA-MD simulations.[41,42] However, as already mentioned, those approaches describe the excitations within a SP framework. In this way, while static TD-DFT calculations in TiO_2-related systems have been reported, they have not been utilized in the NA-MD calculations yet. As a result, a more reliable description of electronic dynamics in such systems is yet to be obtained.

Apart from the previous work of Muuronen et al.[62] who examined the mechanism of water oxidation on the surface of a $(TiO_2)_4$ cluster, we are not aware of other studies of the influence of chemisorbed water on excited-state dynamics in hydrated TiO_2 nanostructures. Considering that in realistic photocatalytic systems, the surfaces of photocatalytic TiO_2-based materials are most often covered with water, understanding the impact of water on the photoinduced dynamics of excited states of hydrated titania nanostructures is essential for providing a better understanding of the photocatalytic performance of these systems.

Here, we present a computational benchmark study of radiative and nonradiative dynamics in small bare and hydrated titania nanoclusters $(TiO_2)_4$ and $(TiO_2)_8$ conducted within a TD-DFT framework with hybrid density functional kernels. These system sizes have been previously studied and have been shown to be good models for capturing essential excited state dynamics in titania and similar systems,[37,63−65] providing a well-established framework for comparison and analysis. By computing the excited states dynamics in a systematically controlled series of systems, we explore the role of nanocluster size and the degree of hydration on the kinetics of the lowest excited state relaxation. Contrary to previously reported works, we utilize a MB description of the electronic excited states in these systems by using LR-TD-DFT with hybrid density functionals. We also conduct a systematic assessment of various components of our computational methodology. In particular, we investigate the applicability of the classical force fields to NA-MD calculations as a computationally feasible alternative to ab initio molecular dynamics (AIMD). We explore the role of hybrid density functional in such simulations. Finally, we conduct a comparative analysis of several trajectory surface hopping (TSH) and decoherence correction methodologies as applied to modeling nonradiative recombination in this class of systems. Overall, this work provides new detailed insights into the role of water in TiO_2 recombination dynamics while offering a detailed methodological evaluation for simulating nonadiabatic molecular dynamics.

2. MODELS AND METHODS

The investigation of the dynamic excited state properties is performed in photoactive titania nanoclusters including anhydrous and hydrated systems with the general chemical formula: $(TiO_2)_n(H_2O)_m$, for $n = 4$ (with $m = 0$, 2, and 4) and $n = 8$ (with $m = 0$, 2, and 5) (see Figure 1). The corresponding

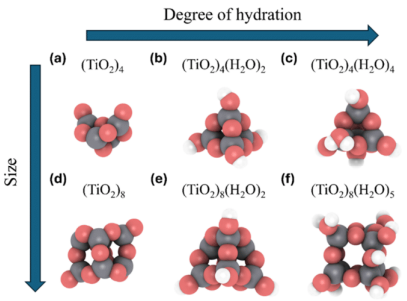

Figure 1. Anhydrous $(TiO_2)_4$ and $(TiO_2)_8$ (a, d) and hydrated $(TiO_2)_4(H_2O)_2$, $(TiO_2)_4(H_2O)_4$, $(TiO_2)_8(H_2O)_2$, and $(TiO_2)_8(H_2O)_5$ nanoclusters (b, c, e, f). Atom key: O—red, Ti—gray, H—white.

nanocluster structures used in all cases correspond to stable low energy minima found from global optimization searches.[66] These globally optimized nanoclusters are known to correspond well to the experimentally prepared hydrated TiO_2 species in cluster beams.[67] Based on the titania/water (m/n) ratio, our selection covers 0% as for the anhydrous $(TiO_2)_4$ and $(TiO_2)_8$ clusters, ~25% for $(TiO_2)_8(H_2O)_2$,

https://doi.org/10.1021/acs.jpcc.4c07180
J. Phys. Chem. C XXXX, XXX, XXX−XXX

~50% for $(TiO_2)_4(H_2O)_2$, ~60% for $(TiO_2)_8(H_2O)_5$, and ~100% for $(TiO_2)_4(H_2O)_4$ hydration degrees. The larger $(TiO_2)_8$-based nanoclusters are most favorably hydrated by dissociated chemisorbed water molecules. In this way, terminal hydrogen (−H) and hydroxyl (−OH) groups bind with uncoordinated O and Ti atoms on the surface of the titania nanoclusters, respectively.[27] This dissociative hydroxylation mechanism is also favorable at initial hydration levels for the $(TiO_2)_4$ system. However, at ~100% hydration $(TiO_2)_4(H_2O)_4$, molecular adsorption occurs instead (as depicted in Figure 1c). The excited state photoreactivity of small titania nanoclusters with water has been studied experimentally[68] and computationally[69] but larger titania nanoparticles are typically considered in experimental photocatalysis studies. Here, our study of smaller nanoclusters aims to establish a reasonable benchmark for applying TD-DFT and NA-MD methodologies to larger photoactive nanostructures using hybrid functionals combined with the LR-TD-DFT calculations. More broadly, it provides an analysis of the role of nanocluster size and hydration degree in determining the resulting dynamic of lowest excited electronic states.

We focus on determining the electron−hole recombination dynamics using TD-DFT calculations to compute the ground state (S_0) population recovery kinetics starting from the first excited singlet state (S_1). The S_1 state represents an important stage in the relaxation process, as it is typically well separated from S_0 by a significant energy gap. The $S_1 \rightarrow S_0$ transition becomes the bottleneck of the excited state relaxation process and largely determines the overall efficiencies of photovoltaic materials.[70]

Our NA-MD simulation workflow involves four sequential steps. At each one of these steps, several methodological choices are possible which are systematically investigated as detailed below. The computational workflow is implemented as part of the open-source Libra package (v5.7.1),[71−73] which is used interfaced with the CP2K code (2023.1 version)[74] for computing all the quantities of interest.

Starting with the first step, two procedures are considered to generate the nuclear trajectories for all considered titania systems (see Figure 1). Such trajectories are next used to conduct the NA-MD calculations in the last step, as explained later. In the Born−Oppenheimer approximation, nuclear motion parametrically perturbs the electronic states and drives the evolution of the corresponding state amplitudes, so the nuclear trajectories obtained in this step for the electronic ground state are referred to as the guiding trajectories. Trajectories are generated via (i) classical MD simulations -using the NanoTiO,[75] and FFTiOH[66] interatomic potentials or force fields (FF) for respectively anhydrous and hydrated systems-, using the GULP4.4 package;[76,77] and (ii) AIMD using the CP2K package. In the latter case, the interatomic interactions are described at the DFT level using the semilocal PBE exchange−correlation functional.[52] The Kohn−Sham (KS) orbitals of valence electrons are expanded in an atom-centered double-ζ-valence-polarized (DZVP) basis set.[78] An auxiliary plane-wave basis is used to fit the electron density with an energy cutoff of 300 Ry. The core electrons for Ti and O are described using Goedecker-Teter-Hutter pseudopotentials.[79] Grimme's D3 method with zero damping is used to account for dispersion.[80]

As the choice of density functional may significantly impact the quality of molecular dynamics trajectories, its selection requires further justification. In this work, the PBE+D3 functional is chosen for its demonstrated accuracy in describing lattice parameters, energetics, and structural stability of various oxide systems.[81] The inclusion of dispersion corrections improves the quality of the standard PBE functional by effectively capturing van der Waals interactions, hence providing more reliable prediction for bulk and interfacial systems. Prior studies demonstrated that PBE and its variants perform well in modeling reaction pathways, diffusion, and interfacial dynamics.[82,83] Additionally, Ohto et al.[84] highlighted the suitability of dispersion-corrected GGA functionals like revPBE-D3(0) for water-based interfacial systems, balancing accuracy and computational cost.

Both FF-based MD and DFT-based AIMD simulations are conducted in the NVT ensemble with the target temperature of 300 K, generating a 4 ps trajectory. The temperature is maintained using the Nosé-Hoover thermostat[85] with the collision frequency parameter set to 100 fs^{-1}. A nuclear integration time step of 1 fs is used, giving rise to a trajectory composed of 4000 structures. The first 1000 fs are considered as an equilibration period, and our NA-MD calculations only use the data for the remaining 3000 nuclear configurations. The comparison of the NA-MD outcomes obtained using FF- and DFT-generated AIMD guiding trajectories allows us to better understand the influence of the level of theory on the resulting excited state dynamics. The atomic vibrational frequencies of our titania clusters along the 3000 fs runs provides a means to compare the two approaches. These vibrational frequencies can be obtained from the atomic velocity-velocity autocorrelation function (VV-ACF).[86] The Fourier transform of the VV-ACF yields the power spectrum which reveals the characteristic frequencies of the active nuclear modes in the MD calculations.

Once the trajectory is generated, the second step comprises TD-DFT calculations for each of the 3000 geometries sampled during the guiding trajectories. The TD-DFT calculations yield the energies of excited states, configuration interaction (CI) amplitudes of the key excited Slater determinants involved in all excited states of interest, as well as the time-overlaps of the selected KS orbitals. Despite that we are only interested in the dynamics involving S_0 and S_1 states only, it is important to compute other excited states, so the dynamical basis, including the vector made of all electronic states involved in the dynamics, is large enough to properly describe possible crossings between S_1 and other higher energy states. To this end, our basis includes up to ten excited states obtained from the TD-DFT calculations. The resulting excited states $\{\Psi_I = \sum_{a\in virt, i\in occ} c_{i,a}\Phi_i^a\}$, are composed by superposition of excited Slater determinants (SDs) $\{\Phi_i^a = \hat{a}_i\hat{a}_a^+\Phi_0\}$, which in turn are composed of the KS molecular orbitals (MO), $\{\psi_i\}$. Here, $\hat{a}_i\hat{a}_a^+$ are the Fermionic annihilation and creation operators, and Φ_0 indicates the ground state SD: $\Phi_0 = \det|\psi_{i_1}\psi_{i_2}...\psi_{i_N}|$. The TD-DFT calculations also provide the excitation energy, E_i, the corresponding transition dipole between excited and the ground states, $\mu_{i,0} = \langle\Psi_i|\hat{\mu}|\Psi_0\rangle$, as well as the corresponding oscillator strength, $f_{i,0} = \frac{2m_e}{3\hbar^2}(E_i - E_0)|\mu_{i,0}|^2$.

Similar to the VV-ACF described above, the autocorrelation function of the energy gap fluctuations characterizes the coupling of the nuclear modes to a particular electronic transition of interest.[87] In this approach, the fluctuation of the energy gap between states Ψ_i and Ψ_j is first computed, $\delta E_{i,j} = E_{ij}(t) - \langle E_{ij}\rangle$, where $E_{i,j} = E_i - E_j$. The Fourier transform of the gap ACF, $C(\tau) = \langle\delta E_{ij}(\tau)\delta E_{IJ}(0)\rangle$ yields the influence

https://doi.org/10.1021/acs.jpcc.4c07180
J. Phys. Chem. C XXXX, XXX, XXX−XXX

spectrum, $I(\omega)$, which shows the vibrational modes that strongly couple to the transition between states Ψ_i and Ψ_j. In our case, only states S_0 and S_1 are considered. The variance of the energy gap, $\langle \delta E_{ij}^2 \rangle^{1/2}$ yields the pure dephasing times between such states,[87] a parameter used in some of our decoherence-corrected TSH calculations (e.g., mSDM):

$$\tau_{IJ} = \sqrt{\frac{12\hbar^2}{S\langle \delta E_{IJ}^2 \rangle}} \tag{1}$$

Besides nonradiative recombination which releases energy as heat through phonons, electrons and holes can recombine radiatively, emitting light. The probability of spontaneous photon emission is quantified by the Einstein $A_1 \rightarrow 0$ coefficient, while its inverse gives the radiative lifetime of the excited state, τ_r, computed as[88]

$$\tau_{r,1\rightarrow 0} = A_{1\rightarrow 0}^{-1} = \frac{3\pi\varepsilon_0\hbar c^3}{\omega_{10}^3 \mu_{1,0}^2} \tag{2}$$

where $\omega_{10} = (E_1 - E_0)/\hbar$ is the transition angular frequency that determines the position of the spectral line in the absorption spectra. Again, $\mu_{1,0}$ represents the transition dipole moment between S_1 and S_0.

KS orbital time-overlaps described as $s_{ij}(t,t + \Delta t) = \langle \psi_i(t)|\psi_j(t + \Delta t)\rangle$, are also computed analytically as detailed elsewhere.[59] Since not all of the KS orbitals are involved in the excitations for the set of excited states of our interest, we only compute the time-overlap matrices for a subset of KS orbitals, which defines the orbital active space. The selection of such an active space is done globally, based on the analysis of the excitations for all nuclear geometries. The KS time-overlap matrices are used to compute the time-overlap matrices of Slater determinants using Lowdin approach,[89] $\langle \Phi_i(t)|\Phi_j(t + \Delta t)\rangle = \det|s_{a,b}(t,t + \Delta t)|_{a\in i,b\in j}$ where $a \in i$ represents that the KS spin−orbital a is present in the SD i and $|s_{a,b}(t,t + \Delta t)|_{a\in i,b\in j}$ represents a matrix of time-overlaps in the KS spin−orbital space.

The third step of the workflow computes the time-overlaps of the excited states included in the dynamical basis as a linear transformation of the SD time-overlap matrices by the CI coefficient matrices, $\langle \Psi_i(t)|\Psi_j(t + \Delta t)\rangle = \sum_{a,b} C_{a,i}(t) C_{b,j}(t + \Delta t)\langle \Phi_a(t)|\Phi_b(t + \Delta t)\rangle$. The resulting TD-DFT time-overlaps can be used to compute NACs, using the Hammes-Schiffer-Tully formula:[90]

$$d_{i,j}\left(t + \frac{\Delta t}{2}\right) \approx \frac{\langle \Psi_i(t)|\Psi_j(t + \Delta t)\rangle - \langle \Psi_i(t + \Delta t)|\Psi_j(t)\rangle}{2\Delta t} \tag{3}$$

As mentioned earlier, one of the aims of this work is to assess the role of the density functional choice in modeling radiative and nonradiative dynamics in titania systems. We consider PBE,[52] a semilocal GGA functional, as well as PBE0[91] and B3LYP,[92] which are hybrid functionals incorporating 25% and 20% of the exact Fock exchange, respectively. The use of hybrid functionals mitigates the underestimation of the charge-transfer energy typically present for calculations with the PBE functional. In addition, prior studies reported that NACs may be overestimated when pure functionals such as PBE are used, especially at the single-particle level.[93]

Finally, NA-MD calculations are performed in the last step of the workflow to predict the coupled evolution of the nuclei and electrons. The starting point of this calculation represents the time-evolved overall wave function of the system in a basis of the adiabatic excited states (dynamical basis), $\{\Psi_i(\boldsymbol{R}(t))\}$, implicitly dependent on time via nuclear geometries:

$$\tilde{\Psi}(t) = \sum_i C_i(t)\Psi_i(\boldsymbol{R}(t)) \tag{4}$$

The amplitudes, $C_i(t)$, evolve according to the time-dependent Schrodinger equation (TD-SE):

$$i\hbar \dot{C}_i(t) = \sum_j H_{i,j}^{vib}(\boldsymbol{R}(t)) C_j(t) \tag{5}$$

where the matrix elements of the vibronic Hamiltonian, H_{ij}^{vib}, are given by

$$H_{ij}^{vib}(\boldsymbol{R}(t)) = E_i(\boldsymbol{R}(t))\delta_{ij} - i\hbar d_{ij}(\boldsymbol{R}(t)) \tag{6}$$

Here, E_i are the state energies, δ_{ij} is the Kronecker delta, and d_{ij} are the NACs introduced in eq 3. The TD-SE in eq 6 is solved using the local diabatization (LD) approach,[94,95] which is known to be more robust compared to the NAC-based integration method. The neglect-of-back-reaction approximation (NBRA)[96−98] is used according to which the electronic dynamics is affected by the nuclear dynamics, but the latter is not responsive to change of the electronic state.

The time-evolved TD-SE amplitudes are used in the TSH algorithms to stochastically sample electronic transitions. Here, four TSH algorithms are used (i) the Tully's fewest switches surface hopping (FSSH),[99] (ii) revised decoherence-induced surface hopping (DISH_rev2023),[100,101] (iii) instantaneous decoherence at attempted hops (IDA),[102] and (iv) the modified simplified decay of mixing (mSDM).[100] While the FSSH algorithm is known for its overcoherent nature, the other three approaches introduce electronic decoherence in different ways and thus are assumed to be more reliable.

The NA-MD calculations are carried out for 3 ps with both electronic and nuclear integration time steps taken as 1 fs. In fact, the nuclear time steps are already predetermined by the MD trajectories obtained in the first step of the overall workflow. The use of the LD integration allows the electronic timesteps to be as large as the nuclear ones. The NA-MD calculations are averaged over 30 initial nuclear conditions that are taken as points of the guiding trajectories and separated by 100 fs. All NA-MD calculations are initiated in the first excited state. For each initial condition (starting geometry and electronic state), 500 stochastic realizations of the TSH process are computed. The averaging over the stochastic realizations yields the results for each batch. The averaging over all batching is used for obtaining a more statistically accurate description of the dynamics as well as to obtain the estimates of the margins of errors for the computed relaxation time scales.

To compute the nonradiative recombination times, we track the population of the ground state, which is fitted by the stretched-exponential function:

$$f(t) = 1 - \exp\left(-\frac{t}{\tau}\right)^{\beta} \tag{7}$$

where, τ and β are fitting parameters, with the former having the interpretation of the lifetime. The β parameter is allowed to vary between 1 and 2 to account for two limiting cases − the Gaussian kinetic ($\beta = 2$) typical for overcoherent methods, and the exponential kinetics ($\beta = 1$) characteristic for the decoherence-corrected calculations. The computed error bar

https://doi.org/10.1021/acs.jpcc.4c07180
J. Phys. Chem. C XXXX, XXX, XXX−XXX

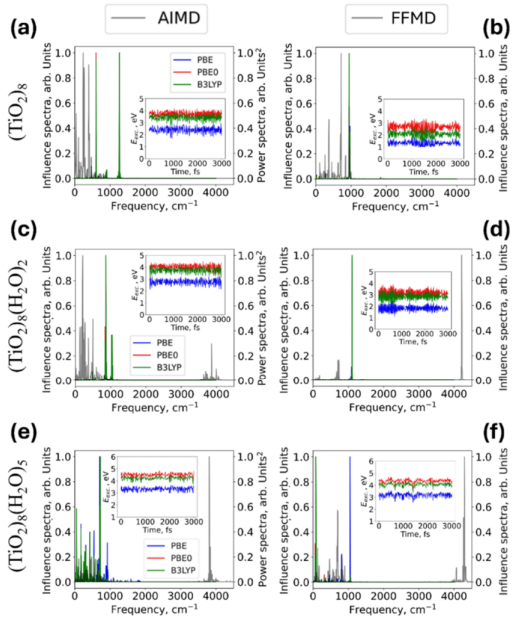

Figure 2. Normalized power (gray) and influence (red) spectra for $(TiO_2)_8$ (a, b), $(TiO_2)_8(H_2O)_2$ (c, d) and $(TiO_2)_8(H_2O)_5$ (e, f) systems. The power spectra are computed using nuclear trajectories obtained with AIMD (a, c, e) or classical FFMD (b, d, f) methods. The influence spectra characterize the vibrational modes that drive the transition between the ground state and first excited state. The insets show the evolution of the ground-to-first-excited-state energy gap in corresponding calculations. Color codes: gray—power spectra, blue, red and green—influence spectra. For the influence spectra, TD-DFT-calculated excitation energies are computed with B3LYP (green lines), PBE0 (red lines) and PBE (blue lines) functionals.

for each trajectory with respect to the average population evolution branch is computed as

$$\epsilon = Z\frac{s}{\sqrt{N}} \tag{8}$$

where s is the standard deviation of the τ parameters sampled from $N = 30$ batches. Following the prior practice,[103] we select the samples having a R^2 value of more than 0.1. Lastly, the Z value is the confidence interval coefficient. For a confidence interval of 95%, it is equal to 1.96.

3. RESULTS AND DISCUSSION

In this section, we present the results in a manner congruent with the above-discussed steps of our NA-MD protocol, i.e., the generation of nuclear trajectories, excited states computation, NACs calculation and excited state dynamics analyses. We perform a comparative analysis of the computational approaches at different steps of the workflow. We discuss the effect of the choice of the method used to obtain the vibrations activated during the generated guiding trajectories, the role of the density functional choice in determining the excited state energies and NAC derived from the TD-DFT calculations. We show a qualitative comparison of the dynamics generated by different TSH schemes within the NA-MD calculations. Further, we analyze chemical aspects of the systems, such as the role of the hydration degree and cluster size on the excited state relaxation times in the selected titania nanoclusters (see Figure 1).

3.1. Power and Influence Spectra. We start comparing the ground state MD trajectories obtained using either FFMD or AIMD by computing the power and influence spectra of the $(TiO_2)_8$, $(TiO_2)_8(H_2O)_2$, and $(TiO_2)_8(H_2O)_5$ systems (Figure 2). Analogous calculations for the $(TiO_2)_4$-derived clusters are reported in Figure S1 of the Supporting Information (SI). The power spectrum (gray lines) represents the vibrational modes that are activated/appeared in the MD trajectory. In the limit of sufficiently long ergodic evolution, this spectrum should also relate to the vibrational density of states with the difference that it also accounts for anharmonic effects, unlike the conventional normal modes analysis. The influence spectrum (colored lines in Figure 2 and Figure S1 of the SI) represents the modes that are coupled to the electronic transition between the states of interest (i.e., S_0 and S_1). To facilitate comparison and visualization, both the influence spectrum and

https://doi.org/10.1021/acs.jpcc.4c07180
J. Phys. Chem. C XXXX, XXX, XXX−XXX

power spectrum are normalized by dividing all values by their respective maximum values, such that the highest value is one. In addition to the choice of method used to generate nuclear trajectories (i.e., FFMD or AIMD), the influence spectra also depend on the electronic structure method used to compute the electronic states. The evolution of the first excited state energy derived from the TD-DFT calculations is shown in the insets of Figure 2. As outlined in the methodology section, the ACF of the excitation energy fluctuation is what determines the frequencies of the modes coupled to the $S_1 \rightarrow S_0$ transition.

Power spectra of the bare $(TiO_2)_8$ cluster (Figure 2a,b) show the vibrational modes at frequencies similar to those observed in titania bulk phase. The vibrational modes ranging between 100 to 200 cm^{-1} correspond to Ti−O stretching modes,[104] while those ones associated with Ti−O−Ti angle bending are in the 500−1000 cm^{-1} range.[105−107] The power spectra of all hydrated $(TiO_2)_8$ clusters (Figure 2c−f) show a characteristic hydroxyl stretching mode around 3700−3900 cm^{-1}.[27] For a fixed nuclear trajectory method, the position and the broadening of the OH-stretching modes are nearly insensitive to the degree of hydration. Qualitatively, the vibrational modes obtained from FFMD are similar to those originating from AIMD (PBE-MD). Although the exact positions of the peaks differ from each other in the two approaches, the power spectra are qualitatively the same. Compared to the AIMD results, the FFMD ones tend to yield slightly blue-shifted overall spectra with a smaller number of well-pronounced peaks. The reduced number of peaks in the FFMD calculations is likely due to the more simplified description of interatomic interactions described by NanoTiO and FFTiOH FFs with respect to the more accurate electronic description of bonding in DFT-based AIMD calculations. The systematically lower frequencies in the AIMD spectra with respect to the FF-based one may be attributed to a better description of anharmonic effects in the former approach. The anharmonicities also realize the cross-coupling of vibrational modes and vibrational energy redistribution between them. Thus, vibrational energy is more likely to diffuse between different modes and activate them, in addition to resonances of vibrational modes. As a result of these two effects, the AIMD approach generates denser vibrational densities of states compared to the FFMD dynamics. Despite the noted differences, the high degree of resemblance between spectra computed with FFMD or DFT-based AIMD points out that the tested FFs are sufficiently accurate to act as computationally efficient counterparts to DFT calculations in potential studies of larger titania-derived systems,[108] where the AIMD based approaches become unattainable.

Figure 2 also shows the influence spectra and the energy evolution of the first excited state (insets) computed for $(TiO_2)_8$-based clusters using TD-DFT calculations with three density functionals: PBE (blue), PBE0 (red) and B3LYP (green). Figure S1 of the SI shows analogous information for $(TiO_2)_4$-based clusters. All spectra indicate that the $S_1 \rightarrow S_0$ transition is driven by the Ti−O−Ti angle bending modes that are in the 500−1000 cm^{-1} range. This finding is in agreement with the previous studies of Alvertis et al.[109−111] who discussed the dominance of low-frequency vibrations in shaping exciton dynamics and influencing nonradiative processes.

In particular, the mode at around 1000 cm^{-1} is present for all methods and in all systems (see Figure 2). Notably, the mode appears to be split when DFT is used for computing the guiding trajectory (e.g., the peaks in the 500 to 1400 cm^{-1} range), while it consists of only one strong peak at around 1000 cm^{-1} when the FF is used for producing the guiding trajectory. The splitting observed in AIMD DFT-based spectra is likely due to the activation of different modes due to the anharmonic effects enabling the vibrational energy transfer between the modes and hence their appearance in the spectrum. This effect is rather general since the AIMD influence spectra show a larger number of modes coupled to the electronic transition of interest than the FF-based influence spectra. The Ti−O stretching modes in the 100 to 200 cm^{-1} range do not show strong coupling to the electronic transition of interest in neither bare nor weakly hydrated clusters (Figure 2a−d). However, these modes are present in the strongly hydrated system and only when DFT is used for producing the guiding trajectory (Figure 2e).

Although all methods show the hydroxyl vibrational modes around 3000 cm^{-1} in the power spectra, this mode is not coupled to the $S_1 \rightarrow S_0$ transition as it is not present in the influence spectrum. Similar results and trends are obtained for the smaller $(TiO_2)_4$-based nanoclusters, as reported in Figure S1 of the SI, suggesting that both power and influence spectra features are size-independent. The strongly hydrated cluster (i.e., $(TiO_2)_4(H_2O)_4$) may need further analysis though, given the different cluster structures rendered by the use of either AIMD- or FF-based trajectories. While the initial shape of the globally optimized structure with an adsorbed water molecule (Figure 1c) is maintained throughout the whole AIMD runs, the use of FFs gives rise to a more symmetric structure which, is slightly higher in energy than the AIMD one. This is due to the intrinsically more simplified nature of the FF parametrized interatomic interactions. Figure S2 shows a comparison between both hydrated NPs at the end of each MD nuclear trajectory. The discrepancies in the morphologies between both NPs thus lead to different power and influence spectra features, especially at around 1500 cm^{-1} (Figure S1e) likely due to the isolated water molecule vibrational modes shifting back to their original frequencies.

3.2. TD-DFT Excited State Energies and NACs. To rationalize the contributions from different vibrational modes as shown in the influence spectra, we analyze the electronic densities corresponding to the highest occupied molecular orbital (HOMO) and the lowest unoccupied molecular orbital (LUMO) of the $(TiO_2)_4(H_2O)_m$ (m = 0, 2, and 4), and $(TiO_2)_8(H_2O)_m$ (m = 0, 2, and 5) nanoclusters. For each system, we select a representative geometry sampled from the precomputed MD trajectory and visualize the orbital iso-value surfaces computed with the PBE density functional (see Figure 3). For all considered functionals, we find that the composition of the lowest excited TD-DFT state, S_1, is dominated by the HOMO → LUMO excitation, as can be quantified by the squares of the CI coefficients with which they mix in the TD-DFT "wavefunctions" (Table S1 in the SI). The PBE functional shows a large dominance of the HOMO → LUMO excitation (larger single-particle character), hence its use as a representative case in Figure 3. We thus only focus on the frontier orbitals to rationalize the observed features of the influence spectra. Regardless of the hydration degree, the larger electronic densities are located around the Ti−O bonds. Thus, the Ti−O bond stretching as well as O−Ti−O or Ti−O−Ti angle bending modes can affect the corresponding MOs and excited states the most and hence reveal themselves in the influence spectrum.

https://doi.org/10.1021/acs.jpcc.4c07180
J. Phys. Chem. C XXXX, XXX, XXX−XXX

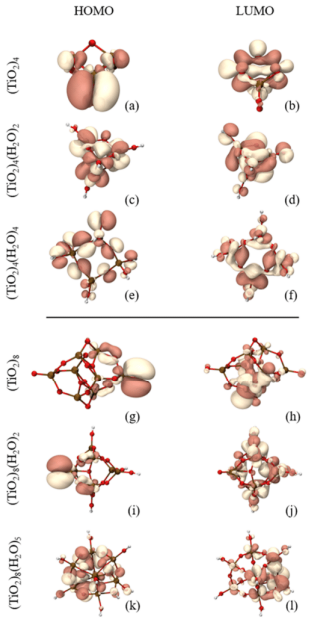

Figure 3. Isosurfaces of HOMO (a, c, e, g, i, and k) and LUMO (b, d, f, h, j, and l) orbitals corresponding to (a–f) $(TiO_2)_4$-based and (g–l) $(TiO_2)_8$-based sets of titania nanoclusters. The cluster geometries are sampled from the corresponding FF-based MD trajectories. Isosurface values are 0.012 $Å^{-1/3}$ (tan) and −0.012 $Å^{-1/3}$ (white). Multiwfn software[112] was employed to generate the isosurfaces. Atom key: O—red, Ti—brown, H—white.

The above argument does not always hold for TD-DFT calculations based on either PBE0 or B3LYP hybrid functionals. The TD-DFT pseudowave functions computed with such hybrid functionals exhibit larger mixing of other single-particle configurations (see Table S1 of the SI). Nevertheless, the orbitals involved in other mixed configurations are in almost all cases localized on the Ti−O fragments (Figure S3 of the SI), and not on the hydroxyl groups. This confirms that the influence spectra are systematically insensitive to the hydroxyl vibrational modes regardless of the exchange−correlation functional used.

The analysis of the trajectory-averaged first excited state energy computed with different methods reveals that the hydration of titania nanoclusters induces a systematic increase of the trajectory-averaged vertical excited state energies, $\overline{E_{exc}}$ (see Figure 4a,b in and insets in Figure 2). We rationalize this effect by two factors, (i) energy gap opening due to the removal of defect states (i.e., uncoordinated O and Ti sites), and (ii) weaker stabilization of charge transfer excitations in hydrated systems. First, the hydration of titania nanoclusters promotes the electronic energy gap opening, as estimated by the HOMO−LUMO difference by passivating defect midgap states originated due to under-coordinated (O_{1c} and Ti_{4c}) surface atoms in the bare or weakly hydrated $(TiO_2)_4$ systems. By increasing the hydration of titania nanoclusters, the "defect" states are removed more completely thus opening the energy gap. This mechanism was already reported by some of us in previous works.[28,66] Second, excited states exhibit more isotropic charge distributions in strongly hydrated systems, leading to smaller excited-state dipole moments and, consequently, reduced Coulombic stabilization of these states. This effect contributes to an increase in the excitation energy of the strongly hydrated clusters. Besides the two main factors detailed above, the cumulative effect of the dipolar −OH ligands introduces an additional electric fieldon the hydrated nanocluster core, which has been shown to influence the energy of frontier orbitals/band edges.[113−115] However, this effect is expected to be similar in both frontier levels and not be correlated with gap opening.

The charge distribution (ii) point raised can be explained by means of the analysis of the orbitals involved in the excitations. The analysis of the CI amplitudes suggests that the S_1 states of nearly all considered clusters are dominated by the HOMO → LUMO excitation. For the bare $(TiO_2)_8$ nanocluster, such a transition is a longer-distance charge transfer that creates a strong dipole moment (Figure 3g,h). The resulting charge-separated state has a notable Coulombic interaction between electron and hole which lowers the energy of the corresponding excited state to a larger extent than in the smaller $(TiO_2)_4$ nanocluster. With the increased degree of hydration, both HOMO and LUMO involved in the excitation tend to become more spatially isotropic and more delocalized. The corresponding HOMO → LUMO transition thus results in a shorter-distance charge transfer, leading to a smaller S_1 dipole moment and a smaller Coulombic stabilization and hence in higher excitation energy of the S_1 excited state. This rationalization is consistent with the magnitudes of the trajectory-averaged dipole moment of S_1 state for all systems compiled in Table S2 of the SI. It should be noted that although the magnitudes of the excited state dipole moment can be indicative of the amount of charge separation in the excited states, other factors such as exchange and correlation effects may come into play nontrivially.

In nanocluster systems, such as those considered in this work, the confinement of electronic states limits the extent of dipole coupling, which reduces the influence of the long-range Fröhlich mechanism that plays a dominant role in nonradiative recombination processes in extended systems (such as bulk TiO_2).[116] This mechanism arises from dipole interactions facilitated by the delocalized nature of electronic states in the bulk, leading to significant long-range effects. However, for small TiO_2 nanoclusters, the electronic and vibrational dynamics differ significantly due to spatial confinement. In this way, short-range coupling mechanisms, realized by localized vibrations and interactions within the cluster become more prominent. Furthermore, surface effects, particularly in hydrated nanoclusters, strongly impact the vibrational modes and charge dynamics, further amplifying the role of short-range coupling.

We observe that the $(TiO_2)_4$ nanocluster exhibits larger $\overline{E_{exc}}$ values than the $(TiO_2)_8$ counterpart for all considered methodologies. This effect can be initially attributed to quantum confinement becoming more prominent when decreasing the nanocluster size. However, the influence of

https://doi.org/10.1021/acs.jpcc.4c07180
J. Phys. Chem. C XXXX, XXX, XXX−XXX

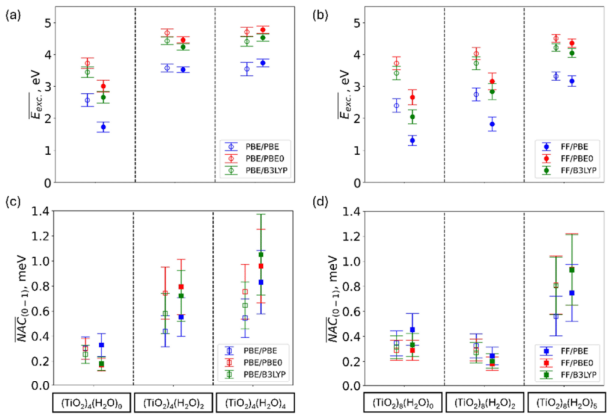

Figure 4. (a, b) Trajectory-averaged values of the first excited state energies (obtained with three DFT functionals) for each of the six clusters. Color codes: blue, red and green − PBE, PBE0, and B3LYP functionals. Empty and solid circles correspond respectively to DFT-based and FF-based nuclear trajectories. (c, d) Trajectory-averaged values of the trajectory-averaged nonadiabatic couplings between ground (S_0) and first excited state (S_1) obtained with three DFT functionals for each of the six clusters. Color codes: blue, red and green—PBE, PBE0, and B3LYP functionals. Empty and solid squares correspond respectively to DFT-based and FF-based nuclear trajectories. Error bars represent the standard deviation for each of the calculations.

quantum confinement at these small sizes can be overshadowed by the effects from specific atomic bonding or the presence of defects in the material. This effect is maintained for the hydrated nanoclusters, e.g., the saturated $(TiO_2)_4(H_2O)_4$ also displays larger $\overline{E_{exc}}$ values than the than the highly hydrated $(TiO_2)_8(H_2O)_5$ nanocluster (see Figure 4a,b and Table S3 of the SI).

There are two methodological issues to explore here: (i) the dependence of $\overline{E_{exc}}$ on the choice of density functional, and (ii) its dependence on the choice of method to produce the trajectories (FFMD *vs* AIMD). First, expectedly, PBE yields systematically the lowest $\overline{E_{exc}}$ values among all the functionals tested. This observation holds for all nanoclusters regardless of the methodology to obtain the trajectories. The shortcomings of pure density functionals such as PBE when used in TD-DFT calculations of excited states, especially those having charge transfer character, are well-known.[117,118] They originate from the incorrect (short-range) behavior of the exchange functional leading to overdelocalization of excited states and significant underestimation of energies of charge transfer states, sometimes including negative excitation energies,[53] and overestimation of NACs.[93] Since the problems are more apparent in extended systems, for the smallest bare $(TiO_2)_4$ nanocluster we observe surprisingly accurate excitation energy using the TD-DFT (PBE) method. Using the DFT-based AIMD nuclear trajectory, the TD-DFT calculation with the PBE functional estimates the $\overline{E_{exc}}$ value for S_1 state to be 2.57 eV, which is perhaps fortuitously closer to the one reported in experiments (2.60 eV)[119] than the ones provided by TD-DFT with PBE0 (3.73 eV) or B3LYP (3.45 eV) functionals. Repeating a similar analysis for the FF-based nuclear trajectory, the underestimation of the S_1 excited state energy by TD-DFT calculations with the PBE functional is more noticeable (1.73 eV). In this case, computing the excitations with the PBE0 (3.01 eV) and specially B3LYP (2.66 eV) functionals lead to values more in line with experiments.

Second, we observe that using FF-derived trajectories instead of the AIMD-based ones generally yields a reasonable agreement of computed $\overline{E_{exc}}$ values. This agreement is improved as the degree of hydration (i.e., m/n) ratio increases. For bare $(TiO_2)_n$ clusters, the largest discrepancies in $\overline{E_{exc}}$ are observed the FF-based nuclear trajectories, which are underestimated by more than 1 eV compared to the DFT-based one. For instance, the case of $(TiO_2)_8$ nanocluster with excitation energies of 1.31 eV (FFMD/PBE), 2.66 eV (FFMD/PBE0), and 2.05 eV (FFMD/B3LYP) vs 2.40 eV (AIMD/PBE), 3.73 eV (AIMD/PBE0), and 3.42 eV (AIMD/B3LYP), respectively. This decrease of the excitation energies can be tentatively attributed to the more symmetrical structures favored by the FF employed to obtain the trajectory. As the degree of hydration increases, the differences in $\overline{E_{exc}}$ tend to become smaller (e.g., 3.17 eV (FFMD/PBE), 4.36 eV (FFMD/PBE0), and 4.05 (FFMD/B3LYP) eV vs 3.32 eV (AIMD/PBE), 4.51 eV (AIMD/PBE0), and 4.22 eV (AIMD/B3LYP) in the case of $(TiO_2)_8(H_2O)_5$ case). The differences in $\overline{E_{exc}}$ values computed with AIMD- or FF-based trajectories become smaller with increased hydration. We note that the tendency of the currently employed FFs to yield more symmetric structures may be problematic in larger titania NPs, where the surface/volume fraction is small and where hydration does not induce a large degree of structural symmetry breaking. Such simulations would likely underestimate the excitation energies and hence overestimate the nonradiative recombination rates. This issue could be alleviated by employing more accurate FFs with more sophisticated parametrizations (e.g., reactive FFs) or machine learned FFs.

https://doi.org/10.1021/acs.jpcc.4c07180
J. Phys. Chem. C XXXX, XXX, XXX−XXX

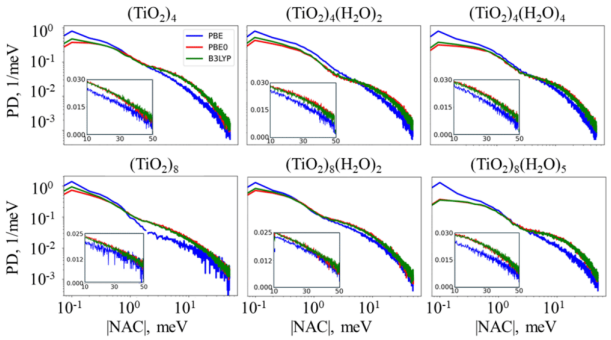

Figure 5. Computed probability distribution (PD) of NACs between pairs of all states in our dynamical basis for all clusters (AIMD-based nuclear trajectories). The inset graphs provide a zoom-in to the larger NACs values region, unveiling larger probability densities with hybrid functionals in most cases.

We now focus on the analysis of the trajectory-averaged nonadiabatic coupling ($\overline{NAC}$) between S_0 and S_1 states as computed with the TD-DFT methodology (Figure 4c,d and Table S4 of the SI). With a few exceptions, the average NAC values obtained for FF-based trajectories are somewhat higher than those for the AIMD-based trajectories, although the values lie within each other's error margin, for each selected combination of system and density functional. Thus, the use of the FF-based trajectories appears to be a reasonable approach for computing NACs when computational demands do not allow using DFT-based AIMD trajectories.

The $\overline{NAC}$ values gradually increase with the increase of the degree of hydration. This effect is, in principle, counterintuitive because the NAC between a pair of states should be inversely proportional to the energy gap between such states. However, the NACs can be regarded as a quantification of the wave function change upon a nuclear perturbation. Thus, for NACs to be large, it is important that (i) the vibrations that couple to the pair of states of interest are activated, and (ii) the wave function changes with symmetries that are distinct to the symmetries of the corresponding vibrational modes. As the degree of hydration increases, the electronic wave functions (specifically the HOMO and LUMO) involved in the $S_0 \rightarrow S_1$ transition tend to become more delocalized. This delocalization arises from the interaction between the nanocluster and surrounding water molecules, which induce polarizing effects and stabilize specific electronic states. The broader spatial extent of delocalized wave functions enhances their sensitivity to nuclear motions. Consequently, additional vibrational modes capable of efficiently coupling to the $S_0 \rightarrow S_1$ electronic transition can be activated, leading to larger average NACs. This is also apparent from the influence spectra in Figure 2 and Figure S1 of the SI. This explanation is also consistent with the presence of an apparent threshold of switching between NACs being sensitive or not sensitive to the degree of hydration of the titania nanoclusters. Indeed, in the small $(TiO_2)_4(H_2O)_m$ nanoclusters, the surface/volume ratio is larger than in the larger $(TiO_2)_8(H_2O)_m$ nanoclusters. Thus, the surface water molecules cause more significant disorder in the former systems leading to immediate nearly linear dependence of $\overline{NAC}$ on the number of water molecules (Figure 4c). In the $(TiO_2)_8(H_2O)_m$ systems, we first observe a plateau suggesting no dependence of $\overline{NAC}$ on the degree of hydration. As this number increases, the disorder caused by the surface hydration becomes sufficient to affect the wave functions and increase the $\overline{NAC}$ values (Figure 4d). The current explanation of the influence of orbital localization on the electron−phonon (or, equivalently, NA) coupling is also in line with the analogous arguments discussed in multiple prior works, although focused on other systems.[55,59,110,120]

Although the above analysis focuses on comparing the averaged NAC values, it is important to note that it is the instantaneous NACs and their distribution what ultimately determines the dynamics of excited state relaxation. Following prior works,[59,103] we compute the distributions of NACs for all systems and using all considered density functionals (Figure 5). Despite the discussed differences in the average NACs between the first excited and the ground states, we observe relatively similar distributions for all systems. These plots are especially convenient for discussing the dependence of NACs on the chosen density functional. As seen from the peaks of the distributions (which gravitate to smaller NAC values), there is a smaller probability to sample smaller NACs when using hybrid functionals (PBE0 or B3LYP) compared to those computed with the PBE functional. These results are consistent with the previous work showing that the use of hybrid functionals leads to decreased NAC values in the KS basis compared to the pure-functional counterparts, especially in rather large systems.[93] Additionally, we observe that the large couplings are more probable when hybrid functionals are used instead of PBE. This effect can be rationalized by the fact that the present couplings are computed at the TD-DFT level rather than at the single-particle one. Indeed, the configurational mixing in TD-DFT wave functions facilitates larger couplings.[47,48] As we mentioned above, hybrid functionals also increase the configuration mixing in the TD-DFT states of $(TiO_2)_n(H_2O)_m$ systems, thus their use leads to higher likelihood of generating larger NACs.

3.3. Nonradiative Recombination. The main outcomes of our NA-MD simulations are the nonradiative recombination

https://doi.org/10.1021/acs.jpcc.4c07180
J. Phys. Chem. C XXXX, XXX, XXX−XXX

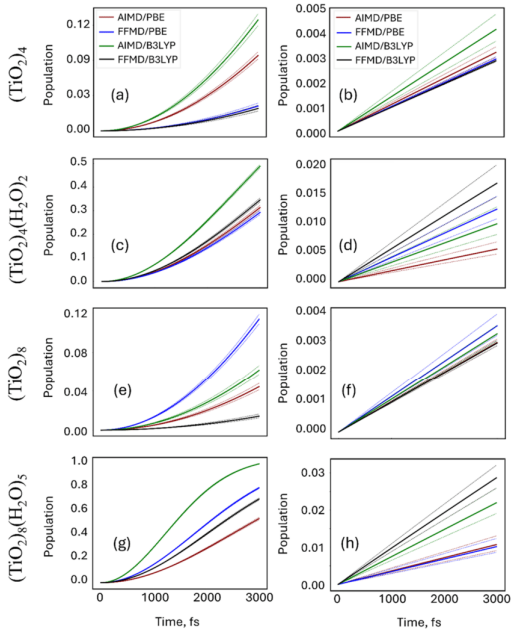

Figure 6. Ground state (S_0) population evolution with FSSH (a, c, e, and g panels) and mSDM (b, d, f, and h panels) TSH approaches. First and second rows (a–d) correspond, respectively, to $(TiO_2)_4$ and $(TiO_2)_4(H_2O)_2$ systems: third and four rows (e–h) to $(TiO_2)_8$ and $(TiO_2)_8(H_2O)_5$ nanostructures. Concerning the underlying DFT functional for computing the excitations, red and blue lines are associated in each plot to PBE, while green and black correspond to the hybrid B3LYP functional. On the other hand, red and green refer to PBE-based AIMD nuclear trajectories, while blue and black to trajectories obtained with FFs. The average population for each case is shown in bold lines, whereas dashed lines account for the error bars at each time.

rates from the first excited state S_1 to the ground state S_0 reported in Figures 6, 7, and Table 1. The $S_1 \rightarrow S_0$ transition corresponds to the charge carrier recombination process, so we often refer to the corresponding time scale as the recombination time. In particular, we focus our analysis on how these times vary with, (i) the choice of the MD approach (i.e., AIMD or FF-based) to generate the guiding nuclear trajectory; (ii) the choice of the employed DFT functional (i.e., PBE, PBE0, B3LYP) to compute NACs or, equivalently, the wave function time-overlaps; (iii) the choice of the TSH scheme to model the NA dynamics (i.e., FSSH, DISH, mSDM, or IDA); and (iv) the size and the hydration degree (none to full coverage) of titania nanoclusters.

First, we analyze the role of the MD approach as well as the effect of the density functional choice for computing excitation energies and NACs (Figure 6). When the PBE functional is used to compute NACs, the FFMD trajectory yields faster recombination compared to using the AIMD trajectory (see blue vs red lines in Figure 6e,g), except for $(TiO_2)_4$ (blue vs red lines, Figure 6a). This trend is reversed when the hybrid B3LYP functional is used to compute NACs (green vs black lines, Figure 6a,e,g). These differences are more pronounced when computed population relaxation is fast such as in when the FSSH method is used (Figure 6a,c,e,g). The differences diminish when decoherence corrections are included and the dynamics is slower, such when the mSDM method is used (Figure 6 panels b, d, f, h). The fast FSSH-based dynamics is controlled by the coherent evolution of electronic states and is strongly affected by the NAC values, which are very sensitive to the details of nuclear motion. Hence, different methods of MD trajectory generation may yield noticeable differences, although the direction of these differences depends on the particularities of the functional used to compute NACs. On the contrary, when methods that account for decoherence, such the mSDM, are used the dynamics is controlled strongly by the fluctuations of the energy gap. Such fluctuations are less sensitive to details of nuclear dynamics, resulting in the observed smaller sensitivity of the population dynamics to the nuclear trajectories. Finally, the difference in population dynamics computed along differently generated guiding trajectories diminishes in more hydrated clusters, which can

https://doi.org/10.1021/acs.jpcc.4c07180
J. Phys. Chem. C XXXX, XXX, XXX−XXX

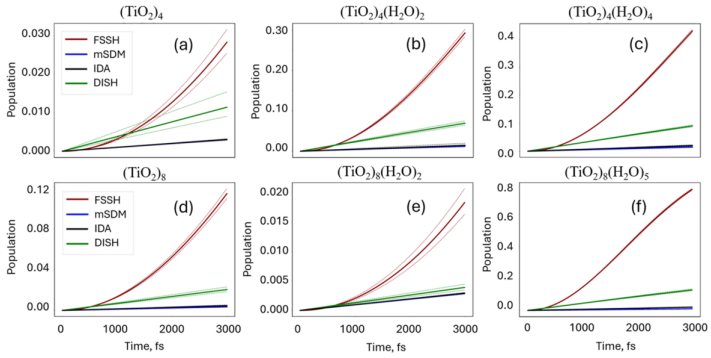

Figure 7. Evolution of the ground state S_0 population for classical FFMD and AIMD nuclear trajectories and fixed PBE functional as the underlying functional for computing the TD-DFT excitations. (a–c) and (d–f) panels illustrate $(TiO_2)_4$ and $(TiO_2)_8$ cluster in their anhydrous and hydrated counterparts. Red, blue, green, and black colored lines represent FSSH, mSDM, DISH and IDA TSH schemes, respectively. The average population for each case is shown in bold lines, whereas dashed lines account for the error bars at each NA-MD time step.

Table 1. Ground State (S_0) Recovery Times, ps, for the Six Cluster Systems Computed with Various Combinations of Guiding Trajectory Generation Method (FFMD—Top of Each Cell or AIMD—Bottom of Each Cell), NAC-Calcuations Method (TDDFT with PBE, PBE0, or B3LYP Functionals), and TSH Algorithms (FSSH, mSDM, IDA, or DISH)

method\system	$(TiO_2)_4$	$(TiO_2)_4(H_2O)_2$	$(TiO_2)_4(H_2O)_4$	$(TiO_2)_8$	$(TiO_2)_8(H_2O)_2$	$(TiO_2)_8(H_2O)_5$
PBE/FSSH	17.7 ± 1.0	5.1 ± 0.1	4.0 ± 0.0	8.6 ± 2.0	22.1 ± 1.3	2.5 ± 0.0
	15.3 ± 0.7	4.9 ± 0.1	4.2 ± 0.1	14.1 ± 0.5	8.3 ± 0.2	4.6 ± 0.1
PBE/mSDM	1013.2 ± 31.7	238.9 ± 36.7	204.1 ± 19.5	859.5 ± 85.0	1055.3 ± 16.8	294.2 ± 52.6
	981.6 ± 42.8	532.8 ± 96.0	327.0 ± 70.0	1018.0 ± 37.0	974.4 ± 60.7	469.26 ± 63.6
PBE/IDA	987.2 ± 57.6	205.5 ± 54.0	149.5 ± 18.6	657.0 ± 95.6	1024.1 ± 35.5	145.7 ± 18.6
	871.6 ± 93.1	338.4 ± 73.3	202.3 ± 53.0	923.5 ± 82.3	31.4 ± 82.4	203.7 ± 31.3
PBE/DISH	261.9 ± 68.6	41.8 ± 3.3	31.6 ± 1.3	146.0 ± 16.5	769.4 ± 94.7	21.8 ± 1.1
	67.7 ± 5.0	37.0 ± 1.5	27.6 ± 1.2	588.9 ± 104.0	194.0 ± 51.0	40.5 ± 18.0
PBE0/FSSH	11.8 ± 0.3	3.2 ± 0.0	3.4 ± 0.0	7.5 ± 0.2	18.2 ± 1.1	2.6 ± 0.1
	6.8 ± 0.1	4.9 ± 0.1	3.4 ± 0.0	8.0 ± 0.2	7.5 ± 0.2	4.4 ± 0.1
PBE0/mSDM	1014.6 ± 44.9	241.8 ± 47.2	166.7 ± 21.7	947.0 ± 64.1	1013.7 ± 49.9	128.3 ± 14.2
	511.8 ± 100.7	305.9 ± 58.6	220.3 ± 25.2	969.0 ± 52.4	718.3 ± 109.3	165.3 ± 36.7
PBE0/IDA	959.5 ± 47.7	140.7 ± 17.9	122.1 ± 23.7	907.0 ± 83.7	974.5 ± 55.0	82.5 ± 10.4
	283.6 ± 54.3	162.4 ± 21.6	107.1 ± 8.4	495.6 ± 76.6	440.6 ± 98.5	97.5 ± 11.0
PBE0/DISH	205.1 ± 27.1	57.2 ± 3.4	65.4 ± 5.6	179.2 ± 31.0	871.6 ± 79.6	45.6 ± 3.1
	104.00 ± 10.69	86.12 ± 8.67	54.6 ± 4.1	165.4 ± 19.2	112.2 ± 11.5	63.9 ± 6.4
B3LYP/FSSH	18.7 ± 1.2	4.6 ± 0.1	4.2 ± 0.1	25.1 ± 1.7	15.5 ± 1.0	2.9 ± 0.0
	8.2 ± 0.2	4.7 ± 0.1	2.5 ± 0.0	11.9 ± 0.4	9.3 ± 0.3	1.7 ± 0.0
B3LYP/mSDM	1039.04 ± 14.4	175.5 ± 28.0	179.0 ± 22.7	1024.9 ± 31.1	1033.5 ± 31.4	103.1 ± 11.1
	717.8 ± 94.0	313.3 ± 77.0	242.4 ± 35.4	929.3 ± 73.2	801.5 ± 99.9	135.0 ± 20.7
B3LYP/IDA	1004.7 ± 48.7	129.4 ± 15.9	112.8 ± 7.9	1032.7 ± 31.0	986.5 ± 43.7	67.2 ± 5.5
	416.5 ± 81.9	174.2 ± 28.0	129.0 ± 11.8	27.8 ± 73.2	587.7 ± 95.1	85.5 ± 9.3
B3LYP/DISH	246.6 ± 52.8	45.9 ± 4.2	58.3 ± 3.2	700.4 ± 83.3	686.5 ± 93.3	23.0 ± 1.3
	98.0 ± 7.6	123.3 ± 12.3	50.0 ± 3.2	212.0 ± 39.9	157.1 ± 18.3	28.7 ± 1.2

be attributed to the smaller differences in NACs and excitation energy values, as shown in Figure 4.

Second, the recombination rates computed using hybrid density functionals are generally increased compared to those computed using the semilocal PBE functional (see Figure 6 and Table 1). A plausible reason for this effect resides in the distribution of NAC values (Figure 5). The smaller NAC values are more frequently sampled when computed using the PBE functional. On the contrary, it is more probable to encounter larger NACs in the dynamics when NACs are computed using hybrid functionals. Thus, the time scales computed with hybrid functionals are generally smaller than the PBE-based counterparts, which are overestimated, $\tau_{PBE} > \tau_{PBE0} \approx \tau_{B3LYP}$. This order of the time scales is observed, with a few exceptions, for all TSH methodologies (Table 1). We stress once again that this effect stems from the multiconfigurational nature of TD-DFT states, where hybrid functionals favor higher configurational mixing and increased

https://doi.org/10.1021/acs.jpcc.4c07180
J. Phys. Chem. C XXXX, XXX, XXX−XXX

Table 2. Transition Dipole Moment ($\times 10^2$) between S_0 and S_1 for All Titania Systems as Computed with Different Approaches. Units are Expressed in 0.01 a.u

method\system	$(TiO_2)_4$	$(TiO_2)_4(H_2O)_2$	$(TiO_2)_4(H_2O)_4$	$(TiO_2)_8$	$(TiO_2)_8(H_2O)_2$	$(TiO_2)_8(H_2O)_5$
AIMD/TD-PBE	5.28 ± 2.97	8.32 ± 2.92	12.61 ± 5.71	9.44 ± 3.55	12.32 ± 0.20	8.81 ± 3.97
AIMD/TD-PBE0	2.82 ± 1.29	6.68 ± 2.24	7.75 ± 3.73	9.32 ± 2.42	6.59 ± 1.87	7.64 ± 2.72
AIMD/TD-B3LYP	4.21 ± 1.84	9.07 ± 3.03	9.35 ± 3.87	11.20 ± 3.67	8.51 ± 2.32	8.22 ± 2.96
FFMD/TD-PBE	6.63 ± 3.60	5.52 ± 2.70	8.00 ± 3.75	13.21 ± 6.67	9.10 ± 3.28	9.66 ± 3.65
FFMD/TD-PBE0	2.91 ± 1.24	4.68 ± 2.10	5.67 ± 2.76	6.66 ± 2.60	5.35 ± 1.83	6.70 ± 2.72
FFMD/TD-B3LYP	4.10 ± 1.30	7.45 ± 2.92	6.11 ± 2.97	7.67 ± 2.85	5.37 ± 1.97	7.81 ± 2.91

Table 3. Computed Radiative Recombination Lifetimes for All Systems; Units are expreesed in μs[a]

method\system	$(TiO_2)_4$	$(TiO_2)_4(H_2O)_2$	$(TiO_2)_4(H_2O)_4$	$(TiO_2)_8$	$(TiO_2)_8(H_2O)_2$	$(TiO_2)_8(H_2O)_5$
AIMD/TD-PBE	19.85	2.96	1.32	7.63	2.98	3.31
AIMD/TD-PBE0	22.77	2.05	1.50	2.08	3.31	1.75
AIMD/TD-B3LYP	12.91	1.31	1.25	1.87	2.50	1.85
FFMD/TD-PBE	41.28	7.01	2.81	23.95	18.82	3.16
FFMD/TD-PBE0	40.69	4.84	2.68	11.25	10.40	2.53
FFMD/TD-B3LYP	29.70	2.22	2.71	18.54	14.22	2.32

[a]The calculations are conducted for trajectories obtained via FFMD or AIMD and with different excited state calculation methods (TD-DFT with PBE, PBE0, or B3LYP functionals).

NAC magnitudes. This effect is contrary to the NAC decrease between molecular orbitals in the single-particle picture reported ealier.[93]

Third, we discuss the dependence of the recombination time scales on the TSH approaches. In general, the following order of the time scales is observed for nearly all titania systems, density functionals, and MD trajectories: $\tau_{mSDM} \geq \tau_{IDA} > \tau_{DISH(rev\ 2023)} > \tau_{FSSH}$ (see Table 1). This order is consistent with the previous assessments.[47,48,103,121,122] Among these approaches, the mSDM is perhaps the most conceptually sound and is sensitive to the details of energy gap evolution.[85] The decoherence correction generally inhibits the recombination comparing to the overcoherent FSSH description. For instance, for the $(TiO_2)_4$ system, the FSSH values vary in the 5−20 ps interval depending on the electronic structure and trajectory generation methodologies used, while the mSDM values vary in the 900−1100 ps interval. The IDA time scales are often comparable to, but usually smaller than, the mSDM values. Note that, for the same $(TiO_2)_4$ system, the IDA values vary in the 200−1000 ps interval. The former method introduces strong decoherence correction via the wave function collapse on the currently active state. Since the collapse is controlled by the hop feasibility criterion, the IDA decoherence correction is weak when the process is fast and, thus, the decoherence is consistent with the state transitions. In such situations, the IDA time scales may be comparable to the FSSH counterparts. The 2023 revision of the DISH algorithm introduces decoherence in a gradual way resembling that of the mSDM. In this approach, the superposition is either projected onto the decohered (pointer) state or such state is projected out of the coherent superposition. The surface hops are determined as in the regular FSSH. Since the stochastic wave function "diffusion" only partially affects the quantum populations of all states, the DISH_rev2023 results are often close to the FSSH, although such time scales may also be notably slower than in FSSH.

Finally, we observe a relatively faster recombination dynamics when increasing the hydration degree on the surface of titania nanoclusters (see Table 1 and Figure 7). This observation holds for nearly all nanoclusters, density functionals and TSH methodologies. Such an acceleration correlates with the trends in average NAC values (see Figure 4c,d). Indeed, Figure 4 shows that the average NAC values increase with the hydration degree as discussed earlier. Analogously, the carrier lifetimes gradually decrease as the amount of incorporated water increases (Figure 7 and Table 1). The most notable deviation from this monotonic dependence is observed for the $(TiO_2)_8(H_2O)_2$ system with the FF-based trajectory (Figure 7e and Table 1), which shows a notably slower recovery dynamics compared to the systems with lower and higher water saturation. This could be associated with the low water coverage (~25%), which is closer to the anhydrous $(TiO_2)_8$ cluster. Indeed, both systems show similar lifetimes (see Table 1). Importantly, this analysis suggests that weakly hydrated systems could be preferred for water splitting purposes, as they promote longer electron−hole recombination times which tends to enhance thephotocatalytic efficiency.

The nonradiative recombination rates computed using DISH are consistent with the previously reported values for larger $(TiO_2)_{35}$ clusters using the same TSH algorithm.[41,42] Previous time-resolved photoelectron spectroscopy (TRPES) measurements on single-crystal surfaces of anatase and rutile TiO_2 estimate the recombination times to be on the order of nanosecond,[123] which is in line with the slower recombination rates we obtain for anhydrous clusters (when accounting for electronic decoherence with the IDA or mSDM schemes). Recently the pump−probe spectroscopy experiments on bare and stoichiometric $(TiO_2)_n$ (n = 4, and 8) nanoclusters have been reported by Sayres and coauthors. The proposed rationalization of the reported measurements suggested than S_1 decay times to be on the sub-picosecond order.[37] Such interpretation disagrees with our current estimates of the nonradiative recombination time scales being off by orders of magnitude. While acknowledging the value of the experimental data, our current calculations suggest an alternative interpretation of these measurements. It is possible that these remarkably fast decay times may be indicative of an ultrafast relaxation from higher excited states to optically forbidden (dark) levels, rather than representing the carrier recombina-

https://doi.org/10.1021/acs.jpcc.4c07180
J. Phys. Chem. C XXXX, XXX, XXX−XXX

tion process between the first excited and the ground state. This could be in agreement with the different order of magnitude in the lifetimes: excited state relaxation in the experimental work (with sub-ps time scales) versus lowest excited state decay studied in this work (with sub-ns time scales).

3.4. Radiative Recombination. While the previous section has extensively analyzed nonradiative recombination processes, which, due to their influence on charge carrier dynamics and efficiency, are often dominant in titania nanoparticles, it is instructional to consider the contribution of radiative recombination, which is crucial for applications where photoluminescence, light emission, or optical properties are the key performance indicators. Our calculations of the transition dipole moments (TDM) and corresponding radiative lifetimes are summarized in Tables 2 and 3, respectively. Expectedly, the computed radiative lifetimes are orders of magnitude larger compared to the nonradiative recombination ones and reach microsecond (μs) scales. Thus, the deactivation of excited states in bare and hydrated titania nanoclusters is dominated by the nonradiative recombination mechanisms.

Although we consider only a limited number of systems, we do observe several notable trends. First, for the bare nanoclusters, the radiative recombination is faster in the larger $(TiO_2)_8$ nanocluster than in the smaller one, $(TiO_2)_4$ (Table 3). This effect can be attributed to a sizable difference of the TDMs, which are larger in $(TiO_2)_8$ than in $(TiO_2)_4$ by a factor of 2−3 (Table 2), leading to the expected 4−9-fold acceleration due to the quadratic dependence of radiative recombination time scales on the TDM magnitude. The larger TDMs in the larger nanoclusters can be attributed to a greater capability for holes and electrons to separate spatially in the larger nanoclusters and hence create a larger dipole. While the actual ratio $\tau_{(TiO_2)_8}/\tau_{(TiO_2)_4}$ varies from 3 to 11 for the calculations involving DFT-based guiding trajectories, in agreement with the expectation, it is smaller for the FF-based guiding trajectories and varies between 2 and 4. This discrepancy can be attributed to the respective energy gap differences (entering the time scales formula, eq 2 cubically). While for the DFT-based trajectories, the difference of energy gaps for the two systems is negligible, the gaps obtained from the FF-based trajectories vary more notably across the two systems. This effect slows down the recombination in larger nanoclusters to a greater extent than in the smallest one, acting in the opposite way to the TDM and hence reducing the differences caused by the TDM differences. However, this effect is still dominated by the large difference in TDMs, leading to the overall acceleration of the radiative recombination in larger nanoclusters.

The second trend we observe is a gradual acceleration of the radiative recombination in the hydrated nanoclusters. As observed from Table 3, the acceleration generally correlates with the degree of hydration, although this trend may be violated for even larger hydrated nanoclusters not considered in this work. The general acceleration of the radiative recombination can be attributed mainly to the increase of the energy gap. This increase is nearly monotonic for progressively hydrated $(TiO_2)_4$ and $(TiO_2)_8$ systems. In addition, for $(TiO_2)_4$ systems, the TDM systematically increases with the degree of hydration, leading to a clear trend in computed radiative recombination time scales. For hydrated $(TiO_2)_8$ systems, there is no clear trend in the TDM as a function of hydration degree. Thus, the dependence of the radiative recombination time scales on the hydration degree is less pronounced for these systems—a notable decrease of the recombination time is observed only while moving from $(TiO_2)_8(H_2O)_2$ to $(TiO_2)_8(H_2O)_5$.

Another set of notable observations concerns the dependence of the computed recombination time scales on the combination of methods used. First, the use of the FFs for generating guiding nuclear trajectories leads to the 2−3-fold larger radiative recombination time scales compared to those obtained from the DFT-based AIMD guiding trajectories. As follows from Figure 4a,b, the FF-based trajectories show notably smaller energy gaps compared to the AIMD counterpart, although this difference decreases with the increased surface hydration degree. Consequently, smaller energy gaps lead to slower radiative recombination and hence larger radiative recombination times. As the difference of the excitation energies predicted by different methods decreases for more hydrated clusters, the radiative lifetimes become more robust with respect to the choice of the guiding trajectory generation approach. Finally, the use of PBE, PBE0, or B3LYP functionals does not greatly affect the results as far as the computations of radiative recombination times is concerned.

As presented in the previous section, nonradiative recombination processes in titania nanoclusters occur on a time scale of nanoseconds, significantly affecting the charge carrier dynamics by quickly removing the electron−hole pairs. In contrast, our analysis of radiative recombination shows that these processes occur at much slower rates, typically on the order of microseconds. The dominance of nonradiative recombination suggests that the majority of excited states decay through these nonradiative mechanisms, leaving only a small fraction of electron−hole pairs available for photon emission. Consequently, the observed photoluminescence and other radiative outputs are relatively weak, which aligns with prior studies.[124]

4. CONCLUSIONS

In this work, we present a comprehensive computational characterization of the radiative and nonradiative recombination dynamics in a series of small bare and hydrated titania nanoclusters: $(TiO_2)_n(H_2O)_m$ for n = 4 and 8. We find that increasing the degree of hydration tends to accelerate both radiative and nonradiative relaxation processes. The acceleration of nonradiative relaxation is attributed to the stronger influence of hydroxyl group vibrations, which significantly perturb the electronic states. In this way, the increasing delocalization and isotropy of the charge distribution in increasingly hydrated nanoclusters facilitate orbital degeneracies, enhancing nonadiabatic couplings and thus nonradiative recombination rates. The nonadiabatic couplings are found to linearly increase with the degree of hydration in the smaller $(TiO_2)_4(H_2O)_m$ nanoclusters and linearly increase after an initial plateau in the larger $(TiO_2)_8(H_2O)_m$ nanoclusters. This also indicates the diminishing influence of hydration in larger systems. Faster radiative recombination in more highly hydrated systems is rationalized by the increased excitation energy of such systems. Interestingly, our calculations predict faster radiative recombination in the bare $(TiO_2)_8$ cluster compared to its smaller counterpart, $(TiO_2)_4$. We attribute this difference to the larger electron−hole separation in the bare

https://doi.org/10.1021/acs.jpcc.4c07180
J. Phys. Chem. C XXXX, XXX, XXX−XXX

$(TiO_2)_8$ cluster, which creates a larger transition dipole moment, hence stimulating the radiative recombination.

We find that the nonradiative $S_1 \rightarrow S_0$ transition is driven primarily by the vibrational modes in the 500−1000 cm^{-1} range which typically correspond to Ti−O−Ti angle bending and related modes. Based on the results of our nonradiative recombination calculation in the studied titania nanoclusters, we suggest that the time scales reported in the recent experimental work on similar-sized TiO_2 nanoclusters by Garcia et al.[37] is more likely to be attributed to the relaxation of higher excited states rather than to the electron−hole recombination process.

Finally, this work reports a detailed comparative analysis of various methodological choices possible for such dynamical calculations. We find that, for all studied systems, the dependence of the computed nonradiative and radiative time scales on the choice of the density functional used in the TD-DFT/NA-MD calculations is relatively weak. On the other hand, the nonradiative time scales are strongly dependent on the choice of the TSH approach: they are normally orders of magnitude larger when decoherence corrected methods such as mSDM, IDA, or DISH are used compared to those obtained with methods lacking such correction, such as FSSH. The time scales obtained with decoherence-corrected methods are in good agreement with previous findings for similar systems. We also find a notable dependence of both radiative and nonradiative time scales on the method used to obtain the guiding MD trajectory. The presently employed titania FFs favor more symmetrical structures and vibrational modes compared to those in the DFT-based AIMD trajectories. As a result, the excitation energies for titania nanocluster trajectories obtained with these FFs are systematically underestimated with respect to those derived from AIMD trajectories, leading both to faster nonradiative recombination and to slower radiative recombination, especially in bare titania clusters. The reported differences are less pronounced in the hydrated systems, where both approaches lead to more consistent time scales. We argue that the limitations of the FFs can be addressed with improved parametrizations, in which case FFs may become a computationally efficient alternative to direct AIMD simulations, especially for larger nanoclusters.

■ ASSOCIATED CONTENT

Data Availability Statement

Detailed scripts and input files used for all types of calculations are available in digital form online at Zenodo server.[125]

Supporting Information

The Supporting Information is available free of charge at https://pubs.acs.org/doi/10.1021/acs.jpcc.4c07180.

Details on the power and influence spectra for $(TiO_2)_4$, TD-PBE0, and TD-B3LYP MO isosurfaces, squares of the largest CI coefficient for S_1, total dipole moments of S_0/S_1 states, first excited state energies, nonadiabatic couplings between S_0 and S_1, and S_0 population evolution for all clusters and methodologies (PDF)

■ AUTHOR INFORMATION

Corresponding Authors

Ángel Morales-García − *Departament de Ciència de Materials i Química Física & Institut de Química Teòrica i Computacional (IQTCUB), Universitat de Barcelona, 08028 Barcelona, Spain;* orcid.org/0000-0003-0491-1234; Email: angel.morales@ub.edu

Alexey V. Akimov − *Department of Chemistry, University at Buffalo, The State University of New York, Buffalo, New York 14260, United States;* orcid.org/0000-0002-7815-3731; Email: alexeyak@buffalo.edu; @AkimovLab

Stefan T. Bromley − *Departament de Ciència de Materials i Química Física & Institut de Química Teòrica i Computacional (IQTCUB), Universitat de Barcelona, 08028 Barcelona, Spain; Institució Catalana de Recerca i Estudis Avançats (ICREA), 08010 Barcelona, Spain;* orcid.org/0000-0002-7037-0475; Email: s.bromley@ub.edu

Authors

Miguel Recio-Poo − *Departament de Ciència de Materials i Química Física & Institut de Química Teòrica i Computacional (IQTCUB), Universitat de Barcelona, 08028 Barcelona, Spain*

Mohammad Shakiba − *Department of Chemistry, University at Buffalo, The State University of New York, Buffalo, New York 14260, United States;* orcid.org/0000-0002-4110-7627

Francesc Illas − *Departament de Ciència de Materials i Química Física & Institut de Química Teòrica i Computacional (IQTCUB), Universitat de Barcelona, 08028 Barcelona, Spain;* orcid.org/0000-0003-2104-6123

Complete contact information is available at: https://pubs.acs.org/10.1021/acs.jpcc.4c07180

Notes

The authors declare no competing financial interest.

■ ACKNOWLEDGMENTS

M.R.-P., F.I., S.T.B., and Á.M.-G. thank the financial support from MCIN/AEI/10.13039/501100011033 through projects PID2020-115293RJ-I00, PID2021-126076NB-I00, PID2021-127957NB-100, TED2021-129506B-C22, TED2021-132550B-C22, and the *María de Maeztu* CEX2021-001202-M project and from the *Generalitat de Catalunya* through the projects 2021-SGR-00079 and 2021-SGR-00354. *Red de investigación* RED2022-134295-T (FOTOFUEL) is also partly acknowledged. The reported research is also involved in the European Cooperation in Science and Technology (COST) Actions: CA18234 (CompNanoEnergy) and CA21101 (COSY). M.R.-P. acknowledges the *Ministerio de Ciencia e Innovación* (MICIN) for a *Formación Personal Investigador* (FPI) fellowship (PRE2019-087627). M.R.-P., F.I., S.T.B., and A.M.G. also thank the *Red Española de Supercomputación* (RES) for the provision of supercomputing time. M.S. and A.V.A. acknowledge the financial support of the National Science Foundation (Grant NSF-2045204). Computational support is provided by the Center for Computational Research at the University at Buffalo.

■ REFERENCES

(1) Lewis, N. S. Research opportunities to advance solar energy utilization. *Science* **2016**, *351* (6271), No. aad1920.

(2) Hota, P.; Das, A.; Maiti, D. K. A short review on generation of green fuel hydrogen through water splitting. *Int. J. Hydrogen Energy* **2023**, *48* (2), 523−541.

(3) Tan, H. L.; Abdi, F. F.; Ng, Y. H. Heterogeneous photocatalysts: an overview of classic and modern approaches for optical, electronic,

and charge dynamics evaluation. *Chem. Soc. Rev.* **2019**, *48* (5), 1255−1271.
(4) Balapure, A.; Dutta, J. R.; Ganesan, R. Recent advances in semiconductor heterojunctions: a detailed review of the fundamentals of photocatalysis, charge transfer mechanism and materials. *RSC Appl. Interfaces* **2024**, *1* (1), 43−69.
(5) Wang, H.; Li, X.; Zhao, X.; Li, C.; Song, X.; Zhang, P.; Huo, P.; Li, X. A review on heterogeneous photocatalysis for environmental remediation: From semiconductors to modification strategies. *Chin. J. Catal.* **2022**, *43* (2), 178−214.
(6) Nijamudheen, A.; Akimov, A. V. Quantum Dynamics Effects in Photocatalysis. In *Visible-Light-Active Photocatalysis: Nanostructured Catalyst Design, Mechanisms, and Applications*; Ghosh, S., Ed.; Wiley-VCH Verlag Gmbh & Co. KGaA: Weinheim, 2018; pp 527−566.
(7) Djurišić, A. B.; He, Y.; Ng, A. Visible-light photocatalysts: Prospects and challenges. *APL Mater.* **2020**, *8* (3), No. 030903.
(8) Ibhadon, A. O.; Fitzpatrick, P. Heterogeneous photocatalysis: recent advances and applications. *Catalysts* **2013**, *3*, 189−218.
(9) Schneider, J.; Matsuoka, M.; Takeuchi, M.; Zhang, J.; Horiuchi, Y.; Anpo, M.; Bahnemann, D. W. Understanding TiO_2 photocatalysis: mechanisms and materials. *Chem. Rev.* **2014**, *114*, 9919−9986.
(10) Kumaravel, V.; Mathew, S.; Bartlett, J.; Pillai, S. C. Photocatalytic hydrogen production using metal doped TiO_2: A review of recent advances. *Appl. Catal., B* **2019**, *244*, 1021−1064.
(11) Ardo, S.; Meyer, G. J. Photodriven heterogeneous charge transfer with transition-metal compounds anchored to TiO_2 semiconductor surfaces. *Chem. Soc. Rev.* **2009**, *38*, 115−164.
(12) Bai, Y.; Mora-Seró, I.; De Angelis, F.; Bisquert, J.; Wang, P. Titanium dioxide nanomaterials for photovoltaic applications. *Chem. Rev.* **2014**, *114*, 10095−10130.
(13) Valero, R.; Morales-Garcia, A.; Illas, F. Theoretical modeling of electronic excitations of gas-phase and solvated TiO_2 nanoclusters and nanoparticles of interest in photocatalysis. *J. Chem. Theory Comput.* **2018**, *14*, 4391−4404.
(14) Akimov, A. V.; Neukirch, A. J.; Prezhdo, O. V. Theoretical insights into photoinduced charge transfer and catalysis at metal oxide surfaces. *Chem. Rev.* **2013**, *113*, 4496.
(15) Dahl, M.; Liu, Y.; Yin, Y. Composite titanium dioxide nanomaterials. *Chem. Rev.* **2014**, *114* (19), 9853−9889.
(16) Pagliaro, M.; Palmisano, G.; Ciriminna, R.; Loddo, V. Nanochemistry aspects of titania in dye-sensitized solar cells. *Energy Environ. Sci.* **2009**, *2*, 838−844.
(17) Adachi, M.; Murata, Y.; Takao, J.; Jiu, J.; Sakamoto, M.; Wang, F. Highly efficient dye-sensitized solar cells with a titania thin-film electrode composed of a network structure of single-crystal-like TiO_2 nanowires made by the "oriented attachment" mechanism. *J. Am. Chem. Soc.* **2004**, *126*, 14943−14949.
(18) Prasad, R. M. B.; Pathan, H. M. Effect of photoanode surface coverage by a sensitizer on the photovoltaic performance of titania based CdS quantum dot sensitized solar cells. *Nanotechnology* **2016**, *27*, No. 145402.
(19) Akhter, P.; Arshad, A.; Saleem, A. M.; Hussain, M. Recent development in non-metal-doped titanium dioxide photocatalysts for different dyes degradation and the study of their strategic factors: A review. *Catalysts* **2022**, *12*, 1331.
(20) Wang, X.; Sun, M.; Murugananthan, M.; Zhang, Y.; Zhang, L. Electrochemically self-doped WO_3/TiO_2 nanotubes for photocatalytic degradation of volatile organic compounds. *Appl. Catal., B* **2020**, *260*, No. 118205.
(21) Hassan, S. M.; Ahmed, A. I.; Mannaa, M. A. Preparation and characterization of SnO_2 doped TiO_2 nanoparticles: Effect of phase changes on the photocatalytic and catalytic activity. *J. Sci.: Adv. Mater. Devices* **2019**, *4*, 400−412.
(22) Fu, Y. S.; Li, J.; Li, J. Metal/semiconductor nanocomposites for photocatalysis: fundamentals, structures, applications and properties. *Nanomaterials* **2019**, *9*, 359.
(23) Yang, H. G.; Sun, C. H.; Qiao, S. Z.; Zou, J.; Liu, G.; Smith, S. C.; Cheng, H. M.; Lu, G. Q. Anatase TiO2 single crystals with a large percentage of reactive facets. *Nature* **2008**, *453*, 638−641.
(24) Liu, G.; Jimmy, C. Y.; Lu, G. Q. M.; Cheng, H. M. Crystal facet engineering of semiconductor photocatalysts: motivations, advances, and unique properties. *Chem. Commun.* **2011**, *47*, 6763−6783.
(25) Wang, S.; Liu, G.; Wang, L. Crystal facet engineering of photoelectrodes for photoelectrochemical water splitting. *Chem. Rev.* **2019**, *119*, 5192−5247.
(26) Morales-García, Á.; Escatllar, A. M.; Illas, F.; Bromley, S. T. Understanding the interplay between size, morphology and energy gap in photoactive TiO_2 nanoparticles. *Nanoscale* **2019**, *11*, 9032−9041.
(27) Mino, L.; Morales-García, Á.; Bromley, S. T.; Illas, F. Understanding the nature and location of hydroxyl groups on hydrated titania nanoparticles. *Nanoscale* **2021**, *13*, 6577−6585.
(28) Recio-Poo, M.; Morales-García, Á.; Illas, F.; Bromley, S. T. Crystal properties without crystallinity? Influence of surface hydroxylation on the structure and properties of small TiO2 nanoparticles. *Nanoscale* **2023**, *15*, 4809−4820.
(29) García-Romeral, N.; Keyhanian, M.; Morales-Garcia, A.; Viñes, F.; Illas Riera, F. Understanding the Chemical Bond in Semiconductor/MXene Composites: TiO_2 Clusters Anchored on the Ti_2C MXene Surface. *Chem. − Eur. J.* **2024**, *30*, No. e202400255.
(30) Alls, M.; Remesal, E. R.; Illas, F.; Morales-García, Á. Structural and Electronic Properties of Metal/Oxide Nanostructures from First-Principles: Ru_{13} Supported on $(TiO_2)_{84}$ as a Case Study. *Adv. Theory Simul.* **2023**, *6*, No. 2200670.
(31) Remesal, E. R.; Morales-García, Á. Carbon-doped anatase titania nanoparticles: similarities and differences with respect to bulk and extended surface models. *Phys. Chem. Chem. Phys.* **2022**, *24*, 21381−21387.
(32) Remesal, E. R.; Morales-García, Á.; Illas, F. Role of N Doping in the Reduction of Titania Nanostructures. *J. Phys. Chem. C* **2023**, *127*, 20128−20136.
(33) Morales-García, Á.; Viñes, F.; Sousa, C.; Illas, F. Toward a Rigorous Theoretical Description of Photocatalysis Using Realistic Models. *J. Phys. Chem. Lett.* **2023**, *14*, 3712−3720.
(34) Bao, J.; Yu, Z.; Gundlach, L.; Benedict, J. B.; Coppens, P.; et al. Excitons and excess electrons in nanometer size molecular polyoxotitanate clusters: electronic spectra, exciton dynamics, and surface states. *J. Phys. Chem. B* **2013**, *117*, 4422−4430.
(35) Bao, J.; Gundlach, L.; Yu, Z.; Benedict, J. B.; Snoeberger, R. C., III; et al. Hot hole hopping in a polyoxotitanate cluster terminated with catechol electron donors. *J. Phys. Chem. C* **2016**, *120*, 20006−20015.
(36) Obara, Y.; Ito, H.; Ito, T.; Kurahashi, N.; Thürmer, S.; et al. Femtosecond time-resolved X-ray absorption spectroscopy of anatase TiO_2 nanoparticles using XFEL. *Struct. Dyn.* **2017**, *4*, No. 044033.
(37) Garcia, J. M.; Heald, L. F.; Shaffer, R. E.; Sayres, S. G. Oscillation in Excited State Lifetimes with Size of Sub-nanometer Neutral $(TiO_2)_n$ Clusters Observed with Ultrafast Pump−Probe Spectroscopy. *J. Phys. Chem. Lett.* **2021**, *12*, 4098−4103.
(38) Berardo, E.; Hu, H. S.; Shevlin, S. A.; Woodley, S. M.; Kowalski, K.; Zwijnenburg, M. A. Modeling excited states in TiO_2 nanoparticles: on the accuracy of a TD-DFT based description. *J. Chem. Theory Comput.* **2014**, *10*, 1189−1199.
(39) Cho, D.; Ko, K. C.; Lamiel-Garcia, O.; Bromley, S. T.; Lee, J. Y.; Illas, F. Effect of size and structure on the ground-state and excited-state electronic structure of TiO_2 nanoparticles. *J. Chem. Theory Comput.* **2016**, *12*, 3751−3763.
(40) Valero, R.; Morales-García, Á.; Illas, F. Investigating the character of excited states in TiO_2 nanoparticles from topological descriptors: implications for photocatalysis. *Phys. Chem. Chem. Phys.* **2020**, *22*, 3017−3029.
(41) Nam, Y.; Li, L.; Lee, J. Y.; Prezhdo, O. V. Size and shape effects on charge recombination dynamics of TiO_2 nanoclusters. *J. Phys. Chem. C* **2018**, *122*, 5201−5208.
(42) Nam, Y.; Li, L.; Lee, J. Y.; Prezhdo, O. V. Strong influence of oxygen vacancy location on charge carrier losses in reduced TiO_2 nanoparticles. *J. Phys. Chem. Lett.* **2019**, *10*, 2676−2683.

https://doi.org/10.1021/acs.jpcc.4c07180
J. Phys. Chem. C XXXX, XXX, XXX−XXX

(43) Sousa, C.; Tosoni, S.; Illas, F. Theoretical approaches to excited-state-related phenomena in oxide surfaces. *Chem. Rev.* **2013**, *113*, 4456−4495.
(44) Livraghi, S.; Paganini, M. C.; Giamello, E.; Selloni, A.; Di Valentin, C.; Pacchioni, G. Origin of photoactivity of nitrogen-doped titanium dioxide under visible light. *J. Am. Chem. Soc.* **2006**, *128*, 15666−15671.
(45) Migani, A.; Blancafort, L. What controls photocatalytic water oxidation on rutile TiO_2 (110) under ultra-high-vacuum conditions? *J. Am. Chem. Soc.* **2017**, *139*, 11845−11856.
(46) Jiang, X.; Zheng, Q.; Lan, Z.; Saidi, W. A.; Ren, X.; Zhao, J. Real-time GW-BSE investigations on spin-valley exciton dynamics in monolayer transition metal dichalcogenide. *Sci. Adv.* **2021**, *7*, No. eabf3759.
(47) Smith, B.; Shakiba, M.; Akimov, A. V. Nonadiabatic dynamics in Si and CdSe nanoclusters: many-body vs single-particle treatment of excited states. *J. Chem. Theory Comput.* **2021**, *17*, 678−693.
(48) Smith, B.; Shakiba, M.; Akimov, A. V. Crystal symmetry and static electron correlation greatly accelerate nonradiative dynamics in lead halide perovskites. *J. Phys. Chem. Lett.* **2021**, *12*, 2444−2453.
(49) Levine, B. G.; Ko, C.; Quenneville, J.; Martínez, T. J. Conical intersections and double excitations in time-dependent density functional theory. *Mol. Phys.* **2006**, *104*, 1039−1051.
(50) Liu, W.; Settels, V.; Harbach, P. H.; Dreuw, A.; Fink, R. F.; Engels, B. Assessment of TD-DFT-and TD-HF-based approaches for the prediction of exciton coupling parameters, potential energy curves, and electronic characters of electronically excited aggregates. *J. Comput. Chem.* **2011**, *32*, 1971−1981.
(51) Zhu, Y.; Long, R. Density Functional Theory Half-Electron Self-Energy Correction for Fast and Accurate Nonadiabatic Molecular Dynamics. *J. Phys. Chem. Lett.* **2021**, *12*, 10886−10892.
(52) Perdew, J. P.; Burke, K.; Ernzerhof, M. Generalized gradient approximation made simple. *Phys. Rev. Lett.* **1996**, *77*, 3865.
(53) Shao, Y.; Mei, Y.; Sundholm, D.; Kaila, V. R. Benchmarking the Performance of Time-Dependent Density Functional Theory Methods on Biochromophores. *J. Chem. Theory Comput.* **2020**, *16*, 587−600.
(54) Kretz, B.; Egger, D. A. Accurate non-adiabatic couplings from optimally tuned range-separated hybrid functionals. *J. Chem. Phys.* **2022**, *157*, No. 101104.
(55) Smith, B.; Akimov, A. V. Hot Electron Cooling in Silicon Nanoclusters via Landau-Zener Nonadiabatic Molecular Dynamics: Size Dependence and Role of Surface Termination. *J. Phys. Chem. Lett.* **2020**, *11*, 1456−1465.
(56) Zhang, Z.; He, J.; Long, R. Ultrafast Charge Separation and Recombination across a Molecule/$CsPbBr_3$ Quantum Dot Interface from First-Principles Nonadiabatic Molecular Dynamics Simulation. *J. Phys. Chem. C* **2019**, *123*, 23800−23806.
(57) Fu, J.; Li, M.; Kang, Y.; Yang, K.; Li, H.; Zhang, J.; Ma, W. Water dopant control of structural stability and charge recombination of perovskite solar cells: A first-principles study. *Appl. Surf. Sci.* **2023**, *612*, No. 155794.
(58) Nelson, T.; Fernandez-Alberti, S.; Roitberg, A. E.; Tretiak, S. Nonadiabatic excited-state molecular dynamics: Modeling photophysics in organic conjugated materials. *Acc. Chem. Res.* **2014**, *47*, 1155−1164.
(59) Shakiba, M.; Stippell, E.; Li, W.; Akimov, A. V. Nonadiabatic Molecular Dynamics with Extended Density Functional Tight-Binding: Application to Nanocrystals and Periodic Solids. *J. Chem. Theory Comput.* **2022**, *18*, 5157−5180.
(60) Duncan, W. R.; Prezhdo, O. V. Theoretical studies of photoinduced electron transfer in dye sensitized TiO_2. *Annu. Rev. Phys. Chem.* **2007**, *58*, 143−184.
(61) Zhang, L.; Chu, W.; Zhao, C.; Zheng, Q.; Prezhdo, O. V.; Zhao, J. Dynamics of photoexcited small polarons in transition-metal oxides. *J. Phys. Chem. Lett.* **2021**, *12*, 2191−2198.
(62) Muuronen, M.; Parker, S. M.; Berardo, E.; Le, A.; Zwijnenburg, M. A.; Furche, F. Mechanism of photocatalytic water oxidation on small TiO_2 nanoparticles. *Chem. Sci.* **2017**, *8* (3), 2179−2183.
(63) Rotteger, C. H.; Jarman, C. K.; Sutton, S. F.; Sayres, S. G. Size onset of metallic behavior in neutral aluminum clusters. *Nanoscale* **2024**, *16* (28), 13516−13524.
(64) Rotteger, C. H.; Jarman, C. K.; Sobol, M. M.; Sutton, S. F.; Sayres, S. G. Sub-picosecond photodynamics of small neutral copper oxide clusters. *Phys. Chem. Chem. Phys.* **2024**, *26* (31), 20937−20946.
(65) Rotteger, C. H.; Jarman, C. K.; Sobol, M. M.; Sutton, S. F.; Sayres, S. G. Subpicosecond Dynamics of Rydberg Excitons Produced from Ultraviolet Excitation of Neutral Cuprite (Cu_2O) n Clusters, n < 13. *J. Phys. Chem. A* **2024**, *128* (39), 8466−8472.
(66) Cuko, A.; Escatllar, A. M.; Calatayud, M.; Bromley, S. T. Properties of hydrated TiO_2 and SiO_2 nanoclusters: dependence on size, temperature and water vapour pressure. *Nanoscale* **2018**, *10*, 21518−21532.
(67) Weichman, M. L.; Debnath, S.; Kelly, J. T.; Gewinner, S.; Schöllkopf, W.; Neumark, D. M.; Asmis, K. R. Dissociative water adsorption on gas-phase titanium dioxide cluster anions probed with infrared photodissociation spectroscopy. *Top. Catal.* **2018**, *61*, 92−105.
(68) Yin, S.; Bernstein, E. R. Experimental and theoretical studies of H 2 O oxidation by neutral Ti 2 O 4, 5 clusters under visible light irradiation. *Phys. Chem. Chem. Phys.* **2014**, *16* (27), 13900−13908.
(69) Wang, T. H.; Fang, Z.; Gist, N. W.; Li, S.; Dixon, D. A.; Gole, J. L. Computational study of the hydrolysis reactions of the ground and first excited triplet states of small TiO2 nanoclusters. *J. Phys. Chem. C* **2011**, *115* (19), 9344−9360.
(70) Kasha, M. Characterization of Electronic Transitions in Complex Molecules. *Discuss. Faraday Soc.* **1950**, *9*, 14−19.
(71) Shakiba, M.; Smith, B.; Li, W.; Dutra, M.; Jain, A.; Sun, X.; Garashchuk, S.; Akimov, A. Libra: A Modular Software Library for Quantum Nonadiabatic Dynamics. *Software Impacts* **2022**, *14*, No. 100445.
(72) Akimov, A. V. Libra: An Open-Source "Methodology Discovery" Library for Quantum and Classical Dynamics Simulations. *J. Comput. Chem.* **2016**, *37*, 1626−1649.
(73) Akimov, A. V.; Shakiba, M.; Smith, B.; Dutra, M.; Han, D.; Sato, K.; Temen, S.; Li, W.; Khvorost, T.et al. *Libra v5.7.1*, Zenodo, 2024.
(74) Kühne, T. D.; Iannuzzi, M.; Del Ben, M.; Rybkin, V. V.; Seewald, P.; et al. CP2K: An electronic structure and molecular dynamics software package-Quickstep: Efficient and accurate electronic structure calculations. *J. Chem. Phys.* **2020**, *152*, No. 194103.
(75) Lamiel-Garcia, O.; Cuko, A.; Calatayud, M.; Illas, F.; Bromley, S. T. Predicting size-dependent emergence of crystallinity in nanomaterials: titania nanoclusters versus nanocrystals. *Nanoscale* **2017**, *9*, 1049−1058.
(76) Gale, J. D. GULP: A computer program for the symmetry-adapted simulation of solids. *J. Chem. Soc., Faraday Trans.* **1997**, *93*, 629−637.
(77) Gale, J. D.; Rohl, A. L. The general utility lattice program (GULP). *Mol. Simul.* **2003**, *29*, 291−341.
(78) VandeVondele, J.; Hutter, J. Gaussian basis sets for accurate calculations on molecular systems in gas and condensed phases. *J. Chem. Phys.* **2007**, *127*, No. 114105.
(79) Hartwigsen, C.; Goedecker, S.; Hutter, J. Relativistic separable dual-space Gaussian pseudopotentials from H to Rn. *Phys. Rev. B* **1998**, *58*, 3641.
(80) Grimme, S.; Antony, J.; Ehrlich, S.; Krieg, H. A consistent and accurate ab initio parametrization of density functional dispersion correction (DFT-D) for the 94 elements H-Pu. *J. Chem. Phys.* **2010**, *132*, No. 154104.
(81) Hinuma, Y.; Hayashi, H.; Kumagai, Y.; Tanaka, I.; Oba, F. Comparison of approximations in density functional theory calculations: Energetics and structure of binary oxides. *Phys. Rev. B* **2017**, *96* (9), No. 094102.
(82) Agosta, L.; Brandt, E. G.; Lyubartsev, A. P. Diffusion and reaction pathways of water near fully hydrated TiO2 surfaces from ab

https://doi.org/10.1021/acs.jpcc.4c07180
J. Phys. Chem. C XXXX, XXX, XXX−XXX

initio molecular dynamics. *J. Chem. Phys.* **2017**, *147* (2), No. 024704, DOI: 10.1063/1.4991381.
(83) Fritsch, D. Amorphous Sn-Ti Oxides: A Combined Molecular Dynamics and Density Functional Theory Study. *Phys. Status Solidi A* **2018**, *215* (13), No. 1800071.
(84) Ohto, T.; Dodia, M.; Xu, J.; Imoto, S.; Tang, F.; Zysk, F.; Kühne, T. D.; Shigeta, Y.; Bonn, M.; Wu, X.; Nagata, Y. Accessing the accuracy of density functional theory through structure and dynamics of the water−air interface. *J. Phys. Chem. Lett.* **2019**, *10* (17), 4914−4919.
(85) Evans, D. J.; Holian, B. L. The nose−hoover thermostat. *J. Chem. Phys.* **1985**, *83*, 4069−4074.
(86) Martinez, M.; Gaigeot, M. P.; Borgis, D.; Vuilleumier, R. Extracting effective normal modes from equilibrium dynamics at finite temperature. *J. Chem. Phys.* **2006**, *125*, No. 144106.
(87) Akimov, A. V.; Prezhdo, O. V. Persistent electronic coherence despite rapid loss of electron−nuclear correlation. *J. Phys. Chem. Lett.* **2013**, *4*, 3857−3864.
(88) Hilborn, R. C. Einstein coefficients, cross sections, *f* values, dipole moments, and all that. *Am. J. Phys.* **1982**, *50*, 982−986.
(89) Löwdin, P.-O. Quantum theory of many-particle systems. I. Physical interpretations by means of density matrices, natural spin-orbitals, and convergence problems in the method of configurational interaction. *Phys. Rev.* **1955**, *97*, 1474.
(90) Hammes-Schiffer, S.; Tully, J. C. Proton Transfer in Solution: Molecular Dynamics with Quantum Transitions. *J. Chem. Phys.* **1994**, *101*, 4657−4667.
(91) Adamo, C.; Barone, V. Toward reliable density functional methods without adjustable parameters: The PBE0 model. *J. Chem. Phys.* **1999**, *110*, 6158−6170.
(92) Becke, A. D. A new mixing of Hartree−Fock and local density-functional theories. *J. Chem. Phys.* **1993**, *98*, 1372−1377.
(93) Lin, Y.; Akimov, A. V. Dependence of Nonadiabatic Couplings with Kohn-Sham Orbitals on the Choice of Density Functional: Pure *vs* Hybrid. *J. Phys. Chem. A* **2016**, *120*, 9028−9041.
(94) Shakiba, M.; Akimov, A. V. Generalization of the Local Diabatization Approach for Propagating Electronic Degrees of Freedom in Nonadiabatic Dynamics. *Theor. Chem. Acc.* **2023**, *142*, No. 68.
(95) Granucci, G.; Persico, M.; Toniolo, A. Direct Semiclassical Simulation of Photochemical Processes with Semiempirical Wave Functions. *J. Chem. Phys.* **2001**, *114*, 10608−10615.
(96) Craig, C. F.; Duncan, W. R.; Prezhdo, O. V. Trajectory surface hopping in the time-dependent Kohn-Sham approach for electron-nuclear dynamics. *Phys. Rev. Lett.* **2005**, *95*, No. 163001.
(97) Duncan, W. R.; Craig, C. F.; Prezhdo, O. V. Time-domain ab initio study of charge relaxation and recombination in dye-sensitized TiO_2. *J. Am. Chem. Soc.* **2007**, *129*, 8528−8543.
(98) Prezhdo, O. V.; Duncan, W. R.; Prezhdo, V. V. Photoinduced electron dynamics at the chromophore−semiconductor interface: A time-domain ab initio perspective. *Prog. Surf. Sci.* **2009**, *84*, 30−68.
(99) Tully, J. C. Molecular dynamics with electronic transitions. *J. Chem. Phys.* **1990**, *93*, 1061−1071.
(100) Smith, B.; Akimov, A. V. A comparative analysis of surface hopping acceptance and decoherence algorithms within the neglect of back-reaction approximation. *J. Chem. Phys.* **2019**, *151*, No. 124107.
(101) Granucci, G.; Persico, M. Critical appraisal of the fewest switches algorithm for surface hopping. *J. Chem. Phys.* **2007**, *126*, No. 134114.
(102) Nelson, T.; Fernandez-Alberti, S.; Roitberg, A. E.; Tretiak, S. Nonadiabatic excited-state molecular dynamics: Treatment of electronic decoherence. *J. Chem. Phys.* **2013**, *138*, No. 224111.
(103) Shakiba, M.; Akimov, A. V. Dependence of Electron−Hole Recombination Rates on Charge Carrier Concentration: A Case Study of Nonadiabatic Molecular Dynamics in Graphitic Carbon Nitride Monolayers. *J. Phys. Chem. C* **2023**, *127*, 9083−9096.
(104) Ohsaka, T.; Izumi, F.; Fujiki, Y. Raman spectrum of anatase, TiO_2. *J. Raman Spectrosc.* **1978**, *7*, 321−324.
(105) Hashimoto, M.; Takadama, H.; Mizuno, M.; Kokubo, T. Enhancement of mechanical strength of TiO_2/high-density polyethylene composites for bone repair with silane-coupling treatment. *Mater. Res. Bull.* **2006**, *41*, 515−524.
(106) Antony, R. P.; Dasgupta, A.; Mahana, S.; Topwal, D.; Mathews, T.; Dhara, S. Resonance Raman spectroscopic study for radial vibrational modes in ultra-thin walled TiO_2 nanotubes. *J. Raman Spectrosc.* **2015**, *46*, 231−235.
(107) Tang, H.; Prasad, K.; Sanjines, R.; Schmid, P.; Levy, F. Electrical and optical properties of TiO_2 anatase thin films. *J. Appl. Phys.* **1994**, *75*, 2042−2047.
(108) Macià Escatllar, A.; Morales-García, Á.; Illas, F.; Bromley, S. T. Efficient preparation of TiO_2 nanoparticle models using interatomic potentials. *J. Chem. Phys.* **2019**, *150*, No. 214305.
(109) Alvertis, A. M.; Schröder, F. A.; Chin, A. W. Non-equilibrium relaxation of hot states in organic semiconductors: Impact of mode-selective excitation on charge transfer. *J. Chem. Phys.* **2019**, *151* (8), No. 084104, DOI: 10.1063/1.5115239.
(110) Alvertis, A. M.; Pandya, R.; Muscarella, L. A.; Sawhney, N.; Nguyen, M.; Ehrler, B.; Rao, A.; Friend, R. H.; Chin, A. W.; Monserrat, B. Impact of exciton delocalization on exciton-vibration interactions in organic semiconductors. *Phys. Rev. B* **2020**, *102* (8), No. 081122.
(111) Ghosh, P.; Alvertis, A. M.; Chowdhury, R.; Murto, P.; Gillett, A. J.; Dong, S.; Sneyd, A. J.; Cho, H.-H.; Evans, E. W.; Monserrat, B.; et al. Decoupling excitons from high-frequency vibrations in organic molecules. *Nature* **2024**, *629* (8011), 355−362.
(112) Lu, T.; Chen, F. Multiwfn: A multifunctional wavefunction analyzer. *J. Comput. Chem.* **2012**, *33*, 580−592.
(113) Recio-Poo, M.; Morales-García, Á.; Illas, F.; Bromley, S. T. Tuning electronic levels in photoactive hydroxylated titania nano-systems: combining the ligand dipole effect and quantum confinement. *Nanoscale* **2024**, *16*, 8975−8985.
(114) Yang, S.; Prendergast, D.; Neaton, J. B. Tuning semiconductor band edge energies for solar photocatalysis via surface ligand passivation. *Nano Lett.* **2012**, *12* (1), 383−388.
(115) Zhang, D.; Yang, M.; Dong, S. Hydroxylation of the rutile TiO_2 (110) surface enhancing its reducing power for photocatalysis. *J. Phys. Chem. C* **2015**, *119* (3), 1451−1456.
(116) Verdi, C.; Giustino, F. Fröhlich electron-phonon vertex from first principles. *Phys. Rev. Lett.* **2015**, *115* (17), No. 176401.
(117) Kronik, L.; Stein, T.; Refaely-Abramson, S.; Baer, R. Excitation gaps of finite-sized systems from optimally tuned range-separated hybrid functionals. *J. Chem. Theory Comput.* **2012**, *8*, 1515−1531.
(118) Alkan, F.; Aikens, C. M. TD-DFT and TD-DFTB investigation of the optical properties and electronic structure of silver nanorods and nanorod dimers. *J. Phys. Chem. C* **2018**, *122*, 23639−23650.
(119) Zhai, H. J.; Wang, L. S. Probing the Electronic Structure and Band Gap Evolution of Titanium Oxide Clusters $(TiO_2)_n$ (n = 1−10) Using Photoelectron Spectroscopy. *J. Am. Chem. Soc.* **2007**, *129*, 3022−3026.
(120) Hele, T. J. H.; Monserrat, B.; Alvertis, A. M. Systematic improvement of molecular excited state calculations by inclusion of nuclear quantum motion: a mode-resolved picture and the effect of molecular size. *J. Chem. Phys.* **2021**, *154* (24), No. 244109.
(121) Zhang, Q.; Shao, X.; Li, W.; Mi, W.; Pavanello, M.; Akimov, A. V. Nonadiabatic Molecular Dynamics with Subsystem Density Functional Theory: Application to Crystalline Pentacene. *J. Phys.: Condens. Matter* **2024**, *36*, No. 385901.
(122) Akimov, A. V. Excited state dynamics in monolayer black phosphorus revisited: Accounting for many-body effects. *J. Chem. Phys.* **2021**, *155*, No. 134106.
(123) Ozawa, K.; Emori, M.; Yamamoto, S.; Yukawa, R.; Yamamoto, S.; Hobara, R.; Kazushi, F.; Hiroshi, S.; Matsuda, I. Electron−hole recombination time at TiO_2 single-crystal surfaces: Influence of surface band bending. *J. Phys. Chem. Lett.* **2014**, *5*, 1953−1957.
(124) Serpone, N.; Lawless, D.; Khairutdinov, R. Size effects on the photophysical properties of colloidal anatase TiO_2 particles: size

https://doi.org/10.1021/acs.jpcc.4c07180
J. Phys. Chem. C XXXX, XXX, XXX−XXX

quantization versus direct transitions in this indirect semiconductor? *J. Phys. Chem. A* **1995**, *99* (45), 16646−16654.
(125) Recio Poo, M.; Akimov, A.; Morales, A. *AkimovLab/Project_TiO_2_water_met-hods_assessment: Nonadiabatic dynamics in hydrated $(TiO_2)_n$ clusters (v1.0.0)*, Zenodo 2024.

https://doi.org/10.1021/acs.jpcc.4c07180
J. Phys. Chem. C XXXX, XXX, XXX−XXX

5.5 References

[1] Schneider, J.; Matsuoka, M.; Takeuchi, M.; Zhang, J.; Horiuchi, Y.; Anpo, M.; Bahnemann, D. W. Understanding TiO_2 photocatalysis: mechanisms and materials. *Chem. Rev.* **2014**, *114*, 9919−9986.

[2] Kumaravel, V.; Mathew, S.; Bartlett, J.; Pillai, S. C. Photocatalytic hydrogen production using metal doped TiO_2: A review of recent advances. *Appl. Catal., B* **2019**, *244*, 1021−1064.

[3] Ardo, S.; Meyer, G. J. Photodriven heterogeneous charge transfer with transition-metal compounds anchored to TiO_2 semiconductor surfaces. *Chem. Soc. Rev.* **2009**, *38*, 115−164.

[4] Bai, Y.; Mora-Sero, I.; De Angelis, F.; Bisquert, J.; Wang, P. Titanium dioxide nanomaterials for photovoltaic applications. *Chem. Rev.* **2014**, *114*, 10095−10130.

[5] Tongay, S., Suh, J., Ataca, C., Fan, W., Luce, A., Kang, J. S., Liu, J.;Ko, C.; Raghunathanan, R.; Zhou, J.; Ogletree, F.; Li, J.; Grossman, J. C.; Wu, J. Defects activated photoluminescence in two-dimensional semiconductors: interplay between bound, charged and free excitons. *Sci. Rep.* **2013**, *3*(1), 2657.

[6] Glazov, M. M.; Iakovlev, Z. A.; Refaely-Abramson, S. Phonon-induced exciton weak localization in two-dimensional semiconductors. *Appl. Phys. Lett.* **2022**, *121*(19), 192106.

[7] Baldini, E.; Chiodo, L.; Dominguez, A.; Palummo, M.; Moser, S.; Yazdi-Rizi, M.; Auböck, G.; Mallett, B. P. P.; Berger, H.; Magrez, A.; Bernhard, C.; Grioni, M.; Rubio, A.; Chergui, M. Strongly bound excitons in anatase TiO_2 single crystals and nanoparticles. *Nat. Commun.* **2017**, *8*(1), 13.

[8] Obara, Y.; Ito, H.; Ito, T.; Kurahashi, N.; Thürmer, S.; et al. Femtosecond time-resolved X-ray absorption spectroscopy of anatase TiO_2 nanoparticles using XFEL. *Struct. Dyn.* **2017**, *4*, No. 044033.

[9] Garcia, J. M.; Heald, L. F.; Shaffer, R. E.; Sayres, S. G. Oscillation in Excited State Lifetimes with Size of Sub-nanometer Neutral $(TiO_2)n$ Clusters Observed

with Ultrafast Pump−Probe Spectroscopy. *J. Phys. Chem. Lett.* **2021**, *12*, 4098−4103

[10] Serpone, N.; Lawless, D.; Khairutdinov, R. Size effects on the photophysical properties of colloidal anatase TiO_2 particles: size quantization versus direct transitions in this indirect semiconductor? *J. Phys. Chem. A* **1995**, *99* (45), 16646−16654.

[11] Nam, Y.; Li, L.; Lee, J. Y.; Prezhdo, O. V. Size and shape effects on charge recombination dynamics of TiO_2 nanoclusters. *J. Phys. Chem. C* **2018**, *122*, 5201−5208.

[12] Nam, Y.; Li, L.; Lee, J. Y.; Prezhdo, O. V. Strong influence of oxygen vacancy location on charge carrier losses in reduced TiO_2 nanoparticles. *J. Phys. Chem. Lett.* **2019**, *10*, 2676−2683.

[13] Osterloh, F. E. (2008). Inorganic materials as catalysts for photochemical splitting of water. *Chemistry of Materials*, *20*(1), 35-54.

[14] Wang, H., Zhang, L., Chen, Z., Hu, J., Li, S., Wang, Z., ... & Wang, X. (2014). Semiconductor heterojunction photocatalysts: design, construction, and photocatalytic performances. *Chemical Society Reviews*, *43*(15), 5234-5244.

[15] Cho, D.; Ko, K. C.; Lamiel García, O.; Bromley, S. T.; Lee, J. Y.; Illas, F. Effect of Size and Structure on the Ground and Excited State Electronic Structure of TiO_2 Nanoparticles. *J. Chem. Theory Comput.* **2016**, *12*, 3751−3763.

[16] Olvera-Neria, O.; García-Cruz, R.; Gonzalez-Torres, J.; García-Cruz, L. M.; Castillo-Sánchez, J. L.; Poulain, E. Strongly Bound Frenkel Excitons on TiO_2 Nanoparticles: An Evolutionary and DFT Approach. *Int. J. Photoenergy* **2024**, *1*, 4014216.

[17] Takagahara, T.; Takeda, K. Theory of the quantum confinement effect on excitons in quantum dots of indirect-gap materials. *Phys. Rev. B* **1992**, *46*(23), 15578.

[18] Shornikova, E. V.; Yakovlev, D. R.; Gippius, N. A.; Qiang, G.; Dubertret, B.; Khan, A. H.; Di Giacomo, A.; Moreels, I.; Bayer, M. Exciton binding energy

in CdSe nanoplatelets measured by one-and two-photon absorption. *Nano Lett.* **2021**, *21*(24), 10525-10531.

[19] Valero, R.; Morales-García, Á.; Illas, F. Investigating the character of excited states in TiO_2 nanoparticles from topological descriptors: implications for photocatalysis. *Phys. Chem. Chem. Phys.* **2020**, *22*(5), 3017-3029.

[20] Zaban, A.; Greenshtein, M.; Bisquert, J. Determination of the electron lifetime in nanocrystalline dye solar cells by open-circuit voltage decay measurements. *ChemPhysChem* **2003**, *4*(8), 859-864.

[21] Chulkov, E. V.; Borisov, A. G.; Gauyacq, J. P.; Sánchez-Portal, D.; Silkin, V. M.; Zhukov, V. P.; Echenique, P. M. Electronic excitations in metals and at metal surfaces. *Chem. Rev.* **2006**, *106*(10), 4160-4206.

[22] Morales-García, Á.; Viñes, F.; Sousa, C.; Illas, F. Toward a rigorous theoretical description of photocatalysis using realistic models. *J. Phys. Chem. Lett.* **2023**, *14*(15), 3712-3720.

[23] Garcia, J. M.; Heald, L. F.; Shaffer, R. E.; Sayres, S. G. Oscillation in Excited State Lifetimes with Size of Sub-nanometer Neutral (TiO2)*n* Clusters Observed with Ultrafast Pump−Probe Spectroscopy. *J. Phys. Chem. Lett.* **2021**, *12*, 4098−4103.

[24] Bao, J.; Yu, Z.; Gundlach, L.; Benedict, J. B.; Coppens, P.; Cheng, H. C; Miller, J. R.; Piotrowiak, P. Excitons and excess electrons in nanometer size molecular polyoxotitanate clusters: electronic spectra, exciton dynamics, and surface states. *J. Phys. Chem. B* **2013**, *117*, 4422−4430.

[25] Obara, Y.; Ito, H.; Ito, T.; Kurahashi, N.; Thürmer, S.; Tanaka, H.; Katayama, T.; Togashi, T.; Owada, S.; Yamamoto, Y.; Karashima, S.; Nishitani, J.; Yabashi, M.; Suzuki, T.; Misawa, K. Femtosecond time-resolved X-ray absorption spectroscopy of anatase TiO_2 nanoparticles using XFEL. *Struct. Dyn.* **2017**, *4*, No. 044033.

[26] Bao, J.; Gundlach, L.; Yu, Z.; Benedict, J. B.; Snoeberger, R. C., III; Batista, V. S.; Coppens, P.; Piotrowiak, P.. Hot hole hopping in a polyoxotitanate cluster terminated with catechol electron donors. *J. Phys. Chem. C* **2016**, *120*, 20006−

20015.

[27] Cheng, C.; Zhu, Y.; Fang, W. H.; Long, R.; Prezhdo, O. V. CO adsorbate promotes polaron photoactivity on the reduced rutile TiO_2 (110) surface. *J. Am. Chem. Soc.* **2021**, *Au*, *2*(1), 234-245.

[28] Muuronen, M.; Parker, S. M.; Berardo, E.; Le, A.; Zwijnenburg, M. A.; Furche, F. Mechanism of photocatalytic water oxidation on small TiO_2 nanoparticles. *Chem. Sci.* **2017**, *8* (3), 2179−2183.

[29] Berardo, E.; Hu, H. S.; Shevlin, S. A.; Woodley, S. M.; Kowalski, K.; Zwijnenburg, M. A. Modeling excited states in TiO2 nanoparticles: on the accuracy of a TD-DFT based description. *J. Chem. Theory Comput.* **2014**, *10*, 1189−1199.

[30] Jiang, X.; Zheng, Q.; Lan, Z.; Saidi, W. A.; Ren, X.; Zhao, J. Real-time GW-BSE investigations on spin-valley exciton dynamics in monolayer transition metal dichalcogenide. *Sci. Adv.* **2021**, *10*(7), No. eabf3759.

[31] Smith, B.; Shakiba, M.; Akimov, A. V. Nonadiabatic dynamics in Si and CdSe nanoclusters: many-body vs single-particle treatment of excited states. *J. Chem. Theory Comput.* **2021**, *17*, 678−693.

[32] Smith, B.; Shakiba, M.; Akimov, A. V. Crystal symmetry and static electron correlation greatly accelerate nonradiative dynamics in lead halide perovskites. *J. Phys. Chem. Lett.* **2021**, *12*, 2444−2453.

[33] Liu, W.; Settels, V.; Harbach, P. H.; Dreuw, A.; Fink, R. F.; Engels, B. Assessment of TD-DFT-and TD-HF-based approaches for the prediction of exciton coupling parameters, potential energy curves, and electronic characters of electronically excited aggregates. *J. Comput. Chem.* **2011**, *32*, 1971−1981.

[34] Shao, Y.; Mei, Y.; Sundholm, D.; Kaila, V. R. Benchmarking the Performance of Time-Dependent Density Functional Theory Methods on Biochromophores. *J. Chem. Theory Comput.* **2020**, *16*, 587−600.

[35] Kasha, M. Characterization of Electronic Transitions in Complex Molecules. *Discuss. Faraday Soc.* **1950**, *9*, 14−19.

[36] Hashimoto, M.; Takadama, H.; Mizuno, M.; Kokubo, T. Enhancement of mechanical strength of TiO_2/high-density polyethylene composites for bone repair with silane-coupling treatment. *Mater. Res. Bull.* **2006**, *41*, 515−524.

[37] Antony, R. P.; Dasgupta, A.; Mahana, S.; Topwal, D.; Mathews, T.; Dhara, S. Resonance Raman spectroscopic study for radial vibrational modes in ultrathin walled TiO2 nanotubes. *J. Raman Spectrosc.* **2015**, *46*, 231−235.

[38] Tang, H.; Prasad, K.; Sanjines, R.; Schmid, P.; Levy, F. Electrical and optical properties of TiO2 anatase thin films. *J. Appl. Phys.* **1994**, *75*, 2042−2047.

[39] Ohsaka, T.; Izumi, F.; Fujiki, Y. Raman spectrum of anatase, TiO_2. *J. Raman Spectrosc.* **1978**, *7*, 321−324.

[40] Recio-Poo, M.; Morales-Garcia, Á.; Illas, F.; Bromley, S. T. Crystal properties without crystallinity? Influence of surface hydroxylation on the structure and properties of small TiO_2 nanoparticles. *Nanoscale* **2023**, *15*, 4809−4820.

[41] Cuko, A.; Escatllar, A. M.; Calatayud, M.; Bromley, S. T. Properties of hydrated TiO_2 and SiO_2 nanoclusters: dependence on size, temperature and water vapour pressure. *Nanoscale* **2018**, *10*, 21518−21532.

[42] Recio-Poo, M.; Morales-Garcia, Á.; Illas, F.; Bromley, S. T. Tuning electronic levels in photoactive hydroxylated titania nanosystems: combining the ligand dipole effect and quantum confinement. *Nanoscale* **2024**, *16*, 8975−8985.

[43] Shakiba, M.; Akimov, A. V. Dependence of Electron−Hole Recombination Rates on Charge Carrier Concentration: A Case Study of Nonadiabatic Molecular Dynamics in Graphitic Carbon Nitride Monolayers. *J. Phys. Chem. C* **2023**, *127*, 9083−9096.

[44] Akimov, A. V. Excited state dynamics in monolayer black phosphorus revisited: Accounting for many-body effects. *J. Chem. Phys.* **2021**, *155*, No. 13410.6

[45] Ozawa, K.; Emori, M.; Yamamoto, S.; Yukawa, R.; Yamamoto, S.; Hobara, R.; Kazushi, F.; Hiroshi, S.; Matsuda, I. Electron−hole recombination time at

TiO_2 single-crystal surfaces: Influence of surface band bending. *J. Phys. Chem. Lett.* **2014**, *5*, 1953−1957.

6 CONCLUSIONS

This thesis presents a comprehensive investigation into the structural, electronic, thermodynamic, and excited-state properties of TiO_2 nanoparticles, elucidating fundamental mechanisms that govern their stability and performance in photocatalytic and optoelectronic applications. Through a synergistic approach that combines density functional theory calculations, advanced thermodynamic modelling, and nonadiabatic molecular dynamics, we provide a detailed understanding of how size, crystallinity, hydroxylation, and hydration influence the properties of TiO_2 at the nanoscale. The results offer new perspectives on material optimization strategies, bridging the gap between amorphous and crystalline structures, bulk approximations, and explicit molecular-scale models.

Our findings establish that hydroxylation plays a crucial role in stabilizing TiO_2 nanoparticles, leading to a convergence in electronic and energetic properties between crystalline and amorphous structures. We demonstrate that through controlled hydroxylation, amorphous TiO_2 NPs can exhibit electronic properties akin to their crystalline anatase counterparts, introducing the concept of "crystalike" nanomaterials. The ability to engineer electronic energy levels without chemical doping or interfacing with other materials expands the versatility of TiO_2 in photocatalysis and optoelectronics. Furthermore, we identify an optimal degree of quantum confinement and hydroxylation that enhances band edge alignment for photocatalytic water splitting, emphasizing the importance of fine-tuning surface chemistry for improved efficiency.

In the realm of thermodynamics, our work introduces $AIAT_{nano}$, a computational framework that refines existing AIAT models by incorporating a size-dependent vibrational free energy correction. $AIAT_{nano}$ addresses the limitations of explicit phonon calculations and bulk approximations, providing a more accurate and computationally feasible approach to studying hydration thermodynamics at the nanoscale. Our results highlight that size-dependent vibrational entropy contributions significantly influence hydration stability, particularly in smaller nanoparticles, an effect often overlooked in traditional models. This framework not only enhances our understanding of nanoscale hydration but also provides a powerful tool for investigating the thermodynamic

behaviour of other nanomaterials in diverse applications, such as catalysis and electrochemistry.

The study of excited-state dynamics further underscores the impact of hydration on charge carrier relaxation in TiO_2 nanoclusters. By employing NA-MD simulations, we reveal that hydration enhances nonadiabatic couplings and accelerates charge recombination due to the introduction of additional vibrational modes. While this effect can be detrimental to photocatalysis, it provides a tunable parameter for optimizing TiO_2-based materials for specific energy conversion applications. Our analysis also highlights the importance of computational methodology selection, demonstrating that hybrid functionals yield more accurate electronic structure predictions, and decoherence-corrected trajectory surface hopping methods provide more reliable recombination times. These insights contribute to resolving discrepancies between computational and experimental charge relaxation times, paving the way for more precise theoretical-experimental correlations in TiO_2 research.

Beyond the scientific insights, this work exemplifies the power of computational modelling in materials chemistry. By integrating first-principles calculations, thermodynamic modelling, and excited-state dynamics simulations, we establish a multi-scale framework for predicting and optimizing material properties. These methodological advancements reinforce the growing importance of computational approaches in modern materials design. By refining existing theoretical frameworks and leveraging high-accuracy electronic structure methods, we enable a more comprehensive exploration of nanoscale phenomena, ultimately contributing to the broader effort of developing efficient and sustainable nanomaterials.

Future research should explore the experimental validation of these findings, particularly through spectroscopic techniques that probe hydroxylation effects and charge carrier dynamics in real-world photocatalytic environments. Additionally, extending the AIATnano framework to other oxide materials could provide valuable insights into nanoscale thermodynamics beyond TiO_2. Finally, further refinement of computational methodologies, including improved machine-learning-driven approaches for excited-state dynamics, could

enhance the predictive power of these models, accelerating the development of next-generation nanomaterials.

7 CONTRIBUTION TO PUBLICATIONS

Publications derived from the thesis:

- **Recio-Poo, M.**; Morales-Garcia, Á.; Illas, F.; Bromley, S. T. Crystal properties without crystallinity? Influence of surface hydroxylation on the structure and properties of small TiO_2 nanoparticles. *Nanoscale* **2023**, *15*, 4809−4820.

Contribution: Formal analysis; Investigation; Data Curation; Writing – Review & Editing.

- **Recio-Poo, M.;** Morales-Garcia, Á.; Illas, F.; Bromley, S. T. Tuning electronic levels in photoactive hydroxylated titania nanosystems: combining the ligand dipole effect and quantum confinement. *Nanoscale* **2024**, *16* (18), 8975−8985.

Contribution: Formal analysis; Investigation; Data Curation; Writing – Original Draft; Writing - Review & Editing.

- **Recio-Poo, M.**; Morales-García, Á.; Illas, F.; Bromley, S. T. Size-Dependent Ab Initio Atomistic Thermodynamics from Cluster to Bulk: Application to Hydration of Titania Nanoparticles. *J. Phys. Chem. Lett.* **2024**, *15*(32), 8240-8247.

Contribution: Formal analysis; Investigation; Data Curation; Writing – Original Draft; Writing - Review & Editing.

- **Recio-Poo, M.**; Shakiba, M.; Illas, F.; Bromley, S. T.: Akimov, A. V.; Morales-García, A. Hydration Accelerates Radiative and Nonradiative Recombination in Small TiO_2 Nanoclusters. *J. Phys. Chem. C* **2025**, 129, 3, 1806–1823.

Contribution: Formal analysis; Investigation; Data Curation; Writing – Original Draft; Writing - Review & Editing.

- **Recio-Poo, M.**; Morales-García, A.; Bromley, S. T. Impact of Surface Hydroxylation on the Structural and Electronic Properties of 2–3.5 nm Diameter Crystalline and Amorphous Titania Nanoparticles. *J. Phys. Chem. C* **2025**, 129, 6, 3299–3309.

Contribution: Formal analysis; Investigation; Data Curation; Writing – Original Draft; Writing - Review & Editing.

Other publications:

- **Recio-Poo, M.**; Lobato, A.; Otero-de-la-Roza, A.; Salvadó, M. A.; Arroyo-de Dompablo, M. E.; Recio, J. M. Temperature and pressure-induced strains in anhydrous iron trifluoride polymorphs. *Phys. Chem. Chem. Phys.* **2021**, *23*(4), 2825-2835.

Contribution: Formal analysis; Investigation; Data Curation; Writing – Review & Editing.

- Lobato, A.; **Recio-Poo, M.**; Otero-de-la-Roza, A.; Salvadó, M. A.; Recio, J. M. Controlling the off-center positions of anions through thermodynamics and kinetics in flexible perovskite-like materials. *Phys. Chem. Chem. Phys.* **2021**, *23*(8), 4491-4499.

Contribution: Formal analysis; Investigation; Data Curation; Writing – Review & Editing.

- Black, A. P.; Frontera, C.; Torres, A.; Recio-Poo, M.; Rozier, P.; Forero-Saboya, J. D.; Fauth, F.; Urones-Garrote, E.; Arroyo-de Dompablo, M. E.; Palacín, M. R. Elucidation of the redox activity of $Ca_2MnO_{3.5}$ and CaV_2O_4 in calcium batteries using operando XRD: charge compensation mechanism and reversibility. *Energy Storage Mater.* **2022**, *47*, 354-364.

Contribution: Investigation; Data Curation.

In preparation:

- Recio-Poo, M.; Rotteger, C. H.; Illas, F.; Bromley, S. T.; Sayres, S. G.; Akimov, A. V.; Morales-García, Á. Developing predictive capabilities

for the ultrafast relaxation and recombination photodynamics of metal (oxide) clusters.

Contribution: Formal analysis; Investigation; Data Curation; Writing – Original Draft; Writing - Review & Editing.

8 APPENDIX

Electronic Supplementary Material (ESI) for Nanoscale.

Electronic Supplementary Information

Crystal properties without crystallinity? How surface hydroxylation affects the structure and properties of TiO_2 nanoparticles

Miguel Recio-Poo,[a] Ángel Morales-García,*[a] Francesc Illas,[a] Stefan T. Bromley*[ab]

[a] Departament de Ciència de Materials i Química Física & Institut de Química Teòrica i Computacional (IQTCUB), Universitat de Barcelona, c/Martí i Franquès 1-11, 08028 Barcelona, Spain

[b] Institució Catalana de recerca i Estudis Avançats (ICREA), Passeig Lluis Companys 23, 08010 Barcelona, Spain

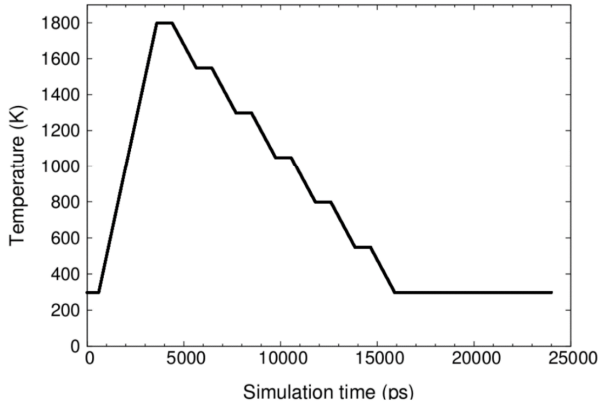

Fig. S1 Temperature evolution profile followed during the stepwise molecular dynamics simulated annealing (MD-SA) procedure.

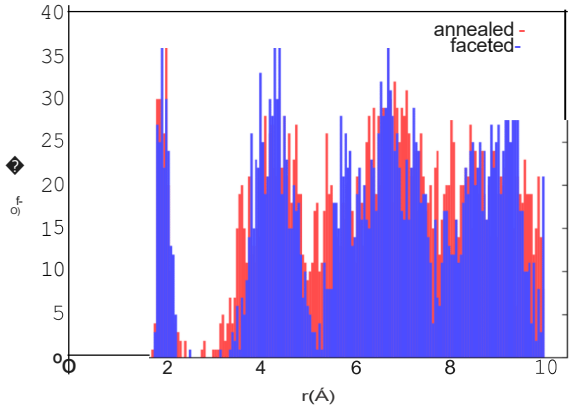

Fig. S2 Pair distribution function, g(r), far Ti-O distances in a faceted crystalline anatase NP (blue) and thermally annealed NP (red) with a (TiO,),s(H,O),s composition. The bin size far the histogram is O.OS A.

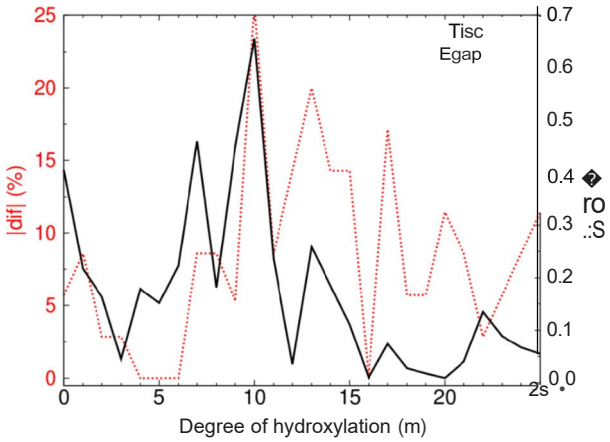

Fig. S3 Difference in the proportion of Ti., centres (left) and *E*,,, (right) between the crystalline anatase and annealed (Ti02hs(H20)mNPs.

Electronic Supplementary Material (ESI) for Nanoscale.

Electronic Supplementary Information for:

Tuning electronic levels in photoactive hydroxylated titania nanosystems: combining the ligand dipole effect and quantum confinement

Miguel Recio-Poo,[a] Ángel Morales-García,*[a] Francesc Illas,[a] Stefan T. Bromley*[a,b]

[a] Departament de Ciencia de Materials i Química Física & Institut de Química Teórica i Computacional (IQTCUB), Universitat de Barcelona, c/Martí i Franques 1-11, 08028 Barcelona, Spain

[b] Institució Catalana de recerca i Estudis Avan̲ats (ICREA), Passeig Lluis Companys 23, 08010 Barcelona, Spain

*Corresponding authors: angel.morales@ub.edu; s.bromley@ub.edu

Table S1. Comparison oftotal energies for hydroxylated anatase slab models with r point and SxSxl k-point sampling.

	Degree of hydroxylation		
	0%	50%	100%
r point	-1972829.149	-1985324.399	-1997809.979
5x5x1	-1972828.579	-1985323.859	-1997809.445
I\.E per TiO, unit (eV)	-0.00791	-0.00749	-0.00741

Figure S1. Evolution of the LUMO+S, LUM0+4, LUM0+3, LUM0+2, LUMO+I, HOM0-1, HOM0-2, HOM0-3, HOM0-4, HOM0-5 orbital energies corresponding to faceted (TiO_2)as NP.

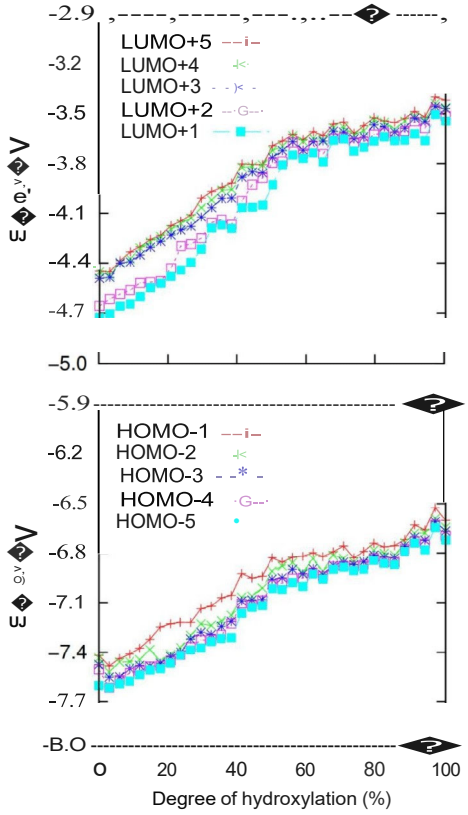

Figure S2 Evolution of HOMO, LUMO anda deeper lying energy level for the faceted (TiO,hsand (Tiü,)," NPs. Besides of proving again the electrostatic nature of the ligand dipole effect, the considerably slower slopes in the HOMO and LUMO levels with respect to the deeper orbitals (i.e. HOMO-250 for the (TiO2)35NP and HOMO-500 for the (TiO2)16SNP) shows the stabilization happening dueto defects healing effect upon hydroxylation.

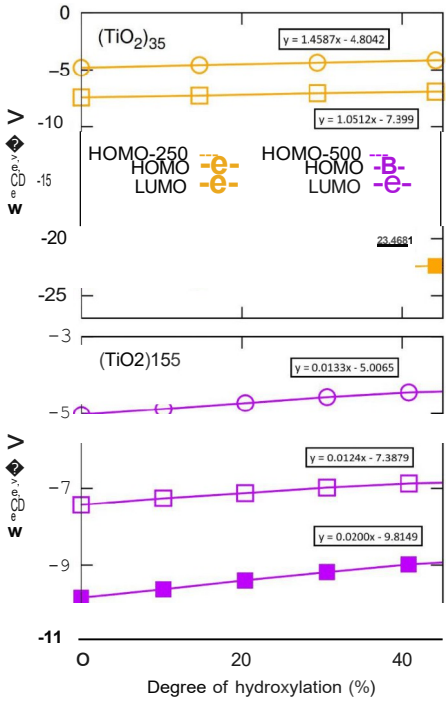

Figure S3 Evolution of both the average value of a and IIOoH with respect to the degree of hydroxylation far the n = 35 and n = 165 (Tiü,), anatase NPs is provided in the 51.

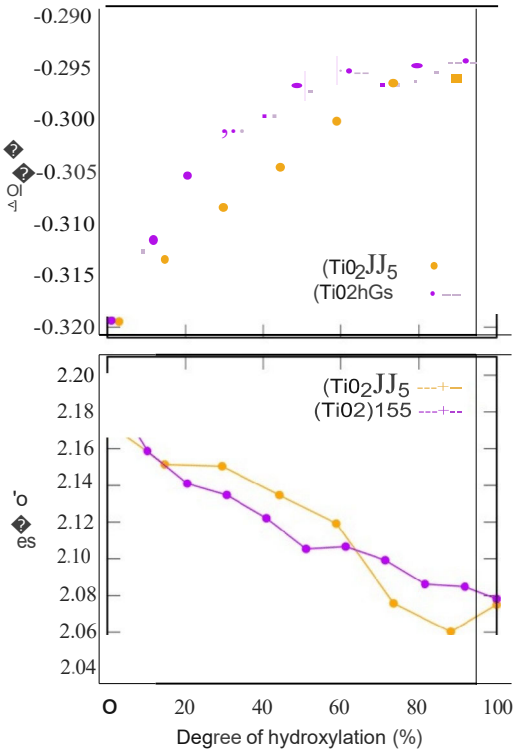

Supporting Information for:

Impact of Surface Hydroxylation on the Structural and Electronic Properties of 2 - 3.5 nm Diameter Crystalline and Amorphous Titania Nanoparticles

Miguel Recio-Poo,[1] Ángel Morales-García,'* Stefan T. Bromley[1]h

[1]Departament de Ciencia de Materials i Química Física & Institut de Química Teorica i Computacional (IQTCUB), Universitat de Barcelona, c/Martí i Franques 1-11, 08028 Barcelona, Spain.

[2]1nstitució Catalana de Recerca i Estudis Avan1;ats (!CREA), Passeig Lluis Companys 23, 08010 Barcelona, Spain.

Sl. Simulated annealing temperature evolution profile

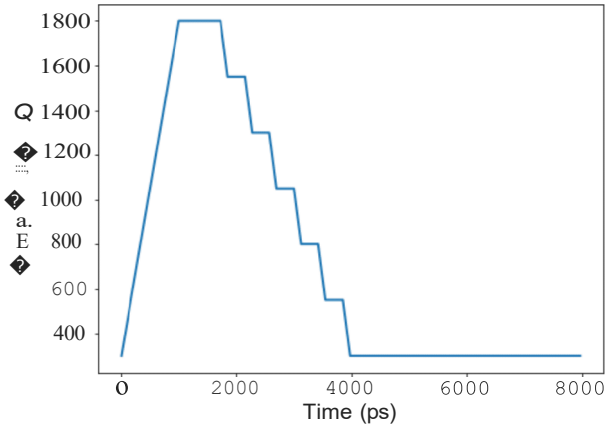

Figure Sl Temperature evolution profile followed during the stepwise molecular dynamics simulated annealing (MD-SA) procedure.

Supporting Information

Size-dependent Ab Initio Atomistic Thermodynamics from Cluster to Bulk: Application to Hydration of Titania Nanoparticles

Miguel Recio-Poo,° Ángel Morales-García,*° Francesc Illas,° Stefan T. Bromley,*ab

[a]Departament de Ciencia de Materials i Química Física & Institut de Química Teórica i Computacional (IQTCUB), Universitat de Barcelona, c/Martí i Franques 1-11, 08028 Barcelona, Spain

blnstitució Catalana de Recerca i Estudis Avan�ats (ICREA), Passeig Lluis Companys 23, 08010 Barcelona, Spain

*Corresponding authors: s.bromley@ub.edu, angel.morales@ub.edu

S1. Comparison of an AIATexplkt *!J.G$_{hyd(T,}$ p)* phase diagram for the globally optimised (Ti02hs(H20)m NP system compared with a AIATnanoapproach

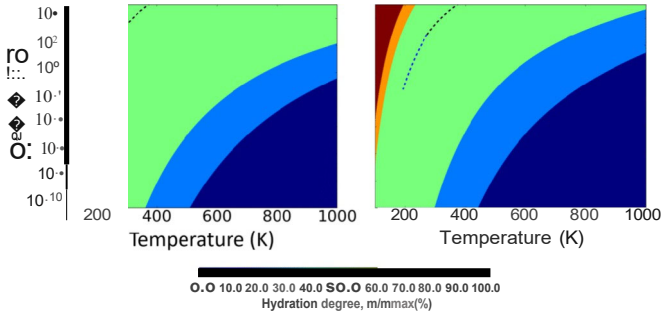

Figure S1. Thermodynamic *!J.Ghyd(T,p)* phase diagrams far the globally optimized (TiO,)i,(H,O)m NPs with all vibrational frequencies explicitly considered (i.e. via a AIAT.,,¡¡,;, approach, left), and estimated using the *fvib* function (i.e. via a AIATmoapproach, right). In the main text we employ (TiO,),e(H,O)mNPs far which the core titania structure is constrained to keep clase to the original cut from the anatase crystal.

S2. Vibrational contributions to *t:.Ghyd(T,p)*

The vibrational contribution to Gibbs free energy, *Fvib,* can be expressed as the sum of three terms:

$$F^{vib}(T,\Theta_k) = E^{ZPE}(\Theta_k) + U^{vib}(T,\Theta_k) - TS^{vib}(T,\Theta_k) \quad (1)$$

where *uviband 5vib* are the vibrational contributions to the interna! energy and entropy and *EZPE* corresponds to the zero-point energy (ZPE) contribution. 0k is the vibrational temperature, which depends on the frequencies (vkl. Using our (TiO,),,(H,O), NP asan example, we explicitly compute the harmonic vibrational frequencies of the system and evaluate the *Fvib(T,* 0k)- In Figure 52 we plot *Fvib(T,* 0k) with respect to vibration frequency and temperature (n.

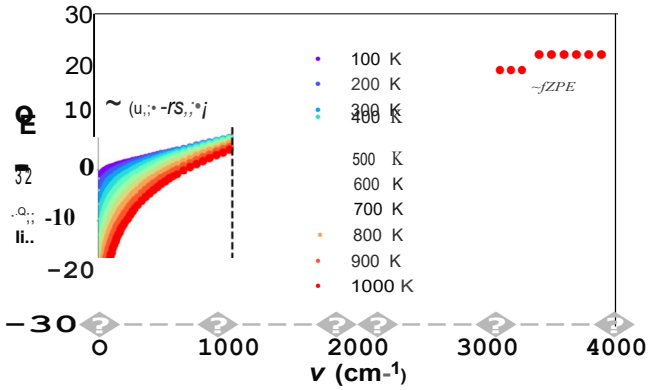

Figure S2. *pvib* with respect to vibrational frequency (v) at different temperatures calculated for the (Tiü,)i,(H,O)aNP. The dominant influence of the temperature-dependent terms (lower frequencies) and the ZPE term (higher frequencies) are clearly differentiated.

Two distinct contributions to *pvib(T,* 0k)are clearly seen. The first one at lower frequencies is almost totally defined by the temperature dependen\ terms and relates to the modes of the bonded Ti-O titania framework. The second contribution for higher frequencies, mainly corresponding to the temperature-independent ZPE term, is dominated by the vibrational modes of the pendant -OH groups.

S3. Fitting parameters for *f"ib(N,T)*

¡vib(N,T) is derived to reproduce *pvib* (i.e. the vibrational contributions to *flGhyd(T, p))* for hydrated (TiO2h•IH2O)mNPs at different temperatures. We partition *¡vib(N, T)*into two terms: *U';b.zPE* (combining temperature-dependent terms and ZPE) approximately accounting for **energetic contributions, and** *svib,* **which estimates the entropic contributions:**

$$¡vib = uvib\text{-}ZPE \_ TSvib \quad (2)$$

We approximate these contributions using the following second arder polynomial expressions:

$$U^{vib-ZPE} = (a_0 + a_1 T + a_2 T^2)\, N_v + (b_0 + b_1 T + b_2 T^2)\, m_v \quad (3)$$

$$S^{vib} = (c_0 + c_1 T + c_2 T^2)\, N_{,,} \quad (4)$$

where Nu = 3(3n + m) - 6, which is total number of vibrations from all Ti and O atoms in a (Ti02),(H20)mNP. Similarly, mu = 2m gives the total number ofvibrations from -0-H groups. The coefficients used are:

$$a_0 = 1.98;\ a_1 = 4.28 \cdot 10^{-3};\ a_2 = 2.47 \cdot 10^{-6}$$

$$b_0 = 21.76;\ b_1 = 3.75 \cdot 10^{-5};\ b_2 = 5.55 \cdot 10^{-7}$$

$$c_0 = 6.32 \cdot 10^{-};\ c_1 = 2.42 \cdot 10^{-5};\ c_2 = -9.74 \cdot 10^{-9}$$

Where a_0 and b_0 are in kJ/mol, a_1, b_1 and c_1 are in kJ/(mol·T), a_2, b_2 and c_2 are in kJ/(mol·T'), and c_2 is in kJ/(mol·T^3).

S4. Temperature dependence of vibration-dependent terms in *t.Ghyd(T, p)*

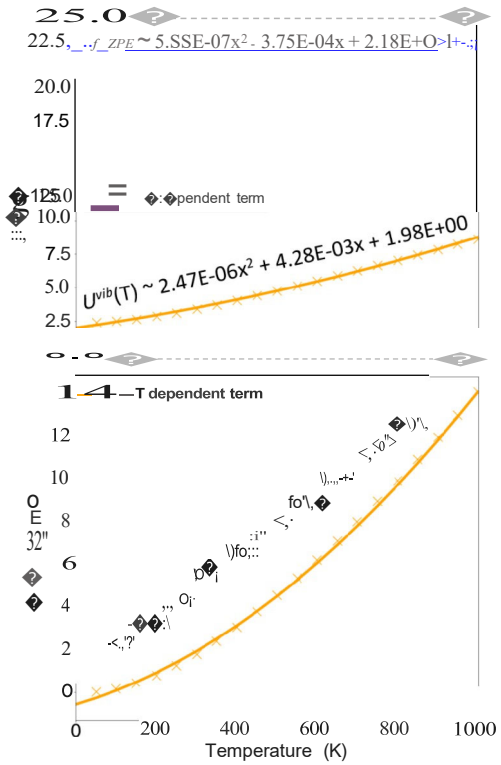

Figure S3. Explicitly calculated data points showing the temperature dependence of two terms making up the *uvib-ZPE* term (above) and the *r5vib* term (below) farthe $(TiO_{2)_6}(H_2O)_8$ NP. Salid lines fallow the corresponding *¡vib* fitted expressions.

SS. Size-dependence of the initial hydration *!!.Ghyd(T, p)* crossover contour

In Figure 54 we show differences in *!!.Ghyd(T,p)* between that of anhydrous NPs and of the initially hydrated NPs at different temperatures (i.e. farmally *ó!!.Ghyd(T, p)*) far a water vapour partial pressure of 1000 Pa far two system sizes ((Tiü,), and (Tiü,h") and far AIATоaoo and AIATsond, Far each system the constan! shift between the AIAT,aaoand AIAT,on,curves leads to a difference prediction in the crossover temperature (i.e. far *!!.!!.Ghyd(T, p)* = O).

In figure 55 we extrapolate the tendencies in figure 54 to larger sizes to show the size-dependency of the predicted difference in crossover temperature as predicted by AIATоa,o and AIAT,ondapproaches far five selected water partial pressures.

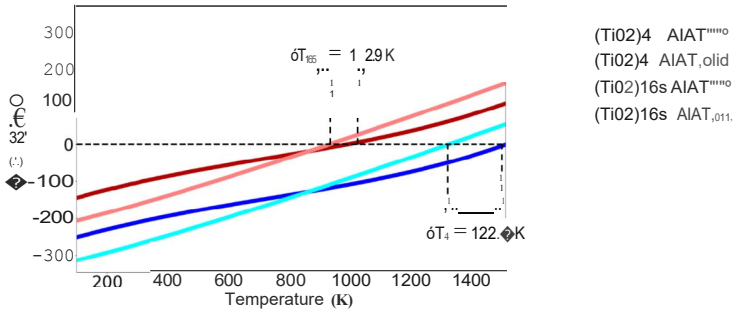

Figure S4. Temperature dependence of *!!.!!.Ghyd(T,p)* fallowing an AIAT,on, approach (light coloured lines) and fallowing our AIATоaoo approach (dark coloured lines) with respect to the anhydrous f--7 initial hydration of a (Tiü,), cluster (blue) and a (Tiü,)," NP (red) far a water vapour partial pressure of 1000 Pa. We highlight the AIATsond versus AIATоa,o temperature differences far this predicted crossover far the two systems considered.

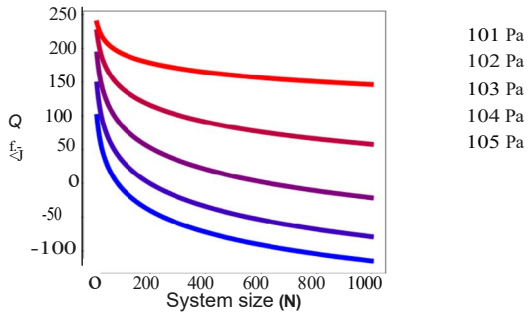

Figure SS. Differences in the predicted temperature of the initial *t:.Ghyd(T, p)* hydration crossover (i.e. between the anhydrous system and adsorption of a single water molecule) between AlAT,ond and AlAT,aoo with respect to system size for selected water vapour partial pressure values.

S6. General size-dependency of AlATnano

Using *¡vib* derived *t:.Ghyd(T,p)* data for four model (TiO2)nlH2O)mNPs (with *n* = 16, 35, 84 and 165) we found the anhydrous B initially hydrated crossover temperature for a set of fixed pressures ranging from 2x10·[10] to 200000 Pa. To do this we can follow the temperature for an incremental change in hydration by calculating differences in *t:.Ghyd(T, p)* between the system at the two degrees of hydration. For a fixed pressure, the condition *t:.t:.Ghyd(T,p)* = O then generally defines the temperature for a NP being at the crossover between the two degrees of hydration Asan example, figure 56 shows the *dt:.G* vs *T* evolution for a constant pressure of 1 Pa, for the anhydrous (TiO,)i, NP and the initially hydrated ITiO2hs(H2O) NP at different temperatures, yielding a limiting Tvalue of ~250 K. Note that as *dGhyd (T, p)* is calculated with respect to the anhydrous system (i.e. for which *dGhyd(T,p)* = O) then *t:.t:.Ghyd(T,p)* is equivalent to *t:.Ghyd(T,p)* in this case.

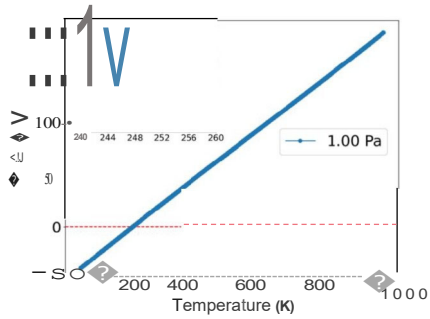

Figure S6. *L\L\G vs* Tplot far a constan! 1 Pa pressure value far the (Ti02l,,(H20)m NP, where M1G refers to the difference in *flGhyd(T,p)* between the anhydrous NP and the initially hydrated NP.

Far each constan! pressure we thus obtain faur points on a size-dependent isobar. We can also estímate the temperature of each isobar in the limit of infinite NP size by using extended periodic Ti0,(101) anatase surface model anda using a standard AIAT,011, approach. By fitting these temperatures toan analytical function (see below), we can then estímate *flGhyd(T,p)* crossover contours far any desired NP size.

To lit the size-dependent temperature profile far each isobar we used the fact that many size-dependency properties (P(N)) can be approximately fitted to a scaling law of the farm'·':

$$P(N) = \text{Pbulk} + a,N\text{-}1, \qquad (4)$$

where $P_{b,lk}$ is a characteristic value of the property P far the chosen bulk phase. A generalisation of this relation leads to a *P/N)* size-dependence of the fallowing form:

$$P(N) = a_0 + a_1x + a_2x^2 + a_3x^3 + \ldots, (5)$$

where $a_{0} = P_{,lk}$, $x = N^{-1/3}$ and the a'' values are (possibly *N* dependent) constants.

In our case the property *P(N)* is the size-dependent crossover temperature far each isobar (i.e. *T(n),* where *n* is the number ofTiO, units and where the ao term corresponds to the bulk limiting *T* value). We find that good fits can be made far each isobar with using polynomials of degree two or three (see examples in Figure 57).

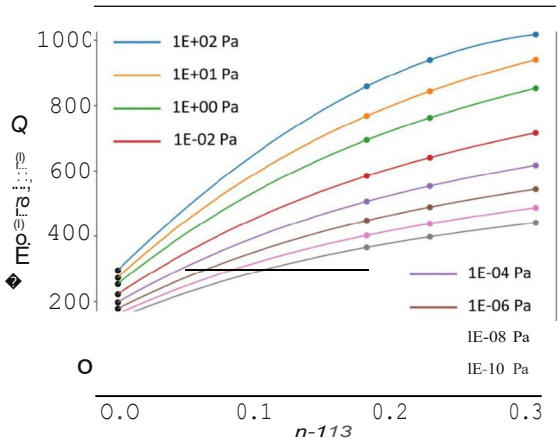

Figure S7. Temperature versus n^{-11}, plot showing the fitted isobars far a range of water vapour pressures. Where the temperature relates to the anhydrous-initially hydrated crossover temperature in each isobar and n corresponds to the number of Tiü, units in the system.

References

(1) R. L. Johnston, R. L. Atomicand Molecular Clusters (Master's Series in Physics and Astronomy) ISBN 13: 9780748409310, Taylor & Francis Ltd **2002.**

(2) Lamiel-Garcia, O.; Cuko, A.; Calatayud, M.; lilas, F.; Bromley, S. T. Predicting size-dependent emergence of crystallinity in nanomaterials: titania nanoclusters versus nanocrystals. *Nanoscale* **2017,** *9,* 1049-1058.

Supporting Information:

Hydration Accelerates Radiative and Nonradiative Recombination in Small TiO_2 Nanoclusters

Miguel Recio-Poo,[1] Mohammad Shakiba,[2] Francesc Illas,[1] Stefan T. Bromley,[1,3]* Alexey V. Akimov,[2]* and Ángel Morales-García[1]*

[1]Departament de Ciencia de Materials i Química Física & Institut de Química Teórica i Computacional (IQTCUB), Universitat de Barcelona, c/Martí i Franques 1-11, 08028 Barcelona, Spain.

[2]Department ofChemistry, University at Buffalo, The State University ofNew York, Buffalo, NY, 14260 USA.

[3]Institució Catalana de Recerca i Estudis Avan9ats (ICREA), Passeig Lluis Cornpanys 23, 08010 Barcelona, Spain.

Table of Content

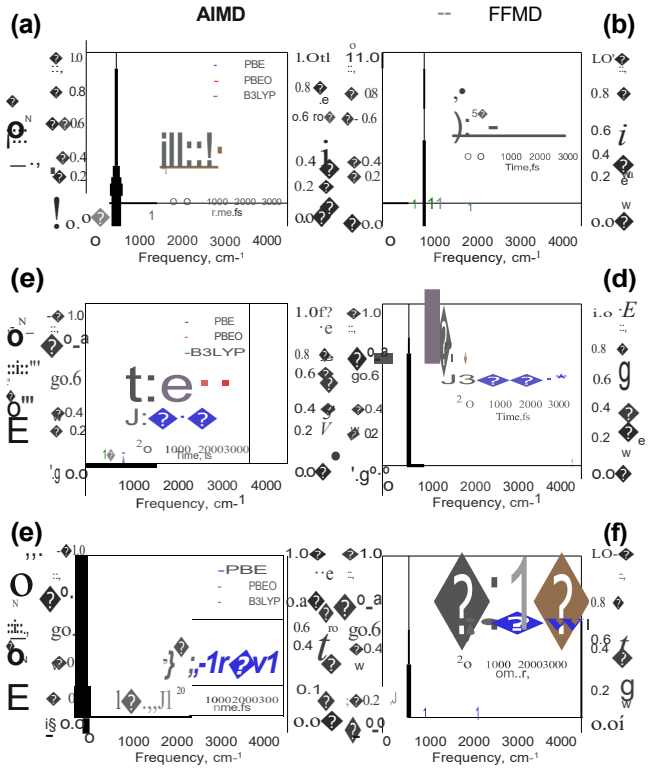

Figure S1. Normalized power and influence spectra for $(TiO_2)_4$ (a, b), $(TiO_2)_4(H_2O)2$(e, d) and $(TiO_2).(H_2O)_4$ (e, f) systems. The influence spectra are computed using nuclear trajectories obtained with AIMD (a, e, e) or classical FFMD (b, d, f) methods. The intluence spectra characterize the vibrational modes that drive the transition between the ground state and first excited state. The insets show the evolution ofthe ground-to-first-excited-state energy gap in corresponding calculations. Color codes: grey - power spectra, blue, red and green -influence spectra. For the influence spectra, TD-DFT excitation energies are computed with B3LYP (green lines), PBE0 (red lines) and PBE (blue lines) functionals.

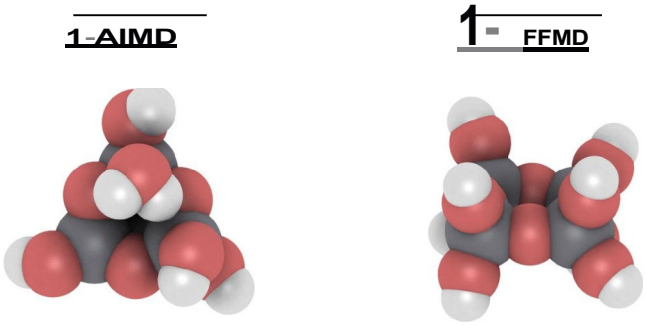

Figure S2. Comparison ofthe last hydrated $(TiO_2)4(H_2O)_4$ nanocluster geometries from AIMD and classical MD nuclear trajectories

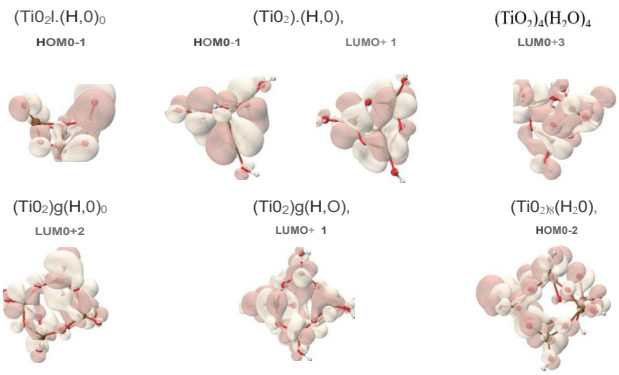

Figure S3. Isosurfaces of the most relevan! molecular orbitals (besides HOMO and LUMO) participating on SD excitations of non-negligible CI coefficients for each of the six titania nanostructures (see Table Sl). In order to show representative cases of **TD-DFT** calculations based on hybrid functionals, the top row corresponds to geometries sampled from PBE/TD-PBE0 methodologies, while bottom geometries were sampled from PBE/TD-B3LYP results. Isosurface values are 0.012 A-^{113} (tan) and -0.012 A-^{113} **(white). Multiwfn software[1] was employed to generate the isosurfaces. Atom key: O- red, Ti -brown, H-white.**

Table SI. Square of the the largest CI coefficients for the first excited state relevan! to each nuclear generation methodology and **DFT** functional. Reference geometries have been sampled from the 3000 fs geometries.

Mcthod\Systcm	(Tl02)4	(Ti02)4(H20h	(Ti02J.(H20)4	(Tl02)s	(Ti02)s(H20h	(Ti02)s(H20)s
PBEffD-PBE	HOMO-LUM0(0.995)	HOMO- LUMO (0.967)	HOMO- LUMO (0.962)	HOMO-LUM0(0.990)	HOMO - LUMO (0.951)	HOMO- LUMO (0.980)
PBEffD-PBEO	HOMO-LUM0(0.712) HOMO-I LUM0(0.104)	HOMO- LUM0(0.612) HOMO-1 LUMo+-I (0.144)	HOMO- LUMO (0.614) HOMO - LUMO+3 (0.202)	HOMO-LUM0(0.726) HOMO-1-LUM0(0.064)	HOMO - LUMO (0.681) H0/-.10-1 - LUMO (0.193)	HOMO - LUMO (0.527) HOMO-J- LUMO (0.179) HOMO-1- LUMO (0.162)
PBEffD-B3LVP	HOMO-LUM0(0.807)	HOMO - LUMO (0.686) HOMO-LUMOtI (Cl.186)	HOMO - LUMO (0.713) HOMO-1 - LUMO (0.182)	HOMO-LUM0(0.789) HOMO-LUMo+2 (0.124)	HOMO-LUMO (0.748) HOMO-LUM0+-1 (0.125)	HOMO - LUMO (0.610) HOMO-2 - LUMO (0.116)
FFffD-PBE	HOMO-LUM0(0.994)	HOMO- LUMO (0.8%)	HOMO - LUMO (0.966)	HOMO-LUM0(0.840)	HOMO - LUMO (0.990)	HOMO - LUMO (0.987)
FFffD-PBEO	HOMO-LUM0(0.966)	HOMO- LUMO (0.691) HOM0-1 - LUMO (Cl.098)	HOMO - LUMO (O.758)	HOMO-!-LUM0(0.737) HOMO-LUM0(0.206)	HOMO- LUMO (0.726) HOMO-LUM0-+-3 (0.203)	HOMO - LUMO (0.601) HOMO-LUM0-+-2 (0.146) HOMO - LUMo+! (0.145)
FFffD-B3LYP	HOMO-LUM0(0.977)	I-IOMO - LUMO (O.749) HOMO-! - LUMO (').!03)	HOMO- LUMO (0.8(12)	MOMO-LUM0(0.746) HOM0-1-LUM0(0.225)	HOMO - LUMO (0.789) HOMO-LUMo+2 (0.171)	I-IOMO- LUM0(0.703) HOMO- LUMO+1 (0.160)

Table S2. Total dipole moments of So / S1 states or ali systems in Debye units (AIMD-based **nuclear** trajectories' **values).**

Method\Systern	(Ti0z)4	(TiOz)4(HzO)z	(TiOz).(Hz0)4	(TiOz)s	(TiOz)s(HzOlz	($Ti0_2$)s(HzO)s
PBE/TD--PBE	6.30/ 3.7	2.5215.72	3.09 /0.49	1.36/ 8.37	5.35 / 1.95	1.27 / 0.90
PBE/TD-PBEO	6.77 / 5.14	2.65 / 5.44	3.28 / 1.46	1.87 / 6.77	5.48/ 1.07	1.39/0.33
PBErfD-B3LYP	6.64 / 4.89	2.62 / 5.73	3.23 / 1.21	1.82 / 7.99	5.47 / 1.29	1.35/0.15
FFn"D-PBE	7.30/5.52	1.60/2.30	1.4212.45	0.54/7.77	11.49/2,02	2.93/4.06
FFrfD-PBEO	7.91/6.31	1.i2/2.31	1.64/2.35	0.64/8.17	12.06/2.42	2.99/1.92
FFrfD-BJLYP	7.75/6.18	1.69/2.29	1.60/2.45	0.62/8.15	11.98/1.63	2.97/1.93

Table S3. First excited state energy and its variation for ali the studied systems as computed with **different methodologies.** Units are **expressed in eV.**

Method\Systern	(Ti0z)4	(TiOz)4(HzOlz	(TiOz).(Hz0)4	(TiOz)s	(TiOz)s(HzOlz	($Ti0_2$)s(HzO)s
PBE/TD-PBE	2.57±0.20	3.58±0.13	3.55±0.21	2.40±0.21	2.75±0.20	3.32±0.13
PBE/TD-PBEO	3.73±0.16	4.68±0.12	4.71±0.14	3.73±0.20	4.03±0.19	4.51±0.12
PBE/TD-B3LYP	**3.45±0.17**	**4.43±0.12**	4.41±0.15	**3.42±0.21**	**3.73±0.20**	**4.22±0.12**
FF/TD-PBE	**1.73±0.16**	**3.53±0.09**	3.74±0.12	**1.31±0.16**	**1.82±0.22**	**3.17±0.16**
FF/TD-PBEO	3.01±0.19	4.46±0.10	4.78±0.11	2.66±0.24	3.16±0.26	4.36±0.13
FF/TD-B3LYP	2.66±0.18	4.24±0. 10	4.53±0.11	2.05±0.22	2.84±0.25	4.05±0.14

Table S4. Nonadiabatic couplings between ground and first excited states (NAC0,) and its variation for ali the studied systems as computed with different methodologies. Units are expressed in meV.

Mcthod\System	(TWz)4	(Ti02)4(H20lz	(Ti02J.CH20)4	(TiOz)e	(Ti02)e(H20lz	(Ti02)e(H20ls
PBE/TD-PBE	0.305±0.089	0.439±0.124	0.544±0.154	0.346±0.100	0.325±0.096	0.562±0.158
PBErTD-PBEO	0.298±0.084	O.743±0.209	0.754±0.218	0.289±0.080	0.293±0.087	0.811±0.231
PBErTD-B3LYP	0.254±0.072	0.580±0.161	0.645±0.187	0.315±0.091	0.270±0.081	0.804±0.229
FF/TD-PBE	0.329±0.090	0.552±0.155	0.830±0.252	0.455±0.127	0.244±0.070	0.747±0.228
FFrTD-PBEO	0.171±0.0SI	O.793±0.220	0.959±0.294	0.289±0.080	0.182±0.053	0.935±0.284
FFrTD-B3L YP	0.180±0.054	o.721 ±0.204	1.050±0.322	0.333±0.092	0.203±0.058	0.931±0.282

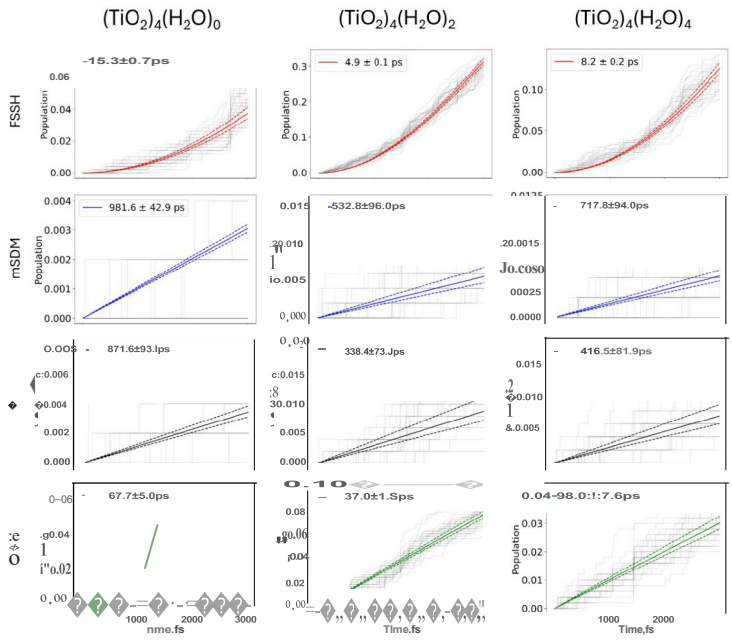

Figure S4. Evolution ofthe ground state S_0 population far AIMD nuclear trajectories of $(TiO_2)_4$ nanostrucures. PBE functional selected as the underlying functional far computing the TD-DFT excitations. Red, blue, black, and green colored lines represen! FSSH, mSDM, IDA and DISH TSH schemes, respectively. The average population far each case is shown in bold lines, whereas background faded lines represen! the population dynamics far each initial condition (excited state + nuclear trajectory).

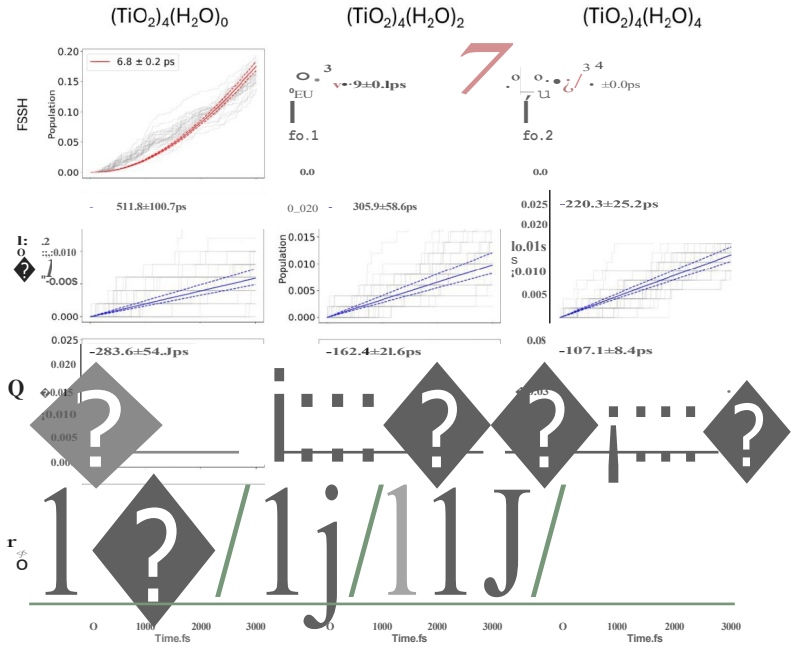

Figure SS. Evolution of the ground state S_0 population for AIMD nuclear trajectories of $(TiO_2)_4$ nanostrucures. PBE0 functional selected as the underlying functional for computing the TD-DFT excitations. Red, blue, black, and green colored lines represen! FSSH, mSDM, IDA and DISH TSH schemes, respectively. The average population for each case is shown in bold lines, whereas background faded lines represen! the population dynamics for each initial condition (excited state + nuclear trajectory).

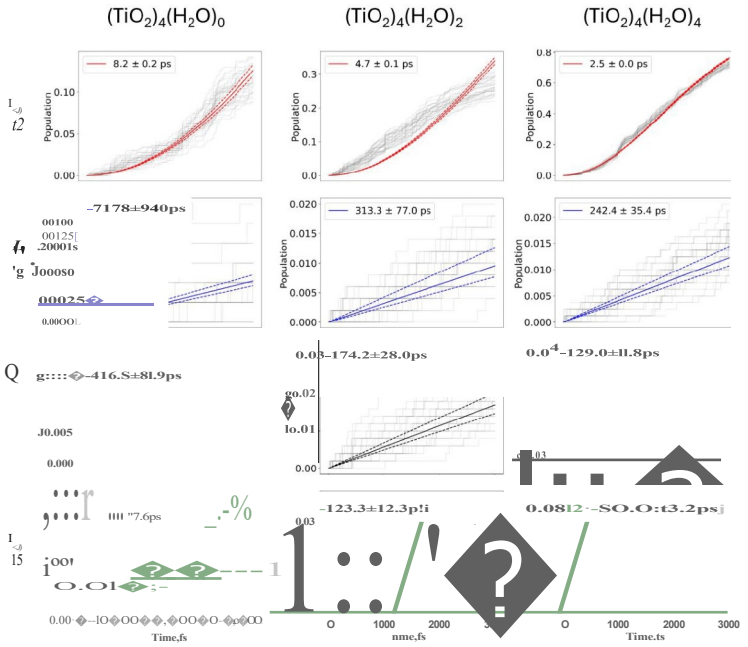

Figure S6. Evolution ofthe ground state S_0 population far AIMD nuclear trajectories of $(TiO_2)_4$ nanostrucures. B3LYP functional selected as the underlying functional far computing the TD-DFT excitations. Red, blue, black, and green colored lines represen! FSSH, mSDM, IDA and DISH TSH schemes, respectively. The average population far each case is shown in bold lines, whereas background faded lines represen! the population dynamics far each initial condition (excited state + nuclear trajectory).

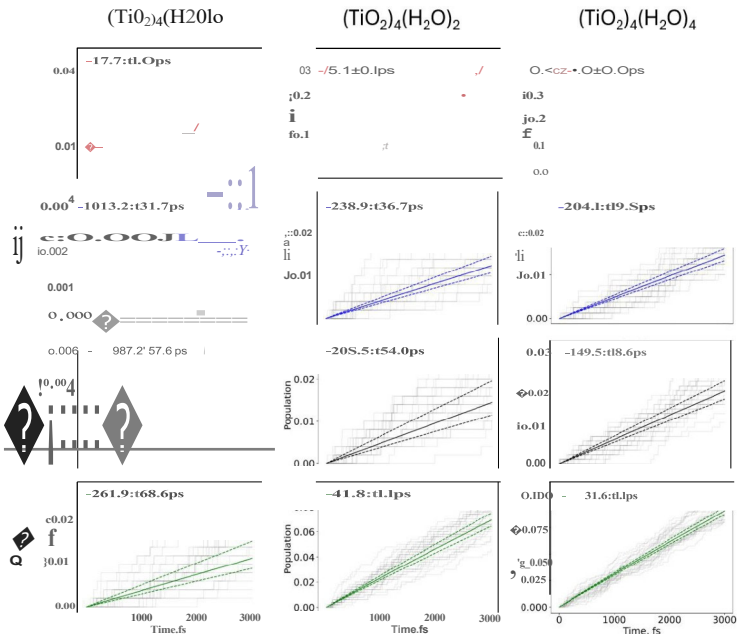

Figure S7. Evolution of the ground state S_0 population for ffMD nuclear trajectories of (Ti0$_{2)4}$ nanostrucures. PBE functional selected as the underlying functional for computing the TD-DFT excitations. Red, blue, black, and green colored lines represen! FSSH, mSDM, IDA and DISH TSH schemes, respectively. The average population for each case is shown in bold lines, whereas background faded lines represen! the population dynamics for each initial condition (excited state + nuclear trajectory).

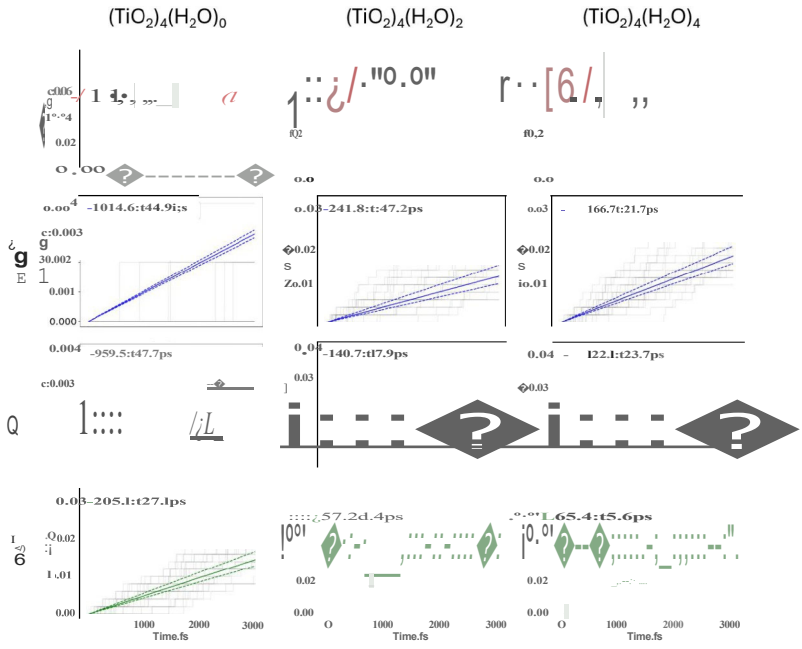

Figure S8. Evolution ofthe ground state S_0 population for ffMD nuclear trajectories of $(TiO_2)_4$ nanostrucures. PBE0 functional selected as the underlying functional for computing the TD-DFT excitations. Red, blue, black, and green colored lines represen! FSSH, mSDM, IDA and DISH TSH schemes, respectively. The average population for each case is shown in bold lines, whereas background faded lines represen! the population dynamics for each initial condition (excited state + nuclear trajectory).

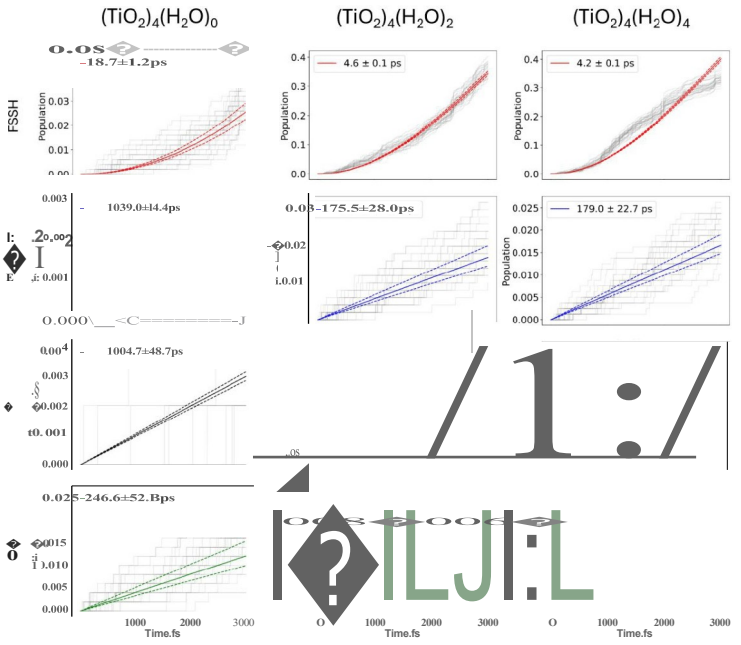

Figure S9. Evolution of the ground state S_0 population for ffMD nuclear trajectories of $(TiO_2)_4$ nanostrucures. B3LYP functional selected as the underlying functional for computing the TD-DFT excitations. Red, blue, black, and green colored lines represen! FSSH, mSDM, IDA and DISH TSH schemes, respectively. The average population for each case is shown in bold lines, whereas background faded lines represen! the population dynamics for each initial condition (excited state + nuclear trajectory).

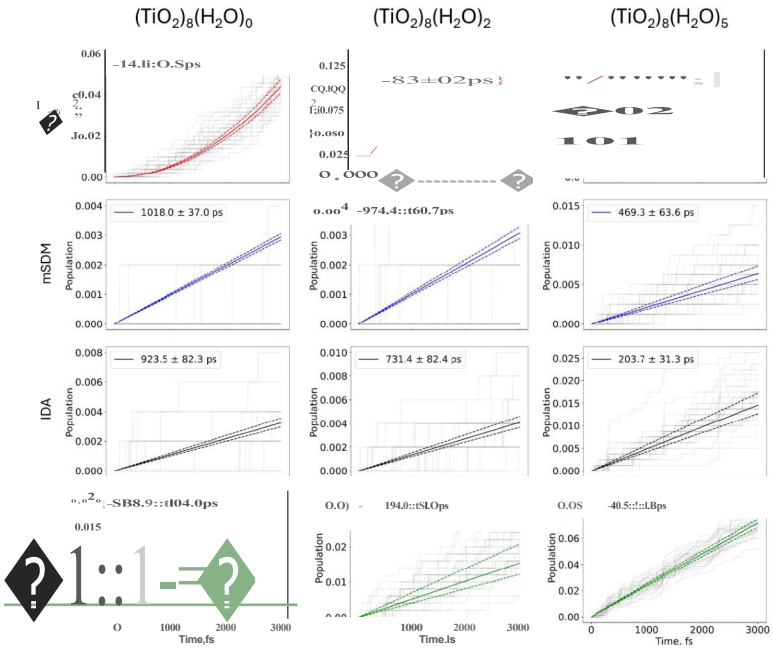

Figure S10. Evolution of the ground state S_0 population for AIMD nuclear trajectories of $(TiO_2)_8$ nanostrucures. PBE functional selected as the underlying functional for computing the TD-DFT excitations. Red, blue, black, and green colored lines represen! FSSH, mSDM, IDA and DISH TSH schemes, respectively. The average population for each case is shown in bold lines, whereas background faded lines represen! the population dynamics for each initial condition (excited state + nuclear trajectory).

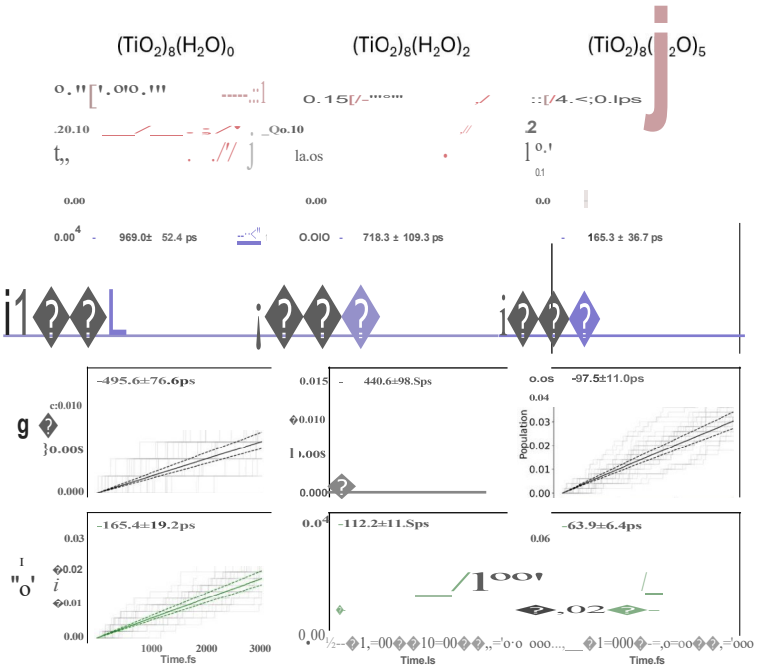

Figure S11. Evolution of the ground state S_0 population for AIMD nuclear trajectories of $(TiO_2)_8$ nanostrucures. PBE0 functional se\ected as the underlying functional for computing the TD-DFT excitations. Red, blue, black, and green colored lines represen! FSSH, mSDM, IDA and DISH TSH schemes, respectively. The average population for each case is shown in bold lines, whereas background faded lines represen! the population dynamics for each initial condition (excited state + nuclear trajectory).

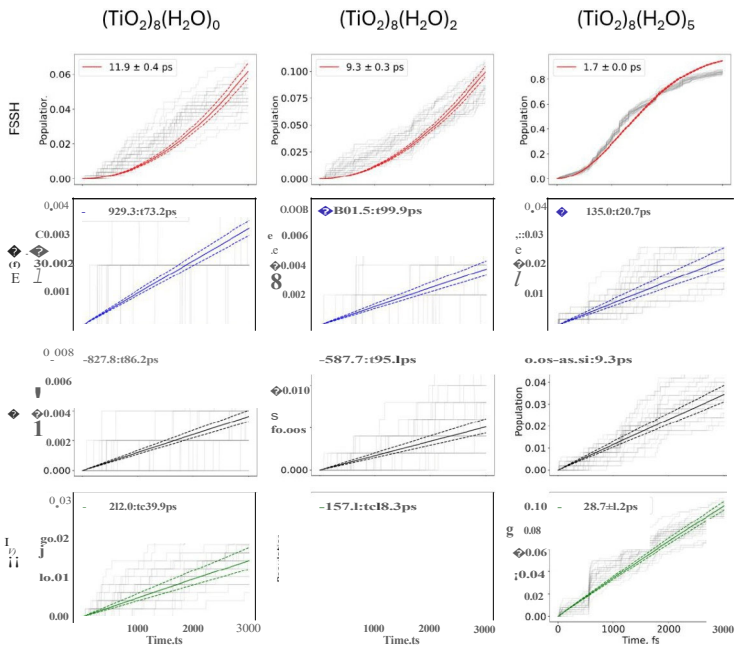

Figure S12. Evolution of the ground state S_0 population for AIMD nuclear trajectories of $(TiO_2)_8$ nanostrucures. B3LYP functional selected as the underlying functional for computing the TD-DFT excitations. Red, blue, black, and green colored lines represen! FSSH, mSDM, IDA and DISH TSH schemes, respectively. The average population for each case is shown in bold lines, whereas background faded lines represen! the population dynamics for each initial condition (excited state + nuclear trajectory).

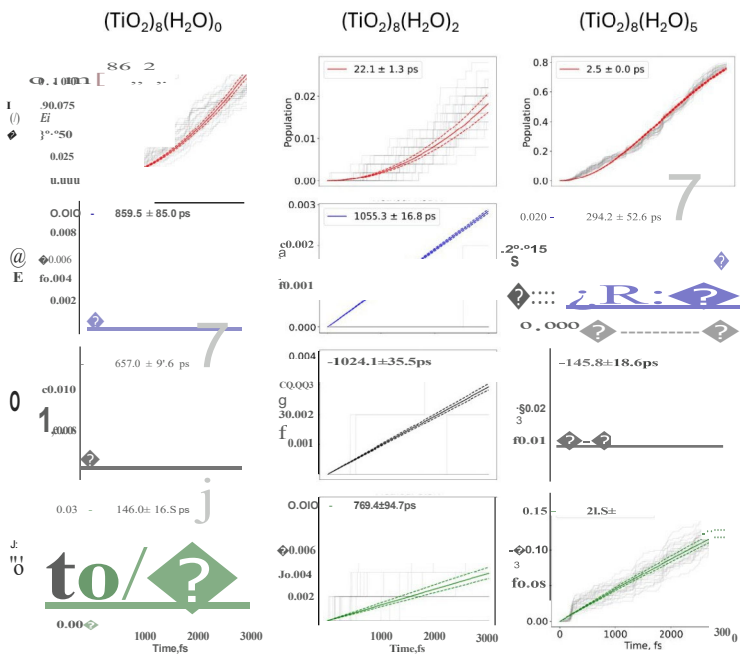

Figure S13. Evolution ofthe ground state S_0 population for ffMD nuclear trajectories of $(TiO_2)_8$ nanostrucures. PBE functional selected as the underlying functional for computing the TD-DFT excitations. Red, blue, black, and green colored lines represen! FSSH, mSDM, IDA and DISH TSH schemes, respectively. The average population for each case is shown in bold lines, whereas background faded lines represent the population dynamics for each initial condition (excited state + nuclear trajectory).

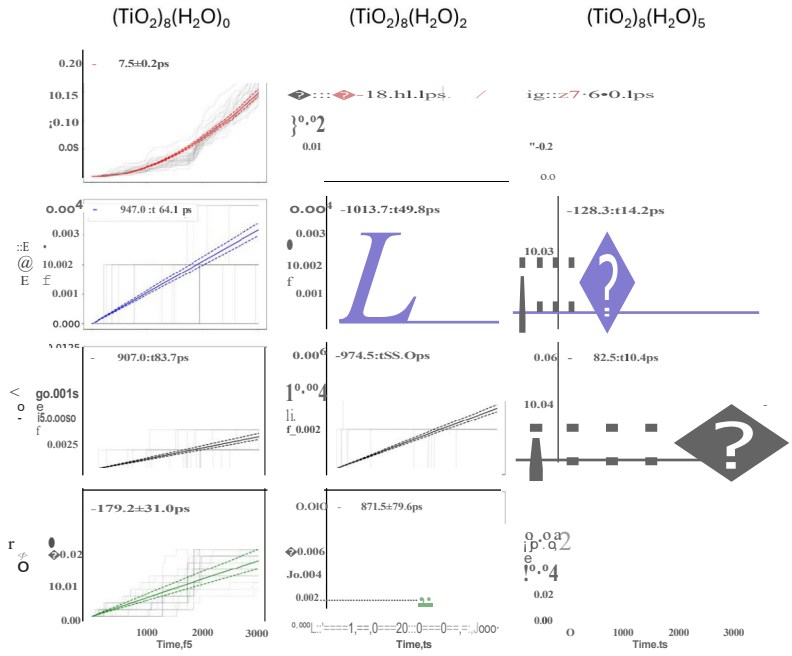

Figure S14. Evolution ofthe ground state S_0 population for ffMD nuclear trajectories of $(TiO_2)_8$ nanostrucures. PBE0 functional selected as the underlying functional for computing the TD-DFT excitations. Red, blue, black, and green colored lines represen! FSSH, mSDM, IDA and DISH TSH schemes, respectively. The average population for each case is shown in bold lines, whereas background faded lines represen! the population dynamics for each initial condition (excited state + nuclear trajectory).

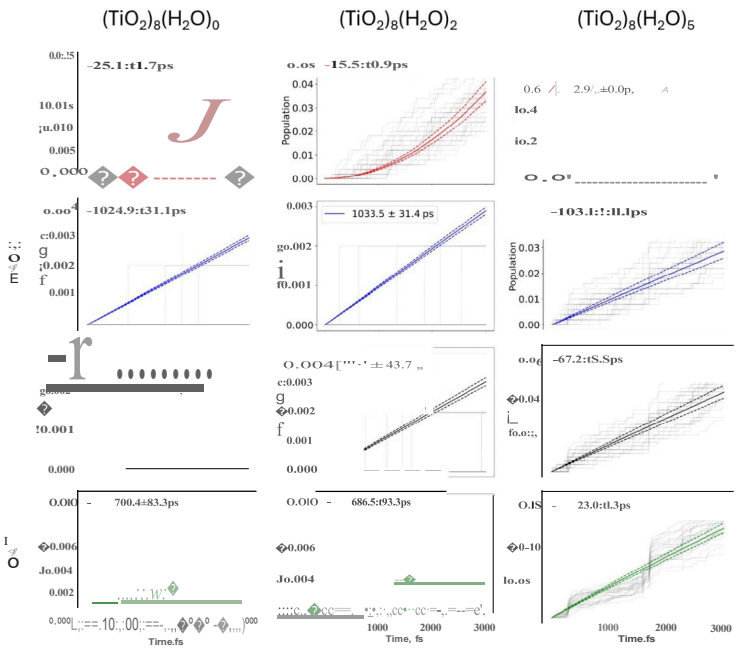

Figure S15. Evolution ofthe ground state S_0 population for ffMD nuclear trajectories of $(TiO_2)_8$ nanostrucures. B3LYP functional selected as the underlying functional for computing the TD-DFT excitations. Red, blue, black, and green colored lines represen! FSSH, mSDM, IDA and DISH TSH schemes, respectively. The average population for each case is shown in bold lines, whereas background faded lines represen! the population dynamics for each initial condition (excited state + nuclear trajectory).

References

(1) Lu, T.; Chen, F. Multiwfn: A multifunctional wavefunction analyzer. *J. Comput. Chem.* **2012,** *33,* 580-592.